Magnetic Reconnection and Particle Acceleration in Semi-Collisional Plasmas

A thesis submitted to the University of Manchester
for the degree of Doctor of Philosophy
in the Faculty of Engineering and Physical Sciences

2013

Adam Stanier
School of Physics and Astronomy

Contents

Word count: 45719

List of Tables

List of Figures

The University of Manchester

Doctor of Philosophy

Adam Stanier

Magnetic Reconnection and Particle Acceleration in Semi-Collisional Plasmas

October 18, 2013

Magnetic reconnection is an important mechanism for the restructuring of magnetic fields, and the conversion of magnetic energy into plasma heating and non-thermal particle kinetic energy in a wide range of laboratory and astrophysical plasmas. In this thesis, reconnection is studied in two semi-collisional plasma environments: flares in the solar corona, and the start-up phase of the Mega-Ampere Spherical Tokamak (MAST) magnetic confinement device. Numerical simulations are presented using two different plasma descriptions; the test-particle approach combined with analytical magnetohydrodynamic fields is used to model populations of high-energy particles, and a two-fluid approach is used to model the bulk properties of a semi-collisional plasma.

With the first approach, a three-dimensional magnetic null-point is examined as a possible particle acceleration site in the solar corona. The efficiency of acceleration, both within the external drift region and in the resistive current sheet, is studied for electrons and protons using two reconnection models. Of the two models, it is found that the fan-reconnection scenario is the most efficient, and can accelerate bulk populations of protons due to fast and non-uniform electric drifts close to the fan current-sheet. Also, the increasing background field within the fan-current sheet is shown to stabilise particle orbits, so that the energy gain is not limited by ejection.

With the second approach, the effects of two-fluid physics on merging flux-ropes is examined, finding fast two-fluid tearing-type instabilities when the strength of dissipation is weak. The model is then extended to the tight-aspect ratio toroidal-axisymmetric geometry of the MAST device, where the final state after merging is a MAST-like spherical tokamak with nested flux-surfaces and a monotonically increasing q-profile. It is also shown that the evolution of simulated 1D radial density profiles closely resembles the Thomson scattering electron density measurements in MAST. An intuitive explanation for the origin of the measured density structures is proposed, based upon the results of the toroidal Hall-MHD simulations.

Declaration

No portion of the work referred to in this thesis has been submitted in support of an application for another degree or qualification of this or any other university or other institution of learning.

Copyright Statement

Acknowledgements

I am deeply grateful to my supervisor Philippa Browning for her support, continuous motivation, and invaluable guidance throughout these three years. I would also like to thank my other collaborators; Silvia Dalla, Mykola Gordovskyy, Ken McClements, Mikhail Gryaznevich, and, in particular, Slava Lukin for all of their patience and helpful suggestions during the course of this work. Additional thanks to STFC for funding my PhD, and the examiners Erwin Verwichte and Paddy Leahy for their helpful suggestions on how to improve this thesis.

The majority of the simulations presented in this thesis were performed on three computer clusters; the STEL-lab supercomputer at Nagoya University, the COMA cluster at Jodrell Bank Centre for Astrophysics, and the UK-MHD cluster at St-Andrews university. Thanks go to Kanya Kusano, Takayuki Umeda, Anthony Holloway, Bob Dickson, Herbert Früchtl, and Keith Bennett for access to these machines and advice on how to speed up computations.

I would further like to thank Kanya Kusano, Motoko Kunieda and all the STEL-lab students at Nagoya University for making me feel welcome on my visit there in March 2013, and Yasushi Ono at University of Tokyo for showing me around the TS3/4 labs in the same trip. Also, thanks to the students from Tokyo who visited Culham on many occasions and with who I was able to discuss the merging-compression data; Hiroshi Tanabe, Takuma Yamada, Keii Gi and Takenori Watanabe.

Finally, I would like to thank my parents and sisters for all their support, and a special thanks to Citlalitl.

Supporting Publications

- **Solar particle acceleration at reconnecting 3D null points**
  A. Stanier, P. Browning and S. Dalla, A&A, 542, A47 (2012)

- **Two-fluid simulations of driven reconnection in the Mega-Ampere Spherical Tokamak**
  A. Stanier, P. Browning, M. Gordovskyy, K. G. McClements,
  M. P. Gryaznevich and V. S. Lukin, Phys. Plasmas (accepted)
  arXiv e-print at http://arxiv.org/abs/1308.2855

Chapter 1

Theoretical Background

In this thesis the phenomena of magnetic reconnection, plasma heating and charged particle acceleration by associated large-scale electric fields are studied in two different plasma environments. The first is a fully three-dimensional magnetic reconnection site within a solar flare current sheet, and the second is magnetic flux-rope merging within the start-up phase of a spherical tokamak magnetic confinement device. Before these applications are described in more detail in Chapter 2, it is important to review some basic theory relating to these phenomena. This will then be utilised throughout the remainder of the thesis.

Firstly, the adiabatic motion of single charged particles within electromagnetic fields will be described, and possible mechanisms of particle acceleration will be identified. Then, several commonly used two-fluid and one-fluid descriptions of a magnetised plasma will be introduced, and used to describe collisional and collisionless reconnection models in two-dimensional magnetic field configurations. Finally, reconnection in fully 3D configurations will be discussed, and previous work on particle acceleration within these configurations will be summarised.

1.1 Charged particle motion

The non-relativistic motion of a charged particle within the electric and magnetic fields, $\boldsymbol{E}(t,\boldsymbol{x})$ and $\boldsymbol{B}(t,\boldsymbol{x})$ respectively, is given by the equations of motion

$$\frac{d\boldsymbol{x}}{dt} = \boldsymbol{v}, \tag{1.1}$$

$$m_s\frac{d\boldsymbol{v}}{dt} = q_s\left(\boldsymbol{E} + \boldsymbol{v}\times\boldsymbol{B}\right), \tag{1.2}$$

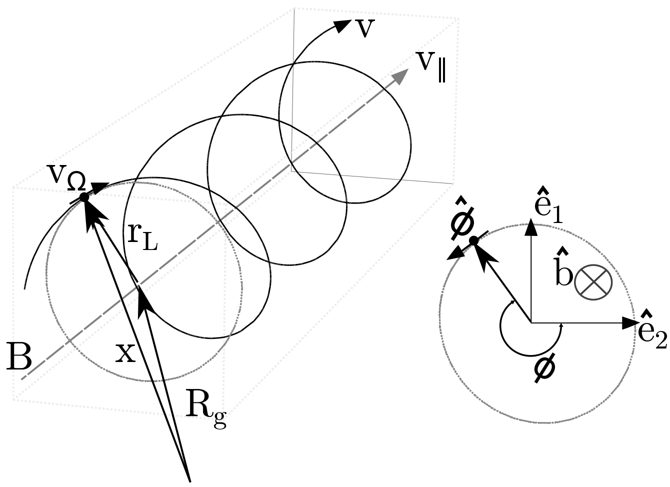

Figure 1.1: Left: Helical motion of a particle around a magnetic field-line in uniform magnetic field and no electric field. Right: Definition of the gyro-phase ϕ, and vector $\hat{\boldsymbol{\phi}}$, in terms of the basis set $(\hat{\boldsymbol{e}}_1, \hat{\boldsymbol{e}}_2, \hat{\boldsymbol{b}})$. Image adapted from de Blank (2008).

where t is time, $\boldsymbol{x}$ is the particle position, $\boldsymbol{v}$ is the velocity, q_s is the charge and m_s is the mass of species s ($s = i, e$ for ions or electrons respectively). A non-zero magnetic field introduces a characteristic anisotropy in the motion of the charged particle. In the absence of an electric field, $\boldsymbol{E} = \boldsymbol{0}$, the force acting on the particle is always perpendicular to both the velocity and the magnetic field direction (the latter direction is $\hat{\boldsymbol{b}} = \boldsymbol{B}/B$ where $B = |\boldsymbol{B}|$ is the field strength). If the magnetic field is uniform in space and time, the particle trajectory describes a helix around the magnetic field-line with constant velocity along the field-line, and a gyration around the field-line with a *cyclotron frequency* of $\Omega_{cs} = |q_s|B/m_s$ and *Larmor radius* $r_L = v_\Omega/\Omega_{cs}$, as shown in Figure 1.1.

It is often useful to describe the position of the particle in terms of its *guiding-centre*, $\boldsymbol{R}_g$, the Larmor radius (the distance from the guiding-centre to the true position), and a *gyro-phase* angle ϕ. The latter can be defined as shown in Figure 1.1 in reference to a set of orthonormal basis vectors $(\hat{\boldsymbol{e}}_\mathbf{1}, \hat{\boldsymbol{e}}_\mathbf{2}, \hat{\boldsymbol{b}})$ centred on the guiding-centre. The velocity can be decomposed into a parallel component, $v_\parallel \hat{\boldsymbol{b}} = (\boldsymbol{v} \cdot \hat{\boldsymbol{b}})\hat{\boldsymbol{b}}$, which for these fields remains constant, and a gyrating component, $\boldsymbol{v}_\Omega = v_\Omega \hat{\boldsymbol{\phi}}$, where v_Ω is also constant and $\hat{\boldsymbol{\phi}} = \hat{\boldsymbol{e}}_\mathbf{1} \cos\phi + \hat{\boldsymbol{e}}_\mathbf{2} \sin\phi$ is a basis vector, perpendicular to $\hat{\boldsymbol{b}}$, that rotates around the field.

A uniform electric field at arbitrary angle to the magnetic field alters the motion in two ways. Firstly, the particle can be directly accelerated along the magnetic field-line; $d_t v_\parallel = q_s E_\parallel / m_s$, where $E_\parallel = \boldsymbol{E} \cdot \hat{\boldsymbol{b}}$. Secondly, the component of the electric field perpendicular to the magnetic field causes acceleration and deceleration of the particle within each single gyration. This causes variation of r_L and a drift of the guiding-centre, given by the *electric-drift* velocity

$$\boldsymbol{v}_E = \frac{\boldsymbol{E} \times \boldsymbol{B}}{B^2}. \tag{1.3}$$

As this is perpendicular to the electric field, and $d_t m v^2/2 = \boldsymbol{v} \cdot q\boldsymbol{E}$, particles travelling along uniform electric drift streamlines do not increase their net energy. This is because during each gyration the energy gain (loss) in the first part of the gyration is cancelled exactly by energy loss (gain) in the remainder (however, this would not be the case if the electric field is not constant over the gyration). Also, the electric drift has the same direction and magnitude for protons and electrons, so it does not give rise to currents.

These effects form a complete description of charged particle motion in uniform and stationary electromagnetic fields. For non-uniform fields additional effects can be simply described if the Larmor radius, r_L, is much less than the length-scale of field variation, L. This branch of plasma physics is called *adiabatic theory*, and it is associated with the conservation of the magnetic moment per unit mass $\mu_m = v_\Omega^2/(2B)$.

If there is a gradient in magnetic field strength along a field-line, the *mirror-force* acts on the parallel momentum,

$$\boldsymbol{F}_M = -m_s \mu_m \nabla_\parallel B, \tag{1.4}$$

where $\nabla_\parallel = \hat{\boldsymbol{b}} \cdot \boldsymbol{\nabla}$. This can cause particles to be reflected, or *mirror bounce*, when entering regions of stronger field, due to the constancy of μ_m. This behaviour is shown in Figure 1.2.

If $\boldsymbol{\nabla} B$ has a component perpendicular to $\boldsymbol{B}$ then r_L can vary over a gyration, leading to the *gradient drift* as shown in Figure 1.2. It is given by

$$\boldsymbol{v}_{\nabla B} = \frac{m_s \mu_m}{q_s B} \hat{\boldsymbol{b}} \times \boldsymbol{\nabla} B. \tag{1.5}$$

This has different sign for protons and electrons and so can give rise to currents, in contrast with the electric drift. In addition, if particles gradient drift in the direction of an electric field they can gain net energy. An example of this will be

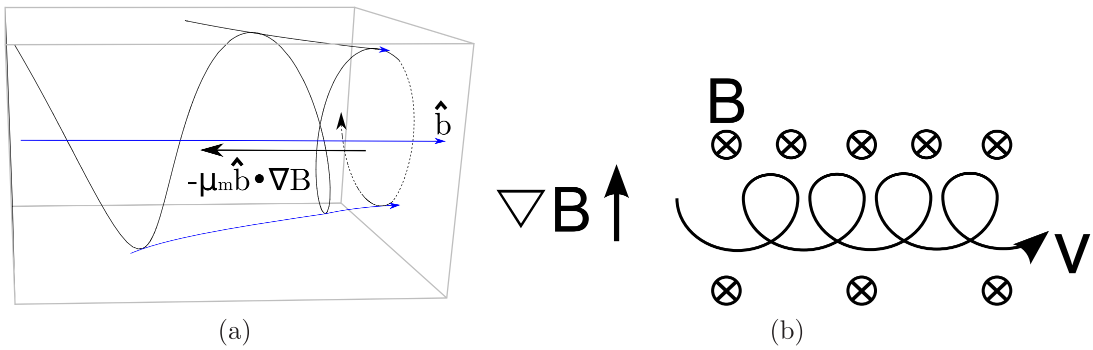

Figure 1.2: Left: Acceleration of a particle by the mirror force, due to converging magnetic field, leading to a mirror-bounce. Right: Magnetic gradient drift. The black line is a proton trajectory, where the arrow indicates the instantaneous velocity. The into-page magnetic field is indicated by crossed circles, and the direction of positive magnetic field gradient shown.

shown in Chapter 4.

Another drift associated with non-uniform magnetic fields is the curvature drift. This is given by

$$\boldsymbol{v}_c = \frac{mv_\parallel^2}{qB}\frac{\boldsymbol{R}_c \times \hat{\boldsymbol{b}}}{R_c^2} = \frac{mv_\parallel^2}{qB}\hat{\boldsymbol{b}} \times \nabla_\parallel \hat{\boldsymbol{b}}, \tag{1.6}$$

where $\boldsymbol{R}_c$ is the radius of curvature. This drift is related to the centrifugal force of a particle moving along highly curved magnetic field-lines (see e.g. de Blank 2008).

Finally, there may also be drifts associated with time dependent fields that are valid (the motion is adiabatic) provided that $\Omega_{cs}T \gg 1$, where T is the time-scale for change in the background fields. We will not list these here, as the fields used for the study of single-particle motion in this thesis are steady (see e.g. Wesson 2011, for a description of these drifts due to time varying fields).

All of these drifts can be found formally (see e.g. Northrop 1963) by substituting $\boldsymbol{x} = \boldsymbol{R}_g + \boldsymbol{r}_L$, where $\boldsymbol{r}_L = r_L(\hat{\boldsymbol{e}}_2 \cos\phi - \hat{\boldsymbol{e}}_1 \sin\phi) = \Omega^{-1}\hat{\boldsymbol{b}} \times (\boldsymbol{v} - \boldsymbol{v}_E)$ into equation (1.2), Taylor expanding about the guiding centre position $\boldsymbol{R}_g$ and then averaging out the gyro-phase, ϕ. This process is rather involved, so here we just give the end result that is valid up to first order in the small parameter r_L/L (in the dimensional form given here the small parameter is represented as m_s/q_s). The equations are

$$\frac{d\boldsymbol{R}_g}{dt} = \boldsymbol{v}_d + v_\parallel \hat{\boldsymbol{b}}, \tag{1.7}$$

$$\boldsymbol{v}_d = \boldsymbol{v}_E + \frac{m_s\mu_m}{q_s B}\hat{\boldsymbol{b}} \times \boldsymbol{\nabla} B + \frac{m_s}{q_s B}\hat{\boldsymbol{b}} \times \left(v_\parallel D_t \hat{\boldsymbol{b}} + D_t \boldsymbol{v}_E\right), \tag{1.8}$$

$$\frac{dv_\parallel}{dt} = \frac{q_s}{m_s}E_\parallel - \mu_m \nabla_\parallel B + \boldsymbol{v}_E \cdot D_t \hat{\boldsymbol{b}}, \tag{1.9}$$

$$\frac{d\mu_m}{dt} = \mathcal{O}(m_s/q_s), \tag{1.10}$$

where $\boldsymbol{v}_d$ is the perpendicular drift velocity of the gyro-centre, and $D_t = \partial_t + \boldsymbol{v}_d \cdot \boldsymbol{\nabla} + v_\parallel \nabla_\parallel \approx \partial_t + \boldsymbol{v}_E \cdot \boldsymbol{\nabla} + v_\parallel \nabla_\parallel$ is the derivative along the particle trajectory ($\boldsymbol{v}_d = \boldsymbol{v}_E + \mathcal{O}(m_s/q_s)$). With this definition, it can be seen that the curvature drift (1.6) is included in the third term on the right-hand-side of equation (1.8), along with other terms due to gradients in the electric field (and thus electric drift) that were not defined above.

There is also an assumption here on the parallel electric field $E_\parallel \sim \mathcal{O}(m_s/q_s)$. This is because the first term on the right hand side of equation (1.9) would be $\mathcal{O}((m_s/q_s)^{-1})$ if $E_\parallel \sim \mathcal{O}(1)$, which is the same order as the gyro-frequency Ω_{cs}.

The kinetic energy is given by Northrop (1963) as

$$\frac{d}{dt}\left(m_s v_\parallel^2/2 + m_s\mu_m B + m v_E^2/2\right) = (v_\parallel \hat{\boldsymbol{b}} + \boldsymbol{v}_d) \cdot q\boldsymbol{E} + m_s\mu_m \frac{\partial B}{\partial t} + \mathcal{O}((m/q)^2). \tag{1.11}$$

One thing to note is that, in contrast to electric drift in uniform fields, non-uniform electromagnetic fields can give rise to secondary drift terms proportional to $|\boldsymbol{v}_e|$, that can have a component parallel to $\boldsymbol{E}$. These secondary terms can be important when $E_\perp \sim \mathcal{O}(1)$.

1.2 A fluid description of a magnetised plasma

The previous section described some aspects of single particle motion within electromagnetic fields. The short range interaction forces (collisions) between particles, and the large scale fields that may be generated by their motions were neglected. Here, we describe the two-fluid and single-fluid models of a magnetised plasma, stating the commonly used assumptions that are used to derive these equations, which will then be used throughout this thesis.

The non-relativistic *two-fluid* equations, describing ion and electron fluids, can be derived by taking moments of the Boltzmann equation (for clear derivations, see e.g. Braginskii 1965; Goedbloed & Poedts 2004). They are given, up to the second moment as

$$\partial_t n_s + \nabla \cdot (n_s \boldsymbol{v}_s) = 0, \tag{1.12}$$

$$\partial_t (m_s n_s \boldsymbol{v}_s) + \nabla \cdot (m_s n_s \boldsymbol{v}_s \boldsymbol{v}_s + p_s \mathbb{I} + \boldsymbol{\pi}_s) = q_s n_s (\boldsymbol{E} + \boldsymbol{v}_s \times \boldsymbol{B}) + \boldsymbol{\Gamma}_s, \tag{1.13}$$

$$(\gamma - 1)^{-1} (\partial_t p_s + \boldsymbol{v}_s \cdot \nabla p_s + \gamma p_s \nabla \cdot \boldsymbol{v}_s) = -\boldsymbol{\pi}_s : \nabla \boldsymbol{v}_s - \nabla \cdot \boldsymbol{q}_s + W_s, \tag{1.14}$$

stating the conservation of mass, momentum and internal energy for species s respectively. Along with these, the non-relativistic Maxwell equations describe the electromagnetic fields

$$\nabla \times \boldsymbol{E} = -\partial_t \boldsymbol{B}, \tag{1.15}$$

$$\nabla \times \boldsymbol{B} = \mu_0 \sum_s q_s n_s \boldsymbol{v}_s \equiv \mu_0 \boldsymbol{j}, \tag{1.16}$$

$$\epsilon_0 \nabla \cdot \boldsymbol{E} = \sum_s q_s n_s, \tag{1.17}$$

$$\nabla \cdot \boldsymbol{B} = 0. \tag{1.18}$$

Here $s = i, e$ for the ion and electron species respectively, n_s is the number density of the species s, $\boldsymbol{v}_s$ is the bulk-flow velocity (we use $\boldsymbol{v}$ for both the single particle and bulk fluid velocities in this thesis, but it will always be clear which is being referred to), $\boldsymbol{j}$ is the current density and $\gamma = 5/3$ is the ratio of specific heats. The momentum change for particles of species s due to collisions with other species is given by $\boldsymbol{\Gamma}_s$, where $\boldsymbol{\Gamma}_e = -\boldsymbol{\Gamma}_i \equiv \boldsymbol{\Gamma}$ is required for total momentum conservation. The heat-flux is $\boldsymbol{q}_s$ and W_s is the heating term for species s. The total pressure tensor $\boldsymbol{P}_s$ has been written $\boldsymbol{P}_s = p_s \mathbb{I} + \boldsymbol{\pi}_s$, in terms of a thermal pressure scalar p_s multiplied by the identity matrix $\mathbb{I}$ (and assuming p_s is related to the temperature T_s via the ideal gas law $p_s = n_s k_B T_s$), and a trace-less stress tensor $\boldsymbol{\pi}_s$ which is responsible for viscous forces (due to like-particle collisions, and also a collisionless contribution for strongly magnetised plasmas, see Braginskii 1965).

To complete this set of equations $\boldsymbol{\Gamma}_s$, $\boldsymbol{q}_s$, $\boldsymbol{\pi}_s$ and W_s need to be defined. Formally, the heat flux $\boldsymbol{q}_s$ is a third-order moment of the distribution function, and would require an evolution equation derived from the third-order moment of the Boltzmann equation. In fact, this third-order equation would include a fourth-order moment term and so on, giving an infinite series of fluid equations. Fortunately, in some cases approximations can be made to define $\boldsymbol{\Gamma}_s$, $\boldsymbol{q}_s$, $\boldsymbol{\pi}_s$ and

W_s in terms of already known magnetohydrodynamic variables, such as gradients of the bulk velocity or magnetic field $\boldsymbol{B}$. Braginskii (1965) gives such an approximation (or closure) that is valid in the limit of short mean-free-path λ_s, where $\lambda_s \ll L$ (L is a typical macroscopic length-scale), and strongly-magnetised plasma $\Omega_{cs}\tau_s >> 1$, where τ_s is the collision time for a particle of species s and Ω_{cs} is the cyclotron frequency as defined previously.

In this thesis we do not use the full Braginskii (1965) formulation, as it is difficult to solve these equations both analytically and computationally at present (some codes have implemented part of the full Braginskii equations, e.g. the NIMROD code uses the full ion stress tensor, see Sovinec et al. 2004). The transport model we will use for our numerical simulations in Chapter 5 is therefore a compromise, which aims to keep some of the important aspects of the Braginskii model, while being simple enough to be solved numerically. For the present discussion on deriving the one-fluid equations we will drop the stress tensors and heat flux-vectors $\boldsymbol{\pi}_i = \boldsymbol{\pi}_e = \boldsymbol{q}_i = \boldsymbol{q}_e = 0$ (but we will include them in some form in Chapter 5), and we will make simplifying approximations for $\boldsymbol{\Gamma}$ and W_s. For $\boldsymbol{\Gamma}$ we keep just the resistive contribution

$$\boldsymbol{\Gamma} \approx n_e e \eta \boldsymbol{j}, \tag{1.19}$$

where $e = |q_e|$ is the fundamental charge and

$$\eta = \frac{m_e}{e^2 n_e \tau_e} \tag{1.20}$$

is the resistivity (this is actually the perpendicular resistivity, see e.g. Goedbloed & Poedts 2004, but we assume resistivity is isotropic in this thesis as there is only a factor of two difference in the anisotropic formulation). This is defined in terms of the electron collision time τ_e given by

$$\tau_e = 6\pi\sqrt{2\pi}\,\epsilon_0^2 \frac{m_e^{1/2}(k_B T_e)^{3/2}}{\ln\Lambda\, n_i\, e^4}, \tag{1.21}$$

where $\ln\Lambda \approx 20$ is the Coulomb logarithm, see Goedbloed & Poedts (2004). An important point here is that the resistivity has a strong inverse proportionality with the electron temperature, $\eta \propto T_e^{-3/2}$.

The heating terms W_s are the collisional heat exchange between the ion and electron fluids, and the electron heating term W_e also has a contribution due to resistive (Ohmic) heating

$$W_i = \frac{3n_e k_B (T_e - T_i)}{2\tau_{eq}}, \tag{1.22}$$

$$W_e = \eta j^2 - W_i, \tag{1.23}$$

where τ_{eq} is the time taken for the ion and electron fluids to relax to a single temperature, given by

$$\tau_{eq} = \frac{m_i}{2m_e}\tau_e. \tag{1.24}$$

The set of Hall-Magnetohydrodynamic (Hall-MHD) equations are an intermediate step between the two-fluid equations and the single-fluid equations. The first assumption used is called *quasi-neutrality*: that charge densities are equal, and $n_i = n_e = n$ assuming a singly-charged ion species. This quasi-neutrality condition holds provided the plasma is large and dense enough to neutralise applied electric potentials, which is typically well satisfied on a macroscopic fluid scale. Thus equation (1.17) can be neglected, and (1.12) can be written for just a single species, noticing that $\boldsymbol{\nabla} \cdot \boldsymbol{\nabla} \times \boldsymbol{B} = 0$ implies $\boldsymbol{\nabla} \cdot (n\boldsymbol{v}_i) = \boldsymbol{\nabla} \cdot (n\boldsymbol{v}_e)$ from equation (1.16). The second set of equations are the components of total momentum, which are found by summing the components of the ion and electron momentum equations (1.13). The third set of equations are just the electron momentum equations. Assuming electron inertial effects are small, setting $m_e \to 0$ where m_e appears explicitly, and defining $\boldsymbol{v} = \boldsymbol{v}_i$ as the ion velocity (the centre of mass velocity when $m_e = 0$) gives

$$\partial_t n + \boldsymbol{\nabla} \cdot (n\boldsymbol{v}) = 0, \tag{1.25}$$

$$\partial_t (m_i n \boldsymbol{v}) + \boldsymbol{\nabla} \cdot (m_i n \boldsymbol{v}\boldsymbol{v}) = \boldsymbol{j} \times \boldsymbol{B} - \boldsymbol{\nabla}(p_i + p_e), \tag{1.26}$$

$$\boldsymbol{E} + \boldsymbol{v}_e \times \boldsymbol{B} = -\frac{1}{ne}\boldsymbol{\nabla} p_e + \eta \boldsymbol{j} \tag{1.27}$$

Strictly, the Hall-MHD equations should keep the separate energy equations

$$(\gamma - 1)^{-1}\left[\partial_t p_e + \boldsymbol{v}_e \cdot \boldsymbol{\nabla} p_e + \gamma p_e \boldsymbol{\nabla} \cdot \boldsymbol{v}_e\right] = \eta j^2 - \frac{3n_e k_B (T_e - T_i)}{2\tau_{eq}}, \tag{1.28}$$

$$(\gamma - 1)^{-1}\left[\partial_t p_i + \boldsymbol{v}_i \cdot \boldsymbol{\nabla} p_i + \gamma p_i \boldsymbol{\nabla} \cdot \boldsymbol{v}_i\right] = \frac{3n_e k_B (T_e - T_i)}{2\tau_{eq}}, \tag{1.29}$$

where the electron flow advects the electron pressure, and the ion flow advects the ion pressure. However, it is sometimes useful to use just a single pressure equation, given by

$$(\gamma-1)^{-1}\left[\partial_t(p_i+p_e)+\boldsymbol{v}\cdot\boldsymbol{\nabla}(p_i+p_e)+\gamma(p_i+p_e)\boldsymbol{\nabla}\cdot\boldsymbol{v}\right]=\eta j^2. \tag{1.30}$$

The neglected terms are small provided $|\boldsymbol{j}/ne| \ll \boldsymbol{v}$ (see e.g. Goedbloed & Poedts (2004) for a more thorough description of this ordering). If p_e is assumed to be proportional to p_i ($p_e/p_i = c$ where c is a constant of proportionality), then only one pressure $p = p_i + p_e$ needs to be solved for, and the term $\boldsymbol{\nabla} p_e = c/(c+1)\boldsymbol{\nabla} p$.

Equations (1.25-1.27) and (1.30), along with the remaining Maxwell's equations (1.15-1.16) and (1.18), are the Hall-MHD equations. At this point it is useful to make these equations dimensionless, and define the important dimensionless parameters of Hall-MHD. This is done by replacing every dimensional variable χ by $\chi = \chi_0\tilde{\chi}$, where χ_0 is a typical value for that variable and $\tilde{\chi}$ is the normalised variable. Choosing $v_0 = L_0/\tau_0 = B_0/\sqrt{\mu_0 n_0 m_i}$ (this v_0 is the *ion Alfvén velocity*, an important fluid velocity), $p_0 = B_0^2/\mu_0$ (so that the dimensionless pressure is half the *plasma-beta*, the ratio of the thermal and magnetic pressures: $\beta = 2\mu_0 p/B^2$, at the location where $B = B_0$), $j_0 = B_0/(\mu_0 L_0)$ and $E_0 = v_0 B_0$ gives

$$\partial_{\tilde{t}}\tilde{n}+\tilde{\boldsymbol{\nabla}}\cdot(\tilde{n}\tilde{\boldsymbol{v}})=0, \tag{1.31}$$

$$\tilde{n}(\partial_{\tilde{t}}\tilde{\boldsymbol{v}}+\tilde{\boldsymbol{v}}\cdot\tilde{\boldsymbol{\nabla}}\tilde{\boldsymbol{v}})=\tilde{\boldsymbol{j}}\times\tilde{\boldsymbol{B}}-\tilde{\boldsymbol{\nabla}}\tilde{p}, \tag{1.32}$$

$$\tilde{E}+\tilde{v}\times\tilde{\boldsymbol{B}}=\frac{\tilde{d}_i}{\tilde{n}}\left(\tilde{\boldsymbol{j}}\times\tilde{\boldsymbol{B}}-\tilde{\boldsymbol{\nabla}}\tilde{p}_e\right)+\tilde{\eta}\tilde{\boldsymbol{j}}, \tag{1.33}$$

$$(\gamma-1)^{-1}\left(\partial_{\tilde{t}}\tilde{p}+\tilde{\boldsymbol{v}}\cdot\tilde{\boldsymbol{\nabla}}\tilde{p}+\gamma\tilde{p}\tilde{\boldsymbol{\nabla}}\cdot\tilde{\boldsymbol{v}}\right)=\tilde{\eta}\tilde{j}^2, \tag{1.34}$$

where there are two important dimensionless parameters; the normalised resistivity, $\tilde{\eta} = \eta/(v_0\mu_0 L_0)$, and the normalised ion skin-depth, $\tilde{d}_i = v_0 m_i/(eB_0\,L_0)$. Note the dimensional ion-skin depth, also known as the ion-inertial length, is the distance beneath which the ion and electron fluids decouple (see below). It is given by

$$d_i=\frac{v_A}{\Omega_{ci}}, \tag{1.35}$$

where $v_A = B/B_0\sqrt{n_0/n}\,v_0$ is the local ion Alfvén velocity. We have also used the conservation of mass equation (1.31) to rewrite the momentum equation (1.32) in another commonly used form, and replaced the electron velocity by the normalised version of equation (1.16) as $\tilde{\boldsymbol{v}}_e = \tilde{\boldsymbol{v}}_i - \tilde{d}_i \tilde{\boldsymbol{j}}/\tilde{n}$. Equation (1.33) is often called Ohm's law, as it relates the electric field $\boldsymbol{E}$ to the current density $\boldsymbol{j}$.

The single-fluid equations, also known as the equations of *resistive MHD*, are obtained from (1.31-1.34) in the limit $d_i/n \to 0$ (from now on we drop the tilde notation). If, in addition, $\eta \to 0$, the equations are then called the *ideal MHD* equations. In astrophysical plasmas these limits can often be achieved because the global length scale L_0 is incredibly large. However, the single-fluid models are always only an approximation to the Hall-MHD equations, which in turn are an approximation to the two-fluid equations. For example, the electron inertia, which was neglected in the simplification of the two-fluid to Hall-MHD equations, becomes important at a scale called the electron skin-depth

$$d_e = \sqrt{m_e/m_i}\, d_i. \tag{1.36}$$

Even in large-scale astrophysical environments, thin (and/or low density) structures may form which the ideal or resistive-MHD models cannot describe well.

1.3 Magnetic reconnection

1.3.1 Frozen-in flux and magnetic reconnection

An important conservation property of the ideal MHD equations is called the *frozen-in field theorem*. Here a brief derivation will be given, see Chapter 2 of Birn & Priest (2007) for a thorough discussion of this theorem and a more exact definition of magnetic reconnection. The frozen-in theorem can be found from Faraday's law (1.15) and the ideal form ($d_i = \eta = 0$) of Ohm's law (1.33), that is $\boldsymbol{E} + \boldsymbol{v} \times \boldsymbol{B} = \boldsymbol{0}$. Consider a control volume that is deformed by the plasma flow field, the rate of change of flux through that control volume is given by

$$\partial_t \int_S \boldsymbol{B} \cdot \boldsymbol{dS} = \int_S (\partial_t \boldsymbol{B}) \cdot \boldsymbol{dS} + \int_S \boldsymbol{B} \cdot \partial_t \boldsymbol{dS} = \int \boldsymbol{v} \times \boldsymbol{B} \cdot \boldsymbol{dl} + \int \boldsymbol{B} \cdot \boldsymbol{v} \times \boldsymbol{dl} = 0, \tag{1.37}$$

after substitution of $\partial_t \boldsymbol{B} = \boldsymbol{\nabla} \times (\boldsymbol{v} \times \boldsymbol{B})$ and application of Stokes law on the first integral, and using $d(\boldsymbol{dS}) = \boldsymbol{v} dt \times \boldsymbol{dl}$ on the second integral (as the control volume is frozen into the fluid flow). Thus, not only is the control volume frozen into the flow, but also the magnetic flux through that control volume is constant. As the

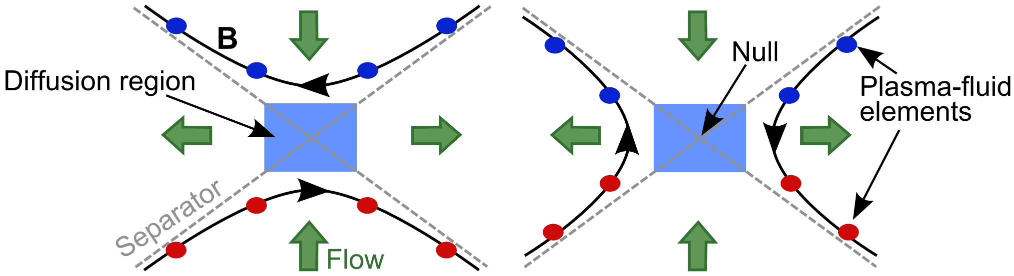

(a) Before reconnection (b) After reconnection

Figure 1.3: A magnetic field-line before and after reconnection at an x-type magnetic null point (x-point). The solid black lines are magnetic field-lines, the dashed grey lines are the separators, which intersect at the null. The solid circles represent plasma fluid elements, and the green arrows show the global flow.

choice of control volume is arbitrary, this must mean that the magnetic field is frozen into the plasma flow. This has the important implication that *magnetic topology*, the connectivity of the magnetic field-lines, is preserved by the plasma flow in the absence of non-ideal terms.

In Hall-MHD, Ohm's law (1.33) can be written as $\boldsymbol{E} = -\boldsymbol{v}_e \times \boldsymbol{B}$, neglecting pressure terms and dissipation. The same result holds, but now the field is frozen into the electron flow, $\boldsymbol{v}_e$, rather than the centre of mass flow $\boldsymbol{v}$.

Magnetic reconnection is the local violation of the frozen-in condition to cause a change in field-line topology. In two dimensions, where the magnetic and velocity fields are in-plane, this topological change can only occur at an x-type magnetic null point (a point where $\boldsymbol{B} = \boldsymbol{0}$). Figure 1.3 shows a diagram of this process. Oppositely directed magnetic field-lines are frozen in to the plasma-fluid elements and advected, typically by a stagnation flow, towards the null point. When the field-line threads a localised *diffusion region* the plasma can detach from the field. This diffusion region is characterised by some strong localised enhancement of out-of-plane electric field, due to some non-ideal term in Ohm's law. For resistive MHD this could be due to the out-of-plane component of $\boldsymbol{E}_\eta = \eta \boldsymbol{j}$, which can be large due to a locally enhanced current density and/or a resistivity. As the plasma exits the diffusion region it becomes frozen again, but the field-line is not frozen in to the same plasma-fluid elements as before the reconnection. From a global perspective the field-lines appear to break and reconnect at the null point and there is a characteristic plasma flow across the *magnetic separators* (lines that separate the different regions of magnetic topology).

A quantitative measure of the reconnected flux can be calculated in 2D. Assume that the inflow and outflow directions are along the y and x-axis respectively in Figure 1.3 such that $x = y = 0$ is the null, and that z is the out of plane direction. The reconnected flux $F_r(t)$ lies along the x-axis at time t, and is given by

$$F_r(t) = \int_0^\infty B_y(t,x)dx - \int_0^\infty B_y(0,x)dx, \tag{1.38}$$

after subtracting the initial flux at $t = 0$. Using the definition of the magnetic potential, $\boldsymbol{B} = \boldsymbol{\nabla} \times \boldsymbol{A}$, gives $B_y(t,x) = -\partial_x A_z(t,x)$, so

$$F_r(t) = -A_z(t,\infty) + A_z(t,0) + A_z(0,\infty) - A_z(0,0) = A_z(t,0) - A_z(0,0), \tag{1.39}$$

as the potential at infinity is fixed. The *reconnection rate* is thus the time rate of change of the out-of-plane vector potential measured at the x-point

$$\partial_t A_z = -E_z, \tag{1.40}$$

which is written in terms of the out-of-plane electric field using Faraday's equation (1.15).

1.3.2 Sweet-Parker reconnection

In early papers by Sweet (1958) and Parker (1957), a 2D steady-state and incompressible resistive MHD reconnection model was developed with the aim of explaining the rapid conversion of magnetic energy into kinetic and thermal energy during a solar flare (see Chapter 2). Figure 1.4 shows a diagram of the Sweet-Parker model. Anti-parallel magnetic fields of strength B_{IN} are advected towards the mid-plane by a perpendicular flow of strength v_{IN}. This creates a long thin layer of strong current density $j \sim B_{IN}/(\mu_0\delta)$, a *current sheet*, which locally enhances the non-ideal electric field and efficiently dissipates magnetic energy. The field-lines break and reconnect at an x-point in the centre of the current sheet before flowing out of the diffusion region with velocity v_{OUT}. Here, we briefly describe the dimensional analysis carried out by Parker (1957). See e.g. Priest & Forbes (2000) for a more detailed discussion, including some generalisations.

Firstly, due to incompressibility and mass conservation, the inflow and outflow

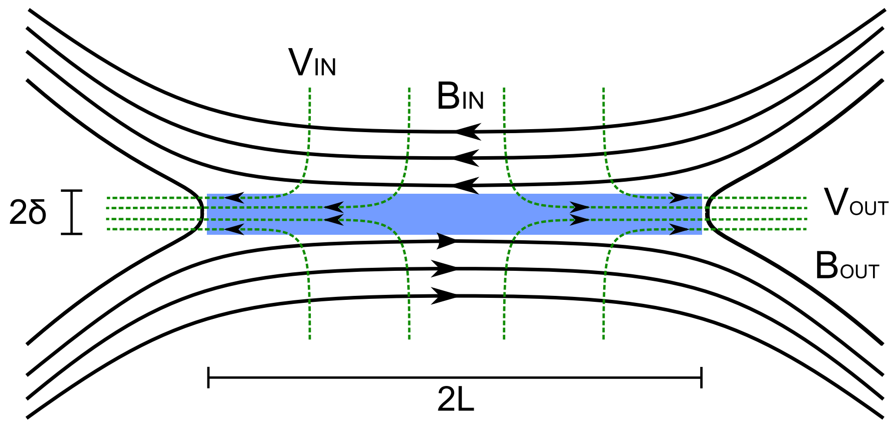

Figure 1.4: The Sweet-Parker reconnection model (Sweet 1958; Parker 1957). The black solid lines are magnetic field-lines, and the green dashed lines are plasma velocity streamlines. A current sheet of length $2L$ and width 2δ is shown in blue.

velocities are related by

$$Lv_{IN} = \delta v_{OUT}. \tag{1.41}$$

Secondly, the outflow velocity can be estimated by considering the horizontal component of the steady momentum equation (1.32). In the simplest case thermal pressure gradients can be neglected (this is valid if the thermal pressure is roughly the same inside and outside the sheet), also neglecting the viscous stresses for now, gives

$$\frac{B_{IN}}{\mu_0 \delta} B_{OUT} \approx \frac{m_i n v_{OUT}^2}{L}, \tag{1.42}$$

which can be simplified, using the solenoidal condition (1.18), $B_{IN}/L \approx B_{OUT}/\delta$, to give the approximate magnitude of the outflow

$$v_{OUT} \approx \frac{B_{IN}}{\sqrt{m_i n \mu_0}} = v_{A,IN}. \tag{1.43}$$

The magnetic tension in the newly reconnected field-lines accelerates the plasma in jets up to the inflow (or upstream) Alfvén speed.

Finally, the resistive Ohm's law is used. At the x-point $\boldsymbol{B} = \mathbf{0}$ and the electric field is supported by the resistive part of Ohm's law $E = \eta j$. Outside the current sheet $j \approx 0$, and there is a convective electric field due to inflow $E \approx v_{IN} B_{IN}$. The 2D and steady-state assumptions give uniform out-of-plane electric field, so

$$E \approx v_{IN} B_{IN} \approx \frac{\eta B_{IN}}{\mu_0 \delta}. \tag{1.44}$$

Rearranging for v_{IN} and using the previous two results gives

$$\frac{v_{IN}}{v_{A,IN}} \sim \frac{\delta}{L} \sim \sqrt{\frac{\eta}{\mu_0 L v_{A,IN}}} \equiv \bar{\eta}^{1/2} \equiv S^{-1/2}, \tag{1.45}$$

where S is called the *Lundquist number*, a dimensionless parameter that is important in resistive-MHD descriptions of reconnection, defined explicitly as

$$S = \frac{\mu_0\, L\, v_{A,IN}}{\eta}. \tag{1.46}$$

In equation (1.45) the notation $\bar{\eta}$ was also used to show that this is the dimensionless resistivity, $\tilde{\eta}$, normalised by the current sheet length and the inflow Alfvén speed. Note that as $E \sim (v_{IN}/v_{A,IN})\, v_{A,IN} B_{IN}$, the quantity $v_{IN}/v_{A,IN}$ is a measurement of the reconnection rate for fixed $v_{A,IN}$ and B_{IN}, see equation (1.40). The problem for Sweet (1958) and Parker (1957) was that this inflow rate was still much too small to explain solar flare energy release. This is because the inflowing Poynting flux $S \sim v_{IN} B_{IN}^2$ depends on the inflow velocity, which itself is extremely small for a coronal value of $S \sim 10^{12} - 10^{14}$ (see Section 2.3). The long thin current sheet, that is a common feature of reconnection in resistive MHD, has an extreme aspect-ratio and forms a bottle-neck on the reconnection rate due to mass conservation.

Here we consider the effects of ion viscosity on the above scalings, in preparation for results presented in Chapter 5 that do not neglect ion-viscous stresses. Park et al. (1984) showed that including a uniform ion viscosity modifies the Sweet-Parker scaling. It does this by reducing the outflow velocity, as the accelerating plasma does work against the viscous forces. The viscous terms within the ion-momentum equation (1.13) scale as $\boldsymbol{\nabla} \cdot \boldsymbol{\pi}_i \sim \mu v/\delta^2$ (as generally $\boldsymbol{\pi}_i \sim \boldsymbol{\nabla} \boldsymbol{v}$). Equation (1.42) now becomes

$$\frac{B_{IN}^2}{\mu_0} \approx m_i n v_{OUT}^2 + \frac{\mu v_{OUT}}{\delta^2}, \tag{1.47}$$

which gives, using equations (1.41) and (1.44), a modified outflow velocity

$$v_{OUT} \approx v_{A,IN} \left(1 + \frac{\bar{\mu}}{\bar{\eta}}\right)^{-1/2}, \tag{1.48}$$

where $\bar{\mu} = \mu/(m_i n\, v_{A,IN}\, L)$ is the inverse Reynolds number calculated with the

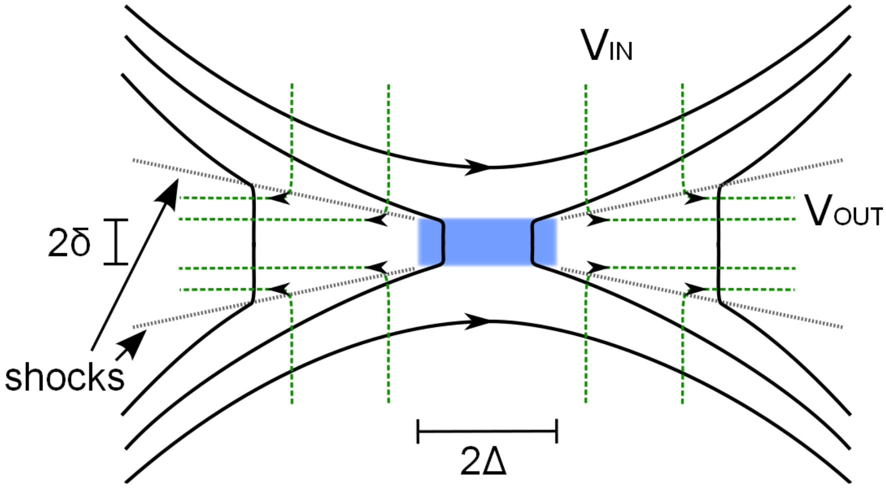

Figure 1.5: The Petschek reconnection model (Petschek 1964). The black solid lines are magnetic field-lines, green-dashed lines are velocity streamlines where the direction of flow is indicated. The blue rectangle is a localised diffusion region, and the dashed diagonal lines are slow-mode shocks.

inflow Alfvén speed and the current sheet length. The modified reconnection rate is

$$\frac{v_{IN}}{v_{A,IN}} \sim \bar{\eta}^{1/2}\left(1+\frac{\bar{\mu}}{\bar{\eta}}\right)^{-1/4}. \tag{1.49}$$

In the limit of large ion viscosity, $\bar{\mu} \gg \bar{\eta}$, the reconnection rate is reduced to $\sim \bar{\eta}^{3/4}\bar{\mu}^{-1/4}$, and for weak viscosity $\bar{\mu} \lesssim \bar{\eta}$ it becomes the Sweet-Parker rate $\sim \bar{\eta}^{1/2}$.

1.3.3 Petschek reconnection

Petschek (1964) proposed an alternative steady-state reconnection model based on the resistive MHD equations, with the aim of achieving faster reconnection than the Sweet-Parker model. In the Petschek model, standing waves are generated on the outflowing (newly reconnected) field-lines, and can form slow-mode shocks. A diagram of the Petschek model is shown in Figure 1.5. The separatrix lines, between the inflow and outflow regions, open up and localise the diffusion region in the outflow direction to a length Δ, where $\Delta \ll L$. There is a characteristic bend in the field-lines as they pass through the shocks. Most of the plasma passes through these shocks, where it is accelerated, rather than passing through a long thin current sheet. This effectively removes the Sweet-Parker bottle-neck.

The Petschek model predicted possible reconnection rates within the range

$$S^{-1/2} \leq \frac{v_{IN}}{v_{A,IN}} \leq \frac{\pi}{8 \ln S}, \tag{1.50}$$

where the lowest is the Sweet-Parker rate, and the fastest has a logarithmic dependence on the Lundquist number which is considerably faster for solar coronal Lundquist numbers $S \sim 10^{12} - 10^{14}$.

Despite the attractiveness of Petschek's solution, numerical simulations of magnetic reconnection, e.g. Biskamp (1986), have not been able to reproduce this configuration with uniform plasma resistivity. It has recently been shown analytically that the Petschek configuration is unstable, and that stable undriven reconnection with uniform plasma resistivity will occur at the Sweet-Parker rate (Malyshkin et al. 2005; Kulsrud 2011; Forbes et al. 2013). However, this magnetic field configuration can be achieved with a spatially non-uniform resistivity that is locally enhanced at the x-point, see e.g. Ugai & Tsuda (1977).

1.3.4 Driven and spontaneous reconnection

So far the discussion has been on steady-state resistive-MHD models of reconnection. An active area in the field of reconnection concerns the reconnection onset, which is necessarily time-dependent. A common approach to onset is related to the stability of sheared magnetic field configurations, such as a current sheet. Furth et al. (1963) performed a resistive-MHD linear stability analysis of such a sheared field equilibrium configuration, finding that it can become unstable to long-wavelength perturbations, which grow exponentially with time ($\propto e^{\gamma t}$) in the linear regime. For a simple current sheet of width δ, this growth rate is

$$\gamma = \left[\tau_d^3 \tau_{A\delta}^2 \left(k\delta\right)^2\right]^{-1/5}, \tag{1.51}$$

where $\tau_d = \mu_0 \delta^2/\eta$ is the diffusion time across the sheet width, $\tau_{A\delta} = \delta/v_A$ is the sheet-crossing Alfvén time, and k is the wave-number of the perturbation, such that $(\tau_{A\delta}/\tau_d)^{1/4} < k\delta < 1$; see e.g. Priest & Forbes (2000). Here the longest wavelength (smallest wave-number) modes, $\lambda_{max} \approx k_{min}^{-1} = (\tau_d/\tau_{A\delta})^{1/4}\delta$, have the largest value of γ, growing on a time-scale of $\tau_{\min} = (\tau_d\, \tau_{A\delta})^{1/2}$ (note that in highly-conducting plasmas $\tau_d >> \tau_{A\delta}$, hence tearing is still slow compared with the Alfvén time).

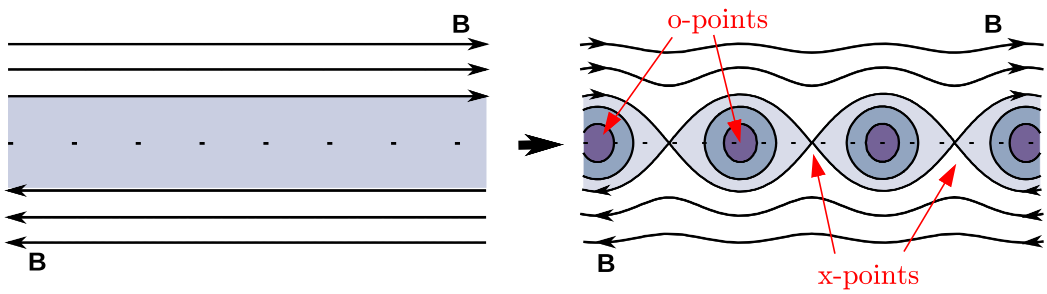

Figure 1.6: Cartoon of the initial equilibrium (left), and the final relaxed state (right) for the resistive tearing instability. The colour-scale indicates current density.

The drive for this instability is the free energy associated with the sheared field. The field tears and is reconnected as the perturbation grows, allowing the configuration to relax towards a state of lower magnetic energy. The relaxed configuration contains *magnetic islands* (or o-type neutral points: *o-points*) that grow in size exponentially in the linear phase of the instability. However, when the island size exceeds the equilibrium width (e.g. the current sheet width δ), the instability enters the non-linear regime where the island growth becomes linear (Rutherford 1973). Eventually these islands saturate and a new magnetostatic equilibrium may established, see Figure 1.6. In Chapter 5, we show how the effects of magnetic island formation can have a large effect on the global magnetic field configuration.

Recently it has been shown that the very long and thin Sweet-Parker type current sheets with Lundquist numbers $S \gtrsim 10^4$ can be highly unstable to the *plasmoid instability* (Shibata & Tanuma 2001; Loureiro et al. 2007). This was proposed as a "super-Alfvénic" instability in the literature; however, the Alfvén time referred to is defined in terms of the sheet length, $\tau_{AL} = L/v_A$, rather than the sheet-crossing timescale, $\tau_{A\delta} = \delta/v_A$. Using the Sweet-Parker scaling $\delta = S^{-1/2}L$ in the timescale of the fastest growing mode gives $\tau_{min} = S^{-1/4}\tau_{AL}$, which is indeed faster than τ_{AL} for $S \gg 1$ (see also Huang & Bhattacharjee 2013, and references therein).

As well as occurring spontaneously from a resistive instability, reconnection can also be driven by (or occur in the non-linear phase of) some ideal instability. An example of this is the *coalescence instability* (Finn & Kaw 1977), where the initial equilibrium consists of neighbouring magnetic islands (similar to the final relaxed state after the tearing-instability, see Figure 1.6). In this case, the linear phase of the instability is ideal and is caused by the attraction of neighbouring islands due to their parallel current distributions. However, as they approach the x-point collapses and a reconnecting current sheet forms. The magnetic islands upstream of the x-point strongly drive the reconnection, leading to *flux pile-up* (increase in the inflowing magnetic field-strength, B_{IN}) on the current sheet edge. As the flux from the pair of islands reconnects at the x-point, the two islands coalesce into one larger island. We show simulations of a similar coalescence process in Chapter 5, see there for detailed description, including the effects of two-fluid physics and toroidal geometry. Here, we briefly mention some of the literature on the island coalescence instability.

Biskamp & Welter (1980) performed numerical simulations of this instability, finding that for a range of Lundquist numbers, $10^2 < S < 10^4$, the reconnection rate becomes independent of the Lundquist number. However, for Lundquist numbers $S \gtrsim 10^4$ the reconnection rate becomes dependent on the Lundquist number again (with similar dependence as the Sweet-Parker model). They also showed some evidence of large-scale oscillations of the islands, referred to as "sloshing", for larger Lundquist numbers $S \gtrsim 10^5$. Recently, Knoll & Chacón (2006a) clearly showed this sloshing behaviour using state-of-the-art (their scheme has low numerical dissipation) resistive MHD simulations, finding that it occurs for $S \gtrsim 10^5$. The authors explain this sloshing as an effect due to magnetic pressure associated with the flux pile-up, which prevents plasma inflow into the current sheet. This work is extended in Knoll & Chacón (2006b) which considers two-fluid effects, and shows that this pressure pile-up can be avoided when including the Hall term. We will now discuss the effects of the Hall term, and other collisionless processes, on steady-state reconnection models.

1.3.5 Semi-collisional and collisionless reconnection

The previously discussed reconnection models were based on the resistive MHD equations. However, these equations are only valid for length-scales in the collisional limit, where large numbers of collisions can prevent the decoupling of ion and electron fluids. This may not be the case in the presence of a current sheet or diffusion region which can be microscopic (orders of magnitude less than a typical length-scale L_0) in at least one direction. Also, the Sweet-Parker width $\delta = S^{-1/2}L \sim \eta^{1/2} \sim T_e^{-3/4}$, see equation (1.20), so even if the current sheet can be described by resistive MHD initially, it will thin after resistive heating.

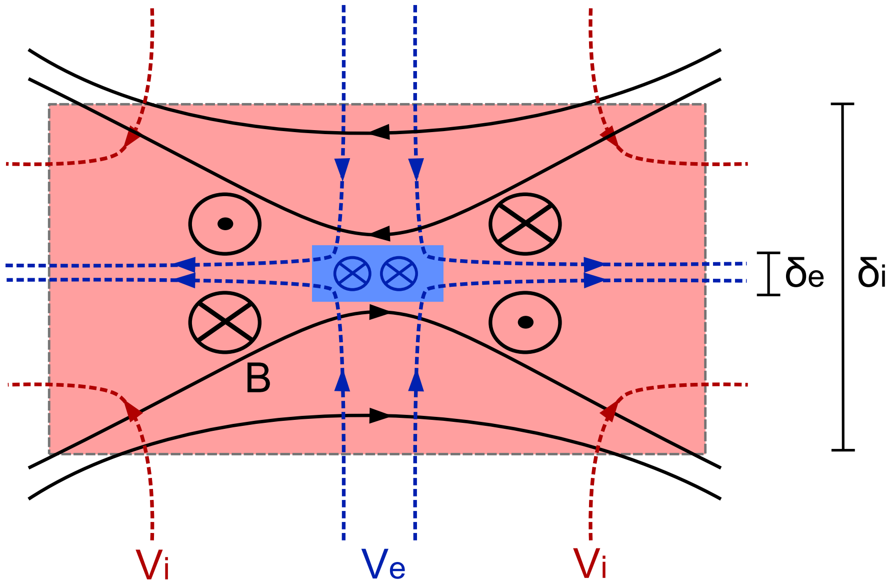

Figure 1.7: Hall-MHD reconnection. The bulk ion (electron) flows are denoted by red (blue) lines, and the respective diffusion regions by red (blue) rectangles. The out-of-plane electron flow is also shown as blue crossed circles. The in-plane and quadrupole out-of-plane field is shown in black.

This may cause other physics to become important. In this thesis, the term semi-collisional will refer to plasmas in which the collision frequencies are non-zero, but small enough so that the plasma is not completely described by resistive-MHD.

The various terms in the electron momentum equation (1.14), also called the *generalised Ohm's law*, cannot be neglected if the current sheet width drops below a characteristic length-scale for that term. It has been mentioned above that the Hall term is characterised by the ion-skin depth d_i, see equation (1.35), and electron inertia becomes important at the electron-skin depth d_e, see equation (1.36). In addition, the scalar electron pressure gradient term becomes important at the *ion-sound Larmor radius* $\rho_{is} = \sqrt{k_B T_e/m_i}/\Omega_{ci}$, which is the ion Larmor radius based on the electron temperature. Finally, ion and electron Finite Larmor Radius (FLR) effects become important at the ion and electron Larmor radii, and some of these effects can be expressed in the off-diagonal terms of the ion and electron pressure tensors respectively. Table 2.3 in Chapter 2 gives the relative size for some of these kinetic scales in two low-β plasma environments.

The Hall term cannot break the frozen in condition and cause reconnection, but it can strongly modify the reconnection process through the decoupling of ion and electron fluids. Figure 1.7 shows how this occurs in 2D. The decoupling of the ions from the magnetic field-lines occurs at a length $\delta_i \sim d_i$ from the null-point, e.g. Mandt et al. (1994), so that the field is frozen into the electron flow within this region. Gradients in the electron out-of-plane flow (as the current density increases closer to the mid-plane) cause the in-plane magnetic field-lines to be bent in the out-of-plane direction, resulting in a characteristic quadrupole structure of the out-of-plane magnetic field. Eventually the frozen-in condition for the electrons is broken at a scale length of δ_e. In a semi-collisional plasma, this could be due to some collisional electron viscosity, or perhaps even normal resistivity. In collisionless Particle-In-Cell (PIC) simulations (Horiuchi & Sato 1994), it has been shown that δ_e corresponds to the meandering width of unmagnetised electron orbits (see Figure 1.10 in Section 1.4 for a description of these orbits), and that the out-of-plane electric field at the x-point is due to gradients of the off-diagonal elements of the electron pressure tensor (Hesse et al. 1999; Ricci et al. 2002).

The electron diffusion region in Figure 1.7 is drawn as being localised in both the inflow and outflow directions. However, this is not always the case. State-of-the-art PIC simulations with open boundary conditions in the outflow direction found extended electron diffusion regions (Daughton et al. 2006), that are limited in length only by collisionless tearing instabilities. Electron pressure anisotropy, where electron pressure is different in the directions parallel and perpendicular to the magnetic field, has been shown to be crucial in establishing these extended layers (see Le et al. 2013, and references therein).

In the Geospace Environmental Modelling (GEM) challenge (see Birn et al. 2001, and references therein), simulations were performed using resistive-MHD, Hall-MHD, Particle-In-Cell and Hybrid codes. It was found that the reconnection rate for all simulations was very similar, apart from that for resistive MHD (which was much slower, at a Sweet-Parker rate). This result implies that the reconnection rate is insensitive to the details of the electron diffusion region, which varied between the different models. The only requirement for a fast reconnection rate is to include the Hall term within the model.

All of these reconnection models used 2D magnetic field configurations (although Hall-reconnection generates quadrupolar fields in the third dimension, see above). The magnetic geometry can be modified by adding a magnetic field component in the out-of-plane direction, a so-called *guide-field*. With the guide-field, the angle between the reconnecting field-lines is less than 180°, which is more applicable to the solar corona or magnetic fusion energy devices (see Chapter 2) than fully 2D models. However, reconnection with a guide field is less well understood than when the reconnecting field is anti-parallel (180°). In terms of the electron diffusion region, this guide-field can magnetise electrons within the diffusion layer so that its thickness δ_e corresponds to the electron Larmor radius ρ_e, rather than the meandering bounce width (Hesse et al. 2002; Ricci et al. 2004). With collisional dissipation, it has been shown that ion-viscosity can be important in setting the current sheet width (Simakov et al. 2010). In terms of the reconnection rate, some studies have shown that fast rates can be achieved when the current sheet width drops below the ion-sound Larmor radius (Kleva et al. 1995; Schmidt et al. 2009; Simakov et al. 2010). In Chapter 5 we present results of driven two-fluid reconnection simulations with strong guide field. Note that although there are now three components of the magnetic field, guide-field simulations are sometimes called 2.5D or even 2D configurations. This is because this field can stabilise a number of current-aligned instabilities. Also, strictly these geometries do not contain null points, but they do have x-point geometry where the in-plane field components go to zero.

1.3.6 3D reconnection models

Here, we refer to reconnection as being fully 3D when it occurs in magnetic field configurations that have no invariant direction. These fully 3D models have significant qualitative differences from the 2D or 2.5D models. Firstly, reconnection in 3D can occur in geometries that do not include magnetic null points (Schindler et al. 1988). In such configurations reconnection can occur if a field-line threading a localised diffusion region has a non-zero value of $\int E_\parallel dl$ integrated along the whole length of the line. However, these configurations are outside the scope of this thesis. Instead we will consider reconnection at a fully 3D magnetic null-point.

Parnell et al. (1996) gives a complete linear description of magnetic field configurations near to a 3D null point (a point in 3D space where $\boldsymbol{B} = \boldsymbol{0}$). The field can be Taylor expanded to first order as

$$\boldsymbol{B} = \frac{\partial B_i}{\partial x_j} dx_j, \tag{1.52}$$

where the Jacobian matrix $\partial B_i/\partial x_j$ at the null has eigenvalues λ_i and eigenvectors $\boldsymbol{x}_i$ ($i = 1, 2, 3$). The solenoidal constraint (1.18) sets the trace of the Jacobian, and thus the sum of the eigenvalues, equal to zero $\lambda_1 + \lambda_2 + \lambda_3 = 0$. For non-zero eigenvalues, two must have the same sign and one of opposite sign. The eigenvectors associated with these eigenvalues define special magnetic field-lines that make up the *magnetic skeleton* of the 3D null point. Parnell et al. (1996) showed that the eigenvector with different eigenvalue sign defines a 1D *spine line*, and those with the same sign a 2D *fan surface* (called γ-line and Σ-surface by Lau & Finn 1990) that separates different magnetic flux domains.

Setting the z-axis parallel to the spine line and the x-y axis as the fan plane, Parnell et al. (1996) showed, without loss of generality, that the Jacobian matrix can be written as

$$\frac{\partial B_i}{\partial x_j} = B_0 \begin{pmatrix} 1 & \frac{1}{2}(q - j_{\|}) & 0 \\ \frac{1}{2}(q + j_{\|}) & p & 0 \\ 0 & j_{\perp} & -(p+1) \end{pmatrix}. \tag{1.53}$$

Here p and q are parameters specifying potential (current free) magnetic field components, and $j_{\perp}$ and $j_{\|}$ are currents perpendicular and parallel to the spine axis respectively. The simplest non-trivial, symmetric null is specified by $p = 1$, $q = j_{\|} = j_{\perp} = 0$. This can be written using a cylindrical coordinate system (r, ϕ, z); where $r = 0$ is the spine-axis, $z = 0$ is the fan plane and $\phi = 0$ is the positive x-axis, as

$$\boldsymbol{B} = \frac{B_0}{L_0}(r\hat{\boldsymbol{r}} - 2z\hat{\boldsymbol{z}}). \tag{1.54}$$

Here B_0 is the field strength at a distance $r = L_0, z = 0$ from the null. This is the geometry shown in Figure 1.8(a). A non-zero $j_{\|}$ skews the radial fan field-lines, and causes them to spiral above a threshold current value. If $j_{\perp} \neq 0$ the fan plane tilts against the spine so that they are no longer orthogonal. These two cases are shown in Figure 1.9.

The type of reconnection that occurs at a 3D null depends upon the magnetic configuration and global plasma flow. Priest & Titov (1996) proposed two models of reconnection using the potential magnetic field of equation (1.54) and prescribed boundary flows that satisfy the ideal MHD equations. As there are no non-ideal terms in these mathematical models, reconnection can only occur if there are singularities in the flow field where the magnetic field vanishes. Clearly these singularities will not exist in reality, they will be smoothed out by some dissipation process such as finite resistivity. The left hand panel in Figure 1.8(b) shows *ideal spine reconnection*. Foot-points of the field-lines at a cylindrical

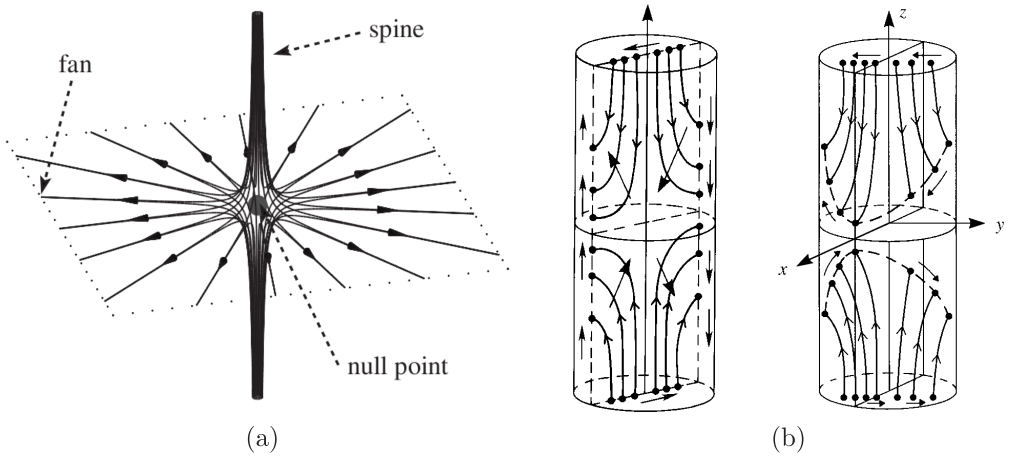

Figure 1.8: a) The magnetic field configuration of a 3D null point, from Priest & Pontin (2009). The black lines are a selection of magnetic field-lines that lie around the 1D spine axis and the 2D fan plane. The null point is at the centre. b) Diagram from Priest & Titov (1996) showing the different driving applied at a cylindrical surface, and the resultant field-line motion, for the ideal spine reconnection model (left) and the ideal fan model (right).

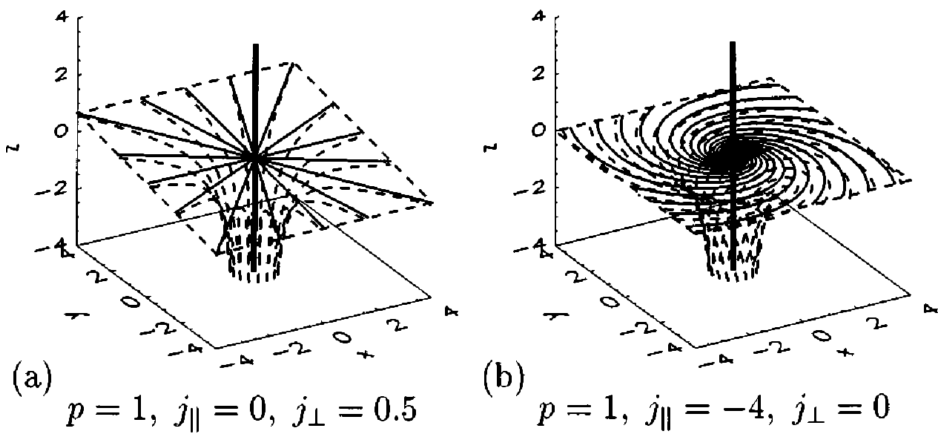

Figure 1.9: Non-potential null points, image from Parnell et al. (1996). a) with non-zero current perpendicular to the spine-axis. b) with non-zero current parallel to the spine-axis.

boundary are driven vertically as shown, creating a shear flow across the fan plane. Priest & Titov (1996) find the plasma velocity to be

$$\boldsymbol{v} = -\frac{E_0 L_0^2 \sin\phi}{B_0\, 3r}\left(\frac{\hat{\boldsymbol{r}}}{z} + \frac{\hat{\boldsymbol{z}}}{r}\right), \tag{1.55}$$

which is supported by a convective electric field of

$$\boldsymbol{E} = \frac{E_0 L_0 \sin\phi}{r}\hat{\boldsymbol{\phi}}. \tag{1.56}$$

The frozen-in flux inflow converges on the spine axis, and the field reconnects at the spine in the presence of singular electric and velocity fields.

The right-hand panel of Figure 1.8(b) shows *ideal fan reconnection*. The foot-points are driven at the top and bottom boundaries to shear the spine-axis. The field-lines in the top half, $z > 0$, rotate as shown for positive x, and in the opposite sense for negative x. For the bottom half the field-lines rotate in the opposite directions as the adjacent field-lines in the top half, so that there are strong counter-swirling flows close to the fan plane. These flows become singular at the fan plane where reconnection occurs.

Craig et al. (1995), Craig & Fabling (1996) and Craig et al. (1997) found exact solutions to the steady and incompressible resistive MHD equations at 3D null points, which are resistive analogues to the ideal reconnection models. The *resistive spine reconnection* and *resistive fan reconnection* models are introduced and the electromagnetic fields are used to study test-particle acceleration in Chapter 4.

These analytic solutions for 3D null reconnection are found using the simplifying assumptions of incompressibility and steady-state reconnection. The fully compressible and time-dependent 3D resistive MHD simulations of Pontin et al. (2007a,b) show that typically current structures, and the diffusion region, spread across both the spine axis and fan plane when either the spine axis or fan plane is sheared. Due to the similarities with the previous two models, they name this *spine-fan reconnection*. Also, recent numerical and analytical study gives additional models for null reconnection when the global plasma motion is rotational rather than a shear flow (see for review Priest & Pontin 2009; Pontin et al. 2011).

1.4 Particle acceleration

1.4.1 Test particle approximation

The reconnection models presented thus far have looked at the collective behaviour of the plasma, often using fluid models that simplify the physics in comparison with the full kinetic treatment. Including all of the physics can be done using Particle-In-Cell simulations (e.g. Daughton et al. 2006). However, this is still difficult, particularly in 3D due to the vast memory requirements of such a simulation. With this method, it is usually only possible to simulate regions with length of several ion-skin depths, d_i see equation (1.35), that is many orders of magnitude less than, for example, the global length-scale for a solar flare (see Chapter 2). Additionally, the kinetic picture is often complicated, due to the presence of micro-instabilities and turbulence, and can obscure the important physics. An alternative approach, that can complement fluid and kinetic models, is to consider single test-particle trajectories in given reconnection electric and magnetic field configurations. However, this approach is not self-consistent, as the electromagnetic fields generated by these test-particles are typically neglected. This approach is valid provided that the energy carried by the test-particle population is small.

1.4.2 Test-particles in current sheets and x-points

A major question within the field of reconnection concerns the acceleration of charged particles into non-thermal distributions. This has major importance for solar flares as it is thought to be a significant channel of flare energy release (see Section 2.1.3). In sub-storms of the Earth magnetosphere, fast particles are thought to be accelerated by *dipolarization fronts*, e.g. Birn et al. (2013), where the newly reconnected magnetic field-lines in the Earth magnetotail snap back towards the dipole shape. Possible acceleration mechanisms for both of these phenomena include a collapsing magnetic trap (Somov & Kosugi 1997), wave-particle interactions (see Miller et al. 1997, for a review with application to solar flares) and direct acceleration by the non-ideal electric fields associated with the reconnection. In this thesis we will concentrate on this latter acceleration mechanism.

Early work on direct acceleration explored charged particle trajectories within

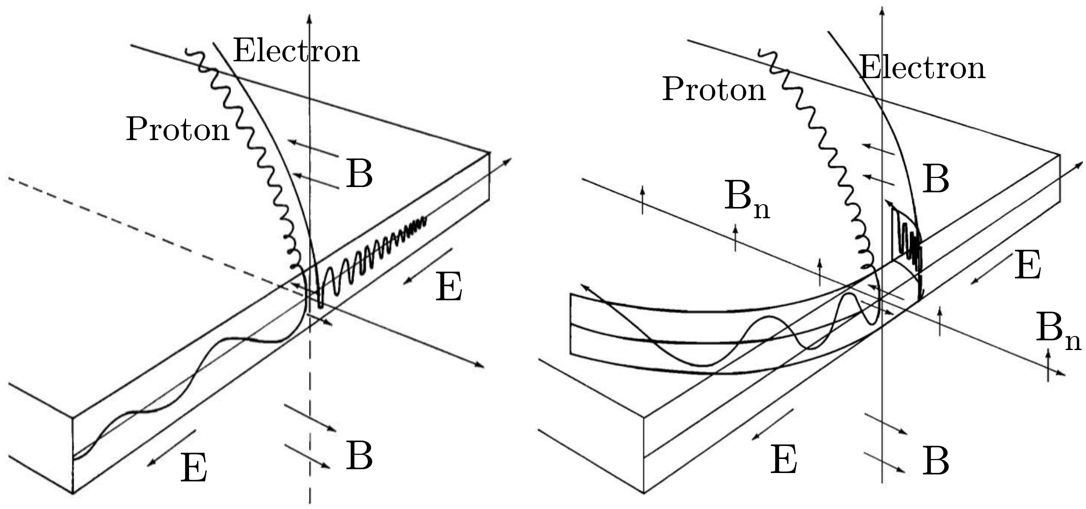

Figure 1.10: Trajectories of charged particles within current sheets, adapted from Speiser (1965). Left: With simple anti-parallel magnetic field configuration $\boldsymbol{B}$, and constant electric field $\boldsymbol{E}$. b) With an additional magnetic field component $\boldsymbol{B}_n$ perpendicular to the sheet.

current sheets. Speiser (1965) considered a current sheet model using anti-parallel magnetic fields and a uniform electric field as shown in the left-hand panel of Figure 1.10. The protons and electrons electric drift into the current sheet, where they become unmagnetised as the Larmor radius r_L becomes comparable to the length-scale of field variation, e.g. $r_L \gtrsim L_{\nabla B} = B/|\boldsymbol{\nabla} B|$. When this occurs, the adiabatic theory discussed in Section 1.1 breaks down. Both species undergo non-adiabatic, or meandering, oscillations as they are accelerated parallel or anti-parallel to the electric field (depending on the sign of the charge). Speiser (1965) showed that the amplitude of these oscillations decayed with time as $t^{-1/4}$ after entering the sheet, and so the particles are trapped. The energy gain is only limited by the sheet length. The right-hand panel in Figure 1.10 shows the trajectories when there is a small and constant magnetic field, $\boldsymbol{B}_n$, perpendicular to the sheet. This field component turns the particle within the current sheet, and causes it to be ejected from the sheet when it turns 90°. In this thesis we refer to these processes as *gyro-turning* and *gyro-ejection* respectively, as they are due to partial magnetisation of the particles by the normal field component. In Chapter 3 we numerically compute these trajectories and use the analytical results of Speiser (1965) to benchmark the test-particle code.

Zhu & Parks (1993), Litvinenko & Somov (1993) and Litvinenko (1996) extended the model of Speiser (1965) by adding a guide field parallel to the electric field. Above a critical guide field the trajectory is stabilised against ejection and the energy gain is once again only bounded by the sheet length (Litvinenko 1996). This is because the particle remains magnetised within the sheet, and tied to the guide field-lines.

Numerical test-particle simulations have been performed in 2D and 2.5D using steady prescribed magnetic and electric fields that are simplified analytic representations of resistive current sheet (Zharkova & Gordovskyy 2004, 2005; Wood & Neukirch 2005) and x-point (Vekstein & Browning 1997; Hannah & Fletcher 2006; Hamilton et al. 2005) models. These simulations also considered the effect of the guide field on particle trajectories and energy spectra.

Heerikhuisen et al. (2002) and Craig & Litvinenko (2002) improved on this method by taking the electric and magnetic fields from the exact analytical solutions of Craig & Henton (1995) to the 2D incompressible, resistive MHD equations in a reconnecting current sheet geometry. The advantage of exact solutions is that the electric field is calculated via the resistive Ohm's law, rather than being prescribed in an *ad hoc* manner. Also, Gordovskyy et al. (2010a,b) used an approach combining numerical MHD simulations with a test particle code, to study 2D forced reconnection including the time-evolution of the electric and magnetic fields.

1.4.3 Particle acceleration in 3D null-point models

In Chapter 2 we discuss some of the observational evidence for the existence of 3D magnetic null points in the solar corona, the Earth magnetotail and also within a laboratory plasma device. Such null points are a natural magnetic configuration in which to study particle acceleration, as particles can be directly accelerated by an electric field when the magnetic field approaches zero and adiabatic motion breaks down. Dalla & Browning (2005, 2006, 2008) and Browning et al. (2010) studied particle trajectories and produced energy spectra for protons and electrons in the ideal spine and fan reconnection models of Priest & Titov (1996). They found that these particles could reach high energies (max$\sim 10^7$ eV) in the spine model fields, using solar coronal values of $B_0 = 0.01$ T and $E_0 = 1500\,\mathrm{V\ m}^{-1}$ in equations (1.54,1.56). The ideal fan reconnection model was less effective for protons, partly as the geometry of the electric drift streamlines was less efficient at delivering particles to regions of high electric field. Guo et al. (2010) studied particle trajectories in fields from ideal MHD simulations, finding that the strong electric fields supporting convective plasma motion can be effective proton accelerators, but less so for electrons.

Litvinenko (2006) was the first study to use the resistive models of Craig et al. (1995), Craig & Fabling (1996) and Craig et al. (1997) and so include the effects of the reconnection non-ideal electric field on the trajectory of particles at 3D nulls. However, they used an approximate analytical analysis, which is valid only within the fan plane, and only for a region around the null point. They used a WKB method of Bulanov & Cap (1988) to show that single protons and electrons close to the null can achieve the energies needed to explain solar flare observations. However, Litvinenko (2006) found that this energy is limited as particles become unstable in the sheet, due to background field components, and are ejected. Stanier et al. (2012) extended this by performing numerical simulations of protons in both resistive spine and fan models, and also studying the transition from the external drift region (that could not be treated with the method of Bulanov & Cap 1988) to the current sheet. This work is given, along with new results on electron trajectories, in Chapter 4.

Finally, there have recently been two attempts at self-consistent Particle-In-Cell simulations of 3D null points. The first, by Baumann et al. (2013), find that direct acceleration from a reconnection electric field was the primary acceleration mechanism. However, to be able to run such a challenging simulation both the charge and the mass of the particles had to be artificially reduced (the ion to electron mass ratio is only 18). The authors do show that this retains the proper ordering of the kinetic scale lengths. However, as the ion and electron skin depths are only separated by $\sqrt{m_i/m_e}$ there is little separation between ion and electron scales. It is unclear whether the results hold up to proper mass ratios. Olshevsky et al. (2013) used a novel implicit-PIC algorithm to simulate a configuration with 8 null points in a self-consistent manner. They found that the dissipation of magnetic energy was five times higher than in a standard current sheet configuration. It is clear that there is still more work to do in understanding the self-consistent mechanisms of particle acceleration in 3D magnetic reconnection configurations.

In this chapter, some basic models for magnetised plasmas, magnetic reconnection and particle acceleration have been introduced. In the next chapter, some application of these models to solar flares and reconnection in laboratory plasmas will be discussed, focusing on the observational and experimental data for reconnection and particle acceleration in both environments.

Chapter 2

Reconnection in Semi-Collisional Plasmas: Context and Applications

Magnetic reconnection is now considered to be a basic plasma phenomenon that has wide application in both astrophysical and laboratory plasmas. It is thought to be one of the primary energy release mechanisms in solar flares (see below), and in the magnetotail of Earth where it has been proposed as a trigger mechanism for magnetospheric sub-storms (e.g. Angelopoulos et al. 2008). In the magnetotail, sheared 3D magnetic null points have been detected *in-situ* by the Cluster satellites (Xiao et al. 2006), and some evidence of fast electron beams accelerated at the null has been found (He et al. 2008). Also close to Earth, magnetic reconnection is thought to be crucial for the transport of solar wind magnetic and particle flux through the magnetopause and into the magnetosphere, see e.g. Dungey (1961) and Chapter 4 of Birn & Priest (2007). Recently, a model of reconnection at the heliopause, based on numerical simulations, has been used to explain the measured signals of the Voyager 1 spacecraft (Swisdak et al. 2013) and show that it crossed into the Local Interstellar Medium. Further away, reconnection has been proposed as an important process in the interaction of stellar magnetospheres with accretion disks (e.g. Ballegooijen 1994; Uzdensky et al. 2002), in pulsar magnetospheres (e.g. Spitkovsky 2008), as well as a mechanism for extreme particle acceleration in gamma-ray flares such as within the Crab Nebula (see e.g. Cerutti et al. 2013, and references therein).

In laboratory magnetised plasma devices, magnetic reconnection is also a common phenomenon, and can have both positive and negative consequences. In a Reversed-Field-Pinch (RFP) magnetic confinement device, reconnection is important for the plasma to relax towards equilibrium during start-up (e.g. Baker 1984). Co-helicity spheromak merging within the Swarthmore Spheromak Experiment (SSX, Brown 1999) involves reconnection at a 3D magnetic null point (Gray et al. 2010; Lukin & Linton 2011). Reconnection is also crucial for flux-rope merging start-up in spherical tokamak plasmas, which is a major topic of this thesis (see Section 2.2.4 and Chapter 5). However, in many devices, such as tokamaks, reconnection can be responsible for degradation in confinement, as formation of magnetic islands can destroy nested flux-surfaces (see below). It can also be responsible for loss of core temperature within sawtooth-crashes (Yamada et al. 1994), and can couple to other instabilities causing major disruptions. Finally, several laboratory devices have been constructed specifically to study reconnection. These include, but are not limited to, the Magnetic Reconnection eXperiment (MRX) at Princeton Plasma Physics Laboratory (Yamada et al. 1997), the TS-3/4 devices at University of Tokyo (e.g. Ono et al. 1993), the Versatile Toroidal Facility (VTF) at Massachusetts Institute of Technology (Egedal et al. 2003) and the Reconnection Scaling eXperiment (RSX) at Los Alamos National Laboratory (Furno et al. 2003). With these machines progress has been made in validating theoretical models against laboratory data, such as the discovery of the Hall quadrupolar out-of-plane magnetic field (see Section 1.3.5) in MRX (Ren et al. 2005).

The details of reconnection in such a large range of plasma environments can vary. In a classical plasma, this depends on the magnetic geometry and collisionality of the plasma, as discussed in the previous chapter. For extreme astrophysical environments, relativistic and quantum effects may become important (for a review see Uzdensky 2011). However, it is conceivable that many of the basic concepts from laboratory and solar system reconnection carry across to the more extreme environments.

In this thesis we will study reconnection in two different plasma environments; within flares of the solar corona, and within the start-up phase of a Spherical Tokamak (ST) laboratory plasma device. Both applications considered are low plasma-β and in the semi-collisional magnetic reconnection regime. In this chapter these applications will be introduced, and the reconnection regime will be described in terms of dimensionless plasma parameters (such as those discussed in the previous chapter).

2.1 Solar flares

2.1.1 Solar coronal plasma environment

The solar corona is the outer-most layer of the solar atmosphere. It extends from a few thousand metres above the Sun's visible surface, known as the photosphere, out to the order of a few solar radii (although this can vary significantly, see e.g. Golub & Pasachoff 1997). It is characterised by low densities, $n \approx 10^{14}\,\mathrm{m}^{-3}$, and much higher temperature, $T \approx 10^6\,\mathrm{K} \approx 86\,\mathrm{eV}$, than the lower chromospheric atmosphere ($T \approx 10^4$ K) and photosphere ($T \approx 6000$ K). A satisfactory explanation as to why the corona is a hundred-fold hotter than the chromosphere has not yet been given and it is a long-standing problem, known as the coronal heating problem, in solar physics (for a recent review, see Parnell & De Moortel 2012). The source of the heating is widely agreed upon to be the stored energy density in the coronal magnetic field; however, it is not known which processes, for example waves (Heyvaerts & Priest 1983), plasma jets (De Pontieu et al. 2009), or magnetic reconnection (Parker 1988), dominantly transport and dissipate this energy within the corona.

The coronal magnetic field is highly structured in the form of *coronal loops* (see e.g. Reale 2010). These are typically anchored at both ends in the photosphere and can extend up into the corona, where they expand due to their large internal magnetic pressure. The ambient magnetic field-strength, B, in the corona ranges from $10^{-5} - 10^{-3}$ T. However, if the field becomes strongly sheared, induced currents can increase the stored energy over the value of the vacuum magnetic field energy. In a low plasma-β equilibrium, these currents are parallel to the magnetic field, which can be seen by setting the inertial, thermal pressure and viscous forces to zero in the momentum equation (1.26)

$$\boldsymbol{j} \times \boldsymbol{B} = \boldsymbol{0} \implies \mu_0^{-1} \boldsymbol{\nabla} \times \boldsymbol{B} = \alpha \boldsymbol{B}, \tag{2.1}$$

using Ampéres law (1.16) for the second equality. In general, each field-line has a single value for α, but this can differ between field-lines. Such a configuration is called a Non-Linear Force-Free Field (NLFFF). The free energy stored can be

Designation	An	Bn	Cn	Mn	Xn
Intensity ($\mathrm{J\,m^{-2}\,s^{-1}}$)	10^{-8}	10^{-7}	10^{-6}	10^{-5}	10^{-4}

Table 2.1: The Soft X-Ray (SXR) classification of a flare, showing spatially-integrated peak flux between 0.1 - 0.8 nm. For example, a peak SXR flux of $8 \times 10^{-7}\mathrm{J\,m^{-2}\,s^{-1}}$ has designation B8.

thought of as the difference between the energy in the NLFFF and the energy in the vacuum field, although in practise other constraints may set a higher minimum magnetic energy state (Taylor 1974, 1986; Yeates et al. 2010).

Active regions can contain collections of current-carrying coronal loops, also known as twisted *flux-ropes*, that emerge from beneath the photosphere and extend well into the corona. The number and typical magnetic field-strength of these active regions varies over an 11-year cycle, that is related to some dynamo process which is not fully understood (see e.g. Jones et al. 2010, for a recent review). In these regions, magnetic field can be amplified to strengths of $B \approx 0.01$ T due to large shear, and they can be a source of energy for many transient and energetic events, such as *solar flares*.

2.1.2 Solar flares

Solar flares are observed as transient brightenings of the corona and chromosphere over a range of wavelengths; from 10 m radio-waves up to gamma-ray line emission in the most energetic events (Lin 2006). The total emission, over all observed wavelengths, for a large flare can be of the order 10^{25} J (Priest 2000); they are essentially the largest explosions in the solar system. The frequency of flares have an inverse power-law dependence with their size. At the lower end are very frequent nano-flares that have been proposed as a mechanism of coronal heating (Parker 1988). At the top end, are the first and largest recorded solar flare (Carrington 1859), and the largest measured with modern equipment on the 4th November 2003 (Kiplinger & Garcia 2004). A classification of flare magnitude by spatially integrated peak soft x-ray flux is given in Table 2.1, the 4th November 2003 event has been estimated as an X30.6 flare.

Figure 2.1, taken from Sun et al. (2012b), shows an example of an active region (NOAA active region 11158) five hours before an X2.2 class flare. The left panel shows a 171 angstrom Extreme Ultra-Violet (EUV) light photograph

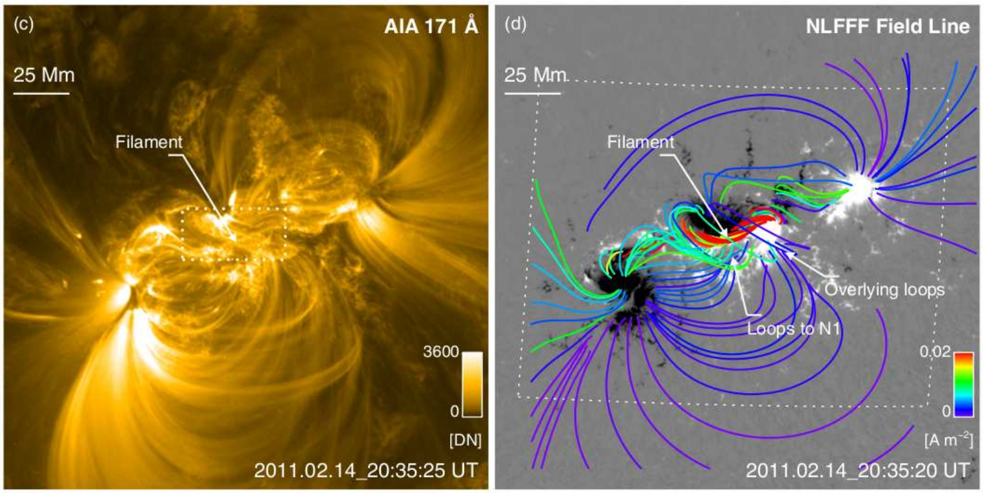

Figure 2.1: Left: 171 Angstrom Extreme Ultra Violet image of NOAA active region 11158, five hours before an X2.2 flare. Right: Non-Linear Force Free Field (NLFFF) extrapolation of the magnetic field (coloured lines, where the colour denotes the vertical current density at the foot-points of the field-lines), and a photospheric vertical field magnetogram (grey-scale). This image is from Sun et al. (2012b).

taken with the Atmospheric Imaging Assembly (AIA, Lemen et al. 2012) instrument aboard the Solar Dynamic Observatory (SDO), and the right panel shows a selection of magnetic field-lines (coloured lines) from a NLFFF reconstruction performed by Sun et al. (2012b). This reconstruction uses, as a boundary condition, a photospheric vector magnetic field map measured by the Helioseismic and Magnetic Imager (HMI, Schou et al. 2012). The regions of strong current density, indicated by the colour of the field-lines on the right hand panel, correspond to regions where there is a large amount of free magnetic energy.

As well as the large variation in flare magnitude, the magnetic geometries of the flaring active region can also differ. The simplest is perhaps an emerged bipolar flux-rope, which appears as a positive and negative sunspot pair in a photospheric magnetogram. However, with more complicated active regions, such as a quadrupole configuration, complicated magnetic topologies can arise that may contain magnetic null points. Several magnetic reconstructions of flaring active regions have found these null points (e.g. Aulanier et al. 2000; Fletcher et al. 2001; Mandrini et al. 2006; Masson et al. 2009; Des Jardins et al. 2009), and they are thought to be common in the low solar corona (Longcope & Parnell 2009). Figure 2.2 shows a recent example of a NLFFF magnetic reconstruction

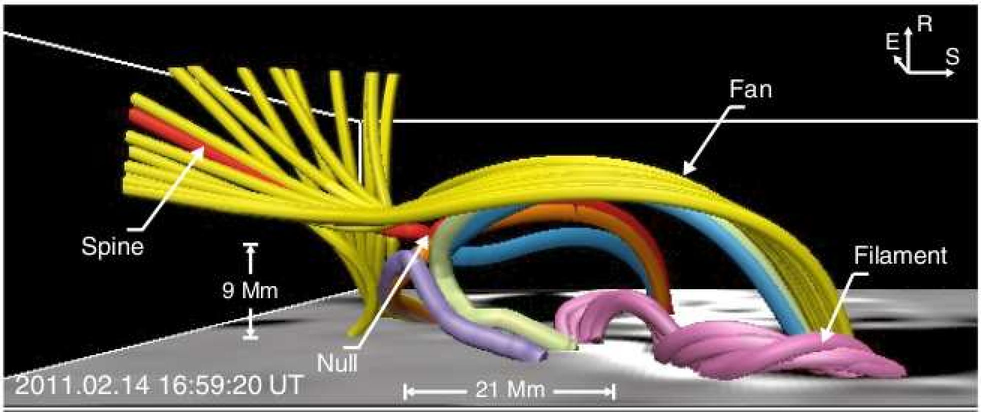

Figure 2.2: NLFFF magnetic reconstruction NOAA active region 11158, showing a spine field-line (red) and a fan surface (yellow) around a 3D magnetic null point. Image from Sun et al. (2012a).

by Sun et al. (2012a) that contains a highly-sheared magnetic skeleton containing such a null-point, also with the spine axis and fan plane (see Section 1.3.6), found at 9 Mm above the solar surface. This extrapolation is from the same active region as in Figure 2.1, but around three hours earlier, and was linked to an eruptive plasma jet (Sun et al. 2012a).

Although the magnetic geometry for a given flare may be unique, it is still useful to introduce the standard flare model, named the CSHKP model (Carmichael 1964; Sturrock 1966; Hirayama 1974; Kopp & Pneuman 1976), as some of its features may be common to many flares, and it is a useful starting point to talk about the observational evidence for magnetic reconnection within flares. Figure 2.3 (a) shows a modern version of the CSHKP model by Shibata et al. (1995). In this model an overlying flux-rope or *filament* (it is common to refer to a two-dimensional slice through a flux-rope as a *plasmoid*, as in the figure), becomes unstable and moves upwards with velocity $v_{\rm plasmoid}$. The associated magnetic pressure decrease causes inflow of oppositely directed field-lines to a reconnection site, shown here as a simple x-point. As the field reconnects, plasma is accelerated in reconnection jets due to the magnetic tension force in the newly reconnected field but then forms a fast magnetohydrodynamic shock, sometimes called the *termination shock*, where it collides with underlying loops. Also, not labelled on the diagram but included in many similar diagrams may be the Petschek (1964) slow-mode shocks between the inflow and outflow regions, see Section 1.3.3. The origin of the "Hard X-Ray (HXR) loop top source" is not decided; it may be

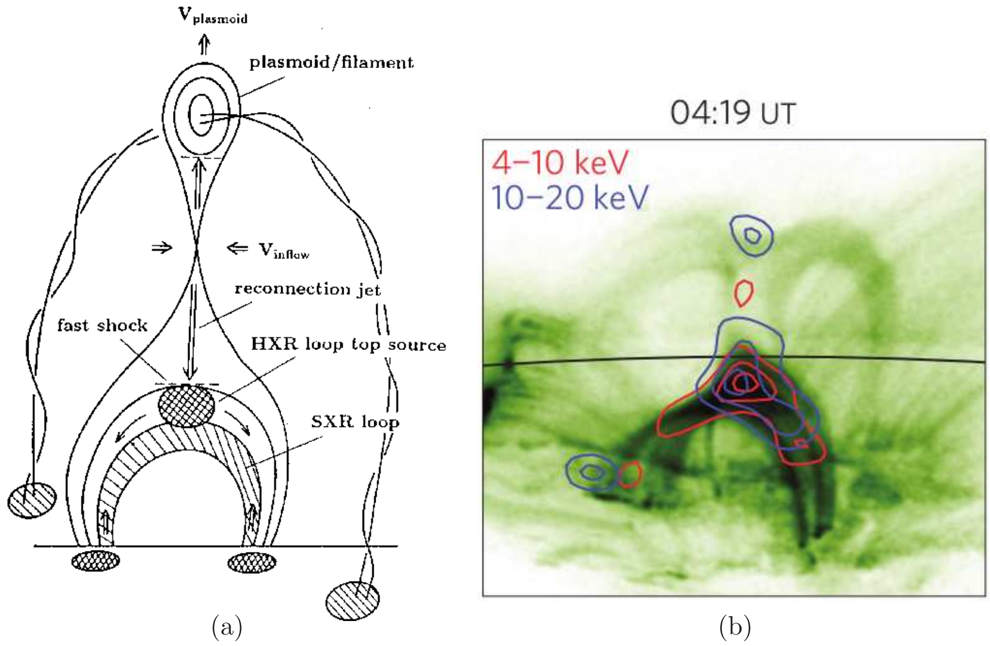

Figure 2.3: a) Cartoon of a solar flare driven by a plasmoid/filament eruption, from Shibata et al. (1995). b) Hard X-ray emission contours for $4-10$ keV (red) and $10-20$ keV (blue), overlayed on a 131 angstrom EUV image. Image from Su et al. (2013), see original article for high resolution movies of inflowing (outflowing) cold (hot) loops to the x-point feature.

due to the fast-shock, or it may be due to the magnetic trapping of fast particles that were accelerated at the reconnection site. In either case, the Hard X-ray emission is due to *Bremsstrahlung*, or breaking radiation. Particles with high energies continue to propagate down the loops until they reach the chromosphere, where the density and thus collision frequency quickly increase. At these chromospheric foot-points more hard x-rays are emitted due to Bremsstrahlung and chromospheric plasma rises, due to evaporation, to fill the post-flare-loops which themselves cool by Soft X-Ray emission (the SXR loops in the figure).

There is a growing body of observational evidence for reconnection in the corona during flares; here we only mention a selection of the literature. Yokoyama et al. (2001) observed a plasmoid ejection with what appears to be a coronal x-point underneath. The authors were able to measure both the speed of the ejected plasmoid $v_{\text{plasmoid}} \approx 37\,\text{km}\,\text{s}^{-1}$ and the inflowing plasma speed $v_{\text{IN}} \approx 1-4.7\,\text{km}\,\text{s}^{-1}$. They estimate the reconnection rate $v_{IN}/v_A = 0.001-0.03$, although there is considerable uncertainty in the value of the magnetic field used to calculate v_A. Further evidence was found by Tsuneta et al. (1992), who found a hot cusp-shaped region in SXR with the YOHKOH satellite that looks remarkably similar to the lower outflow region in Figure 2.3 (a). Hard X-ray emission from the chromospheric foot-points of the flare is regularly observed (see discussion below), but Masuda et al. (1994) found the first example of a HXR source above the top of the SXR loops. Furthermore, Sui & Holman (2003) found a double HXR coronal source that moved apart over time, and interpret these sources as lying above and below the x-point in the flare current sheet. Figure 2.3 (b) shows a recent example of a flare, from Su et al. (2013), that displayed many of the observational features listed above. In EUV with SDO, they simultaneously measure the velocity of cold ($0.05 - 2$ MK) loops inflowing horizontally towards what appears to be an x-point structure, and hot outflowing loops (≈ 10 MK) moving vertically away from that structure. At the same time they measure with the Reuven Ramaty High-Energy Solar Spectroscopic Imager (RHESSI, Lin et al. 2002) a double coronal hard x-ray source above and below the x-point structure. They make an estimate of the reconnection rate, assuming that the outflow speed is equal to the inflow Alfén speed, of $v_{IN}/v_{A,IN} \approx v_{IN}/v_{OUT} \approx 0.05 - 0.5$.

2.1.3 Signatures of accelerated particles

As mentioned, HXR emission is generally observed at chromospheric foot-point sources, and occasionally at coronal sources above the SXR loops. The above-loop-top sources are typically much fainter than the foot-point sources, due to the weaker emission measure, but they become easier to detect if the foot-point sources become obscured by the solar limb. Figure 2.4 shows an example of a HXR spectrum from a flare where one of the foot-points is obscured by the limb, but it contains features that are typical of flare HXR spectra; there is a thermal component (red) at lower energy, and a characteristic broken-power law tail at higher energy.

The inversion of these Hard X-ray spectra, to find the electron energy spectra prior to the Bremsstrahlung emission, is an active topic in solar flare research. There are two classical models for the emission, the *thin-target* model in which the electrons pass through a rare thermal plasma, and the *thick-target* model where the electrons are stopped fully by collisions and thermalised in the source region. Brown (1971) solved this inversion for the thick-target model, assuming that electrons are continually injected into the HXR source region and that they are stopped by binary collisions.

This technique has been applied to many flare events, to calculate the required electron numbers and energies needed to produce the observed HXR emission. Emslie et al. (2004) used this technique for two flares to estimate that around 10% of the free magnetic energy was converted into non-thermal electrons (they also found about 10% in non-thermal ions). Further, Miller et al. (1997) estimates the number of electrons accelerated to energies above 20 keV in a typical large flare to be $10^{37}\,\mathrm{s}^{-1}$. To put this figure in perspective, they compare it to the number of electrons in a typical coronal loop of length 10^7 m, area 10^{14} m, and with a coronal loop density of $n \approx 10^{16}\,\mathrm{m}^{-3}$, which gives 10^{37} electrons. This huge demand on the efficiency of the acceleration region, and the need for accelerated electrons to be replenished over a 100 second event, is sometimes referred to as the *number problem* in the literature. This technique has also been applied specifically to the coronal above-loop-top HXR source by Krucker et al. (2010), finding that all of the electrons contained within the source region needed to be accelerated to above 16 keV. Finally, Ishikawa et al. (2011) studied a similar event, shown in Figure 2.4, where they were able to measure a separate HXR power law for the coronal above-loop-top source and the foot-point source. They estimate that the number of electrons accelerated at the coronal above-loop-top source is sufficient to explain the HXR emission at the foot-points.

As well as fast electrons, there is evidence of fast ion production in solar flares. Collisions between fast ions and ambient plasma can give γ-ray line emission from nuclear de-excitation lines, as well as secondary positron and neutron emission that is then responsible for observed positron annihilation lines and neutron capture lines (see e.g. Vilmer et al. 2011, for a review). Figure 2.5 shows a count-rate spectrum from RHESSI for the October 28th 2003 X17 flare. Visible at lower energies is the electron HXR Bremsstrahlung emission, which continues into γ-rays as the background (dotted line). Also, clearly visible are the positron annihilation line at 511 keV and the 2.2 MeV neutron-capture line (from deuterium nuclei). Many of these features are consistent with the accelerated ions having energies $\sim 1 - 100\,\mathrm{MeV\,nucleon}^{-1}$ (e.g. Murphy et al. 2007).

An important result found by the RHESSI telescope was that the source region for 2.2 MeV neutron capture line emission can be spatially separated from the HXR foot-points (this was measured for the July 23rd 2002 X4.8 flare, see Hurford et al. 2003), suggesting a different acceleration region or mechanism for the ion acceleration than the electron emission.

Finally, it is important to mention that not all observations of accelerated

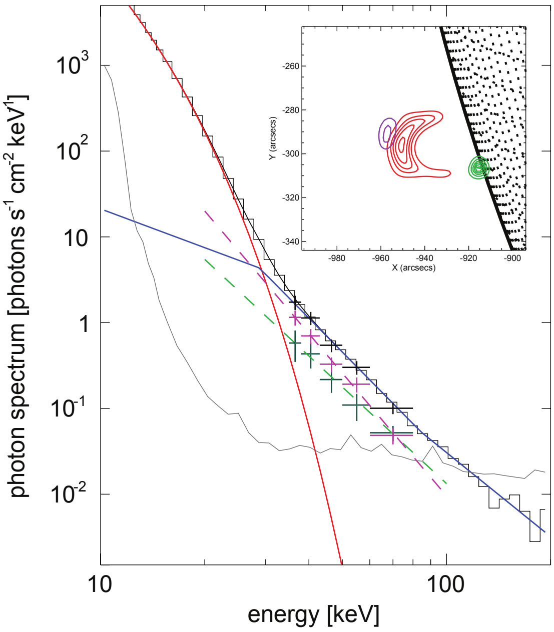

Figure 2.4: Hard X-ray spectrum from the October 22nd 2003 M9.9 flare, from Ishikawa et al. (2011). The spatially integrated HXR spectrum is shown as a histogram, with a thermal component ($T = 33$ MK) fit in red, and a broken power law component in blue. Inset shows the solar limb and HXR contours for the foot-point source (green), the thermal component (red) and an above-loop-top HXR source (magenta), and the green and magenta lines show the respective power laws for that emission. The grey line is the background emission.

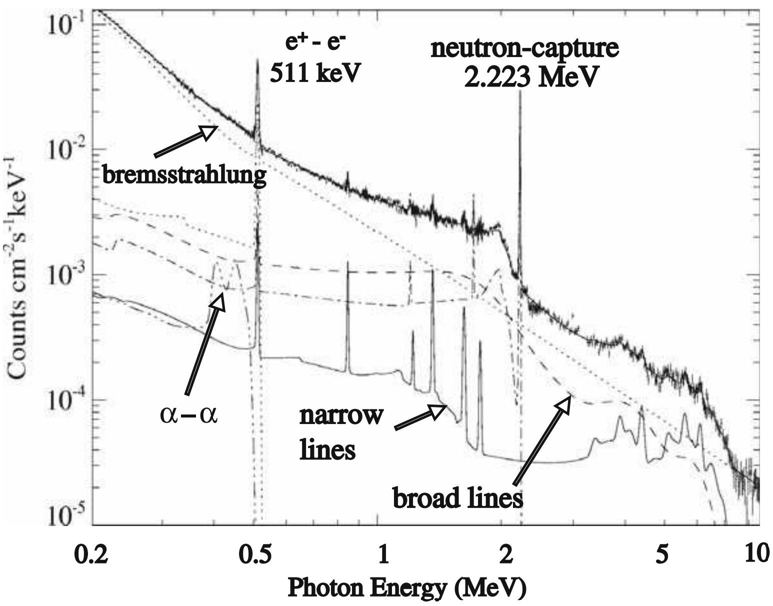

Figure 2.5: RHESSI γ-ray count rates from October 28th 2003 X17 flare. Image from Dennis et al. (2007).

particles are due to above-loop-top coronal HXR sources and foot-point HXR and γ-ray sources. Fast particles can also travel upwards into the corona where electron wave particle interactions lead to radio emission at the local plasma frequency (or a harmonic). This emission is referred to as a Type-III burst, and decreases in frequency with height due to the reduction of density ($\omega_{pe} \propto n_e^{1/2}$). Some particles can escape the corona on open field-lines, where they can be detected *in-situ* by spacecraft at Earth, such as the WIND spacecraft (Lin et al. 1995).

It is clear that there are stringent requirements from the observations on any proposed electron and ion acceleration mechanisms. In Chapter 4 we will explore one possibility, that the ions and electrons are accelerated by the large DC electric fields associated with reconnection at a 3D magnetic null point. This mechanism is unlikely to be responsible for particle acceleration in all solar flares, but it may be important in flare geometries with more complicated active regions, such as NOAA active region 11158 in which the NLFFF extrapolation has a highly sheared 3D null point, shown in Figure 2.2.

2.2 Tokamak: a magnetic confinement fusion energy device

The word *tokamak* is from a Russian acronym meaning a toroidal chamber with magnetic coils. The Joint European Torus (JET) tokamak is based at Culham Centre for Fusion Energy in the UK, and is operated by the European Fusion Development Agreement (EFDA). The JET tokamak currently holds the world record of just over 16 MW of deuterium-tritium fusion power (Keilhacker et al. 1999). Currently the ITER (latin for "the way") tokamak is being constructed in Cadarache, France, as a collaboration between the European Union, Russia, Japan, China, USA, India and South Korea. According to the design specification (ITER/EDA 2001), ITER will produce up to 500 MW of fusion power, which will be a factor of 10 higher than the power used in the plasma heating systems.

Figure 2.6 (a) shows a schematic diagram of a tokamak device, showing a number of coils that are used to confine the plasma torus. Currents in the toroidal field coils are used to generate a strong vacuum magnetic field in the toroidal direction B_ϕ (the long way around the torus). The plasma gyrates around this main field component but, due to magnetic curvature and gradients in field strength,

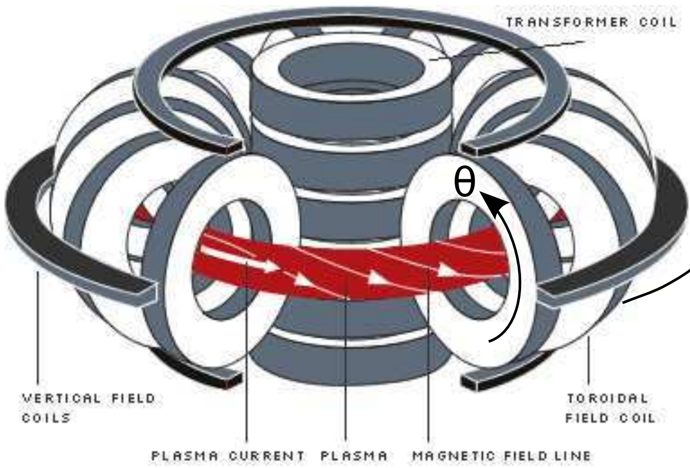

(a)

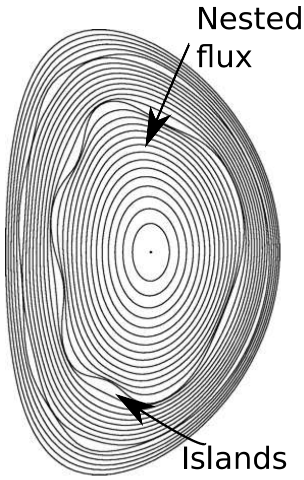

(b)

Figure 2.6: a) Schematic diagram of a tokamak magnetic confinement plasma device (Image from Max-Planck-Institut fur Plasmaphysik 2009). b) Cross-section of the plasma showing an equilibrium containing magnetic islands (Image from Garabedian 2006).

the plasma can drift across the field causing loss of confinement. The situation is improved by adding a poloidal field component B_θ (the short way around the torus). In a tokamak this is achieved by using the transformer, known as the *central solenoid*, to drive a toroidal current in the plasma, which has an associated B_θ component. The resulting Lorentz force causes the plasma to pinch, improving confinement.

The combination of the B_ϕ and B_θ magnetic field components results in helical field-lines as shown in Figure 2.6. A useful quantity when comparing the magnitude of these components is called the *safety factor*, or *q-profile*, which is defined as the number of times the field-lines loop around the vessel toroidally for each poloidal rotation. The simplest equilibrium configuration consists of nested flux-surfaces, where a thermal pressure gradient balances the pinch-force such that the pressure has a single value on each flux-surface (for more detail on how these equilibria are constructed see Grad & Rubin 1958; Shafranov 1966). However, on flux-surfaces that have a rational value of q, known as rational surfaces, tearing modes (see Section 1.3.4) may become unstable to produce configurations containing magnetic islands as shown in Figure 2.6 (b).

A self-sustaining fusion reaction can be achieved if the product of the plasma density n, temperature T and confinement time τ_E is above the value $nT\tau_E >$

$3 \times 10^{21}\,\mathrm{m}^{-3}\,\mathrm{keV\,s}$ (Lawson 1957). In practise, there are several obstacles to overcome to achieve this value. Firstly, careful empirical studies have found a limit on the achievable plasma density, known as the *Greenwald limit*. Greenwald et al. (1988) showed that the average electron density n_e is limited by

$$n_e < \frac{I_p}{\pi a^2}, \tag{2.2}$$

where I_p is the plasma current and a is the minor radius (the distance from the centre of the nested flux-surfaces to the last closed flux-surface, see Figure 2.7). Above this value a disruption is often triggered, causing loss of core current and temperature. The theoretical origin for this limit is not well understood, but recently Gates & Delgado-Aparicio (2012) have proposed this is related to island formation and radiative cooling.

Reaching high temperatures is complicated by the fact that the plasma resistivity scales inversely with the temperature $\eta \propto T_e^{-3/2}$ (see equation (1.20)); the traditional method of heating the plasma by Ohmic dissipation of the toroidal current is effective at low temperature, but the heating power at high temperatures is weak. To reach and maintain high temperatures in the core of the plasma, additional heating mechanisms (see e.g. Wesson 2011) are commonly used, such as Electron Cyclotron Resonance Heating (ECRH) where microwave radiation at the electron cyclotron frequency Ω_{ce} is effectively absorbed and heats the plasma, or Neutral Beam Injection (NBI) in which Coulomb collisions heat the plasma as an injected beam slows and becomes thermalised.

Finally, the confinement time τ_E is the internal energy, divided by the total input power P_{IN} (Wesson 2011). That is

$$\tau_E = \frac{1}{P_{IN}} \int \frac{3}{2} n(T_i + T_e) dV. \tag{2.3}$$

The classical transport model of Braginskii (1965), based on Coulomb collisions in a strongly magnetised plasma, predicts for example perpendicular heat conductivities that are some orders of magnitude lower than what is measured in experiment. This is also the case when this theory is extended to include the effects of toroidal geometry and/or low collisionality in the so-called *neoclassical transport* regime. One effect of lowering the collision frequency is that particles can be trapped by the mirror force, see equation (1.4), on the outer edge of the torus thus modifying the orbits. The difference between the experimentally

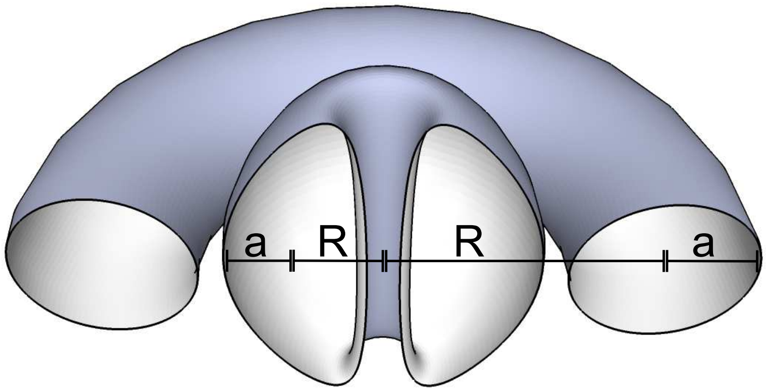

Figure 2.7: Relative sizes of a conventional tokamak (outer) and spherical tokamak (inner) magnetic confinement devices, where R and a are the major and minor radii respectively for each device (Image from Imazawa 2009).

measured transport and the neoclassical theory is referred to as *anomalous* or turbulent transport. Progress has been made with *gyro-kinetic codes* in simulating this transport regime, the enhanced transport levels are thought to be related to the growth of micro-instabilities, see e.g. Garbet et al. (2010) for a review.

2.2.1 The Spherical Tokamak (ST)

Figure 2.7 shows the major radius R, the distance from the centre of the machine to the centre of the plasma, and the minor radius a, the distance from the centre to the edge of the plasma, for a conventional tokamak (outer donut-shaped device). Conventional tokamaks are often referred to as large aspect-ratio devices, where the aspect-ratio is defined as $R/a \gg 1$ (for example JET has $R = 2.96$ m and $a = 1.25$ m). There are also tight-aspect-ratio tokamaks which have $R/a \approx 1$, known as *Spherical Tokamaks* (STs) due to their cored apple shape (inner device in Figure 2.7).

The cost efficiency of a tokamak is related to the plasma β, as the aim is to create high temperature and dense plasmas, while strong magnetic field coils can be costly to build and operate. The Small Tight Aspect Ratio Tokamak (START, operated by UKAEA Fusion at Culham UK between 1991 and 1998) demonstrated that high-plasma beta values could be achieved with this design. Gryaznevich et al. (1998) describe a START experimental shot with $\beta_T = 34\%$, where β_T is the average plasma-β given by

$$\beta_T = \frac{1}{B_0^2/(2\mu_0)} \frac{1}{V} \int_v p dV, \tag{2.4}$$

where B_0 is the vacuum toroidal field at the centre of the nested flux-surfaces. This value was more than a factor of two higher than the β_T achieved by conventional tokamaks at that time (the next highest was the conventional DIII-D tokamak that had achieved $\beta_T = 12.6\%$, see Strait 1994).

At present the largest ST devices in operation are the National Spherical Torus Experiment (NSTX; see e.g. Gerhardt et al. 2011) at the Princeton Plasma Physics Laboratory (PPPL), and the Mega-Ampere Spherical Tokamak (MAST; see Section 2.2.2) at Culham Centre for Fusion Energy (CCFE) that is described below.

2.2.2 The Mega-Ampere Spherical Tokamak

The MAST device was constructed as a larger version of the START experiment, and began operation in 1998 (Sykes et al. 2001). Figure 2.8 (a) shows the stainless-steel MAST vacuum vessel with copper central post, and an impression of the equilibrium plasma is shown in purple. Around the outside edge of the plasma are poloidal field coils that can be used to control the plasma position and shape. These coils wrap around the vessel toroidally. Figure 2.8 (b) shows a schematic cross-section of the vacuum vessel with poloidal field coils labelled P1-P6, and an impression of the plasma shape in grey. The P1 coil is the central solenoid (the transformer of Figure 2.6) used to drive current in the plasma. This coil is wound around the toroidal field rod in the central post and then surrounded by a graphite limiter. In a cross-section of constant toroidal angle, the vessel dimensions are $R \in [0.2, 2.0]$ m, $Z \in [-2.2, 2.2]$ m, where $R = 0.2$ m is the outer radius of this central column graphite limiter and the other values are the walls of the vessel. The toroidal field coil is wound 24 times around the vessel, so that the toroidal field can be estimated using the simple formula

$$B_\phi = \frac{\mu_0 24 I_{TF}}{2\pi R}, \tag{2.5}$$

where I_{TF} is the current in the toroidal field coil and R is the cylindrical radius from the vessel centre. Here the ripple in the toroidal field due to the spacing

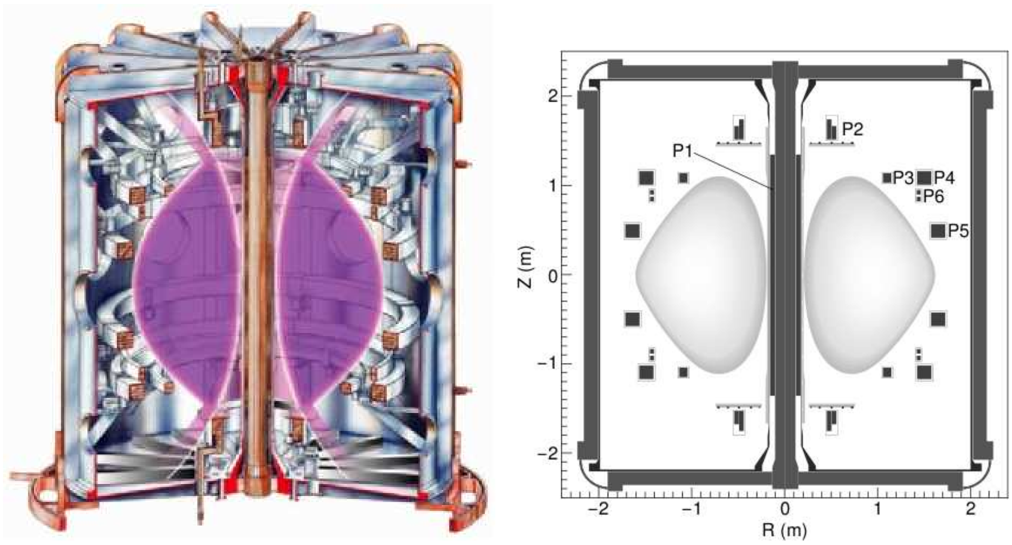

(a) (b)

Figure 2.8: a) Cut-away of the MAST vacuum vessel and plasma (Culham Centre for Fusion Energy). b) Schematic cross-section of MAST with poloidal field coils labelled P1-P6 (Image from Sykes et al. 2001).

Quantity	R (m)	a (m)	$B_\phi(R)$ (T)	I_{plasma} (MA)	T (keV)	n (m^{-3})
Value	0.85	0.65	0.52	≤ 1.5	$0.1 - 3$	10^{18-20}

Table 2.2: Typical parameters for MAST at flat-top operation.

between the coils (e.g. Wesson 2011) has been neglected. The P2-P6 coils labelled in the top half ($Z > 0$) are paired with an identical coil in the lower half ($Z < 0$). The pair of P2 coils are used for divertor control, the P3 coils for merging-compression start-up (see below), P4 and P5 coils for radial position and the P6 coils for vertical position. The radial position control is needed because a toroidal current ring experiences a hoop-force (see e.g. Goedbloed et al. 2010) in the radial direction. The P4 and P5 coils thus supply a vertical field that balances this radial force so that the plasma does not hit outer wall of the vessel.

Table 2.2 gives some plasma parameters typical of MAST in the flat-top, or steady equilibrium, phase of a MAST experimental shot.

The MAST tokamak is equipped with a broad range of diagnostics; there are too many to list here so only the ones referred to in this thesis will be mentioned. Firstly, there are many pick-up coils mounted onto the vessel walls and poloidal field coils that can measure the magnetic field around the edge of the plasma. These are commonly used to numerically calculate plasma equilibrium using, for example, the EFIT code (Lao et al. 1990). We will discuss data from the Central Column MirnoV (CCMV20) pick-up coil that measures the time rate of change of the vertical magnetic field component at the central post. The position of pick-up coil is shown in Figure 2.9. There are several visible light fast cameras fitted to viewports in MAST. In this thesis we will show images from the *Bullet Cam. B* which is fitted to the mid-plane of the vessel. The camera is fitted with a wide angle lens, so that the field of view covers the whole plasma, but this does mean the image has some distortion. In the experiments discussed below, ion temperatures have been measured with a Neutral Particle Analyser (NPA). This diagnostic measures energetic deuterium atoms that are produced by charge exchange between fast ions and neutrals in the plasma. MAST is also equipped with two extremely high spatial resolution Thomson Scattering (TS) laser diagnostic systems. The Ruby TS laser takes profiles of electron temperature and density at $Z = -1.5$ cm below the mid-plane with 284 spatial points, but can only be used once in each experiment described below. The second TS system is a 130 spatial point Nd:YAG system, comprised of eight lasers each with 30 Hz repetition (Scannell et al. 2010). However, these can be used in "burst-fire" mode to give extremely high time resolution. The Nd:YAG lasers are positioned at $Z = 1.5$ cm above the geometric mid-plane, indicated in Figure 2.9.

2.2.3 Non-solenoidal start-up

It has been suggested that the Spherical Tokamak (ST) magnetic confinement concept should be developed further, towards a ST Power Plant (ST-PP, e.g. Voss et al. 2002) or ST-based Component Test Facility (ST-CTF, e.g. Peng et al. 2005). The latter device would produce via fusion an extremely high flux of neutrons that would be used to test wall materials for future devices. In both the ST-PP and ST-CTF machines, significant neutron shielding would be required for the toroidal field coils at the central column, leaving little space for a central solenoid. An attractive option is to remove the central solenoid and to achieve plasma formation and current drive through other methods. Towards this goal several non-solenoidal start-up methods have been investigated on a number of devices, including; the use of radio-frequency waves (e.g. Shiraiwa et al. 2004; Gryaznevich et al. 2006), co-axial and DC helicity injection (e.g. Raman et al. 2010; Battaglia et al. 2011), and flux-rope merging start-up via poloidal field coil induction (e.g. Sykes et al. 2001; Yamada et al. 2010). In this thesis, we will consider the latter start-up method, within the Mega-Ampere Spherical Tokamak, as a magnetic reconnection experiment.

2.2.4 Merging-compression in MAST

The merging-compression start-up method, first performed on the Small Tight Aspect Ratio Tokamak (Gryaznevich et al. 1992), is now routinely used on MAST (Sykes et al. 2001). After gas filling and ramp-up of currents in toroidal and poloidal field coils, to supply the vacuum field, the current in the pair of P3 poloidal field coils (see Figure 2.9) is ramped back down towards zero on a millisecond timescale. This causes breakdown and induces toroidal current rings, or co-helicity flux-ropes, in the plasma surrounding the P3 coils. When the parallel toroidal plasma current within the flux-ropes becomes greater than the current in the respective P3 coils, the mutual attraction between the flux-ropes causes them to detach from the coils and move towards the mid-plane of the vessel, where they merge together to form a single ST plasma. The relaxation from two flux-ropes with parallel currents to one ST plasma involves magnetic reconnection of poloidal field. With this technique, up to 0.5 MA of plasma current has been obtained, and electron and ion temperatures up to 1.2 keV have been achieved on a timescale of ≈ 10 ms (Ono et al. 2012; Yamada et al. 2012).

Figure 2.10 shows four visible light photographs taken from the fast camera (Bullet Cam. B) for MAST experimental shot 25656. This is one of the few merging-compression shots where the camera was operated at a fast time resolution of 0.1 ms (other shots typically have 1 ms resolution). The top-left image shows the formation of two flux ropes around the P3 poloidal field coils at $t = 2.1$ ms. At $t = 4.4$ ms, in the top-right image, the flux-ropes have moved towards the centre post, and they appear to have detached from the P3 coils (although there is still some emission from the plasma around these coils). At this time the flux ropes are in contact with each other across the mid-plane of the vessel, where there appears to be a region of increased emission. At $t = 4.5$ ms (the bottom-left image) there is no visible flux-rope structure; the flux-ropes appear to have merged. Finally, the bottom-right image shows the plasma at the later time of $t = 117.6$ ms, when the plasma is in the flat-top phase and the current has increased from use of the central solenoid. It should be noted that the detachment of the flux-ropes from the P3 coils prior to merging is not clearly shown in the fast-camera videos for some other shots. It is not clear whether this is due

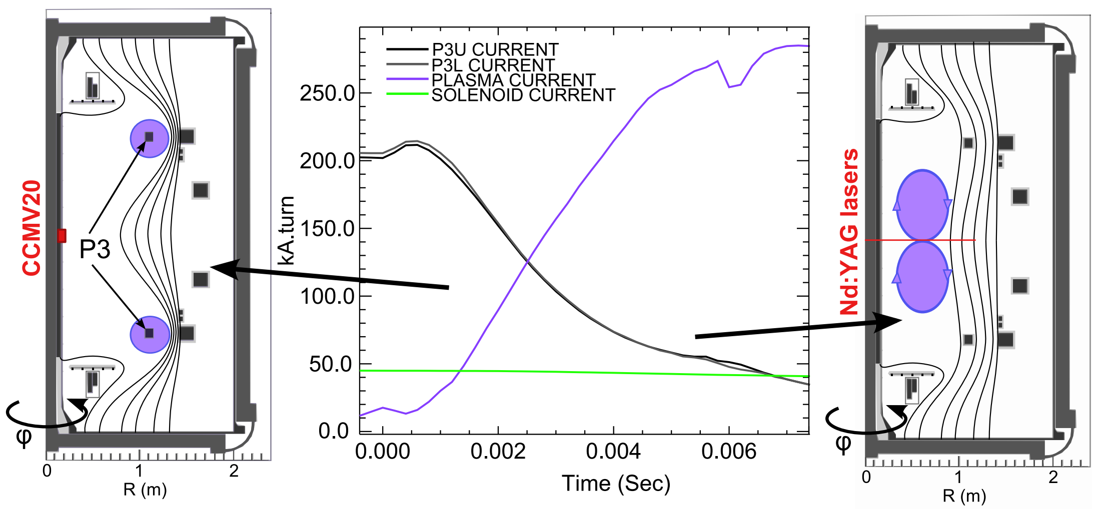

Figure 2.9: Centre: Currents in the upper and lower poloidal P3 coils (P3U and P3L as black and grey lines respectively), with the central solenoid current (green) and the plasma current (purple), during the start-up phase of MAST shot 25740. The cartoons on either show the plasma shape at that approximate time (inferred from the fast-camera images of shot 25656, see below). The two diagnostics labelled are the Central Column MirnoV (CCMV20) pick-up coil, and the position of the Nd:YAG Thomson scattering lasers.

to slower time resolution of the fast camera (1 ms), or whether the plasma can sometimes merge before it is fully detached. For the simulations in Chapter 5 we will assume that this detachment prior to merging has occurred, as shown for this shot.

There is a wealth of data on electron temperature T_e and density n_e during merging-compression from the TS laser systems. Figure 2.11 shows radial profiles of n_e (top) and T_e (middle) taken with four of the Nd:YAG lasers in burst-fire mode (with 0.1 ms between each laser) for shot 25740. This is the same shot as the current traces in Figure 2.9 (the density and temperature traces for this shot are also published in Ono et al. (2012) for a larger range of times but with a narrower range of radial values). The bottom panel shows a trace against time of the CCMV20 pick-up coil signal (measuring the time derivative of the vertical magnetic field at the position shown in Figure 2.9). The colours of the top profiles indicate the times which the Thomson scattering lasers fire; at $t = 5.4$ ms (purple), 5.5 ms (light blue), 5.6 ms (dark blue) and 5.7 ms (green). At $t = 5.4$ ms, before the peak in the pick-up coil signal, there is a double-peaked density profile that is also present in many other MAST merging-compression shots. Over

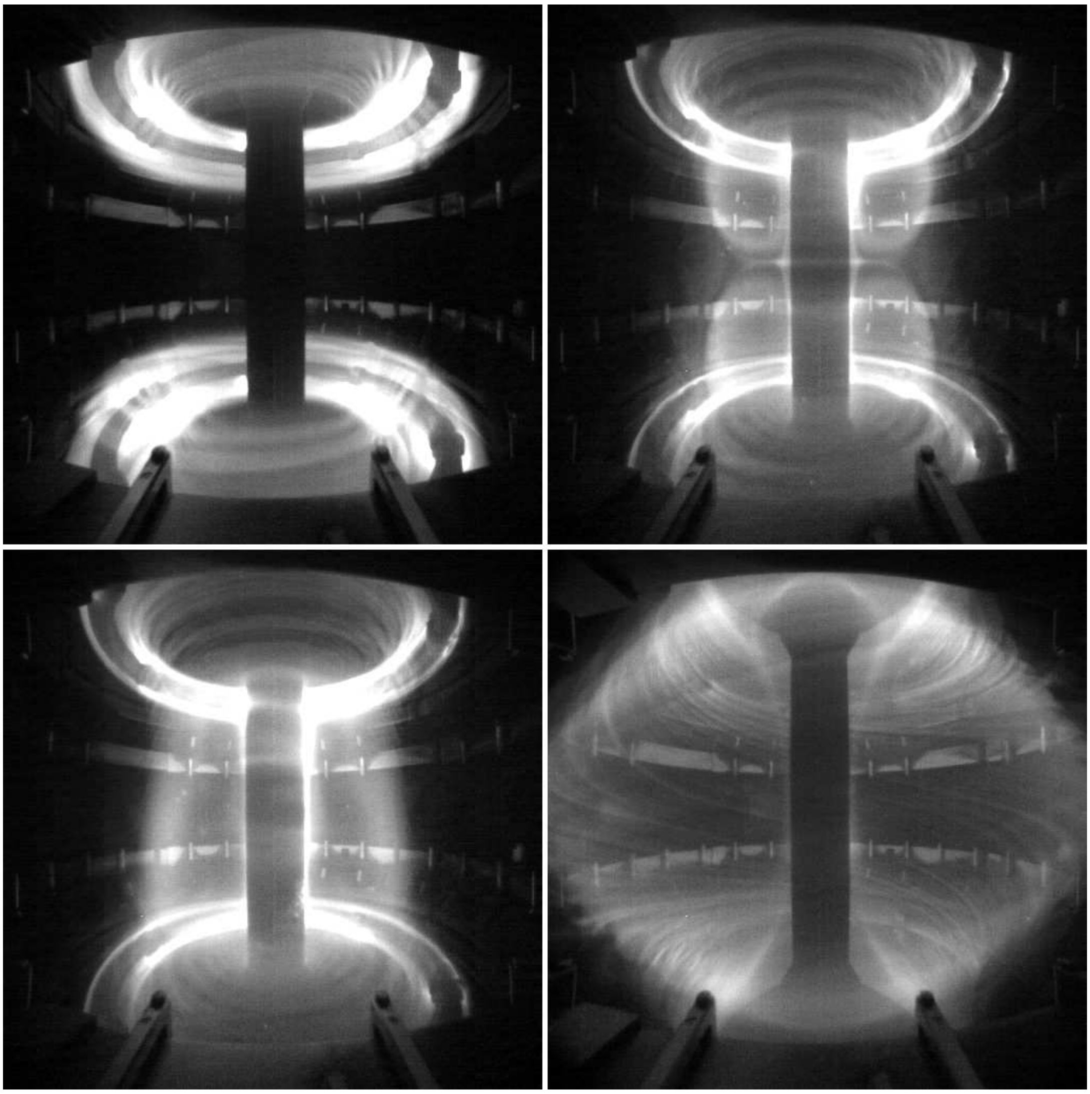

Figure 2.10: Fast camera visible light images from MAST experimental shot 25656 at $t = 2.1$ ms (top left), $t = 4.4$ ms (top right), $t = 4.5$ ms (bottom left), $t = 117.6$ ms (bottom right). This data is obtained from the Culham Centre for Fusion Energy (CCFE) MAST shot database.

time the inner peak moves towards the inboard side, and the outer peak is pushed radially outwards and decays. The electron temperature rises from $\approx$ 10 eV to $\approx$ 80 eV between $t = 5.4$ ms and $t = 5.5$ ms, and at later time there is a localised T_e peak of 260 eV and a full-width half-maximum of a few cm. It is not clear whether the peak is not present before this time, or whether the hot plasma was moving vertically so the peak intersected the laser at this time (Yamada et al. 2013). Finally, there are oscillations in the CCMV20 trace after the main peak with a period of $\approx 30\,\mu s$. These oscillations will be discussed again in Chapter 5.

As well as 1D profiles of electron temperature and density, there are also some 2D T_e profiles. These 2D profiles have been compiled from a number of shots which are identical, apart from the current in the P6 coils that control the vertical position of the plasma. By changing the P6 currents the whole plasma is shifted vertically between shots, and 2D maps can be constructed from the 1D TS measurements assuming that there is sufficient reproducibility. Figure 2.12 shows 2D T_e maps from two groups of experimental shots with different gas filling densities. These are both taken with the Ruby laser ($Z = -1.5$ cm) at $t = 10.0$ ms. In the "peaked" shots there is a peak in line integrated density and in deuterium-alpha emission at $t \approx 5$ ms, suggesting this was the time of merging. In the "hollow" shots there is no line integrated density data, but there are peaks in the deuterium-alpha emission and CCMV20 signal also at around $t \approx 5$ ms. Similar 2D profiles taken with the Nd:YAG lasers (not shown here, see Yamada et al. (2012)) from 8 ms to 11 ms indicate that the electron temperature is still increasing at 10 ms, despite this being approximately 5 ms after the merging. A combination of Ohmic heating of electrons within the current sheet and electron heating via temperature equilibration with hot ions has been suggested as an explanation for these temperature profiles (e.g. Yamada et al. 2012). The latter would occur on the ion-electron equilibration timescale τ_{eq}, given by equation (1.24). For merging-compression parameters $n_0 = 5 \times 10^{18}\,\mathrm{m}^{-3}$, $T_0 = 10$ eV this is given by

$$\tau_{\mathrm{eq}} \approx 0.2\,\mathrm{ms} \times (T_e[\mathrm{eV}]/T_0)^{3/2}, \tag{2.6}$$

so, if the ions are preferentially heated by the reconnection process, the electrons will be heated by equilibration on a millisecond timescale. Initial ion temperature measurements with the Neutral Particle Analyser (NPA, see above) do indicate

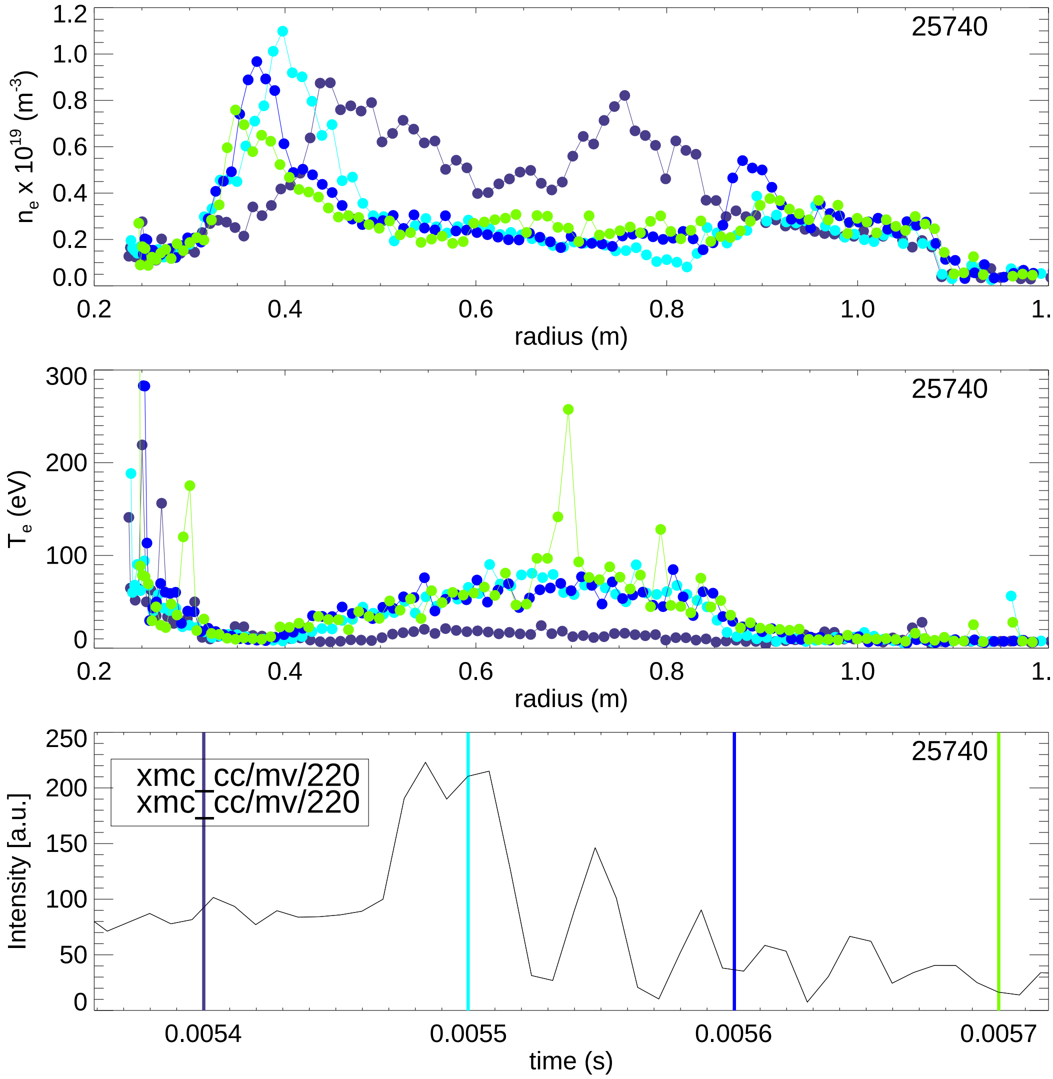

Figure 2.11: Electron density n_e (top panel) and temperature T_e (middle panel) measured by four Nd:YAG Thomson Scattering (TS) lasers with 0.1 ms time interval for MAST experimental shot 25740. In the bottom panel is the CCMV20 pick-up coil trace (black line), where the times at which the TS lasers fire is indicated. This data is obtained from the CCFE MAST shot database. The density and temperature plots are also shown in Ono et al. (2012), for a narrower range of R.

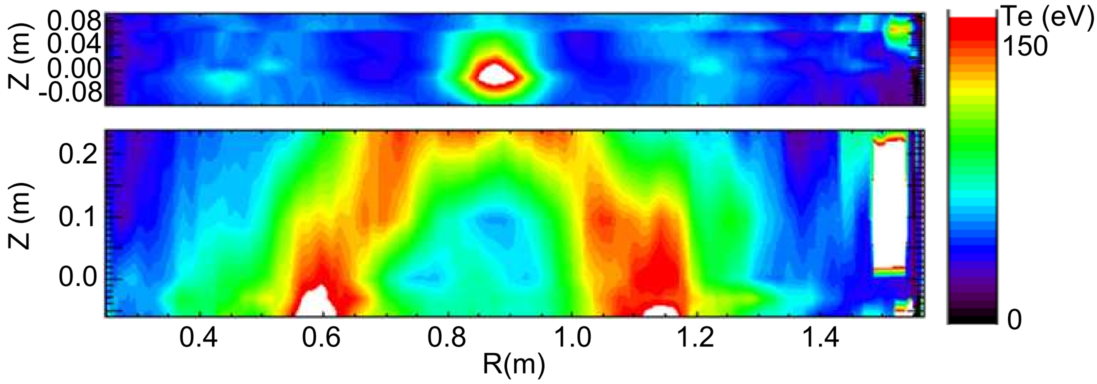

Figure 2.12: 2D electron temperature maps built from many MAST merging-compression shots using the Ruby TS system at $t = 10$ ms. The top plot is made from shots 21374-21380 with different P6 coil currents (vertical shift) (Yamada et al. 2012) and feed gas density $n \approx 10^{19}\,\mathrm{m}^{-3}$ (Imazawa 2009). The bottom plot is made from shots 21390, 21405-21407 and 21409 (Imazawa 2009) with different P6 coil currents and feed gas density $n \approx 2 \times 10^{18}\,\mathrm{m}^{-3}$.

that ions are heated on a shorter timescale than electrons during a merging-compression shot, see Figure 2.13. This will be explored further with possible future experiments along with numerical simulations.

2.3 Comparing coronal and merging-compression reconnection

Two different applications for magnetic reconnection have been described in some detail in this chapter. The first was magnetic reconnection within solar flare active regions, and the second within the start-up phase of the Mega-Ampere Spherical Tokamak. Table 2.3 shows a comparison of these two plasma environments, and the important reconnection parameters associated with them. At first glance, in particular at the length-scale, these two applications seem wildly different. The dominant ion-species for the corona is typically proton (hydrogen) compared to deuterium for MAST, but it should be noted that there is also some higher mass ion content in both plasmas. The magnetic fields in MAST are stronger than the corona (the poloidal field B_p for MAST is estimated from the time integrated CCMV20 signal), and the temperature is comparable, but the plasma is much denser. However, both merging-compression and coronal plasmas are in the low-β regime, having comparable values (here β_T and β_p are defined in terms

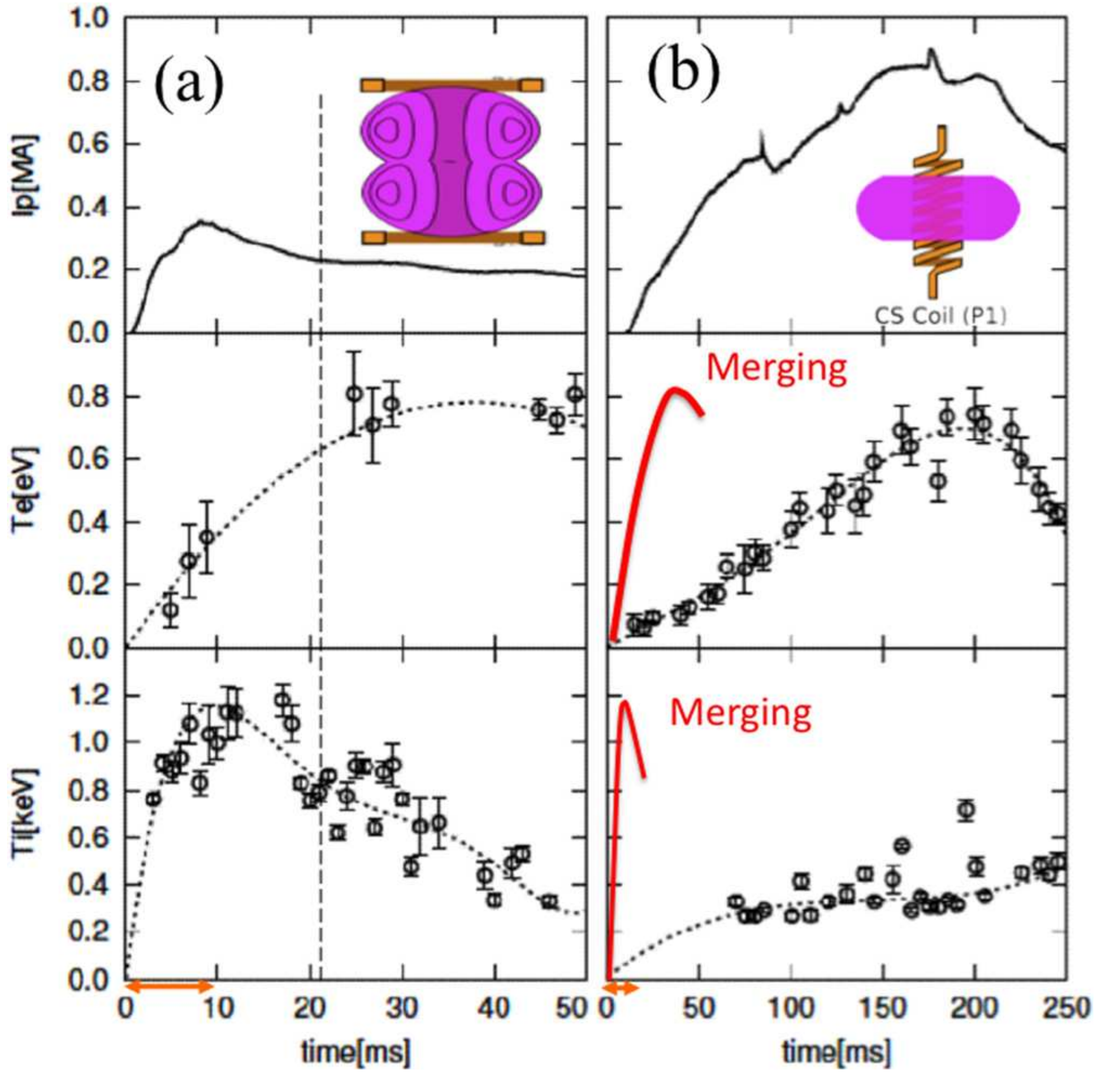

Figure 2.13: Comparison of electron and ion heating for a merging-compression shot (a), and a direct-induction shot using the central solenoid (b). In the top row is plasma current I_p in MA, the second row is electron temperature T_e in keV, and the bottom row is ion temperature T_i in keV. The red lines in (b) indicate the merging-compression shot values and duration. Image from Ono et al. (2012).

Quantity	Solar flare	MAST merging-compression
Typical values:		
Global length	$L \sim 10^7$ m	$L = 1$ m
Ion species	Proton	Deuterium
Magnetic	$B \sim 0.01$ T	$B_p = 0.1$ T, $B_T = 0.5$ T
Temperature	$T \sim 100$ eV	$T = 10 - 1000$ eV
Density	$n \sim 10^{15}\,\mathrm{m}^{-3}$	$n = 5 \times 10^{18}\,\mathrm{m}^{-3}$
Dimensionless:		
Plasma-β	$\beta = 10^{-4} - 10^{-2}$	$\beta_T = 10^{-4} - 10^{-2}$, $\beta_p = 10^{-3} - 10^{-1}$
Lundquist number	$S = 10^{12-14}$	$S = 10^{4-7}$
Non-MHD:		
Ion skin-depth	$d_i = 10$ m	$d_i = 14.5$ cm
Ion gyro-radius	$\rho_i = 0.1 - 1$ m	$\rho_i = 0.15 - 1.5$ cm
Current-sheet:		
Sweet-Parker width	$\delta_{SP} = 1 - 10$ m	$\delta_{SP} = 0.03 - 1$ cm
δ_{SP}/d_i	$0.1 - 1$	$0.002 - 0.07$

Table 2.3: Table showing comparison of typical values for magnetohydrodynamic variables, dimensionless parameters, non-MHD (two-fluid and kinetic) scales, and current-sheet parameters.

of the toroidal and poloidal fields). The Lundquist number is much higher in the corona than in MAST; however, the Lundquist numbers achieved in MAST merging-compression are higher than any other currently operating magnetic reconnection experiment (see Ono et al. 2012, for a comparison between MAST and other reconnection experiments). Finally, in terms of the importance of two-fluid physics, the Sweet-Parker width is below the ion-skin depth for both environments, although the table suggests that two-fluid effects may be more important in MAST.

It is worth mentioning another similarity between coronal reconnection associated with solar flares and merging-compression: in both cases the reconnection is coupled to an ideal driver. In Figure 2.3(a) the x-point reconnection is driven by the erupting flux-rope (this is not just a feature of this cartoon, but it is a feature of many solar flare models). A coronal Alfvén time can be estimated from Table 2.3 as $\tau_0 \approx \sqrt{n m_i \mu_0} L/B \approx 1$ second. Thus a 100 second duration energy release phase (HXR emission timescale) is much closer to an ideal timescale than to, for instance, a Sweet-Parker timescale $\tau_{SP} \sim S^{1/2}\tau_0 \sim 10^6 - 10^7$ seconds (see also the discussion in Chapter 5 of Birn & Priest 2007). In MAST the driving is due to the ideal attraction between the flux-ropes with parallel current.

In the remainder of this thesis, numerical simulations of magnetic reconnection will be described in these two plasma environments. However, before the results are presented, the numerical techniques and codes that will be used will be introduced and tested in the next chapter.

Chapter 3

Simulation Techniques and Code Development

In this Chapter we describe the numerical codes that are used in the remainder of the thesis. Firstly, we describe a test-particle code (Dalla & Browning 2005) that is used to study test-particles within 3D null point geometries in Chapter 4, then we describe the HiFi framework (Glasser & Tang 2004; Lukin 2007) that will be used for the fluid simulations in Chapter 5.

3.1 Test-particle code

3.1.1 Existing formulation

The work presented in Chapter 4 is an investigation of test-particle motion in supplied magnetic and electric fields. This is performed with the same test-particle code used in Dalla & Browning (2005, 2006, 2008) and Browning et al. (2010). We mention some details of the code here, and describe the modifications that were made to the code in the course of this work. The equations of motion solved by the code are the relativistic versions of equations (1.1) and (1.2). They are

$$\frac{d\boldsymbol{x}}{dt} = \frac{\boldsymbol{p}}{\gamma m_s}, \tag{3.1}$$

$$\frac{d\boldsymbol{p}}{dt} = q_s \left(\boldsymbol{E} + \frac{\boldsymbol{p}}{\gamma m_s} \times \boldsymbol{B} \right), \tag{3.2}$$

where $\boldsymbol{p} = \gamma m_s \boldsymbol{v}$ is the momentum, $\gamma = (1 - v^2/c^2)^{-1/2}$ is the Lorentz factor (c is the speed of light) and m_s is the rest mass for particle of species s.

3.1.2 Core algorithm

Equations (3.1) and (3.2) are solved using the `D02cjf` integration routine from The Numerical Algorithms Group (NAG) (2013) library. This is a Variable-Step Variable-Order (VSVO) Adams method (see e.g. Johnson & Riess (1982) for a description of this widely used method). The `D02cjf` routine solves a set of coupled first-order ordinary differential equations of the form

$$\dot{y}_i = f_i(t, y_1, y_2, ..., y_n), \quad i = 1, 2, ..., n, \tag{3.3}$$

where $\dot{y}_i$ is the time derivative of the solution vector y_i. The test-particle code is set up to find the solution vector $(\boldsymbol{x}, \boldsymbol{p})$, by specifying f_1,f_2 and f_3 as the right-hand-sides of equations (3.1), and f_4,f_5,f_6 as the right-hand-sides of equations (3.2). Crucially, this routine monitors local error e_i to the solution y_i. This local error is checked against user supplied relative error and absolute error tolerances, τ_r and τ_a respectively, with the following test

$$est = \sqrt{\sum_{i=1}^{n} \left(\frac{e_i}{\tau_r \times y_i + \tau_a} \right)^2} \leq 1, \tag{3.4}$$

(The Numerical Algorithms Group (NAG) 2013). If this is not satisfied then the solver recalculates the step-size accordingly. Such a variable-step method was chosen to resolve the fastest timescale in the problem, $\Omega_{cs}^{-1} \propto B^{-1}$, when there is a large variation in the magnetic field strength inside the simulation domain. In all simulations presented we use the minimum possible tolerances of $\tau_r = \tau_a = 10^{-15}$. This tolerance was also varied to check for solution convergence (see below).

3.1.3 Verification of the test-particle code

Although the test-particle code has been used previously in Dalla & Browning (2005, 2006, 2008) and Browning et al. (2010), it has not been used to model particle trajectories within reconnecting current sheets. Here we benchmark the code against the analytical results of Speiser (1965) to show how well it resolves

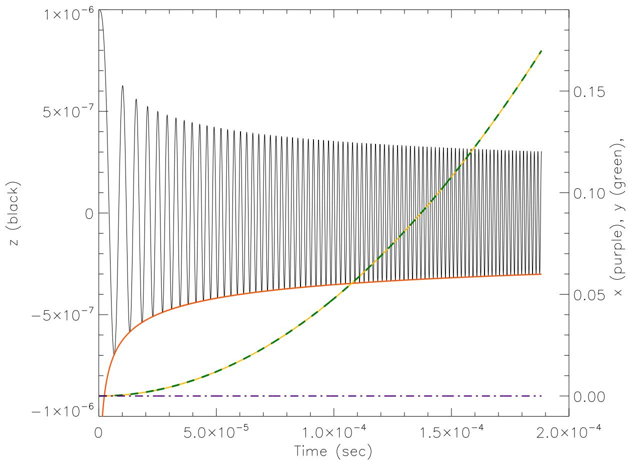

Figure 3.1: Proton trajectory in a reconnecting current sheet with no background field ($\epsilon_B = 0$). The z-position (black-solid line) has axis on the left hand side, and the x (purple dash-dotted) and y (green-dashed) positions use the right hand axis. Also plotted for reference is a line with $z \propto t^{-1/4}$ (red-solid), and the line y_{acc} (orange-solid). Distances are in units of $L_0 = 10^4$ m.

the Speiser-like (meandering) motion discussed in Chapter 1, and shown in Figure 1.10.

The electric and magnetic fields take the simple form

$$\boldsymbol{E} = E_y \hat{\boldsymbol{y}} \quad [v_0 B_0], \tag{3.5}$$

$$\boldsymbol{B} = \frac{z}{\delta}\hat{\boldsymbol{x}} + \epsilon_B \hat{\boldsymbol{z}} \quad [B_0], \tag{3.6}$$

where E_y is a constant electric field, δ is the current sheet width, ϵ_B gives the strength of a magnetic field perpendicular to the plane of the sheet, v_0 is a characteristic velocity and B_0 a characteristic magnetic field. We choose $E_y = 10^{-2}$, $\delta = 10^{-4}$, and typical solar coronal values of $B_0 = 0.01$ T and $v_0 = 10^7$ m s^{-1}.

For the case of $\epsilon_B = 0$, the analytical results of Speiser (1965) give stable non-adiabatic oscillations within the current sheet, which have an amplitude that decays as $t^{-1/4}$. Provided the particle remains sub-relativistic, the distance travelled in the direction parallel to the electric field at time t is simply $y_{\text{acc}} = qE_y t^2/2m$. Figure 3.1 shows the position of a proton with initial position $\boldsymbol{x} = (10^{-10}, 10^{-10}, 10^{-6})\, L_0$, and velocity $\boldsymbol{v} = \boldsymbol{0}$ (where $L_0 = 10^4$ m). There are

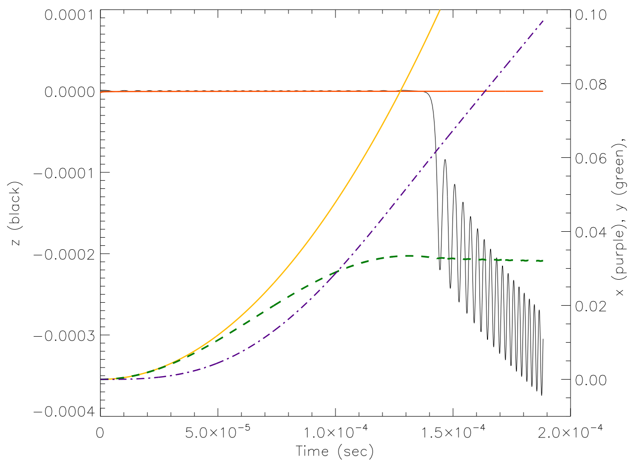

Figure 3.2: Proton trajectory in a reconnecting current sheet with background field $\epsilon_B = 0.025$. The z-position (black-solid line) uses the left-hand axis (which is zoomed-out compared with the previous figure). The x (purple dash-dotted) and y (green-dashed) positions use the right-hand axis. Also plotted are the $z \propto t^{-1/4}$ (red-solid), and y_{acc} (orange-solid) lines. Distances are in units of $L_0 = 10^4$ m.

decaying oscillations in the z-direction (black line and left hand axis) in agreement with Speiser (1965). The red line over-plotted is $z = Ct^{-1/4}$, where C is chosen to fit the line to the first oscillation peak. This line fits the amplitude of the subsequent oscillations extremely well. Also shown is the y-position of the proton (green dashed line with right hand axis), and the predicted position y_{acc} in orange. These lines appear identical for the duration of the motion as expected. The x-position remains at $x \approx 10^{-10}$ for the duration (purple dash-dotted line).

A finite ϵ_B gives a Lorentz force in the x-direction that can gyro-turn the particle, see Figure 1.10, and cause it to be gyro-ejected after it turns 90°. Speiser (1965) gives the time until ejection as

$$t_{\text{eject}} = \frac{\pi m}{qB_n}, \tag{3.7}$$

where $B_n = \epsilon_B B_0$ is the normal field component to the sheet in this notation. For the parameters used $t_{\text{eject}} = (3.28 \times 10^{-6}/\epsilon_B)$ sec. Figure 3.2 shows the same simulation as before, but with $\epsilon_B = 0.025$. For $t \lesssim 5 \times 10^{-5}$ sec, the oscillations look very similar to the case with $\epsilon_B = 0$ (note that the z-range in this figure is zoomed out so that these oscillations are not visible). However, the amplitude of the oscillations begins to grow after this time. The proton becomes unstable and is ejected at $t \approx 1.3 - 1.4 \times 10^{-4}$ sec which is in good agreement with the analytical result. Note that it is difficult to compare an exact time, as ejection is not an instantaneous event. This ejection occurs after the proton has been gyro-turned in the positive x-direction, and the acceleration is reduced as the particle becomes magnetised around the B_x component of the magnetic field, which is perpendicular to $\boldsymbol{E}$; it is ejected into the external (electric) drift region. Thus the actual y position is less than the direct acceleration, y_{acc}, line.

Figure 3.3 shows an electron trajectory (the previous simulations used protons) in the Speiser model fields with no background field component $\epsilon_B = 0$. The four panels show the same run but with different values of τ_r and τ_a; the relative and absolute tolerances for the numerical integrator, see Section 3.1.2. The electrons are followed for many meandering oscillations in strong direct electric fields, and as a result they become ultra-relativistic (at the final time $t = 3.5 \times 10^{-6}$ s the Lorentz factor is $\gamma = 2.32$). Note that we do not show the case of $\epsilon_B \neq 0$ as the ejection time (3.7) is only valid in the non-relativistic limit, $v \ll c$. The y-position (green dash-dotted) is between two orange lines that are y_{acc} (curved) and a straight-line with gradient equal to the speed of light ($\dot{y} = -c$). The amplitude of the oscillations agrees with the $z = Ct^{-1/4}$ curve fit (red) well for $\tau_r = \tau_a = 10^{-15}$ and up to $\tau_r = \tau_a = 10^{-6}$. However, for $\tau_r = \tau_a = 10^{-5}$ the fit is worse, and is clearly wrong for $\tau_r = \tau_a = 10^{-4}$ due to accumulation of numerical error. We conclude that the lowest tolerance value $\tau_r = \tau_a = 10^{-15}$ is sufficient for the test-particle simulations presented in Chapter 4.

3.1.4 Test-particle code modifications

During the course of this work, some major modifications were made to the test-particle code. Firstly, for the model fields used in Chapter 4, a routine was needed to numerically calculate the confluent hypergeometric function (or *Kummer function*) $M(a, b, x)$, see e.g. Abramowitz & Stegun (1972). As the fields need to be evaluated at every timestep, there are very strict specifications on the accuracy and speed of calculating the result. We describe the algorithm used in Appendix A.1, where we also verify the routine against values generated by the proprietary software `Mathematica 8` (Wolfram Research, Inc. 2010).

One of the functions of the test-particle code is to loop through a list of particles and integrate their trajectories consecutively. After integrating on the order of a thousand particle trajectories, energy spectra (such as the one in Figure 4.12)

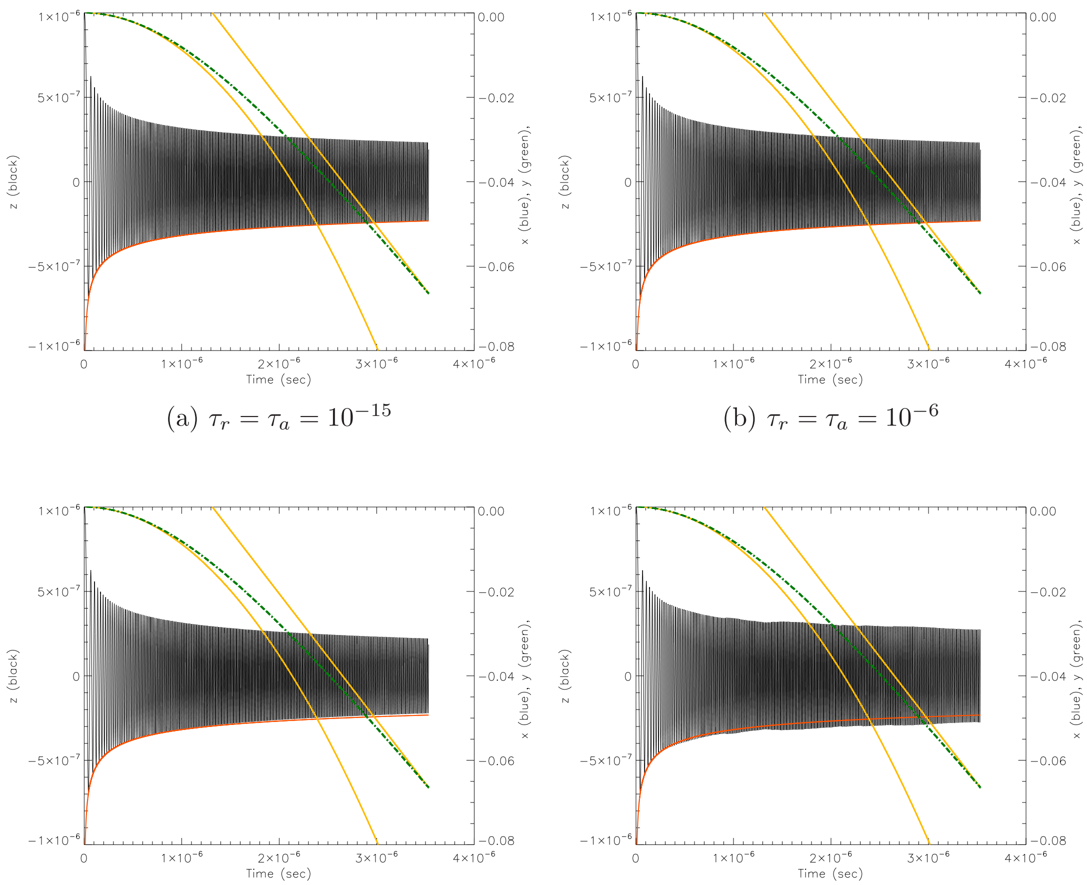

(a) $\tau_r = \tau_a = 10^{-15}$

(b) $\tau_r = \tau_a = 10^{-6}$

(c) $\tau_r = \tau_a = 10^{-5}$

(d) $\tau_r = \tau_a = 10^{-4}$

Figure 3.3: Electron meandering orbits in the Speiser current sheet with no background field component for four different tolerances of the numerical integration routine, τ_r and τ_a. The z-position (black-solid line) has axis on the left hand side of each panel, and the x (blue-dashed, not visible) and y (green dash-dotted) positions use the right hand axis of each panel. Also plotted in each panel for reference are lines with $z \propto t^{-1/4}$ (red-solid), y_{acc} (orange-solid curve) and a line with gradient equal to the speed of light, $\dot{y} = -c$ (orange, linear). Distances are in units of $L_0 = 10^4$ m.

can be calculated. To significantly speed up this process we parallelised this loop using OpenMP directives. With this modification, up to 16 particle trajectories can be integrated concurrently on the local cluster (where 16 is the number of threads in one node). Further speed-up could achieved by parallelising further onto many nodes, but this was deemed unnecessary here.

Finally, even with the parallelised many-particle code, electron trajectories were found to take a prohibitively long time to integrate. Below we describe how we modified the test-particle code to implement a guiding-centre formulation, and developed routines that allow switching from guiding-centre to full-orbit equations when particle motion becomes non-adiabatic (for example close to a null point).

3.1.5 Relativistic guiding-centre formulation

As mentioned above, the integrator within the test-particle code calculates the time-step size adaptively to reduce numerical error. For this, it is required that the timestep for a particle of species s is much less than the local gyro-time $(\Delta t)_s \ll \Omega_{cs}^{-1} \propto m_s$, which can be particularly prohibitive for electrons. However, in Chapter 4 we will need to follow full particle trajectories, within fields of global length-scale, for times that are long enough to show interesting behaviour. For the electron trajectories we will use the guiding-centre approximation, discussed in Chapter 1, to average over the fast gyro-motion and allow much larger time-steps to be used.

We extensively modified the test-particle code to evolve both the non-relativistic version of the guiding-centre equations (1.7-1.10), and the more general relativistic version (Vandervoort 1960; Northrop 1963). The non-relativistic version was only developed as an intermediate step towards the full relativistic version. All of the results that use the guiding-centre code given in Chapter 4 use the relativistic version. Furthermore, the fields used in this study are all stationary, so we neglect all drift terms related to time dependent fields. The relativistic guiding-centre equations that are valid for $r_L/L \ll 1$ (in dimensional notation $m_s/q_s \ll 1$ is used as the small parameter, see Northrop 1963), and assuming $E_\parallel \sim \mathcal{O}(m/q)$, $E_\perp \sim \mathcal{O}(1)$ are given by Vandervoort (1960) and Northrop (1963) as

$$\frac{d\boldsymbol{R}_g}{dt} = \boldsymbol{v}_d + v_\parallel \hat{\boldsymbol{b}}, \tag{3.8}$$

$$\boldsymbol{v}_d = \boldsymbol{v}_E + \frac{m_s}{q_s}\frac{\mu_r}{\gamma\kappa^2 B}\hat{\boldsymbol{b}}\times\boldsymbol{\nabla}(\kappa B) + \frac{m_s}{q_s}\frac{\gamma}{\kappa^2 B}\hat{\boldsymbol{b}}\times\left[v_\parallel D_t\hat{\boldsymbol{b}} + D_t\boldsymbol{v}_E\right] + \frac{v_\parallel E_\parallel}{c^2\kappa^2 B}\hat{\boldsymbol{b}}\times\boldsymbol{v}_E, \quad (3.9)$$

$$\frac{d(\gamma v_\parallel)}{dt} = \gamma\boldsymbol{v}_E\cdot D_t\hat{\boldsymbol{b}} + \frac{q_s}{m_s}E_\parallel - \frac{\mu_r}{\gamma}\hat{\boldsymbol{b}}\cdot\boldsymbol{\nabla}(\kappa B), \quad (3.10)$$

$$\frac{d\mu_r}{dt} = \mathcal{O}(m_s/q_s), \quad (3.11)$$

where $\boldsymbol{R}_g$ is the guiding centre position defined by

$$\boldsymbol{R}_g = \boldsymbol{x} - \boldsymbol{r}_L = \boldsymbol{x} + \frac{(\gamma\boldsymbol{v} - \gamma\boldsymbol{v}_E)\times\hat{\boldsymbol{b}}}{|q_s|B/m_s}, \quad (3.12)$$

t is time, $\boldsymbol{v}_d$ is the guiding-centre perpendicular drift velocity vector, $\boldsymbol{v}_E$ is the electric drift velocity, γ is the Lorentz factor, $v_\parallel = \hat{\boldsymbol{b}}\cdot\boldsymbol{v}$ is the parallel velocity, $\kappa = \sqrt{1 - E_\perp^2/c^2B^2} = \sqrt{1 - v_E^2/c^2}$ is a relativistic correction for fast electric drift (due to the $E_\perp \sim \mathcal{O}(1)$ ordering), $D_t = (v_\parallel\hat{\boldsymbol{b}} + \boldsymbol{v}_E)\cdot\boldsymbol{\nabla}$ is the derivative along the drift orbit (where $\boldsymbol{v}_E$ is the only drift retained, and the time derivative is neglected for steady fields), $\mu_r = \gamma^2 v_\Omega^2/(2B)$ is the relativistic magnetic moment per unit rest mass. Note that these equations reduce to the non-relativistic stationary guiding-centre equations in the limit $v_\parallel, v_\Omega, v_E \ll c$ (where $\gamma, \kappa \to 1$). Some of these terms can be identified as the relativistic versions of the drifts terms presented in Chapter 1. For example, the second term in equation (3.9) is relativistic gradient drift, the final term within equation (3.10) is the mirror force per unit rest mass. However, the final term in equation (3.9) is only present in the relativistic formulation (see Northrop (1963)).

The energy evolution for the charged particle in stationary electromagnetic fields is given by

$$\frac{d(\gamma m_s c^2)}{dt} = q_s\left[\boldsymbol{v}_d + v_\parallel\hat{\boldsymbol{b}}\right]\cdot\boldsymbol{E}. \quad (3.13)$$

Before these equations are put into the test-particle code, they are made dimensionless using the pre-existing code normalisation scheme. We write every variable χ in the form $\chi = \chi_0\tilde{\chi}$. Magnetic fields are normalised by a typical coronal value, $B_0 = 0.01$ T, lengths by the simulation box size $x_0 = L_{\rm box}$ (in fact for this code there is no true edge to the domain, so this is just chosen as a free parameter), velocities by a coronal Alfvén speed $v_0 = 6.5\times10^6\,\mathrm{m\,s^{-1}}$, time by $t_0 = 2\pi/\Omega_{cs0}$ where $\Omega_{cs0} = |q_s|B_0/m_s$ is a typical species gyro-frequency, electric fields by $E_0 = v_0 B_0$, and the magnetic moment by v_0^2/B_0. This choice of normalisation gives two dimensionless parameters $c_1 = t_0 v_0/x_0$, which is the ratio of a typical gyration time to the Alfvén time, and $c_2 = q_s B_0 t_0 / m_s = \mathrm{sgn}\,(q_s) 2\pi$ where $\mathrm{sgn}\,(q_s)$ gives the sign of the charge. Note that the choice of normalisation is flexible. For instance, a natural choice of x_0 might be the ion skin-depth that sets $c_1 = 1$. However, we do not choose this here, so that our results are more in line with Dalla & Browning (2005) who use $x_0 = L_{\mathrm{box}}$.

To integrate equations (3.8-3.11), the Lorentz factor γ must also be determined explicitly (on the left hand side it is only present in $\gamma v_\parallel$ and in $\mu_r \propto \gamma v_\Omega$). Noting that γ can be written as $\gamma = \sqrt{1 + \gamma^2 v^2/c^2}$, and writing $v^2 = v_\parallel^2 + v_\Omega^2 + v_d^2$ (where the term involving $\boldsymbol{v}_\Omega \cdot \boldsymbol{v}_d$ is averaged to zero over a gyration), then γ can be expressed as

$$\gamma \approx \sqrt{\frac{1 + \left[(\gamma v_\parallel)^2 + 2\mu_r B\right]/c^2}{1 - v_d^2/c^2}}. \tag{3.14}$$

However, this expression can not be used directly, as $v_d = v_d(\gamma)$ is a function of γ. Instead, we compute γ to a first guess as

$$\gamma \approx \sqrt{\frac{1 + \left[(\gamma v_\parallel)^2 + 2\mu_r B\right]/c^2}{1 - v_E^2/c^2}}, \tag{3.15}$$

before computing v_d and using it in expression (3.14). We iterate on the last two steps until γ converges to a value, but in practise we find that this occurs to a sufficient number of significant figures after just one iteration.

The normalised form of the equations passed to the `D02CJF` integration routine is written below, in the form of equation (3.3). Here, we have dropped the tilde notation, and introduced a third dimensionless parameter $c_3 = v_0^2/c^2$.

$$\frac{d\boldsymbol{R}_g}{dt} = c_1 \left[\boldsymbol{v}_d + \frac{(\gamma v_\parallel)}{\gamma}\hat{\boldsymbol{b}}\right], \tag{3.16}$$

$$\begin{aligned}\boldsymbol{v}_d =& \boldsymbol{v}_E + \frac{c_1}{c_2 \kappa^2 B}\Big[\frac{\mu_r}{\gamma}\hat{\boldsymbol{b}} \times \boldsymbol{\nabla}(\kappa B) + \frac{(\gamma v_\parallel)^2}{\gamma}\hat{\boldsymbol{b}} \times \hat{\boldsymbol{b}} \cdot \boldsymbol{\nabla}\hat{\boldsymbol{b}} \\ &+ (\gamma v_\parallel)\hat{\boldsymbol{b}} \times \boldsymbol{v}_E \cdot \boldsymbol{\nabla}\hat{\boldsymbol{b}} + (\gamma v_\parallel)\hat{\boldsymbol{b}} \times \hat{\boldsymbol{b}} \cdot \boldsymbol{\nabla}\boldsymbol{v}_E + \gamma\hat{\boldsymbol{b}} \times \boldsymbol{v}_E \cdot \boldsymbol{\nabla}\boldsymbol{v}_E\Big] \\ &+ c_3 \frac{(\gamma v_\parallel) E_\parallel}{\gamma \kappa^2 B}\hat{\boldsymbol{b}} \times \boldsymbol{v}_E,\end{aligned} \tag{3.17}$$

$$\frac{d(\gamma v_\parallel)}{dt} = c_1 (\gamma v_\parallel)\boldsymbol{v}_E \cdot \hat{\boldsymbol{b}} \cdot \boldsymbol{\nabla}\hat{\boldsymbol{b}} + c_1 \gamma \boldsymbol{v}_E \cdot \boldsymbol{v}_E \cdot \boldsymbol{\nabla}\hat{\boldsymbol{b}} + c_2 E_\parallel - c_1 \frac{\mu_r}{\gamma}\hat{\boldsymbol{b}} \cdot \boldsymbol{\nabla}(\kappa B), \tag{3.18}$$

$$\frac{d\mu_r}{dt} = 0, \tag{3.19}$$

where $\kappa = \sqrt{1 - c_3 v_E^2}$ and $\gamma = \sqrt{1 + c_3[(\gamma v_\|)^2 + 2\mu_r B]/\kappa}$.

For the model fields used in Chapter 4, we define and store two Cartesian second-rank tensors $\boldsymbol{\nabla}\hat{\boldsymbol{b}}$ and $\boldsymbol{\nabla}\boldsymbol{v}_E$, as well as the vector $\boldsymbol{\nabla}B$ (we write the expression $\boldsymbol{\nabla}(\kappa B) = \kappa\boldsymbol{\nabla}B - (c_3 B/\kappa)\boldsymbol{\nabla}v_E^2/2$, which can be calculated from $\boldsymbol{\nabla}B$ and the components of $\boldsymbol{\nabla}\boldsymbol{v}_E$). The components of these tensors and vectors are calculated analytically for the fields used and given in Appendix A.2. The complicated vector operations are then computed at double precision using a custom `vector` fortran type. These are solved by specifying in equation (3.3) $(y_1, y_2, y_3) = \boldsymbol{R}_g$, $y_4 = \gamma v_\|$ and $y_5 = \mu_r$.

3.1.6 Switching

Provided that the orderings of the guiding-centre equations are well satisfied, this method only results in a small loss of accuracy for a large increase in computational efficiency. Unfortunately, this is not always the case for the model fields used in Chapter 4. In particular, the models contain reconnecting current sheets with strong $E_\|$, and a magnetic null point where $\boldsymbol{B} = \boldsymbol{0}$. For a particle approaching the latter, the "small" parameter $r_L/L \to \infty$! However, this ordering violation only occurs in localised regions of the domain, and the guiding-centre approximation can be used when the particle is adiabatic provided it switches to full-orbit when these orderings begin to break down. It should be noted that a form of switching mechanism was used in Browning et al. (2010), where a switch from non-relativistic guiding-centre equations to full-orbit equations was done within a certain distance from a null point. The authors state that this distance was found empirically. However, this method is only useful in simple fields, such as the potential magnetic field (1.54) used in that paper. In addition, Birn et al. (2004) has used a switching algorithm, determined the ratio of the local magnetic field strength to some critical value, to study electron orbits in the magnetotail. As far as we know, a switching mechanism based on the direct calculation of the local gradient length-scale has not been done before. Here we can do this accurately, as we have calculated the analytic expressions for $L_{\nabla B}$ for the model fields used, see Appendix A.2.

The switching mechanism we use tests the ratio of the instantaneous Larmor radius divided by the local magnetic gradient length scale,

$$r_L/L_{\nabla B} < K_s, \tag{3.20}$$

against a user-defined switching parameter K_s. When this inequality is violated the code switches to a full-orbit calculation. However, first we discuss the switch from full-orbit to guiding-centre, as it is the simpler case.

To switch from full-orbit to guiding-centre requires changing from the 6D phase-space $(\boldsymbol{x}, \boldsymbol{p})$ to the 5D guiding-centre phase-space $(\boldsymbol{R}_g, \gamma v_\parallel, \mu_r)$. The threshold quantities $L_{\nabla B} = B/|\boldsymbol{\nabla} B|$ and $r_L \approx c_1|\gamma \boldsymbol{v} - \gamma \boldsymbol{v}_E|/(c_2 B)$ are evaluated at $\boldsymbol{x}$. To switch from $\boldsymbol{x}$ to $\boldsymbol{R}_g$, we use the normalised version for the definition of the instantaneous gyro-centre in equation (3.12), that is

$$\boldsymbol{R}_g = \boldsymbol{x} + \frac{c_1(\gamma \boldsymbol{v} - \gamma \boldsymbol{v}_E) \times \hat{\boldsymbol{b}}}{c_2 B}, \tag{3.21}$$

where $\boldsymbol{v}_E$, B and $\hat{\boldsymbol{b}}$ are evaluated at $\boldsymbol{x}$. The parallel velocity is evaluated as $\gamma v_\parallel = \boldsymbol{p} \cdot \hat{\boldsymbol{b}}$ ($\gamma v_\parallel = p_\parallel$ in normalised units, as $p_0 = m_s v_0$). Finally, the relativistic magnetic moment per unit mass is evaluated at $\boldsymbol{x}$ as $\mu_r = \gamma^2 v_\Omega^2/2B$, where $v_\Omega^2 \approx v^2 - v_\parallel^2 - v_E^2$ is accurate to $\mathcal{O}((r_L/L)^2)$.

While integrating guiding-centre equations the threshold test parameters, r_L and $L_{\nabla B}$, are evaluated at $\boldsymbol{R}_g$. As the definition of this threshold is marginally different before and after switching, it was common for the code to switch back immediately after switching. To prevent this, the value of K_s was set to be a factor of 0.9 as large when switching to guiding-centre, making it harder to switch to guiding-centre than to full-orbit. The switch from guiding-centre to full-orbit involves a change from the 5D guiding-centre phase-space $(\boldsymbol{R}_g, \gamma v_\parallel, \mu_r)$ to the 6D full-orbit phase space $(\boldsymbol{x}, \boldsymbol{p})$. To do this we randomly generate a gyro-phase $\phi \in [0, 2\pi]$, and make the transformation as

$$\boldsymbol{x} = \boldsymbol{R}_g + \boldsymbol{r}_L = \boldsymbol{R}_g + r_L(\hat{\boldsymbol{e}}_{\boldsymbol{2}} \cos\phi - \hat{\boldsymbol{e}}_{\boldsymbol{1}} \sin\phi), \tag{3.22}$$

$$\boldsymbol{p} = \gamma v_\parallel \hat{\boldsymbol{b}} + \gamma v_\Omega(\hat{\boldsymbol{e}}_1 \cos\phi + \hat{\boldsymbol{e}}_2 \sin\phi) + \gamma \boldsymbol{v}_d, \tag{3.23}$$

where we construct two orthonormal basis vectors in the plane perpendicular to $\hat{\boldsymbol{b}}$ as $\hat{\boldsymbol{e}}_{\boldsymbol{1}} = (\boldsymbol{R}_g \times \hat{\boldsymbol{b}}) \times \hat{\boldsymbol{b}}/|\boldsymbol{R}_g|$ and $\hat{\boldsymbol{e}}_2 = \hat{\boldsymbol{b}} \times \hat{\boldsymbol{e}}_{\boldsymbol{1}}$.

In addition to the threshold test described, which is generic and can be used for many analytic model fields, we impose specific conditions on model fields containing current sheets. We prevent the particle switching back to guiding-centre close to, or within, the current sheet so that the ordering of $E_\parallel \sim \mathcal{O}(r_L/L)$ is not violated. Thus, within the current sheet the switching from full-orbit to guiding-centre is overridden, and the integration is continued in $(\boldsymbol{x}, \boldsymbol{p})$ space.

3.1.7 Testing the guiding-centre switching code

Here we present a selection of results from the testing of this guiding-centre switching code. For each test a completely full-orbit trajectory is calculated for comparison, then a series of runs with the guiding-centre approximation are performed for various K_s.

The first test is a single proton trajectory. This is the same as the proton trajectory '2' shown in Figure 4.17 and discussed in Chapter 4, except that the particle is given at $t = 0$ the electric drift velocity $\boldsymbol{v}_E(\boldsymbol{x}(t = 0))$ in addition to its thermal velocity. This is so that full-orbit results can be directly compared with guiding centre. It was not done for the full-orbit proton calculations in Chapter 4, where the initial velocity was only thermal. This trajectory was chosen because it drifts into the current sheet from the external region and also passes close to a magnetic null point, making it a challenging trajectory for a guiding-centre computation.

Several parameter traces from these test-particle trajectories are shown in Figure 3.4. In each panel a trace is plotted from four different simulations, where the first simulation is a full-orbit calculation (blue), and the other three are guiding-centre calculations with $K_s = 10^{-5}$ (green), $K_s = 10^{-4}$ (orange) and $K_s = 10^{-3}$ (red), where K_S is the switching parameter in equation (3.20). The solid lines in the top panel are traces of the small parameter $r_L/L_{\nabla B}$ (note that these lines almost exactly overlap). The horizontal dotted lines indicate the different K_s values used, and the vertical dotted lines indicate the time at which $r_L/L_{\nabla B} = K_s$ for each value of K_s used. The next panel shows the relativistic magnetic moment per unit rest mass, μ_r. It can be seen that the switching occurs for all three guiding-centre simulations before any visible violation in the constancy of μ_r in the full-orbit simulation (this switching occurs before the proton enters the current sheet). In the kinetic energy (K.E.) and potential energy (P.E.) plots the effect of the switching can be seen more clearly. At

$t = 1002\,t_0$ the guiding-centre calculation with $K_s = 10^{-5}$ (green) switches to full-orbit. Before this time, oscillations in the energies can only be seen in the purely full-orbit calculation (blue), and the energies for the guiding centre calculations are identical to each-other (red). However, after $t = 1002\,t_0$ oscillations are seen in green, and then later in orange ($K_s = 10^{-4}$ switches at $t = 1159\,t_0$) and finally in red ($K_s = 10^{-3}$ switches at $t = 1319\,t_0$). The kinetic and potential energies of the full-orbit calculation appear to be extremely well reproduced by the guiding-centre switching code both before and after switching (apart from the phase of the oscillations after switching). To highlight the small differences in the runs we plot the total energy (K.E. + P.E.) for the four simulations in the final panel. The guiding centre trajectories do deviate slightly in total energy from the full-orbit trajectory. However, this is within 1 eV for $K_s = 10^{-5}$ and 10^{-4}, reaching up to only 2 eV for $K_s = 10^{-3}$ before switching. The change in total energy during the switch is 1.5 eV for $K_s = 10^{-5}$ and 10^{-4}, and 2.2 eV for $K_s = 10^{-3}$. These changes are all dominated by a change in total energy that occurs when the particle enters the current sheet when the kinetic and potential energies change very quickly (this change can be seen just after the 10^{-3} switch, however, shortly afterwards the total energy recovers).

The previous test showed that the guiding-centre switching code works well up to large values of K_s ($K_s \leq 10^{-3}$) for a single proton trajectory. However, one trajectory only traces out a very small part of the total phase-space within these model fields. Here we calculate the trajectories of 5000 protons within the same model fields, and give the final positions, in terms of longitude and latitude from the origin (see Chapter 4 for more information), as well as the final energies. The full-orbit calculation is the same as that in Figure 4.16, except that we add the electric drift velocity here at $t = 0$. Figure 3.5 shows a comparison between the full-orbit calculation in (a) and guiding-centre switching calculations with $K_s = 10^{-5}$ in (b), $K_s = 10^{-4}$ in (c) and $K_s = 10^{-3}$ in (d). The final positions and energies for (a), (b) and (c) are in satisfactory agreement. However, there are some noticeable differences in the final plot for $K_s = 10^{-3}$. In particular there are more high energy protons at longitude $\phi \approx 180°$ and latitude $\beta \approx 45°$, and also at longitude $\phi \approx 0$ and latitude $\beta \approx 0$ that are not present for lower values of K_s. For $K_s = 10^{-2}$ (not shown) there are a significant number of particles that are in a different position than the full-orbit calculation at the same time. All of these simulations were run a total of $t = 5000t_0$, where t_0 is a gyro-time based

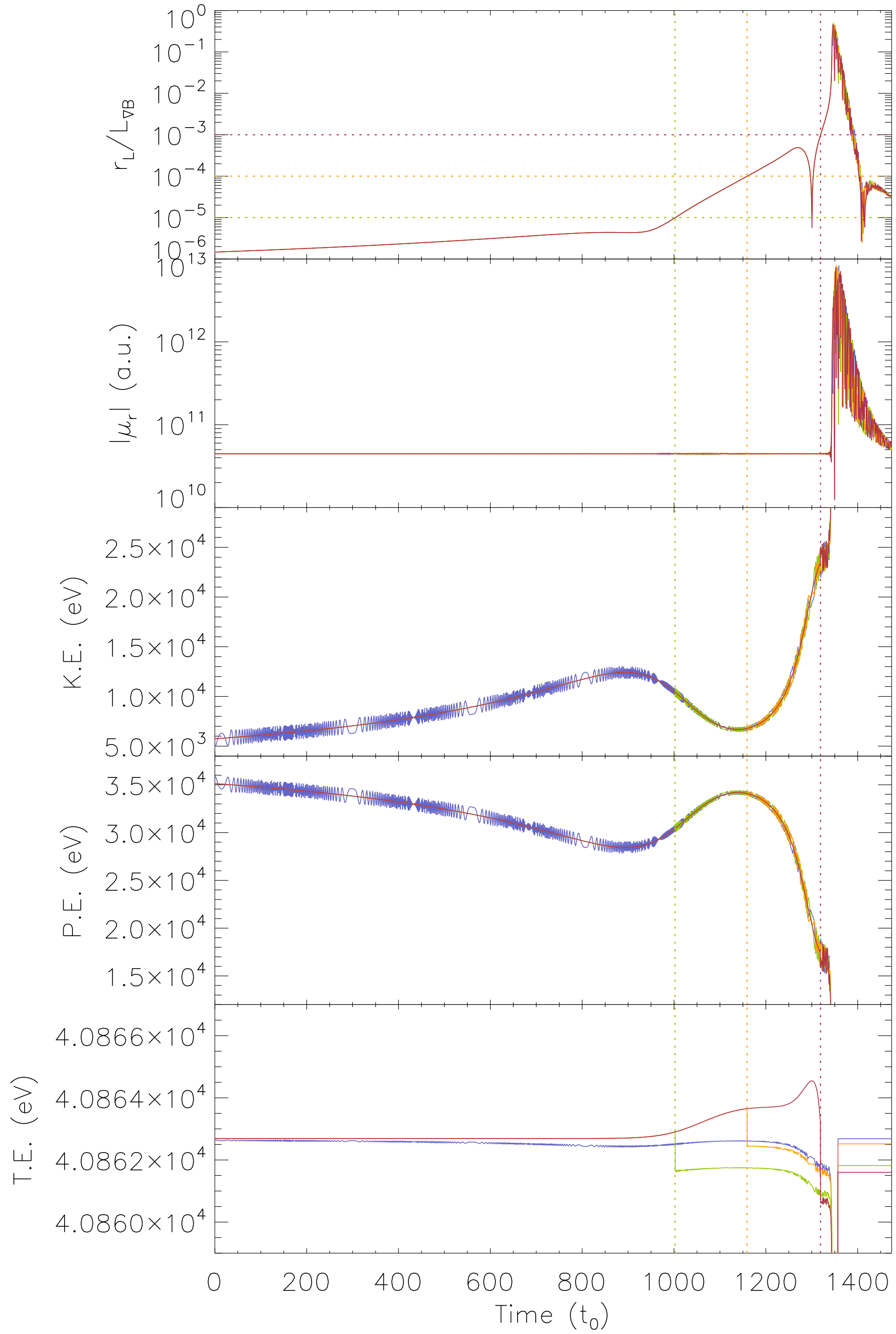

Figure 3.4: Parameter traces for proton trajectory '2' in Figure 4.17. Four simulations are shown in each panel; full-orbit (blue), and guiding-centre switching with $K_s = 10^{-5}$ (green), 10^{-4} (orange) and 10^{-3} (red). The panels show, in order, the adiabatic parameter, magnetic moment, kinetic energy, potential energy and total energy. Horizontal dashed lines give values of K_S, and vertical show the switch times.

upon characteristic field parameters, however there were large differences in the wall-clock time taken. In particular, there is an order of magnitude decrease in computational time for $K_s = 10^{-5}$ over full orbit, and another order of magnitude decrease at $K_s = 10^{-3}$.

In Figure 3.6 we perform a test of the guiding-centre switching code for an electron trajectory. This is done with the same model fields as the proton single-particle test in Figure 3.4, and with the same field parameter values, however a different initial position and velocity was chosen. This simulation was performed using a full-orbit calculation (blue), and guiding-centre calculations with $K_s = 10^{-6}$ (green), 10^{-5} (orange) and 10^{-4} (red). This trajectory was chosen because it shows the electron switching from guiding-centre to full orbit, and switching back again after passing through a region where it is partially unmagnetised. Note that the switch back (FO to GC) occurs at the vertical dotted lines at later times during the figure. This is when the value of $r_L/L_{\nabla B} < 0.9\,K_s$ (which is why the horizontal and vertical dotted lines do not intersect on the solid $r/L_{\nabla B}$ line at the switch back). For the guiding-centre calculations with $K_S = 10^{-6}$ and $K_s = 10^{-5}$ the total energy is sufficiently well conserved in the GC to FO switch, as well as the switch back. The total energy is also well conserved for $K_s = 10^{-4}$ in the first GC to FO switch, but shortly after there is a fast decrease in $r_L/L_{\nabla B}$ (that is also present in the fully full-orbit calculation). This causes a switch to GC at $r/L_{\nabla B} = 0.9 \times 10^{-4}$ in which total energy conservation is violated by approximately 12 eV. The calculation then quickly switches back to FO before finally switching to GC when $r_L/L_{\nabla B}$ is smoothly decaying. The violation of total energy occurs during a fast decrease in kinetic energy of around 10 keV, so this is an error of approximately 0.1%. This has no observable effect on the final particle postion and energy compared with the full-orbit calculation.

Finally, we perform a many-particle simulation test for the electrons, shown in Figure 3.7. Here, we only show the results for $K_s = 10^{-4}$, along-side the full-orbit calculation, but the spatial positions and energies look the same for $K_s = 10^{-5}$ and $K_s = 10^{-6}$. Due to the time needed to calculate the full-orbit trajectories (2.5 days) we only integrated 64 trajectories in this figure, instead of the 5000 used for the proton many-particle tests in Figure 3.5. However, every one of the electrons in the guiding-centre calculation has approximately the same energy and position as in the full-orbit calculation, and the speed-up is over a factor of 2500! In Chapter 4 we use the full-orbit code for all of the proton calculations

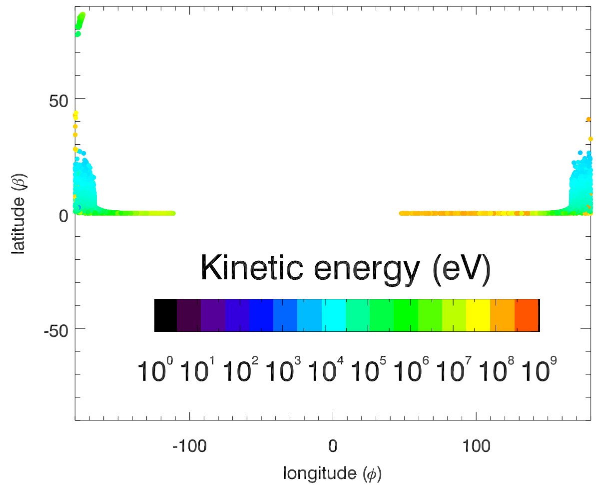

(a) Full-orbit. $T_{wc} = 8329.2$ sec.

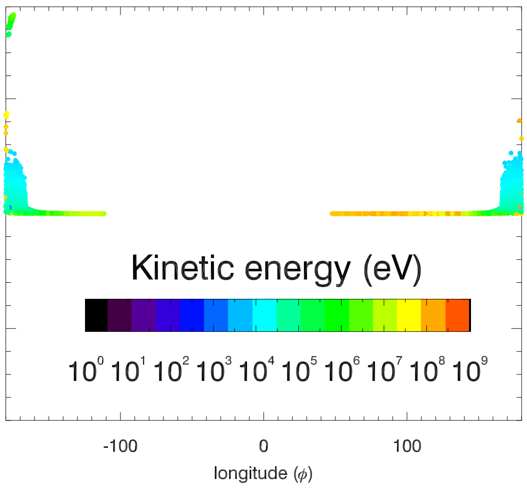

(b) Switch $K_s = 10^{-5}$. $T_{wc} = 710.7$ sec.

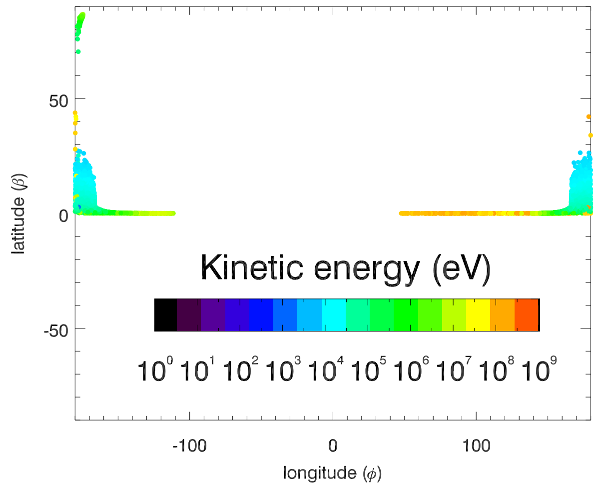

(c) Switch $K_s = 10^{-4}$. $T_{wc} = 489.9$ sec.

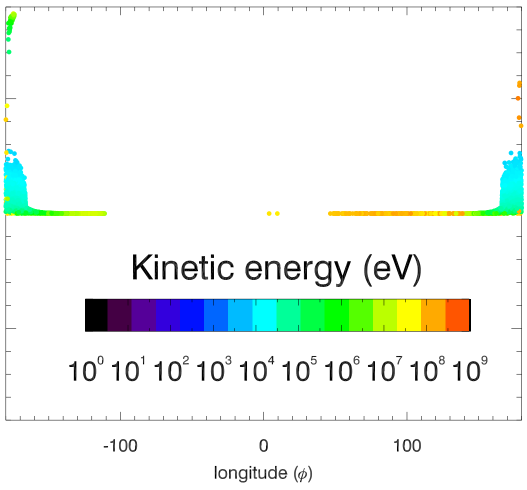

(d) Switch $K_s = 10^{-3}$. $T_{wc} = 89.9$ sec.

Figure 3.5: Latitude β and longitude ϕ of protons from the origin at $t = 4000$ in the fan reconnection model fields (same as Figure 4.16 but with given an initial electric drift velocity). Panel a) shows a full-orbit calculation, and the rest are guiding-centre switching calculations with b) $K_s = 10^{-5}$ c) $K_s = 10^{-4}$ and d) $K_s = 10^{-3}$. The colour of the proton gives the energy in eV, and the wall-clock times T_{wc} for each simulation are given.

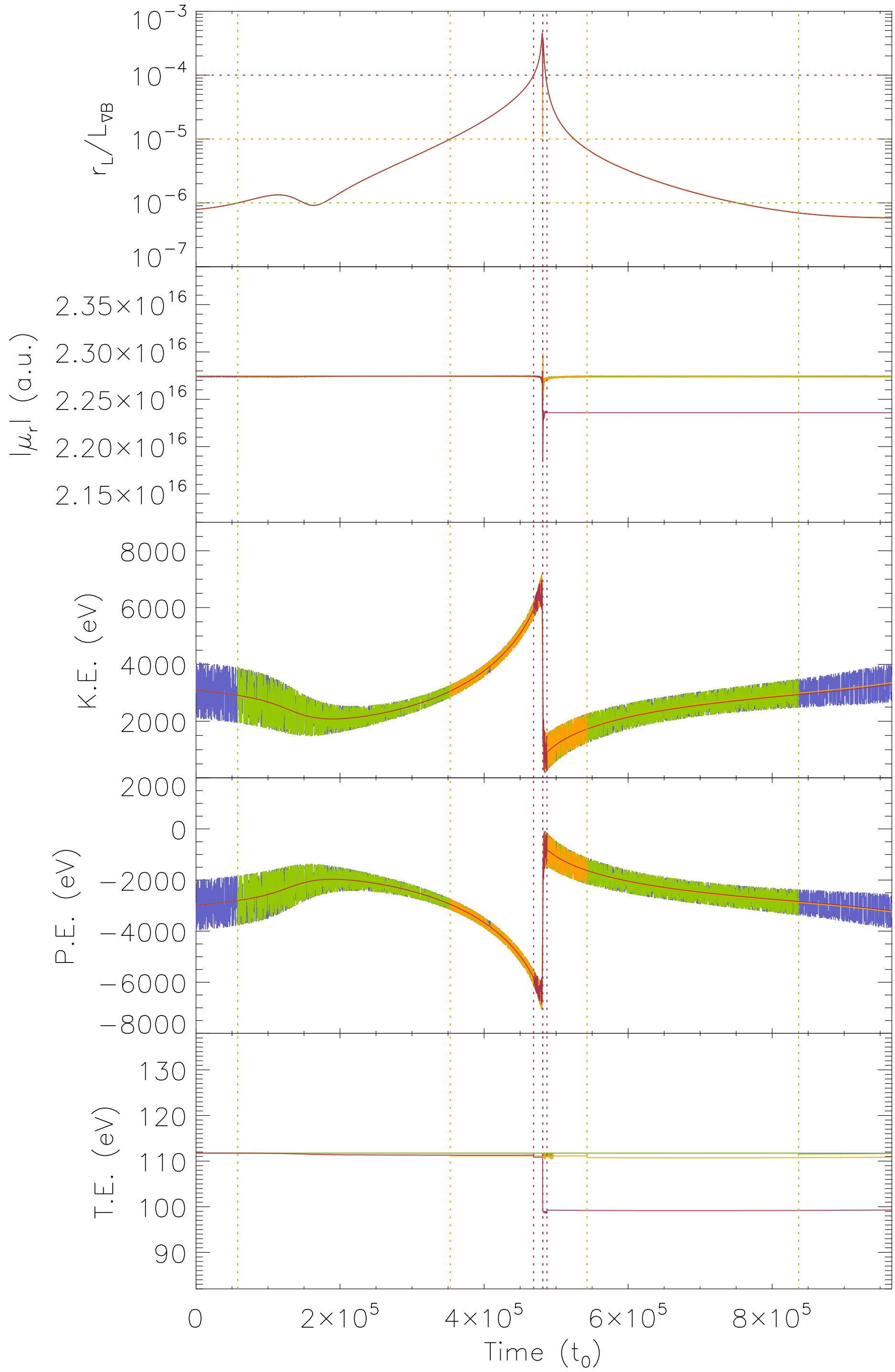

Figure 3.6: Parameter traces for an electron trajectory in the fan model fields. The four simulations shown in each panel are; full-orbit (blue), and guiding-centre switching with $K_s = 10^{-6}$ (green), 10^{-5} (orange) and 10^{-4} (red). The panels show, in order, the adiabatic parameter, the magnetic moment, kinetic energy, potential energy and total energy. The dashed horizontal lines give the switching constants, and the vertical lines the switch times.

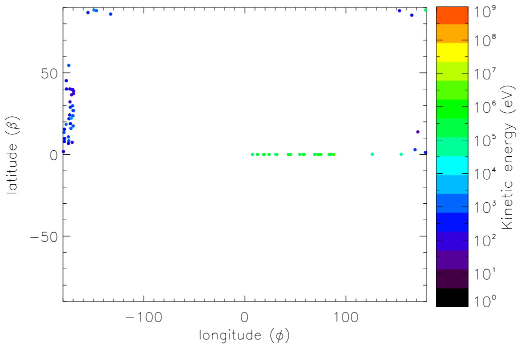

(a) Full-orbit. $T_{wc} = 213101$ sec.

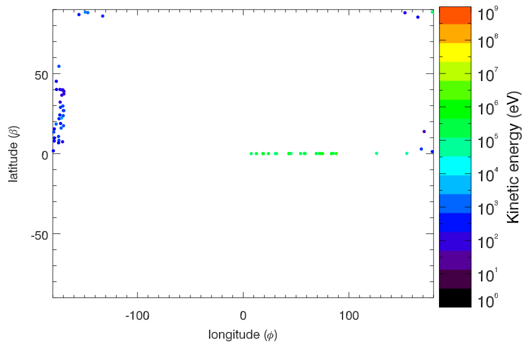

(b) Switch $K_s = 10^{-4}$. $T_{wc} = 78.9$ sec.

Figure 3.7: Latitude β and longitude ϕ of electrons from the origin at $t = 9.2 \times 10^6 t_0$ in the fan reconnection model fields. Panel a) shows a full-orbit calculation, and panel b) shows a guiding-centre switching calculations with $K_s = 10^{-4}$. The colour of the electron gives the energy in eV, and the wall-clock times T_{wc} for each simulation are given.

presented. However, at the end of this chapter, we will use the guiding-centre switching code to get results for electrons. For this we will use the switching constant $K_s = 10^{-4}$, as we are satisfied that this value can reproduce the kinetic energy and position of the full-orbit calculations with sufficient accuracy.

For the remainder of this chapter we will discuss the HiFi framework, that is used in the fluid simulations of merging-compression discussed in Chapter 5.

3.2 The HiFi code

3.2.1 Flux-source form

The HiFi code is a high-order finite (spectral) element framework for solving systems of Partial Differential Equations (PDEs). The first version of the code, known previously as SEL, was developed to solve two-dimensional problems by Glasser & Tang (2004). This 2D version was bench-marked for magnetic reconnection problems by V.S. Lukin, A. H. Glasser and E. Meier (Lukin 2007; Meier 2011), and the 3D version has been bench-marked by W. B. Lowrie (Lowrie 2011). Here we describe some of the main properties of the code, assuming a two-dimensional coordinate system (x, y) for simplicity. For a more thorough guide, including discussion of the three-dimensional code (which is not used in this thesis), see Lukin (2007); Lowrie (2011); Meier (2011).

The HiFi framework solves a system of M PDEs to give a solution vector U_i of M primary dependant variables $U_i = (U_1, ..., U_M)$. Both the number M and the equations themselves are user defined, but the equations must be in the following flux-source form (e.g. Lukin 2007)

$$\partial_t Q_k + \boldsymbol{\nabla} \cdot \boldsymbol{F}_k = S_k, \tag{3.24}$$

where the expression within the time derivative can either be $Q_k = \delta_{ki} U_i$, where δ_{ki} is the Kronecker delta, or more generally

$$Q_k = (A_{ki}(x, y) + B_{ki}(x, y)\partial_x + C_{ki}(x, y)\partial_y)U_i, \tag{3.25}$$

some linear combination of U_i and its spatial derivatives (A_{ki}, B_{ki} and C_{ki} are matrices). The flux is given by

$$\boldsymbol{F}_k = [F_{kx}(t, x, y, U_i, \partial_x U_i, \partial_y U_i), F_{ky}(t, x, y, U_i, \partial_x U_i, \partial_y U_i)], \tag{3.26}$$

and the source-term by

$$S_k = S_k(t, x, y, U_i, \partial_x U_i, \partial_y U_i). \tag{3.27}$$

In addition, equations can be set as *static*, so that the time-derivative term for that equation is equal to zero. An example of a simple static equation that can be written in flux-source form is

$$-\nabla^2 U = f(x, y), \tag{3.28}$$

by setting $F_x = \partial_x U$, $F_y = \partial_y U$, and $S = -f$ for a given source function $f(x, y)$. This can be solved in HiFi provided the boundary conditions are chosen carefully. In fact, we solve this equation in HiFi to set-up initial conditions for the simulations in Chapter 5.

HiFi solves equations (3.24) on a structured grid in *logical space* $\xi, \zeta \in [0, 1]$, in which the grid spacing is uniform. This is mapped to real space through the user-specified functions $x = x(\xi, \zeta)$, $y = y(\xi, \zeta)$. With these HiFi has the capability of, for example, curved boundaries. In this thesis we use straight boundaries, but these functions are used to give high resolution in regions of interest: see equations (5.6-5.7) in Chapter 5. HiFi also has the capability for grid adaption, through a variational method called harmonic grid generation (Glasser & Tang 2004; Lukin 2007). However, we do not make use of this feature in this thesis.

3.2.2 Spatial discretisation

HiFi uses a *spectral/hp element* spatial discretisation, which is a high-order method that is a combination of the spectral and the finite element methods. The domain is divided up into a grid of $N_x \times N_y$ finite elements, that are C^0-continuous at the element boundaries, and within these elements the solution is discretised onto a set of polynomial basis functions. The name "hp" means that there are two possible ways of increasing accuracy; the h corresponds to the cell size, and p gives the order of polynomial expansion. A clear description of the spectral/hp element method applied to problems in computational fluid dynamics can be found in Karniadakis & Sherwin (1999). In HiFi, the polynomial basis functions are Λ_i for $i = 0, .., N_p$, given by

$$\Lambda_i = \begin{cases} (1-\bar{x})/2 & i = 0, \\ (1-\bar{x})(1+\bar{x})\ P_i^{1,1} & i = 1, ..., N_p - 1, \\ (1+\bar{x})/2 & i = N_p. \end{cases} \tag{3.29}$$

Here, $\bar{x} = \pm 1$ gives the boundary between finite elements, where the $i = 0$ basis function is continuous with the $i = N_p$ basis function (the C^0-continuity). The other basis functions are defined in terms of Jacobi polynomials $P_i^{\alpha,\beta}$ (see e.g. Chapter 22 of Abramowitz & Stegun (1972) for a description of their properties), and are zero at ± 1 as shown in Figure 3.8.

3.2.3 Weak form and the Galerkin approximation

The equations (3.24) are written in *weak form* before they are converted to an algebraic system using the *Galerkin approximation*, as is standard procedure for finite element methods (e.g. Johnson & Riess 1982). Here we describe the weak form of the Poisson equation (3.28) with Dirichlet boundary conditions as an example; see Karniadakis & Sherwin (1999) for a rigorous approach in one-dimension, including extension to other boundary conditions. The weak form is found by taking the inner product of equation (3.28) with a *test-function* $V(x, y)$

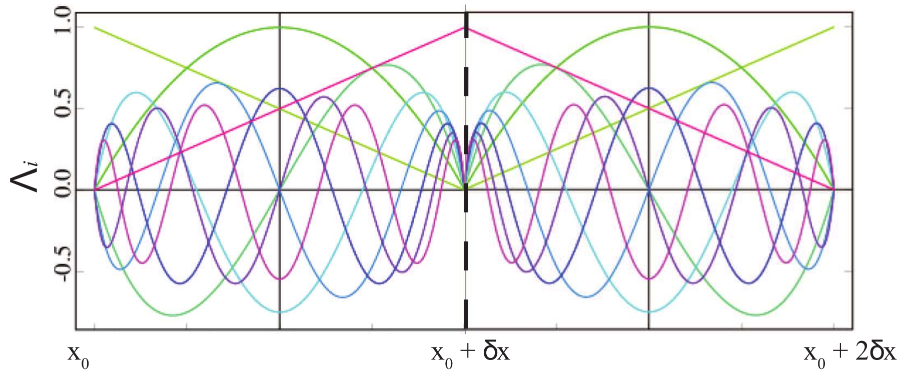

Figure 3.8: The basis functions for the HiFi code across two grid cells of width δx. The Λ_0 and Λ_8 basis functions are linear and equal at the boundaries x_0, $x_0 + \delta x$,$x + 2\delta x$, where the other elements are zero. The expressions are given in equation (3.29), where the domain $[x_0, x_0 + 2\delta x]$ has been scaled to $[-1, 1]$. The colours show the connections between elements of different order at the $x_0 + \delta x$ boundary. Image from Lukin (2007).

over a domain Ω with boundary Γ. Here we assume all boundary conditions are Dirichlet boundary conditions; $\Gamma = \Gamma_D$, and $U = U_D$ on Γ_D. Also, a standard condition on the test-functions is that they are identically zero on Dirichlet boundaries. The inner product is

$$-\int_\Omega V\nabla^2 U d\Omega = \int_\Omega V f d\Omega, \tag{3.30}$$

which can be written using Green's identity as

$$\int_\Omega \boldsymbol{\nabla} V \cdot \boldsymbol{\nabla} U d\Omega - \int_\Gamma V \hat{\boldsymbol{n}} \cdot \boldsymbol{\nabla} U d\Gamma = \int_\Omega V f d\Omega, \tag{3.31}$$

where $\hat{\boldsymbol{n}}$ is a unit normal to the boundary Γ, $\hat{\boldsymbol{n}} \cdot \boldsymbol{\nabla} U \equiv \partial_n U$. As $V = 0$ on Γ_D, this simplifies to

$$\int_\Omega \boldsymbol{\nabla} V \cdot \boldsymbol{\nabla} U d\Omega = \int_\Omega V f d\Omega, \tag{3.32}$$

which is called the weak form of equation (3.28) with Dirichlet boundary conditions. If more complicated boundary conditions are given, such as Neumann $\partial_n U = g_N$ on Γ_N, or a mixed boundary condition, then the second term in equation (3.31) is not necessarily zero. HiFi can use Dirichlet, Neumann or mixed (also known as Robin) boundary conditions.

The Galerkin approximation is the discretisation of U and V in equation (3.32) by a finite number of basis functions. The same set of functions are used for both U and V; although for U, extra functions are needed to satisfy the Dirichlet boundary conditions (as $V = 0$ on Γ_D). In HiFi, an element of the solution vector U_i is approximated as

$$U_i(t, x(\xi, \zeta), y(\xi, \zeta)) = \sum_{j,k=0}^{N_p} u_{i\,jk}(t)\Lambda_j(\xi)\Lambda_k(\zeta). \tag{3.33}$$

where $u_{i\,jk}(t)$ are the basis function amplitudes for U_i, and Λ are the basis functions in equation (3.29).

Applying these methods to the general flux-source form (3.24) in HiFi, and using the spectral-element basis, gives a set of algebraic equations

$$\mathbb{M}\dot{\boldsymbol{u}} = \boldsymbol{r}(t, \boldsymbol{u}), \tag{3.34}$$

where $\boldsymbol{u}$ and $\dot{\boldsymbol{u}}$ are the vector of amplitudes and its time derivative, respectively. The matrix $\mathbb{M}$ specifies the coupling of primary variables on the left-hand side of the equation (it is the time-derivative term in equation (3.24) in weak form, after expansion in the basis functions, and also includes a Jacobian of the transformation between (x, y) and (ξ, ζ); see Lukin (2007) for the full expression), and $\boldsymbol{r}$ is the right-hand-side involving the flux-terms, sources and boundary terms. The integrals within the weak-form expressions are calculated using *Gaussian quadrature* (e.g. Johnson & Riess 1982), where the number of quadrature points must be at least equal to the number of basis functions to ensure accuracy.

3.2.4 Time-stepping

Two methods are currently available within HiFi for time-advance of equation (3.34): the θ-method, and a second-order backward-differencing method (called BDF2). Here we mention only the θ-method that we use for the simulations in Chapter 5; see Lukin (2007) for a description of BDF2. The θ-method involves the time-discretisation of (3.34) as

$$\mathbb{M}\left(\frac{\boldsymbol{u}^{n+1} - \boldsymbol{u}^n}{\Delta t}\right) = \theta\boldsymbol{r}(t^{n+1}, \boldsymbol{u}^{n+1}) + (1-\theta)\boldsymbol{r}(t^n, \boldsymbol{u}^n), \tag{3.35}$$

where θ is a user-chosen constant $0 \leq \theta \leq 1$. For $\theta = 0$ this reduces to an *explicit* time-stepping method, known as the *Forward Euler method*, where the solution at the new timestep $\boldsymbol{u}^{n+1}$ is calculated from the solution and right-hand-side at the previous timestep, $\boldsymbol{u}^n$ and $\boldsymbol{r}(t^n, \boldsymbol{u}^n)$ respectively. The advantages of this explicit method are that the right-hand side is already known, and only the previous timestep needs to be stored in memory to calculate the new timestep. However, there is a strict constraint on the timestep Δt that can be used in an explicit method, called the Courant-Friedrichs-Lewy (CFL) condition. In 1D this condition can be written as

$$C = v_{max}\frac{\Delta t}{\Delta x} < 1. \tag{3.36}$$

The timestep Δt must be chosen using the fastest possible speed within the problem v_{max}, usually the fastest wave speed, and grid-spacing Δx, so as to give $C < 1$. The Δt from this expression may be prohibitively small compared to the timescale of interest for the problem, especially in regions that need to be finely resolved. It is important to note that there are also stability constraints on the timestep due to diffusion terms, but we will not discuss these in this thesis.

For $\theta = 1$, equation (3.35) is an *implicit* method, known as the *Backward Euler method*. This method allows much larger time-steps than the CFL limited timestep of the explicit method while remaining numerically stable. Both the forward and backward Euler methods are $\mathcal{O}(\Delta t)$ accurate in time.

In the case of $\theta = 0.5$, equation (3.35) is known as the Crank-Nicolson time-stepping method. This method has the advantage of being able to take larger time-steps than the CFL condition (however, it is not as stable as the backwards Euler method), while being non-dissipative. It also is $\mathcal{O}((\Delta t)^2)$ accurate in time.

If $\theta > 0$, an iterative procedure must be used to calculate the solution for the new timestep. HiFi does this through a *Newton* iterative procedure that attempts to converge the solution to a given tolerance at the new timestep. The initial guess for the $(n+1)$th timestep, $\boldsymbol{u}_0^{n+1}$, is just the converged solution at the previous timestep $\boldsymbol{u}_0^{n+1} = \boldsymbol{u}^n$. The $(i+1)$th Newton iteration, $i = 0, .., N_{it} - 1$, for that timestep is calculated as

$$\boldsymbol{u}_{i+1}^{n+1} = \boldsymbol{u}_i^{n+1} - \mathbb{J}^{-1}\boldsymbol{R}_i, \tag{3.37}$$

where $\boldsymbol{R}_i$ is called the *residual*, given by

$$\boldsymbol{R}_i \equiv \mathbb{M}(\boldsymbol{u}_{i+1}^{n+1} - \boldsymbol{u}_i^{n+1}) - \Delta t \left[\theta \boldsymbol{r}(t^{n+1}, \boldsymbol{u}_i^{n+1}) + (1-\theta)\boldsymbol{r}(t^n, \boldsymbol{u}^n)\right], \tag{3.38}$$

and $\mathbb{J}$ is the Jacobian of the iteration

$$\mathbb{J} \equiv \mathbb{M} - \Delta t \theta \left\{ \frac{\partial r_i}{\partial u_j} \right\}_{t=t^{n+1}, \boldsymbol{u}=\boldsymbol{u}^n}. \tag{3.39}$$

If the code does not converge to the new timestep in a given number of Newton iterations then the step-size is adaptively reduced.

3.2.5 PETSc

Routines from the Portable, Extensible Toolkit for Scientific Computation Library (Balay et al. 2013) are used to perform the Newton iterations (3.37) discussed above. These Newton iterations are the most intensive routines within the HiFi code, with respect to memory and processor usage. However, the rate of convergence to $\boldsymbol{u}_{i+1}^{n+1}$ can be greatly speeded up through the use of *Krylov subspace methods* along with applying *preconditioners* to the matrix system. A description of these methods is outside the scope of this thesis, but can be found in Freund et al. (1992). The PETSc library has many preconditioning methods that can be chosen at run-time, which are available for use with the HiFi code. For reference, we use the widely used *Generalized Minimal Residual Method* (GMRES) with an *additive Schwarz method* preconditioner.

3.2.6 Hall-MHD formulation

The results presented in Chapter 5 are numerical solutions to the set of Hall-MHD equations, that is equations (1.25-1.30) but including some form of the viscous stress tensors. There is an existing Hall-MHD module within the 2D version of the HiFi code, the current version of which is given in flux-source form in equations (A.34-A.41) in Appendix A.3. It evolves eight primary dependent variables

$$\boldsymbol{U} = (n, -A_z, B_z, nv_x, nv_y, nv_z, j_z, p),$$

where n is the normalised density, A_z is the out-of-plane (z is the invariant direction) magnetic potential, B_z is the out-of-plane magnetic field, v_x and v_y are the in plane components of the ion velocity and v_z is the out-of-plane component, j_z is the out-of-plane current density and p is the total thermal pressure.

Two modifications were made to this set of equations before using them in Chapter 5. These were to add a higher order dissipation term in to Ohm's law (along with an associated heating term in the energy equation), and to modify the formulation to evolve electron and ion temperatures separately. The latter formulation is only used for the two-temperature results at the end of Chapter 5. These changes are given in Appendix A.4 in flux-source form. Here we describe the motivation for the extra dissipation term.

3.2.7 Dispersive waves and hyper-resistivity

The introduction of the Hall term within Ohm's law introduces dispersive waves, such as the *Whistler wave*, into the system. To derive the dispersion relation for the Whistler wave we consider the Hall-MHD equations (1.25-1.27) and (1.30). To simplify things, we assume incompressibility, $n = 1$ in normalised units, so equation (1.25) can be neglected. Further, by taking the curl of the momentum equation (1.26) and Ohms law (1.27), the pressure terms disappear. Finally, we consider the length-scales in the limit $d_e \ll L \ll d_i$, so that the Hall term dominates the convective electric field in Ohm's law (see Biskamp (2000) for a treatment where this latter condition is relaxed, to include electron inertia and incompressible MHD waves). The dimensionless governing equation is

$$\partial_t \boldsymbol{B} = -d_i \boldsymbol{\nabla} \times (\boldsymbol{j} \times \boldsymbol{B}) - \boldsymbol{\nabla} \times (\eta \boldsymbol{j}). \tag{3.40}$$

Re-writing the Hall term using a vector identity, also using $\boldsymbol{\nabla} \cdot \boldsymbol{B} = \boldsymbol{\nabla} \cdot \boldsymbol{j} = 0$, and assuming uniform resistivity gives

$$\partial_t \boldsymbol{B} = -d_i(\boldsymbol{B} \cdot \boldsymbol{\nabla} \boldsymbol{j} - \boldsymbol{j} \cdot \boldsymbol{\nabla} \boldsymbol{B}) + \eta \nabla^2 \boldsymbol{B}. \tag{3.41}$$

This is then linearised, assuming a uniform background field $\boldsymbol{B}_0 = B\hat{\boldsymbol{b}}$ (so that $\boldsymbol{j}_0 = \boldsymbol{0}$), and assuming perturbations of the form $\boldsymbol{\delta B} = \boldsymbol{B}_1 \exp\left[i(\boldsymbol{k} \cdot \boldsymbol{x} - \omega t)\right]$ (where $\boldsymbol{\delta B} \ll \boldsymbol{B}_0$) to give

$$\omega \boldsymbol{B}_1 = i d_i B k_\parallel \boldsymbol{k} \times \boldsymbol{B}_1 - i \eta k^2 \boldsymbol{B}_1, \tag{3.42}$$

where $k_\parallel = \hat{\boldsymbol{b}} \cdot \boldsymbol{k}$. Taking the cross-product of equation (3.42) with $\boldsymbol{k}$, then using $\boldsymbol{k} \cdot \boldsymbol{B}_1 = 0$ and substituting the resulting expression for $\boldsymbol{k} \times \boldsymbol{B}_1$ back into equation (3.42) gives the following dispersion relation

$$\omega = -ik^2\eta \pm d_i v_A k_\parallel k, \tag{3.43}$$

where $v_A = B$ in dimensionless units. This is the dispersion relation for the Whistler wave damped by resistivity.

Two numerical issues arise when including Whistler-waves, caused by the above form of the dispersion relation. Firstly, the phase speed of the Whistler wave is $v_{wp} = \omega/k = d_i v_A k_\parallel$, so for $d_i k_\parallel \gg 1$ this can be much larger than the Alvén speed (the short wavelength perturbations travel faster). Whistler waves are named as such due to this dispersive property; they can be excited in the ionosphere by lightning, and have a characteristic rising to falling tone due to the frequency dependent arrival time. The maximum possible Whistler wave speed, with the highest wave-number k_{max}, in a numerical simulation is limited by the grid resolution $k_{max} \approx 1/(\Delta x)$ (unless the waves are dissipated at a larger scale by specific dissipation terms, see below). The timestep needed to satisfy the CFL condition (3.36) scales as $\Delta t \sim (\Delta x)^2$, which can be extremely prohibitive in, for example, simulations of magnetic reconnection where small-scale structures need to be resolved over many Alfvén times. For this reason we were motivated to use the HiFi code, which allows Crank-Nicolson time advance ($\theta = 0.5$). All of the simulations in Chapter 5 were performed with this implicit method.

The second issue with the dispersion relation (3.43) is related to numerical instability. Comparing the resistive and Whistler parts of the expression, it can be seen that resistivity cannot set a dissipation scale. As both expressions scale as k^2, there is no $k = k_{\max}$ above which (or no minimum wavelength below which) Whistler waves are strongly dissipated. Hence, there can be waves present in the simulation that have wavelength comparable to the grid-scale, which may cause numerical instability. Figure 3.9 shows an example of such an instability for a Hall-MHD simulation (with just the convective electric field, the Hall term and resistivity within Ohm's law). There is a characteristic aliasing of the plasma density at the grid-scale, which is also visible when plotting other variables. We performed this simulation in the Lagrangian remap code Lare2D (Arber et al. 2001), but very similar results were also present in the HiFi code with the same equations.

To deal with this numerical instability we use the following version of Ohm's

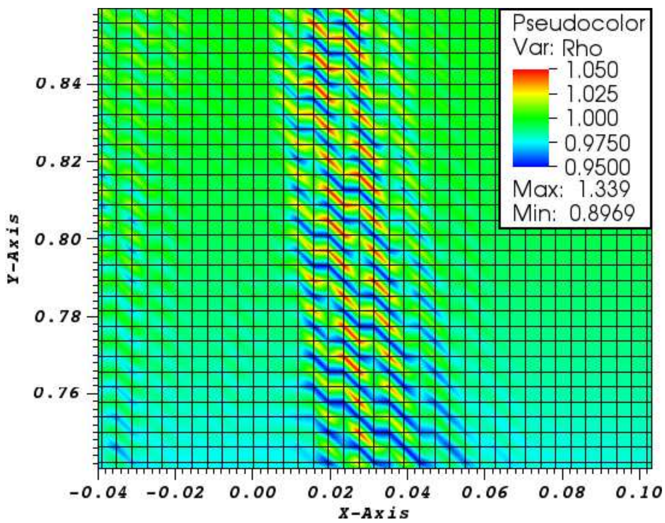

Figure 3.9: An example of a numerical instability using the Hall term in Ohm's law. The black lines show the numerical grid, and the colour scale shows the plasma density.

law

$$\boldsymbol{E} = -\boldsymbol{v}_e \times \boldsymbol{B} - \frac{d_i}{n}\boldsymbol{\nabla} p_e + \eta \boldsymbol{j} - \eta_H \nabla^2 \boldsymbol{j}, \tag{3.44}$$

where the final term is a higher-order dissipative term, known as hyper-resistivity. The modified dispersion relation, again assuming incompressibility and $d_e \ll L \ll d_i$, or equivalently $kd_e \ll 1 \ll kd_i$, is

$$\omega = -ik^2\eta - ik^4\eta_H \pm d_i v_A k_\parallel k. \tag{3.45}$$

Balancing the final two terms on the right-hand-side gives a dissipation scale λ of

$$\lambda \approx 2\pi \left(\frac{\eta_H}{d_i v_A}\right)^{1/2}. \tag{3.46}$$

The hyper-resistive diffusion term has been commonly used in Hall-MHD simulations of magnetic reconnection (see Ma & Bhattacharjee 2001, and references therein). As it is a dissipative term, it requires the associated heating term $\eta_H \boldsymbol{\nabla} \boldsymbol{j} : \boldsymbol{\nabla} \boldsymbol{j}$, in the internal energy equation (1.30) so that total energy conservation is satisfied. In Appendix A.4 we show how the HiFi code is modified to include this term, and in Appendix A.5 we show that this term balances the dissipative part of the hyper-resistive term within Ohm's law to give total energy conservation.

3.3 Cross-code verification study

The 2D version of the HiFi code has been extensively bench-marked for magnetic reconnection problems in Lukin (2007). In particular, the linear growth rate of the resistive tearing mode (see Section 1.3.4) has been reproduced to within 1% of the analytical value, and the Hall-MHD HiFi module has been bench-marked against the NIMROD (Sovinec et al. 2004) and M3D-C[1] (e.g. Jardin et al. 2008) computational codes for the Hall-MHD version of the GEM challenge problem (Birn et al. 2001). Good agreement was found for the evolution of the total kinetic energy between the three codes.

All the simulation results presented in Chapter 5 are performed with the HiFi code, but initial test-runs for this project used the Lare2D code (Arber et al. 2001). The code is a *Lagrangian-remap* code, meaning that for each timestep the equations are solved in Lagrangian form (where mesh moves with the fluid), before remapping the solution onto the original grid at the end of the timestep. The Lagrangian step uses a second-order accurate (in time and space) predictor corrector scheme (see e.g. Johnson & Riess 1982). An advantage of solving the equations in Lagrangian form is that it is simple to add new terms into the equations. The existing formulation of Lare2D does have an option to use the Hall-term, but it does not contain a hyper-resistive diffusion term (in the course of this work we added this term into the Lagrangian step, to suppress numerical instabilities). In addition, the time-stepping in Lare2D is explicit and it was found that simulations including the Hall-term could take weeks to run on 16-32 processors, due to the prohibitively small timestep set by the CFL condition (3.36). A final reason for choosing the HiFi code, in preference to Lare2D for simulations of merging-compression, was that HiFi can be easily set up for different geometries, such as the tight-aspect ratio toroidal geometry in MAST. In Lare2D this would require major modifications to all aspects of the Lagrangian and remap steps.

In order to switch from Lare2D to HiFi it was natural to do some code-comparisons. Here we show a comparison of HiFi and Lare2D for the Hall-MHD GEM challenge problem, where we have modified both codes to include the extra hyper-resistive current diffusion term. We do not describe the GEM challenge problem set-up here in detail as it is well documented in the original papers (Birn et al. 2001), as well as many other sources. However, for reference, we use equations (5.1-5.5) with normalised resistivity $\eta = 10^{-3}$, hyper-resistivity $\eta_H = 10^{-5}$ and viscosity $\mu = 10^{-5}$. No heat conduction was used, and the electron pressure term within Ohm's law and hyper-resistive heating terms were set to zero. Although the latter means that energy conservation is violated, this does not matter for the purposes of code comparison (it should be violated identically for both codes). The initial conditions are a long current sheet of width equal to the ion-skin depth $\delta = d_i$, which is then given a significant perturbation to trigger the non-linear phase of a tearing instability.

Figure 3.10 shows the out-of-plane current density, called "*U07*" in HiFi and "*current/jz*" in Lare2D at three different snapshots during the reconnection. In each panel the top half ($y > 0$) shows a snapshot of half the domain from the HiFi simulation, and in the lower half ($y < 0$) from the Lare2D simulation. The snapshots are output at slightly different times between each simulation for the top and middle panels (there is about $0.3\,\tau_0$ difference in the top, and $0.2\,\tau_0$ in the middle panel, where $\tau_0 = d_i/v_A$ is the Alfvén travel time across the ion-skin depth or, equivalently, the inverse ion-cyclotron frequency). However, it is clear that the evolution is very similar over time for both simulations. In the final panel, the output snapshots are closer together (only $0.07\,\tau_0$ difference) and the current density is almost identical for the two codes suggesting that the minor differences between simulations in the top and middle panels is just due to different snapshot time. The final panel shows an open x-point fast-reconnection regime, as discussed in Chapter 1, for both simulations. As this is well into the non-linear phase of reconnection, it is remarkable that two codes with completely different algorithms are so similar.

With the extensive testing of HiFi for reconnection problems in Lukin (2007), and with this test of the additional dissipation terms added, we are satisfied that it has the capability to model the MAST merging-compression experiment (see Chapter 2). The problem set-up and results of this study are given in Chapter 5. However, before they are discussed, we will describe the results of test-particle trajectories within 3D magnetic null-point reconnection geometries using both the full-orbit and guiding-centre codes introduced earlier in this chapter.

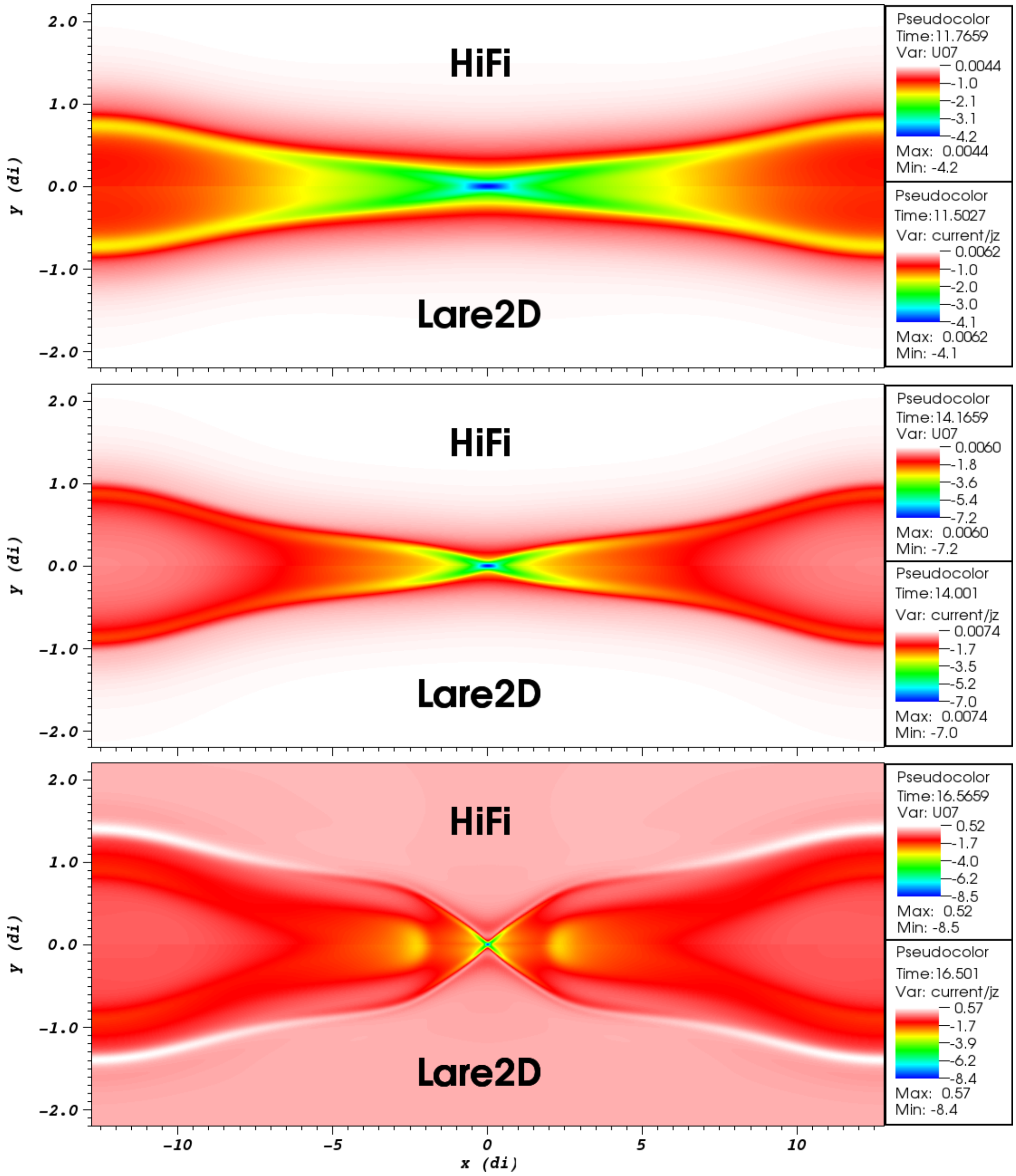

Figure 3.10: Successive snapshots of the GEM challenge problem for the HiFi code (Glasser & Tang 2004; Lukin 2007) ($y > 0$ in each panel), and Lare2D (Arber et al. 2001) ($y < 0$ in each panel). Each code uses the Hall-MHD equations and has been modified to include the hyper-resistive current diffusion term. The top (bottom) legend for each panel is for the HiFi (Lare2D) simulation respectively. Note that there is a small time difference in each snapshot between the two codes.

Chapter 4

Particle Acceleration at 3D magnetic null points

In this chapter we present results from test-particle simulations within 3D null-point model-fields, with particular application to particle acceleration within solar flares. See Chapter 2 for a discussion on the existence of null points in magnetic reconstructions of flaring active regions. Firstly, we introduce the model-fields of Craig & Fabling (1996) and Craig et al. (1997) and then, for the majority of the chapter, examine proton trajectories and energy spectra within these fields. At the end of the chapter we will give results for electrons using both the full-orbit and guiding-centre-switching codes, within the same model fields. This chapter is partially adapted from Stanier et al. (2012), which includes results for protons only.

4.1 Solutions of Craig and Fabling

Craig & Fabling (1996) and Craig et al. (1997) find analytic solutions for reconnecting current sheets in 3D null point geometries (See Section 1.3.6 for an introduction to 3D reconnection models), that are exact solutions to the steady and incompressible resistive MHD equations; equations (1.32-1.34) with $d_i = 0$, and without the time derivative terms. In this chapter, these solutions are developed further, and the model fields are used to study test-particle acceleration. The main advantage of the Craig & Fabling (1996) and Craig et al. (1997) models over the ideal models of Priest & Titov (1996), is that they contain the dissipation region and thus avoid the singularities present in the ideal models (see Section 1.3.6). In this work we will extend the previous test-particle studies of Dalla & Browning (2005, 2006, 2008) and Browning et al. (2010) who used the ideal model fields, see Section 1.4, to include the effects of the dissipation regions on test-particle motion. We will also extend the work of Litvinenko (2006) who used an approximate analytical technique to study the stability of particle orbits very close to the null point in the resistive fan current sheet (see Section 4.3.3).

For completeness, the main properties of the solutions of Craig & Fabling (1996) and Craig et al. (1997) are described here (more detail can be found within these papers). These models are then developed further, by calculating the electric fields and potentials that are needed within the test-particle code. It will be shown that the spine-model of Craig et al. (1997) can be matched to the earlier ideal model of Priest & Titov (1996) within the external ideal region, where the latter model was used in the test-particle study of Dalla & Browning (2005). Finally, we will calculate how important field quantities, such as the electric drift velocity, scale with the free parameters in these models.

The governing equations solved by Craig & Fabling (1996) and Craig et al. (1997) consist of the time-independent, incompressible resistive-MHD momentum equation, which in curled form is

$$\boldsymbol{\nabla} \times (\boldsymbol{\omega} \times \boldsymbol{v} - \boldsymbol{j} \times \boldsymbol{B}) = 0 \tag{4.1}$$

and the induction equation,

$$\boldsymbol{\nabla} \times (\boldsymbol{v} \times \boldsymbol{B} - \eta \boldsymbol{j}) = 0 \tag{4.2}$$

with the solenoidal and incompressibility conditions,

$$\boldsymbol{\nabla} \cdot \boldsymbol{B} = 0, \quad \boldsymbol{\nabla} \cdot \boldsymbol{v} = 0. \tag{4.3}$$

Here $\boldsymbol{j}$ is the current density and $\boldsymbol{\omega}$ is the vorticity in terms of the bulk plasma velocity $\boldsymbol{v}$. In this normalised form, they are

$$\boldsymbol{j} = \boldsymbol{\nabla} \times \boldsymbol{B}, \quad \boldsymbol{\omega} = \boldsymbol{\nabla} \times \boldsymbol{v}. \tag{4.4}$$

The three-dimensional analytic solutions of Craig et al. (1995), Craig & Fabling (1996) and Craig et al. (1997) suppose magnetic and flow fields of the form

$$\boldsymbol{B} = \lambda \boldsymbol{P} + \boldsymbol{Q}, \tag{4.5}$$

$$\boldsymbol{v} = \boldsymbol{P} + \lambda \boldsymbol{Q}, \tag{4.6}$$

where the scalar $0 \leq \lambda < 1$ gives a shear between the $\boldsymbol{B}$ and $\boldsymbol{v}$ fields. The vector field $\boldsymbol{P}(x, y, z)$ is a potential background field, and $\boldsymbol{Q}$ is an additional non-potential field, here called the *displacement field*, which gives rise to plasma current in the models, $\boldsymbol{j} = \boldsymbol{\nabla} \times \boldsymbol{Q}$.

To make it easier to compare with the previous results from particle acceleration studies within 3D null points (Dalla & Browning 2005), we choose, without loss of generality, that the z-axis be aligned with the spine and take $z = 0$ as the fan plane. It must be noted that this choice of axis differs from that used by Craig et al. (1997). We have also used a normalisation scheme that makes it easier to compare with Dalla & Browning (2005). Magnetic fields are normalised by $B_0 = 0.01$ T, and velocities by $v_0 = v_{A0} = 6.5 \times 10^6\,\mathrm{ms}^{-1}$ (the Alfvén speed using B_0 and a typical solar coronal density of $n_0 = 1.126 \times 10^{15}\,\mathrm{m}^{-3}$). Length-scales are normalised by $L_0 = 10^4$ m. This is somewhat smaller than the length of a typical active region. It can considered as a local region around the null at which the fields given below are good approximations (and a reconnection site is much smaller than an active region). Also, limiting the simulation box to several L_0 allows reasonable integration times for particles crossing the domain, and makes the simulation domain comparable to that used in Dalla & Browning (2005)-Browning et al. (2010). Dimensionless times quoted in the proton simulations below are in terms of the proton gyro-period $T_\omega = 2\pi m_p/(|e|B_0)$.

The background field we use, $\boldsymbol{P}$, is the *proper radial null*, see Figure 1.8 (a) and equation (1.53) with $q = j_\parallel = j_\perp = 0$. Note that we use both Cartesian (x, y, z) and the usual cylindrical co-ordinates (r, ϕ, z) in this chapter, where z is aligned with the spine, $r = \sqrt{x^2 + y^2}$ is the radial distance from the spine, and $\phi = \tan^{-1}(y/x)$. This background field is then written as

$$\boldsymbol{P} = \frac{\alpha}{2}(x\hat{\boldsymbol{x}} + y\hat{\boldsymbol{y}} - 2z\hat{\boldsymbol{z}}) = \frac{\alpha}{2}(r\hat{\boldsymbol{r}} - 2z\hat{\boldsymbol{z}}), \tag{4.7}$$

with α giving the sign and strength of the field. For the *spine-reconnection* model,

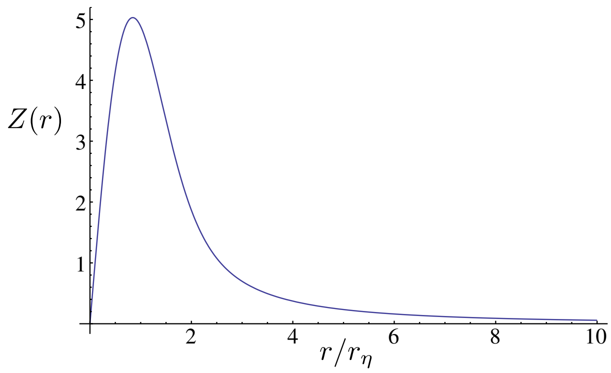

Figure 4.1: The displacement field for the spine model fields $Q_s = Z(r, \phi = \pi/2)$ for $B_s = 10$.

a form of the displacement field, $\boldsymbol{Q}$, is chosen that distorts the fan plane in the z-direction $\boldsymbol{Q}_S = Z(x, y)\hat{\boldsymbol{z}}$. For the *fan-reconnection* model it is chosen to distort the spine in the x-direction $\boldsymbol{Q}_F = X(z)\hat{\boldsymbol{x}}$ (the more general fan case given in Craig et al. (1997) of $\boldsymbol{Q}_F = X(z)\hat{\boldsymbol{x}} + Y(z)\hat{\boldsymbol{y}}$ is not considered here).

4.2 Spine model

4.2.1 Spine model fields

The displacement field for the spine model is derived, from Craig & Fabling (1996) and Craig et al. (1997), in Appendix B.1. In cylindrical co-ordinates it is

$$\boldsymbol{Q}_S = Z(r, \phi)\hat{\boldsymbol{z}} = \frac{B_s r}{r_\eta} M\left(\frac{3}{2}, 2, -\frac{r^2}{r_\eta^2}\right)\sin(\phi)\hat{\boldsymbol{z}}, \tag{4.8}$$

in terms of the confluent hypergeometric (Kummer) function $M(a, b, \zeta)$, (see e.g. Chapter 13 of Abramowitz & Stegun 1972). This function is plotted on $\phi = \pi/2$ against r/r_η in Figure 4.1. The *flux pile-up factor*, B_s, determines the strength of the magnetic field at a dimensionless distance r_η from the spine axis ($Z(r_\eta) \approx 0.49B_s$), where r_η is defined as

$$r_\eta \equiv \sqrt{4\bar{\eta}} \equiv \sqrt{\frac{4\eta}{|\alpha|(1-\lambda^2)}}. \tag{4.9}$$

It is the radius of a cylindrical region centred on the spine axis where resistive effects become significant.

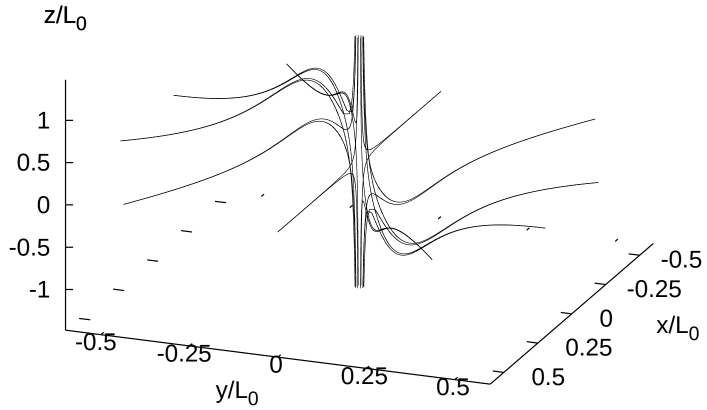

Figure 4.2: a) Representative magnetic field lines for the spine model with parameters $\lambda = 0.75$, $B_s = 3.4$, $\alpha = -2$, $\eta = 3 \times 10^{-3}$. The field lines are seeded from the top and base of the spine axis.

The form of the displacement field in equation (4.8) is only a solution to the governing equations provided $\alpha < 0$, see Appendix B.1. This condition, along with equation (4.6), gives global frozen-in plasma inflow along the fan plane, towards the spine, and outflow in the $\pm z$ directions, away from the null point. The magnetic field in the outer (ideal) region is also directed inwards along the fan plane and outwards along the spine axis. Some representative magnetic field lines for this model are shown in Figure 4.2. The displacement term shears the fan plane, with maximum shear along the y-axis (at $\phi = \pm\pi/2$), in the z-direction so that the angle between the spine axis and fan plane has closed up. For $\phi = 0, \pi$, along the x-axis, the field-lines are not sheared and remain perpendicular to the spine.

To integrate particle trajectories with the test-particle code the electric field is required. We calculate this from the resistive Ohm's law, the uncurled form of equation (4.2), as

$$\boldsymbol{E}(r,\phi) = \frac{\eta}{r}\frac{\partial Z}{\partial \phi}\hat{\boldsymbol{r}} + \left[(1-\lambda^2)P_r Z - \eta\frac{\partial Z}{\partial r}\right]\hat{\boldsymbol{\phi}}, \tag{4.10}$$

where $P_r = \alpha r/2$ is the radial part of the potential field, $\partial Z/\partial\phi = f(r)\cos\phi$ (where $f(r)$ is the radial part of the displacement field in (4.8), $Z(r,\phi) = f(r)\sin\phi$), and

$$\frac{\partial Z}{\partial r} = \frac{Z}{r} - \frac{3}{2}\frac{B_s r^2}{r_\eta^3} M\left(\frac{5}{2}, 3, -\frac{r^2}{r_\eta^2}\right)\sin\phi. \tag{4.11}$$

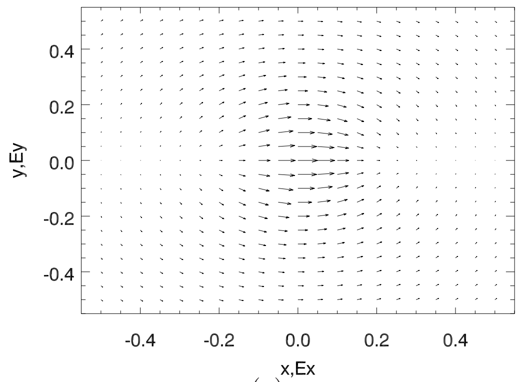

(a)

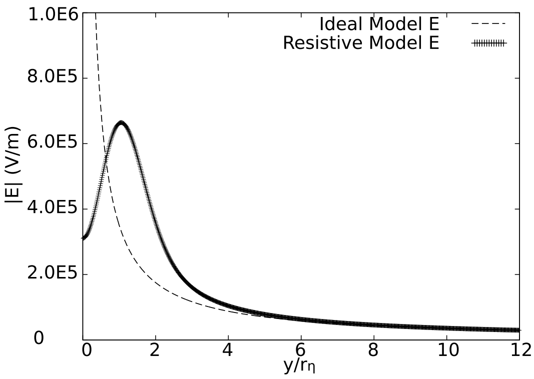

(b)

Figure 4.3: a) Vector plot of the electric field $\boldsymbol{E}(x, y)$ for $B_s = 3.4$, $\alpha = -2$, $\lambda = 0.75$, $\eta = 3 \times 10^{-3}$. The distances are in units of L_0. b) Magnitude of electric field at $x = 0$ across several resistive-regions. For comparison this is plotted against the ideal model electric field used in Dalla & Browning (2005), the curves are matched in the external region by setting $v_0 B_0\, E(y = 1\, L_0) = 1500\mathrm{V\,m}^{-1}$.

This electric field is curl-free (as required for steady-state) and so the electric potential, V, can be calculated to check energy conservation in the test-particle calculations. This can be found by integrating $\boldsymbol{E} = -\boldsymbol{\nabla} V$ to get

$$V(r, \phi) = \cos\phi \left[\frac{\alpha\,(1-\lambda^2)\, r^2\, f(r)}{2} - \eta\, r\, f'(r) \right]. \tag{4.12}$$

Figure 4.3 (a) shows a vector plot of equation (4.10) over a large part of the domain (L_0 is the simulation box length). Simpler expressions can be found for the electric field very close to or far from the spine, by using the truncated power series and asymptotic formulae for the Kummer function, respectively (Abramowitz & Stegun 1972). For all cases, the third argument in the Kummer function is negative. For $0 \leq \xi \ll 1$, the truncated power series gives

$$M(a, b, -\xi) \approx 1 - a\xi/b, \tag{4.13}$$

and for $\xi \gg 1$, the asymptotic formula is

$$M(a, b, -\xi) \approx \frac{\Gamma(b)}{\Gamma(b-a)} \xi^{-a}, \tag{4.14}$$

in terms of the Gamma function $\Gamma(b)$. Near the spine axis, $r \approx 0$, the only

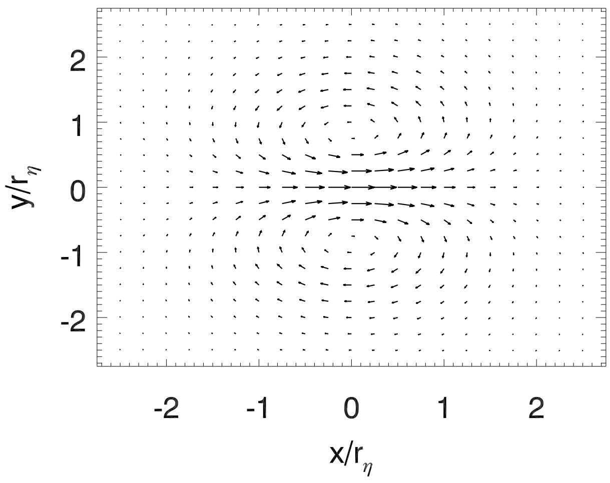

Figure 4.4: The direction and relative strength of the current, $\boldsymbol{j}$, in a plane of constant z for $\lambda = 0.75$, $B_s = 3.4$, $\alpha = -2$, $\eta = 3 \times 10^{-3}$. Here, $r_\eta = \sqrt{4\bar{\eta}} \approx 0.12$ is the size of the resistive region centred on the spine axis.

contribution to the electric field is from current in the x-direction

$$\boldsymbol{E}(r \ll r_\eta) \approx \eta \boldsymbol{j}(0) = \frac{\eta B_s}{r_\eta} \hat{\boldsymbol{x}}. \tag{4.15}$$

The full current distribution is plotted in Figure 4.4, it forms two cylindrical vortex structures that are localised with respect to the resistive region and invariant in the z-direction.

At large distances from the spine, the electric field goes as

$$\boldsymbol{E}(r \gg r_\eta) \approx \frac{-2\eta B_s}{\sqrt{\pi}} \frac{\sin\phi}{r} \hat{\boldsymbol{\phi}} + \mathcal{O}\left([r/r_\eta]^{-3}\right). \tag{4.16}$$

This has the same functional form as the ideal spine solution of Priest & Titov (1996), which is given in equation (1.56) and used in the ideal test-particle simulations of Dalla & Browning (2005, 2006) and Browning et al. (2010). Figure 4.3 (b) compares the magnitude of the electric field-strength, $|\boldsymbol{E}(r, \pi/2)|$, between the ideal electric field (1.56) and the resistive electric field (4.10). These are matched in the external region at $r = 1 \gg r_\eta$ by setting both equal to $1500\,\mathrm{V\,m^{-1}}$ (the electric field value that gives strong proton acceleration in Dalla & Browning 2005). It is clear that the resistive electric field (4.10) avoids the singularity of the ideal model. Dalla & Browning (2005) studied test-particles within *positive* *nulls*, where $B_0 > 0$ in equation (1.54), whereas we have a negative null as $\alpha < 0$. In this thesis, we match the electric drift inflow and outflow quadrants, by having opposite sign to Dalla & Browning (2005) for both the electric field and magnetic field. However, we will only qualitatively compare particle trajectories in the ideal and resistive spine models as an asymptotic match will give rise to unphysical hydromagnetic pressures on the edge of the resistive region $r \approx r_\eta$ that were absent in the simplified ideal model (see below).

The thermal pressure profile for the spine model can be found from integrating the uncurled form of equation (4.1). It is given in Craig et al. (1997), and derived in Appendix B.2, to be

$$p = p_0 - \frac{1}{2}\left(P^2 + Z^2\right) + \lambda\alpha z Z, \tag{4.17}$$

where p_0 is the gas pressure at the null point, the first term inside the brackets is due to dynamic pressure from the background flow and the other two terms are from balance with magnetic pressure. All terms except for p_0 are negative, in at least some part of the domain, so constraints must be put on the values of α and B_s in order to avoid unphysical negative pressures, as discussed in Litvinenko et al. (1996); Litvinenko & Craig (1999); Craig et al. (1997) and Craig & Watson (2000). We give some of the arguments here for the sake of completeness (see above references for more detail).

The strong electric field (fast electric drift) simulations in Dalla & Browning (2005), using the ideal spine model, were characterised by a dimensional value of the electric field $E_0 = 1500$ V/m on the $r = 1\,L_0$, $\phi = \pi/2$ boundary. Crucially, to match the electric field in equation (4.16) to this fixed amplitude electric field E_0 at $r = 1\,L_0$ requires the scaling $B_s \sim \eta^{-1}$, as η is reduced towards suitable solar coronal values (Craig et al. (1997) showed that if we require the displacement field at the boundary to be order 1, $Z(1, \pi/2) \sim 1$, this also gives $B_s \sim \eta^{-1}$). However, this scaling gives rise to large magnetic pressure on the sheet edge for small values of η. The maximum of the displacement field occurs at $r \approx r_\eta$ where $Z(r_\eta) \approx B_s/2$, see Figure 4.1, giving magnetic pressure $Z^2 \approx B_s^2/4 \sim \eta^{-2}$ from equation (4.17). To avoid negative thermal pressure in the model this requires the null point pressure $p_0 > (Z(r_\eta))^2 \sim \eta^{-2}$ which is unphysically large for coronal values of η ($\eta \sim 10^{-12} - 10^{-14}$).

Craig et al. (1997) showed that B_s must be limited to a saturation value on $r = r_\eta$, giving weak electric fields and small amplitude displacement field on the boundary: $Z(1, \pi/2) \ll 1$. Also, at $r = 1$, $z \ll 1$, we have dynamic pressure due to bulk fluid inflow $p \approx p_0 - P^2/2$, where $P(1) \sim \alpha$. We must constrain $\alpha \leq B_s$ or this dynamic pressure will require the gas pressure at the null to be even larger. The maximum value we can take for p_0 is the largest possible hydro-magnetic pressure available to drive the reconnection. We follow Craig et al. (1997) and choose this as the maximum external magnetic field $B_{e,max}^2/2$, where $B_{e,max} = 0.3$ T is a strong photospheric sunspot field, giving $B_{s,\max} = 30$ (note we use this as an upper limit when seeing how the value of B_s effects the energy gain, see below, and we typically use $B_{s,\max} = 5 - 10$ as the saturation value).

So far we do not know the value α should take, but expect that the bulk fluid exhaust from the reconnection region is of the order of the local Alfvén speed. The exhaust on the edge of the current sheet at a global distance from the null, $r = r_\eta$, $\phi = \pi/2$, $z = 1$, is given by

$$|v(r_\eta, \tfrac{\pi}{2}, 1)| \approx |\lambda B_s - \alpha|,$$

where the local Alfvén speed is

$$|v_A(r_\eta, \tfrac{\pi}{2}, 1)| = |B(r_\eta, \tfrac{\pi}{2}, 1)| \approx |B_s - \lambda\alpha|$$

for our choice of normalisation. As we are not interested in the case where $\lambda = 1$ (where there is no shear between the velocity and magnetic fields, and so no reconnection), and we must have $\alpha < 0$, this gives $\alpha \approx -B_s$ for Alfvénic exhaust. This is the largest magnitude of α we can take without having problems due to dynamic pressure. It also leads to the thinnest current sheet and thus maximises the current density in the resistive region. However, as Craig & Watson (2000) show, the Ohmic dissipation rate per unit height is

$$W_\eta = \eta \int j^2 dV \approx \pi\eta B_s, \tag{4.18}$$

which has no α dependence, as the increase in current density due to resistive region thinning is cancelled by the r_η^2 dependence of the total dissipation volume.

We calculate an approximate expression for the bulk electric drift velocity in the external region, using the asymptotic formula (4.14), to be

$$v_E(r \gg r_\eta) \approx \frac{\eta B_s \sin\phi}{\lambda|\alpha|\sqrt{\pi}} \left(\frac{-2z\hat{\boldsymbol{r}} - r\hat{\boldsymbol{z}}}{r(r^2/4 + z^2)} \right) \quad [v_A], \tag{4.19}$$

which is very slow when $|\alpha| = B_s$. It is thus necessary to limit the magnitude of α so that results can be obtained with reasonable integration times. For the simulations in Section 4.2.2 we use $B_s = 10$, $\alpha = -0.1$: this limits the reconnection exhaust close to the spine current sheet to sub-Alfvénic speeds.

The bulk electric drift can also be approximated close to the spine axis. Using equation (4.15), and with $\boldsymbol{B} \approx B_s y/r_\eta \hat{\boldsymbol{z}}$ gives

$$v_E(r \ll r_\eta) \approx -\frac{\eta}{y}\hat{\boldsymbol{y}}, \tag{4.20}$$

so particles approaching the spine (within the resistive region) will experience drifts directly towards the current sheet, provided that they are still magnetised to the extent that the drift approximation is valid. Equations (4.19) and (4.20) give the limiting electric drift velocities in the limits $r \gg r_\eta$ and $r \ll r_\eta$ respectively. Figure 4.5 shows numerically integrated electric drift streamlines in the plane $x = 0$ from the resistive spine model electric and magnetic fields. These streamlines are seeded from the upper-right and lower-left inflow quadrants. They are qualitatively different from the electric drift streamlines of the ideal model fields (dotted lines, seeded from the same points) as they can drift into the spine axis even after they have passed through the fan plane, $z = 0$, and are within the global outflow quadrants. Note the size of the resistive region is $r_\eta = 0.014$ for these parameters, so this inflow extends for a much larger range than the range of validity for equation (4.20).

4.2.2 Spine global trajectories

All of the proton calculations presented here are performed with the full-orbit version of the test-particle code, that solves the relativistic equations (3.1-3.2).

Initially, we place a distribution of 5 000 protons with Maxwellian velocities, based on a coronal temperature of $T = 10^6$ K (86 eV), in the spine model fields. The protons have positions from a uniform random distribution on a spherical surface at a global distance $R = \sqrt{x^2 + y^2 + z^2} = 1$ from the null point. We only discuss here protons that start in the upper right inflow region of longitude $0° < \phi < 180°$ and latitude $0° < \beta < 90°$ (here $\phi = 0°$ is the x-axis and $\beta = 0°$ is the fan plane). We find that for protons in the opposite inflow quadrant ($-180° < \phi < 0°$ $-90° < \beta < 0°$) the results are the same after reflections in both $\phi = 0°$ and $\beta = 0°$, apart from statistical differences.

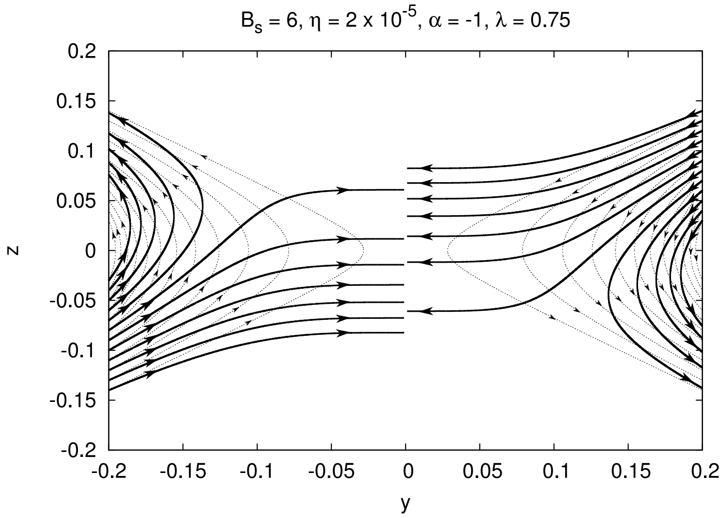

Figure 4.5: Representative electric drift streamlines in the plane, $x = 0$, seeded from the upper-right and lower-left electric drift inflow quadrants of the resistive spine model fields (solid lines). The parameters used are $B_s = 6$, $\eta = 2 \times 10^{-5}$, $\alpha = -1$ and $\lambda = 0.75$. Also plotted for comparison are drift streamlines of the ideal spine model (dotted lines).

Figure 4.6 shows the initial and final values of longitude and latitude for this distribution of protons. The final state is at time $t = 1.6 \times 10^6\, T_{\omega,p} \approx 10$ s (where $T_{\omega,p} = 2\pi m_p/(|e|B_0)$ is the characteristic proton gyro-period), at which the energy spectrum becomes approximately steady-state. Both the initial and final spatial distributions of protons are colour-coded by the energy at this final time (as the initial, $t = 0$, distribution of energies is purely thermal; we do not start the particles with an initial electric drift velocity, although they acquire this local drift speed very quickly). The spine model field parameters used are $B_s = 10$, $\eta = 10^{-6}$, $\alpha = -0.1$. This value of α limits the bulk flow exhaust speed to be sub-Alfvénic, but it increases the electric drift speed in the external region, see equation (4.19). This gives reasonable simulation times, but there are still some particles in the upper-right inflow quadrant at the end of the simulation.

The distribution of final energy with respect to initial position, in panel a) of Figure 4.6, suggests that there is no preferred initial latitude for gaining maximum energy. However, there is some structure in longitude, with particles within $80° < \phi < 170°$ gaining typically higher energies.

At the final time, there are two main populations of accelerated particles. The population labelled 'A' in Figure 4.6 is close to the fan plane, $|\beta| \lesssim 10°$, with energy $\epsilon_k \gtrsim 1$ keV, and with longitude $-90° \lesssim \phi \lesssim 90°$ comprising of about 8%

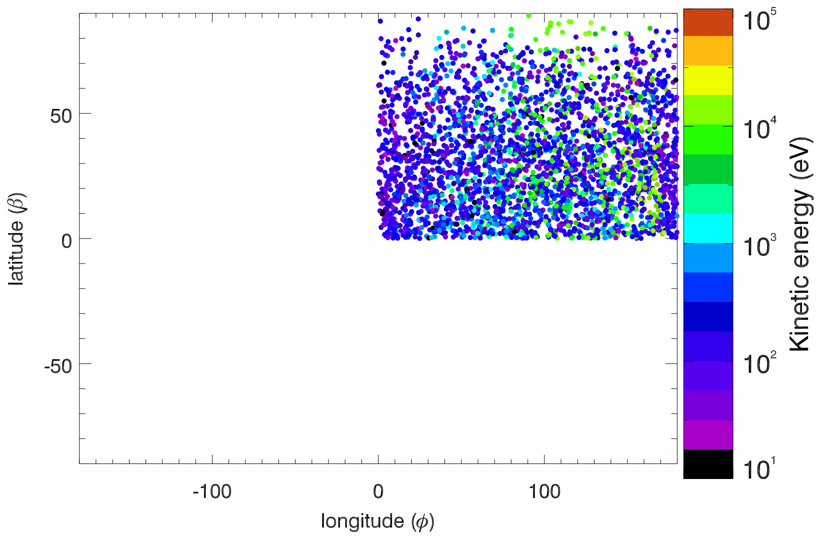

(a)

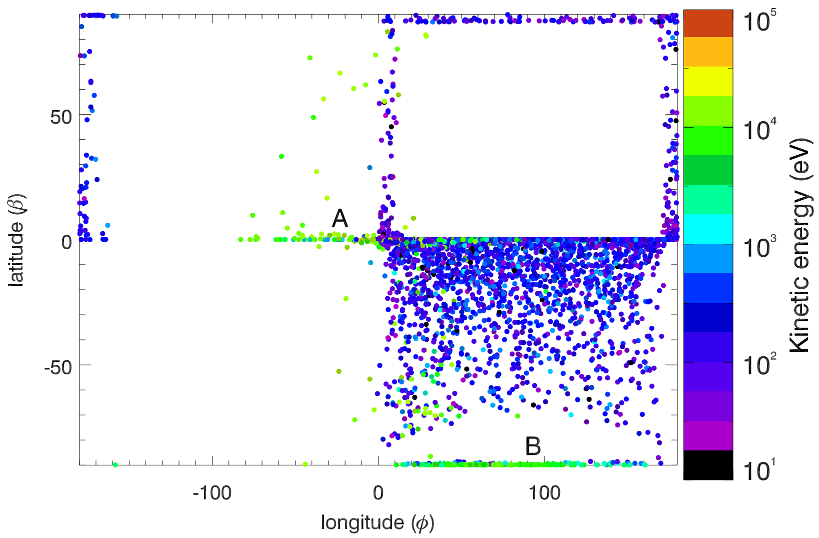

(b)

Figure 4.6: a) Initial angular distribution of 5000 particles in the electric drift inflow quadrant $0 < \phi < \pi$, $z > 0$ of the spine model fields, at $x^2 + y^2 + z^2 = 1$ from the null point. These particles are coloured by their energies in part b) of the Figure (the actual energy distribution in part a) is a Maxwellian with $T_0 = 86$ eV). The parameters used are $\lambda = 0.75$, $B_s = 10$, $\alpha = -0.1$, $\eta = 10^{-6}$. b) Angular distribution of protons at $t = 1.6 \times 10^6\, T_{\omega,p}$, at which the energy spectrum is steady state.

of the total proton number. The maximum particle energy of this population is about 15 keV. Note that the current in the spine axis is aligned with $\phi = 0°$: through the centre of this population. There are also some high energy protons scattered at large positive latitudes for $\phi \lesssim 0°$, and at large negative latitudes for $\phi \gtrsim 0°$. To look more closely at what is happening here we will choose a typical proton from this population and follow its trajectory below.

For those particles that have crossed the fan plane, $\beta = 0°$, into the lower right outflow quadrant, the spatial and energy distribution looks similar to the ideal spine case in Dalla & Browning (2006). The accelerated population which has $\epsilon_k \gtrsim 1$ keV and $\beta \lesssim -85°$ is labelled 'B'. This population is about 6% of the total protons in the simulation, and the maximum kinetic energy in this population is $\epsilon_{k,max} \approx 12$ keV. The angular distribution differs slightly with the ideal case of Dalla & Browning (2006) in that there are few particles found between the latitudes $-70° < \beta < -85°$; particles appear to be closer to the negative spine axis in the resistive case.

A typical proton trajectory from population 'A' is shown in Figure 4.7 (it, along with the field-lines, is projected into the y-z plane to show the global motion more clearly). The proton, which starts at $(x_0, y_0, z_0) = (-0.52, 0.80, 0.29)$ in the upper right hand inflow quadrant, initially moves away from the null, but mirror bounces and travels back towards the spine along the fan plane. The electric drift speed increases towards the spine causing the proton to enter the resistive region, which has radius $r_\eta \approx 0.01$, about the spine axis. It enters at $(x, y, z) \approx (-0.01, 0, 0.95)$ after $t = 3 \times 10^5\, T_{\omega,p} \approx 2$ s (inset is the full 3D trajectory in a localised region around the spine axis). At this point the proton becomes unmagnetised as the gyro-radius becomes comparable to the length-scale of magnetic field gradient. The proton is then directly accelerated in the x-direction, parallel to the current at the spine (we checked that the acceleration is $dv/dt \approx qE_0/m$ as it crosses $r = 0$). For small displacements in the y-direction a strong Lorentz force due to the B_z field returns it to $y = 0$ line. These oscillations are Speiser-like (Speiser 1965), also known as meandering-orbits, see also Sections 1.4 and 3.1.3.

Figure 4.8 shows plots of the particle energy, magnetic moment μ_m, and the *adiabatic parameter* $r_L/L_{\nabla B}$ (see e.g. Section 3.1.6) as the proton passes through the spine diffusion region. It can be seen that there is a large jump in kinetic energy associated with a violation in the constancy of μ_m. This occurs at the same

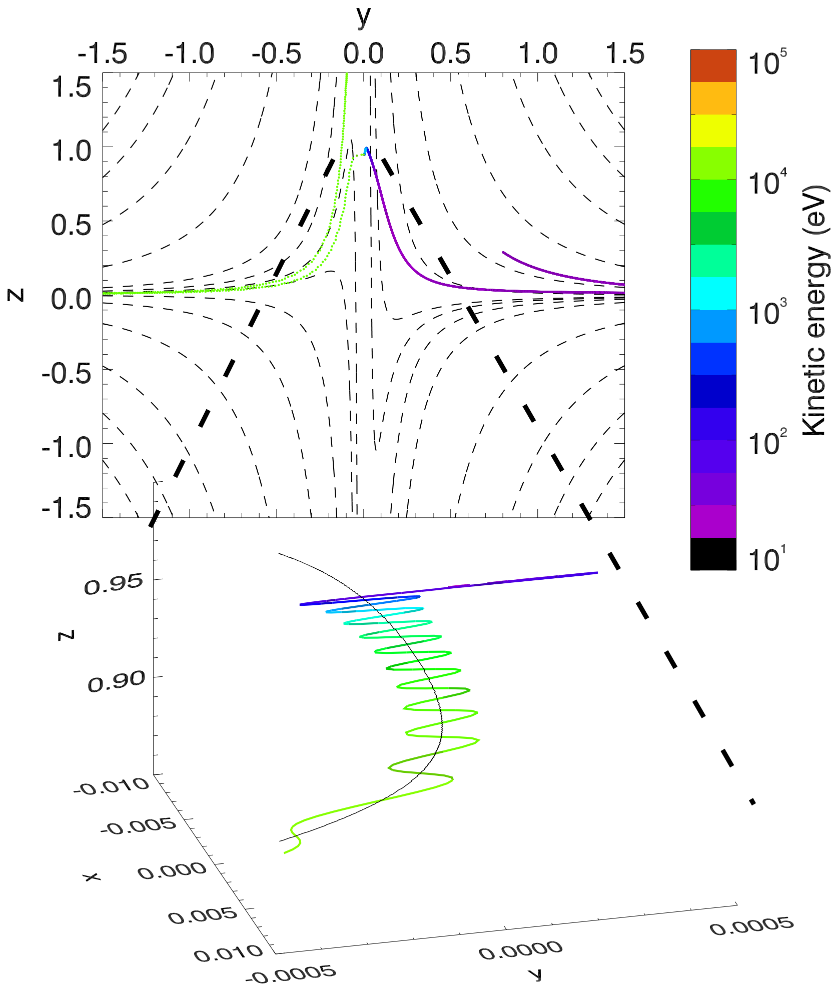

Figure 4.7: Typical proton global trajectory from population 'A' for parameters $\lambda = 0.75$, $B_s = 10$, $\alpha = -0.1$, $\eta = 10^{-6}$. The particle is taken from the many particle simulation, having initial position $x = (-0.52, 0.80, 0.29)$ and velocity $v = (-0.0044, 0.0013, -0.0088)v_0$. The magnetic field lines (thin dashed) are a projection of the field from the plane of the trajectory $\phi \approx 120°$. Inset shows the 3D trajectory of the proton as it crosses the spine-axis, the solid line in the centre is the line $B_z(x, y, 0.95) = 0$.

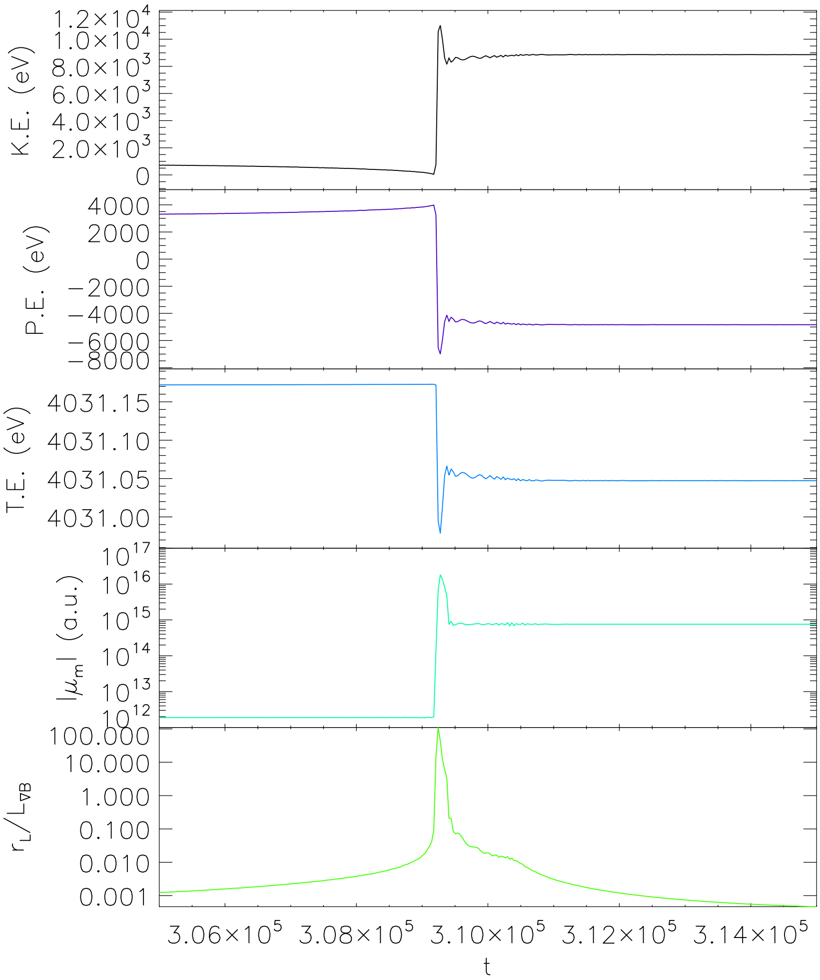

Figure 4.8: Traces of the Kinetic Energy (K.E., top), Potential Energy (P.E., second panel), Total Energy (T.E., third panel), magnetic moment μ_m (fourth panel, in arbitrary units) and the gyro-radius divided by the gradient length scale $r_L/L_{\nabla B}$ (bottom panel) as the proton crosses into the spine current sheet.

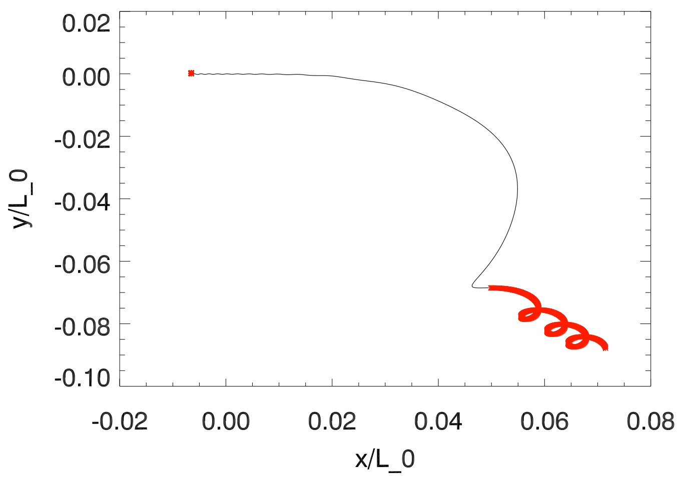

Figure 4.9: Proton trajectory around the spine axis, $r_\eta \approx 0.01$, projected on to the x-y plane. The thick red dots are over-plotted onto the trajectory when the quantity $r_L/L_{\nabla B} < 1$.

time as $r_L/L_{\nabla B} \gtrsim 10^{-2}$, which is typical for all proton trajectories we studied. Although the kinetic energy increases by more than an order of magnitude in just a few Speiser-oscillations, the total energy is conserved up to the fifth significant digit.

Figure 4.9 also shows the trajectory of the proton close to the spine axis, although it is further zoomed out so that the Speiser oscillations are not visible. The proton begins to re-magnetise and starts to gyrate when it reaches $r \approx 5r_\eta$, at which $r_L/L_{\nabla B} \lesssim 1$. However, the energy gain of $\epsilon_k \approx 11$ keV is localised to within $x \approx 2r_\eta$ (not shown), during which the trajectory does not deviate much from the x-direction. In effect, the proton has left the localised current sheet while unmagnetised but before it can be ejected by the background field components, in contrast to 2D current sheet configurations with weak guide field (eg. Speiser 1965; Litvinenko 1996). Figure 4.7 may give the impression that the particle is being ejected, however, this is just the centre of the Speiser-like oscillations following the $B_z(x, y, z = const.) = 0$ line (which here is not straight as in the usual 2D configurations). This behaviour occurs because the $\boldsymbol{F} = q\boldsymbol{v}\times\boldsymbol{B}$ force, with the dominant velocity component in the $\hat{\boldsymbol{x}}$ direction and with B_z the dominant component of the magnetic field, returns the particle to the $B_z = 0$ line.

After the proton becomes re-magnetised at $r \approx 5r_\eta$ it has weak electric drift,

$v_E \ll v_\omega$. It follows the field-lines closely and mirror bounces, travelling back towards the spine: there the proton is taken up to high latitude before it bounces again. This mirror bouncing is the reason for the 'scattered' accelerated protons in Figure 4.6, some of which are at large latitudes.

A typical particle trajectory chosen from population 'B' is shown in Figure 4.10. The proton starts at $(-0.54, 0.78, 0.31)$ and drifts towards the spine but bounces and crosses the fan plane instead at $t \approx 3 \times 10^5 \tau_0$. It exits the simulation box down the base of the spine axis, reaching an energy $\epsilon_k = 6.72$ keV as it crosses $z = -5$. As there is no electric field in the z-direction, the energy gain must occur due to motion in the x-y plane, which is also shown in Figure 4.10. The proton enters the region close to the spine axis parallel to a contour of the electric potential, but then drifts across the contour due to strong gradient drift. Figure 4.11 shows parameter traces for this proton as it crosses the fan plane. The increase in the potential magnetic field term as the proton moves down the spine axis (namely the P_z) reduces the electric drift speed. At the time of energy gain, the magnetic gradient drift speed $\boldsymbol{v}_{\nabla B}$ increases, but the proton remains adiabatic as $r_L/L_{\nabla B} < 10^{-2}$ and the magnetic moment μ_m is well conserved. This acceleration mechanism of gradient drifting parallel to the electric field is thus a distinct acceleration mechanism from the proton of population 'A'. The proton is stopped as it reaches $z = -5L_0$, which we do consistently throughout these simulations (we choose this to be the artificial size of the simulation box). At the time we stop this trajectory the proton is actually losing energy as it re-crosses the same electric potential contours. However, some other protons from population 'B' in Figure 4.6 reach the current sheet at low latitudes, gaining higher energy as they are accelerated in the positive x-direction to regions of lower electric potential.

The energy spectrum for the spine simulation is shown in Figure 4.12. If protons cross the $R = 5L_0$ spherical boundary we use the energy at the instant of crossing (if this is not done some protons reach order $\sim 10^2 L_0$ which becomes unrealistic as the background field increases without bound away from the null, also causing the time-step to decrease and simulation time to increase). The initial Maxwellian spectrum hardens to what appears to be a broken power law with maximum energy of about $\epsilon_k \approx 15$ keV. This maximum energy can be understood as the difference in potential energy across the spine current sheet, $\epsilon_k \sim qEx_{acc}$ where $E \approx E_0 \approx \eta B_s/r_\eta$ $[v_0 B_0]$ and $x_{acc} \approx 2r_\eta$ $[L_0]$ is the acceleration distance

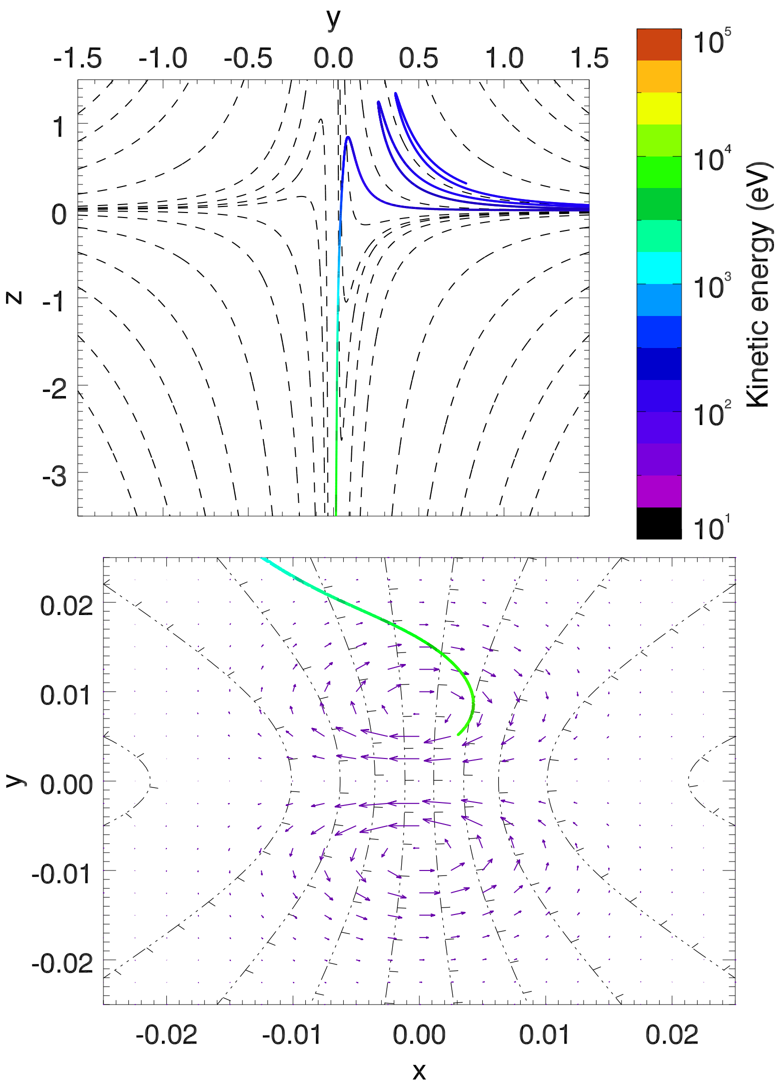

Figure 4.10: Typical proton trajectory from population 'B' in the many particle simulation, with initial position $x = (-0.54, 0.78, 0.31)L_0$ and velocity $v = (-0.004, -0.006, 0.002)v_0$. The dashed lines show the projection of the magnetic field from the plane of motion, $\phi \approx 110°$, onto the y-z plane. Inset shows the motion in the x-y plane close to the spine axis. The purple arrows show the direction and relative magnitude of the gradient drift velocity and the dash-dotted lines show contours of the electric potential, with the intersecting tick mark indicating lower potential energy to the right.

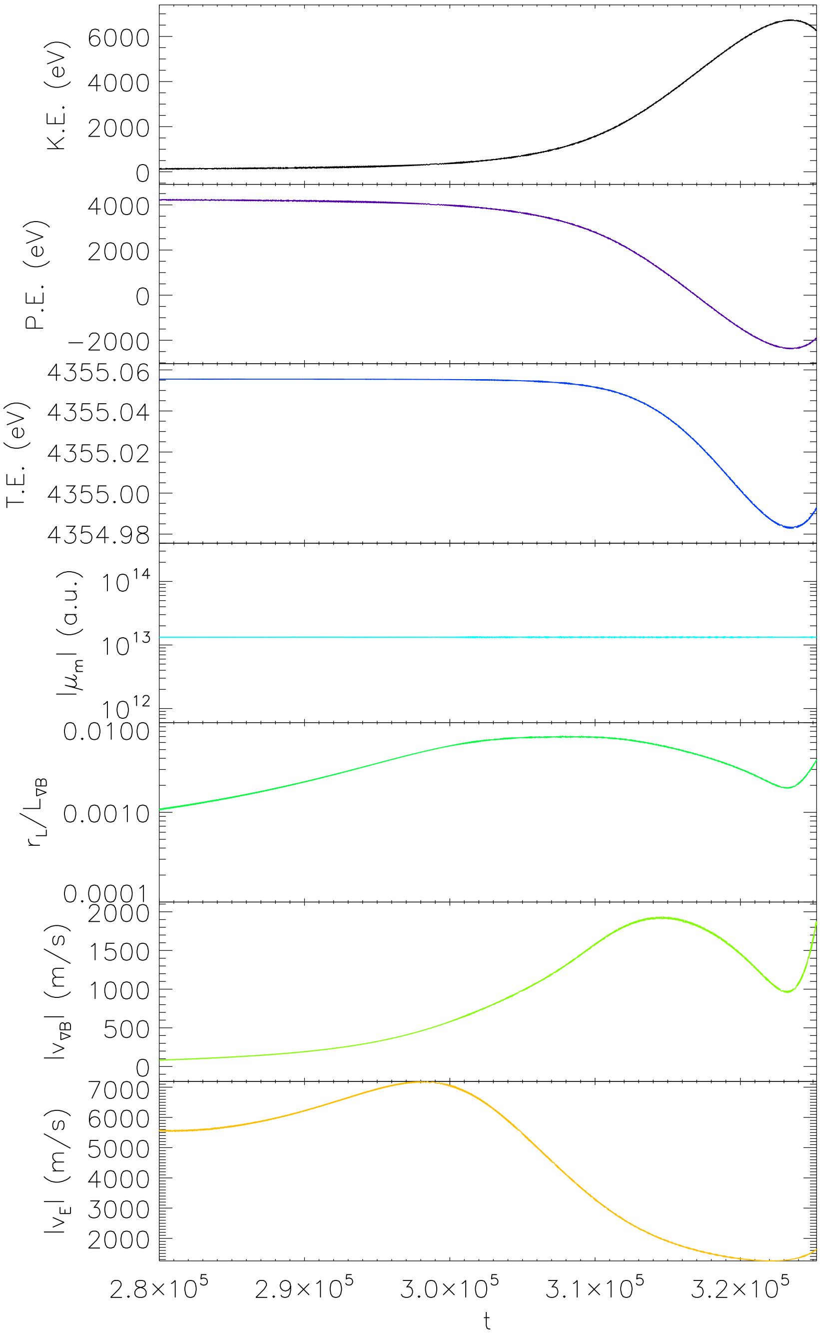

Figure 4.11: Traces of the Kinetic Energy (K.E., top), Potential Energy (P.E., second panel), Total Energy (T.E., third panel), magnetic moment μ_m (fourth panel, in arbitrary units), the adiabatic parameter $r_L/L_{\nabla B}$ (fifth panel), the magnitude of the $\boldsymbol{v}_{\nabla B}$ drift (sixth panel) and the magnitude of the electric drift $|\boldsymbol{v}_E|$ (bottom panel) for the typical proton trajectory from population 'B' (the same as in Figure 4.10).

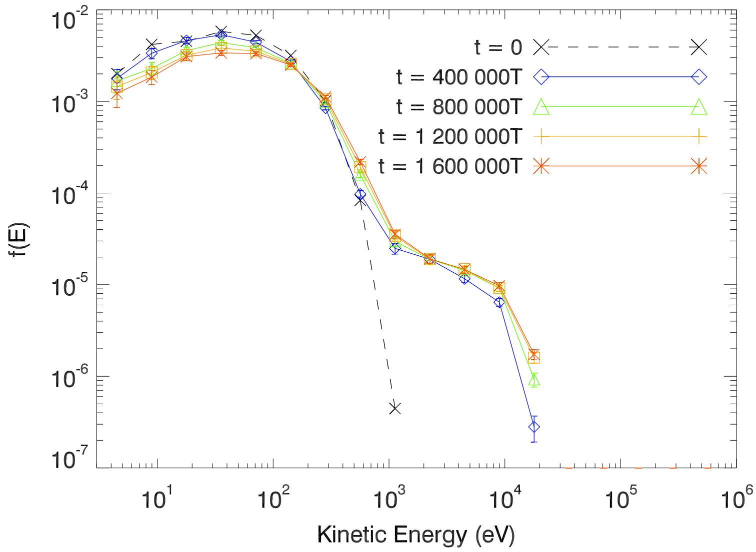

Figure 4.12: Energy spectrum from the many particle simulation for protons in the spine model, with parameters $\lambda = 0.75$, $B_s = 10$, $\alpha = -0.1$, $\eta = 10^{-6}$. For particles leaving the $R = 5$ sphere, the energy at the time of crossing is used.

(from $-r_\eta \lesssim x \lesssim r_\eta$), as the reconnection electric field drops off quickly for $|x| > r_\eta$. For the parameters used, this gives $\epsilon_k \approx 13$ keV. This approximate expression has no dependence upon the parameter α, so the limiting of $|\alpha| < B_s$ should not have a large effect on this result.

4.3 Fan model

4.3.1 Fan model fields

The displacement field for the fan model is

$$\boldsymbol{Q}_F = X(z)\hat{\boldsymbol{x}} = \frac{B_s\, z}{\bar{\eta}^{1/2}} M\left(\frac{3}{4}, \frac{3}{2}, \frac{-z^2}{2\bar{\eta}}\right)\hat{\boldsymbol{x}}, \tag{4.21}$$

where M is again a confluent hypergeometric function (Craig et al. 1997). We define z_η as

$$z_\eta \equiv \sqrt{2\bar{\eta}} \equiv \sqrt{\frac{2\eta}{\alpha(1-\lambda^2)}}, \tag{4.22}$$

the approximate height at which X takes the maximum value, $X(z_\eta) \approx 0.9B_s$. This is a measure of the height for a resistive region centred on the fan plane,

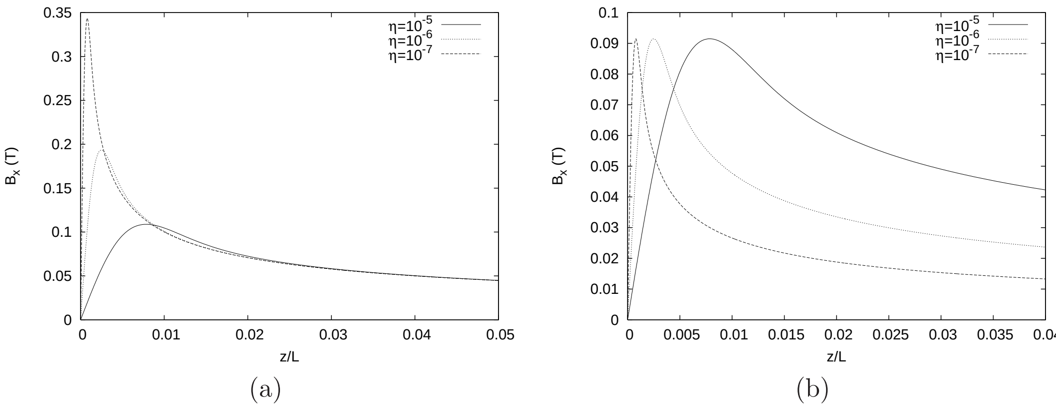

Figure 4.13: Plots of $B_x(x = 0, z) = X(z)$ for the fan-model for three different values of resistivity $\eta = 10^{-5}, 10^{-6}$ and 10^{-7}. a) Setting the fields equal at a global distance; $X(z = 1L_0) = 1B_0 = 0.01$ T for all three values of η. b) Saturating the peak field at $B_{s,\max}$ for all three cases.

$z = 0$.

Figure 4.13 shows this displacement field, $B_x(x = 0, z) = X(z)$, when; (a) the field is set to order unity at a global distance, and (b) a saturation value of $B_{s,\max} = 10B_0$ is imposed. In both cases there is magnetic *flux pile-up*; an increase in the magnetic field-strength just upstream of the current sheet. However, the magnetic pressure ($\approx B_x^2/2$) on the sheet edge is much greater for the unsaturated case, see below.

The form solution (4.21) is only valid for $\alpha > 0$ (Craig et al. 1997), which gives a positive null point, and the field is washed in from the global boundaries at $z = \pm 1$ before exiting the simulation box radially along the fan plane. Some representative magnetic field lines are shown in Figure 4.14; the displacement field shears the spine axis as it approaches the fan plane, giving rise to strong current inside the resistive region.

We calculate the electric field from Ohm's law as

$$\boldsymbol{E} = \hat{\boldsymbol{y}} \left[\eta \, X'(z) - (1 - \lambda^2) P_z X(z)\right] + \hat{\boldsymbol{z}} \left[(1 - \lambda^2) P_y X(z)\right], \tag{4.23}$$

where the current density $\boldsymbol{j}$ is

$$\boldsymbol{j} = X'(z)\hat{\boldsymbol{y}} = \frac{X(z)}{z} - \frac{B_s z^2}{2\bar{\eta}^{3/2}} M\left(\frac{7}{4}, \frac{5}{2}, -\frac{z^2}{2\bar{\eta}}\right)\hat{\boldsymbol{y}}. \tag{4.24}$$

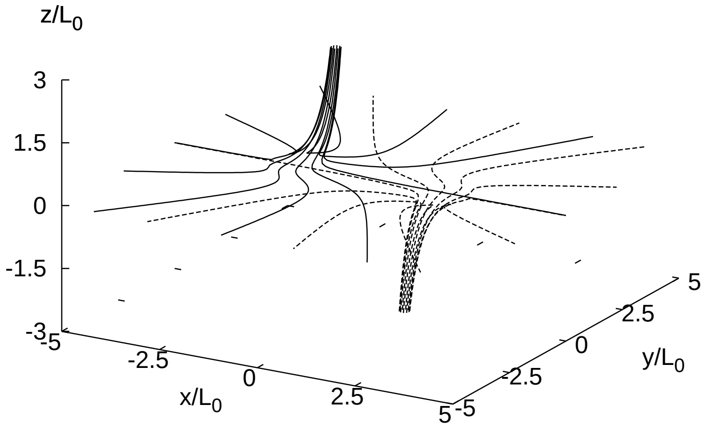

Figure 4.14: Representative magnetic field lines for the fan solution with parameters $\lambda = 0.75$, $B_s = \alpha = 10$, $\eta = 10^{-6}$. The lines are again seeded from the top (solid lines) and base (dashed lines) of the spine.

Figure 4.15 shows this current density $j(z)$, and the contribution from each of the two terms in equation (4.24). There are reversed current layers on either side of the main current sheet caused by a flux pile-up effect (the strong gradients upstream of the current sheet in Figure 4.13). These reversed current layers will be discussed further in Section 4.4 below. The maximum current density is $\boldsymbol{j}(z = 0) = X'(0)\hat{\boldsymbol{y}} = B_s/\bar{\eta}^{1/2}\,\hat{\boldsymbol{y}}$, the magnitude of the current density at the centre of the current sheet. For $B_s = \alpha = 10$, $\eta = 10^{-6}$, $\lambda = 0.75$ this is $j_{\max} = 2.09 \times 10^4\,[B_0/(\mu_0 L_0)]$. The current density only has z-dependence; it is infinite in extent in the x and y directions. This is clearly unrealistic, although resistive MHD simulations by Pontin et al. (2007b) find that *spine-fan* reconnecting current sheets formed due to shear flows around a null point spread out along the fan plane in the incompressible limit. Note that analytic multiple null solutions found by Craig et al. (1999) have finite current sheets, avoiding this problem. In our simulations below we consider particle acceleration only within a restricted range of $5\,L_0$, effectively limiting the size of the current sheet.

The electric potential, to be used for energy conservation, is again found by solving $\boldsymbol{E} = -\boldsymbol{\nabla} V$ to give

$$V(y, z) = -\alpha y(1 - \lambda^2)\,[\bar{\eta} X'(z) + zX(z)]\,. \tag{4.25}$$

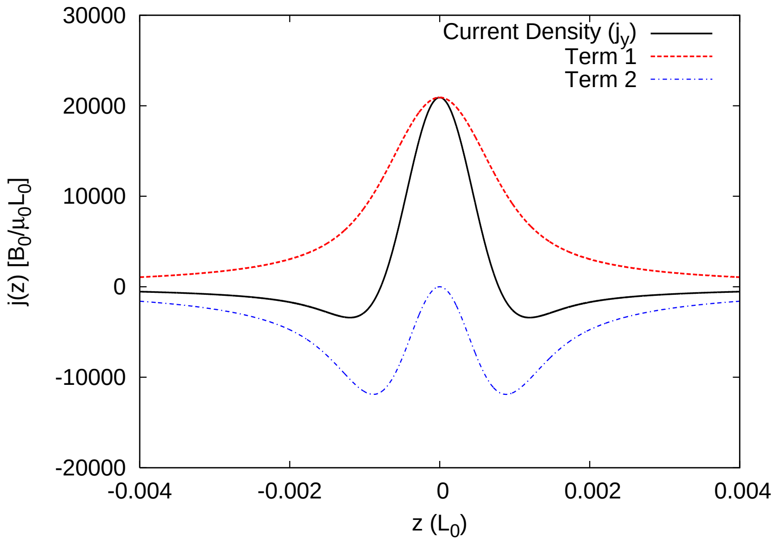

Figure 4.15: Normalised current density, j_y, plotted against z for the parameters $\lambda = 0.75$, $B_s = \alpha = 10$, $\eta = 10^{-6}$. The red dashed line is the first term in equation (4.24) and the blue dash-dotted line is the second term.

The thermal pressure profile for the fan model is (Craig et al. 1997)

$$p = p_0 - (P^2 + X^2)/2 - \alpha\lambda x X/2. \tag{4.26}$$

However, in this case, a displacement field of order unity on the $z = 1$ boundary, $X(1) \sim 1$, gives the scaling $B_s \sim \eta^{-1/4}$ (see Craig et al. 1997, and Figure 4.13 (a)). This gives much weaker magnetic pressure on the current sheet edge compared to the spine model, but it is still too large for the values of η considered. Again we saturate $B_{s,max} = 30$ and we have $\alpha \leq B_s$ to avoid problems from dynamic pressure.

Craig & Watson (2000) show that the Ohmic dissipation rate per unit area of the fan current sheet is

$$W_\eta = \eta \int j^2 dV \sim \eta B_s^2 / z_\eta \tag{4.27}$$

and so in this case, for fixed (saturated) B_s, the maximum dissipation occurs with the thinnest current sheet (the so called optimised solution). The thinnest sheet we can have subject to the dynamic pressure constraint is when $\alpha = B_s$ (for any fixed value of λ). Also, as this choice gives the largest current density, it maximises the resistive electric field within the sheet which is interesting for particle acceleration. As above, this choice of α sets the bulk fluid exhaust at $x^2 + y^2 = 1$, $z = z_\eta$ to the local Alfvén speed.

Using the asymptotic approximation (4.14) we find that the z-component of the electric drift that brings the particles to the fan plane is, for $x,\, z \gg \eta^{1/2}$,

$$v_{Ez} \approx \frac{(1-\lambda^2)P_x P_z X(z)}{\lambda P^2} \sim \frac{(1-\lambda^2)^{3/4}}{\lambda} B_s\, \alpha^{-1/4} \eta^{1/4} \tag{4.28}$$

which scales as $\sim B_s^{3/4}\eta^{1/4}$ for the optimised solution $\alpha = B_s$. This gives electric drift inflow for positive x, z (as $P_z < 0$), and outflow for positive z and negative x. It is much faster than the spine case due to the more favourable scaling with resistivity. The streamlines in the x-y plane can be found from the numerical (or approximate analytical) solution of

$$\frac{dx}{v_{Ex}} = \frac{dy}{v_{Ey}}; \tag{4.29}$$

we numerically plot these streamlines, and also the drift streamlines in the x-z plane, on top of the single particle trajectory results for the fan model below.

4.3.2 Fan global trajectories

The many-particle simulation for the fan model is shown in Figure 4.16 for the optimised solution $B_s = \alpha = 10$, with $\eta = 10^{-6}$, $\lambda = 0.75$, $z_\eta = 6.76 \times 10^{-4}\, L_0$, where the protons are again colour-coded by the final energy. The initial distribution has thermal energy $\epsilon_k = 86$ eV with uniform random position in the upper inflow quadrant $-90^\circ < \phi < 90^\circ$ and $0^\circ < \beta < 90^\circ$. The final angular distribution is taken from when the proton distribution reaches a steady state in energy at $t = 4000\, T_{\omega,p} \approx 0.025$ s. This occurs more than two orders-of-magnitude faster than the spine model for similar parameters (even after the spine drift was increased by limiting $\alpha < B_s$), as the external electric drift (equation 4.28) scales more favourably with the resistivity. Protons that cross the $R = 5L_0$ spherical boundary from the null point before this time are stopped and the energy and angular position at time of crossing is used. For the fan model, the $t = 0$ angular distribution is structured in terms of final energy gain (protons that are within specific solid angles from the null point at $t = 0$ gain higher energy than others). This is in contrast to the lack of structure in the spine-model (see Figure 4.6) as the ratio of the electric drift to thermal velocity is much larger in the fan model

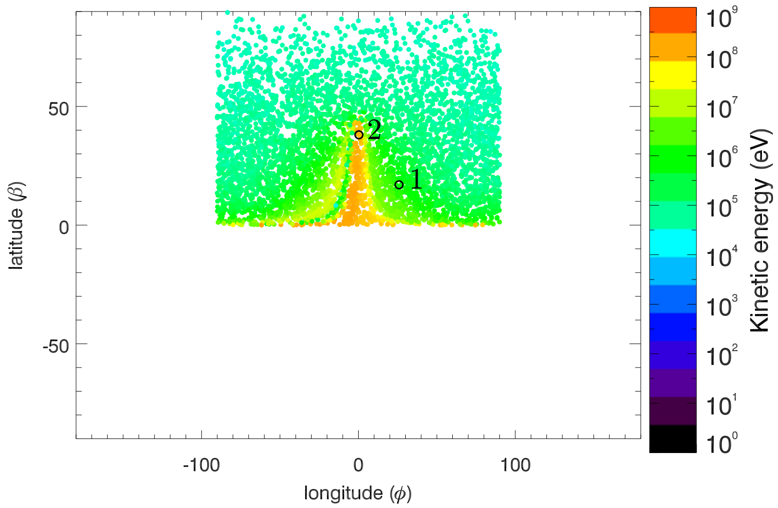

(a)

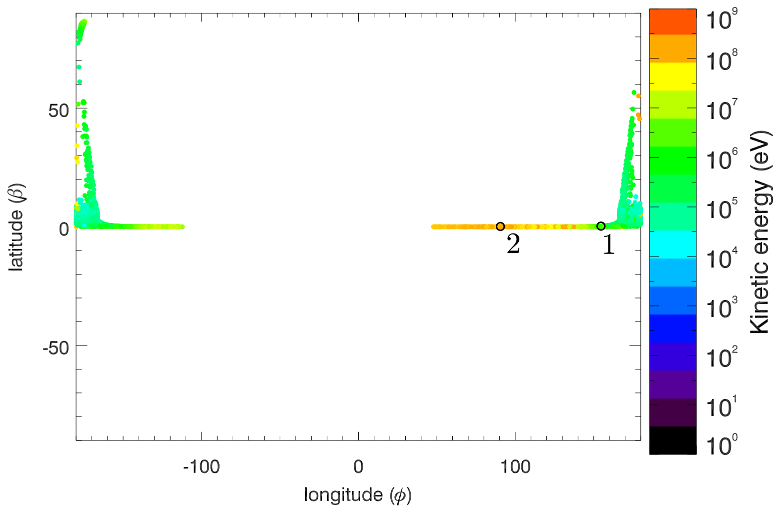

(b)

Figure 4.16: a) Angular distributions of protons in fan model at $t = 0$, with initial temperature $T = 86$ eV. The x-axis is $\phi = 0°$ and the fan plane is $\beta = 0°$. Protons are coloured by the final energy at $t = 4\,000$. Parameters used are $\lambda = 0.75$, $B_s = \alpha = 10$, $\eta = 10^{-6}$. b) Angular distributions at time $t = 4\,000 T_{\omega,p}$ when the energy spectrum has reached steady state. The trajectories of protons labelled ‘1’ and ‘2’ are shown in Figure 4.17.

(see Vekstein & Browning (1997); Browning & Vekstein (2001) for a discussion on the importance this ratio for the 2D x-point). Within this structure, there is some asymmetry in ϕ, which differs from the final energy dependence of the initial proton distribution in the ideal fan model in Dalla & Browning (2008). Indeed, we do not expect symmetry between particles drifting clockwise and anti-clockwise about the null here, now that there is current and associated electric field in the y direction.

We now explore trajectories and energy gain in more detail. First the not-so-typical cases will be mentioned, before showing single-proton trajectories for the more typical cases.

Those protons with $\epsilon_k \approx 10^7$ eV at $\phi \approx -20°$ (the yellow vertical band to the left of the green vertical band in Figure 4.16(a)) do not enter the current sheet but gain high energy, as they get close to z_η, from very fast and non-uniform electric drifts. They become unmagnetised slightly with $r_L/L_{\nabla B} \sim 10^{-3}$, and the first adiabatic invariant, the constancy of μ, is also violated.

At $t = 4\,000\,T_{\omega,p}$ there are a small number of high energy protons scattered at high latitudes (about 0.1% with $\epsilon_k > 10$ MeV). These enter the current sheet temporarily within $-180° < \phi < 0°$ but far from the null point. However, they exit into the external region again without any Speiser-like motion. They become slightly unmagnetised, with maximum $r_L/L_{\nabla B} \approx 10^{-2}$, following complicated trajectories. As they are not typical we do not investigate these further in the external region, but their behaviour within the current sheet (how they are ejected) is discussed in Section 4.3.3.

Typically, the high energy protons of Figure 4.16 start either close to the x-axis at low to mid latitudes (about 7% of the total number at latitude $\beta \gtrsim 1°$ with final energy $\epsilon_{k,fin} \gtrsim 10$ MeV), or they start at very low latitude close to the fan plane ($< 1\%$ of total at $\beta \lesssim 1°$ and $\epsilon_{k,fin} \gtrsim 10$ MeV). At $t = 4\,000\,T_{\omega,p}$ these energetic protons are found at $\beta \approx 0$ either side of $\phi = 90°$ (the y-axis), which is the direction of the current in the fan current sheet.

Figure 4.17 shows the trajectory of two typical protons taken from the simulation. Proton '1' starts at $(x_0, y_0, z_0) = (0.86, 0.41, 0.30)$ and drifts around the null point due to the strong azimuthal electric drift. Although it drifts down towards the current sheet, it reaches a minimum height of $z \approx 15\,z_\eta$ before it flows into the outflow quadrant, not entering the sheet. Parameter traces for this proton are shown in Figure 4.18. The main velocity contribution is electric drift

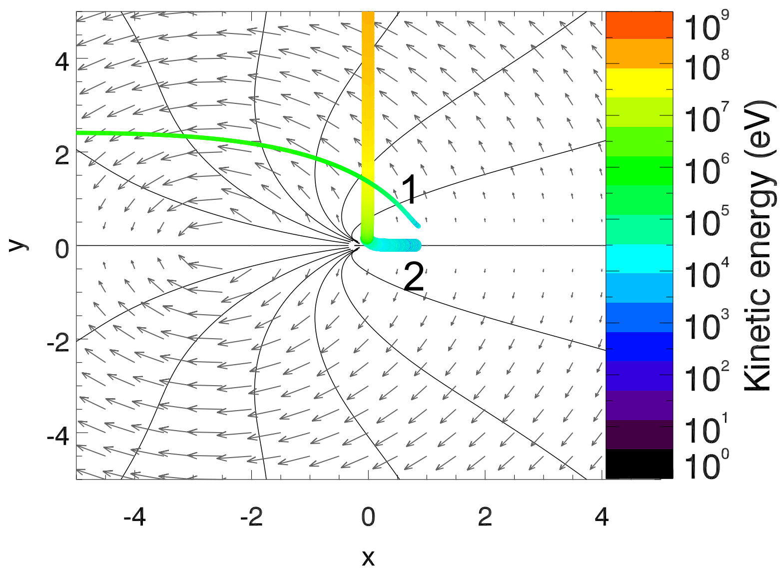

(a)

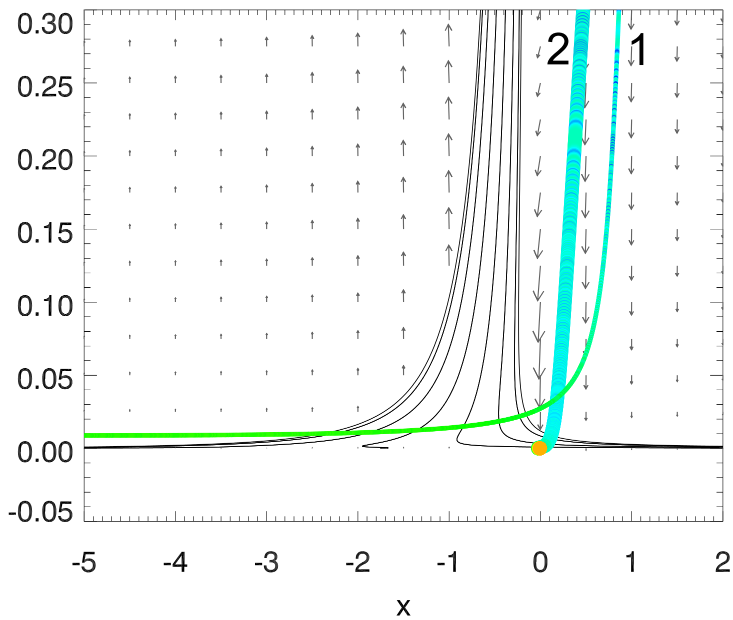

(b)

Figure 4.17: Two typical proton trajectories from the many particle simulations in the fan model. Proton '1' is represented by a thin line with initial position $(0.86, 0.41, 0.30)$, and proton '2' by a thick line with initial position $(0.8, 0.003, 0.6)$. The parameters are $\lambda = 0.75$, $B_s = \alpha = 10$, $\eta = 10^{-6}$. The solid lines are representative magnetic field lines (seeded from the top of the spine axis and projected into the 2D planes) and the arrows show the direction and relative magnitude of the electric drift velocity. a) In the x-y plane, where the electric drift arrows are from the edge of the current sheet $z = z_\eta$. b) In the x-z plane close to the current sheet, where the electric drift arrows are plotted on $y = 0$. The initial positions are not shown in this plane.

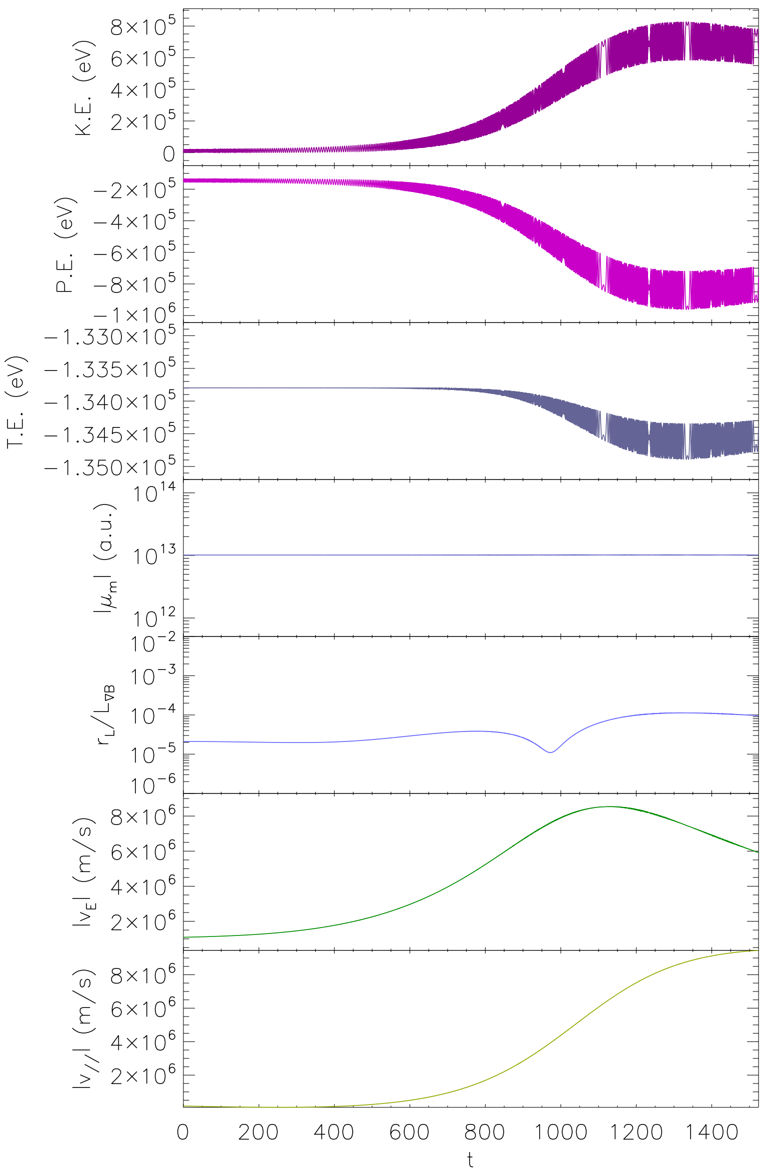

Figure 4.18: Parameter traces for proton '1' of the many particle simulation in the fan model fields. Shown are the Kinetic Energy (K.E., top), Potential Energy (P.E., second), Total Energy (T.E., third), magnetic moment (μ_m, in arbitrary units), the adiabatic parameter $r_L/L_{\nabla B}$, the magnitude of the electric drift velocity $|\boldsymbol{v}_E|$, and the magnitude of the parallel velocity $\boldsymbol{v}_\parallel$.

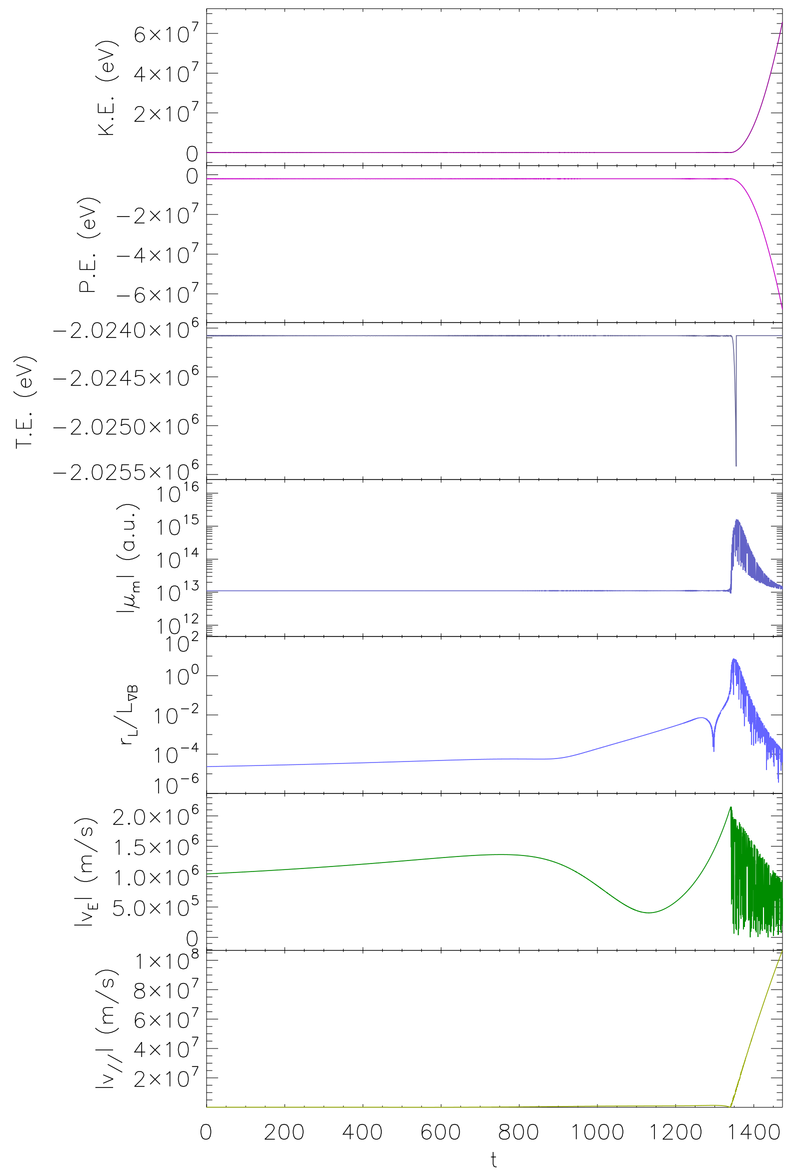

Figure 4.19: Parameter traces for proton '2' of the many particle simulation in the fan model fields. Shown are the Kinetic Energy (K.E., top), Potential Energy (P.E., second), Total Energy (T.E., third), magnetic moment (μ_m, in arbitrary units), the adiabatic parameter $r_L/L_{\nabla B}$, the magnitude of the electric drift velocity $|\boldsymbol{v}_E|$, and the magnitude of the parallel velocity $\boldsymbol{v}_\parallel$.

as it moves around the null point, but $v_\parallel$ becomes dominant as the particle exits the simulation box parallel to the negative x-axis. The first adiabatic invariant is not violated, $\mu = const.$ and the maximum $r_L/L_{\nabla B} \sim 10^{-4}$ at closest point of approach to the sheet. The proton is strongly magnetised throughout. Despite not reaching the current sheet the energy gain is still considerable, reaching 0.5 MeV as it crosses the $R = 5$ sphere.

Particle 2 starts at $(0.8, 0.003, 0.6)L_0$, and the traces for this trajectory are shown in Figure 4.19. The azimuthal component of the electric drift is weak close to the x-axis, so the proton electric-drifts down to the fan current sheet. It enters the sheet at $(x, y) = (-0.02, 0.15)$ and becomes unmagnetised: $r_L/L_{\nabla B} > 1$ and μ is not conserved. We observe Speiser-like oscillations (not shown) as the proton is accelerated in the y-direction. At $t = 129\,T_{\omega,p} = 0.846$ ms after entering the sheet, it passes out of the simulation box at $R = 5$. Here, the particle is still within the sheet with $v_\parallel = 0.36c$ and $\epsilon_k = 67$ MeV. Using this time period in the direct acceleration formula, $y = qE_0t^2/2m$, with the electric field on $z = 0$, $E_0 = \eta B_s/\bar{\eta}^{1/2} \quad [v_0B_0]$ from (4.23), gives $y \approx 5$. Thus the proton is directly accelerated in the current sheet for the entire length of the simulation box. However, this motion is not Speiser-like throughout as $r_L/L_{\nabla B} < 10^{-2}$ when the proton reaches $y = 1.5L_0$. The proton reaches a global distance in the y-direction and becomes magnetised by the background B_y component of the magnetic field, which acts as a guide field that increases with distance from the null. When the simulation is run without stopping the proton at $R = 5$, it is still not ejected (as, for example, the proton within the model fields of Speiser (1965) shown in Figure 3.2) from the current sheet throughout the whole simulation time $t = 4\,000\,T_{\omega,p}$ (not shown). In Section 4.3.3 below, we investigate whether this trapping within the current sheet is typical for the fan model fields.

This particle enters the current sheet at a distance $R \approx 0.15$ from the null point; however, this distance is not typical for the many-particle simulation in Figure 4.16. Figure 4.20 shows the spatial positions, (x, y), for protons that enter the current sheet, at the time of their entry. The horse-shoe structure is caused by the fast and non-uniform azimuthal electric drifts, with particles that have drifted further gaining higher energy. In this many-particle simulation, 9.3% of the total particles reach the current sheet, after a mean time of about $800T_{\omega,p}$. The average distance from the null point of particles entering the sheet is $R \approx 2.2$. This means that there is a large number of particles that enter the current sheet, but they do

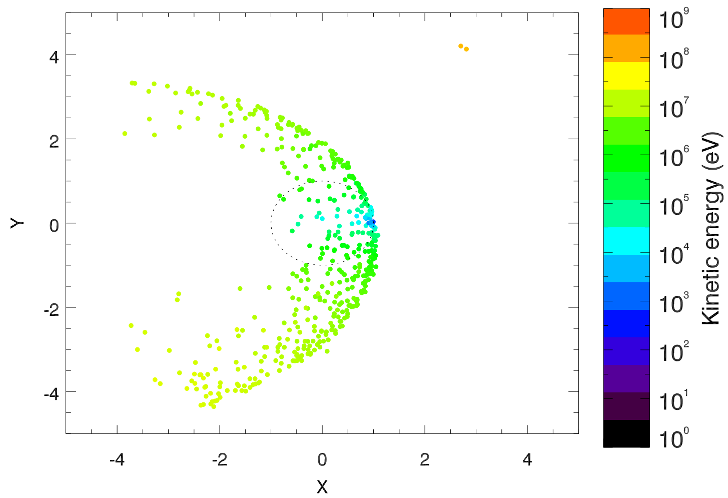

Figure 4.20: Positions at which protons in the many-particle fan simulation enter the current sheet, $z < z_\eta$ (with parameters $\lambda = 0.75$, $B_s = \alpha = 10$, $\eta = 10^{-6}$). These are coloured by the kinetic energy at the time of entering the sheet.

so far enough away from the null point that they are not unmagnetised.

The energy spectrum for the fan simulation is shown in Figure 4.21. Almost all the protons are accelerated, as the fast electric drift speed in the fan model is typically larger than initial thermal velocity. The energy spectrum appears steady state by $t = 4\,000 T_{\omega,p}$. Between $\epsilon_k \approx 10^5$ eV and $\epsilon_k \approx 10^{7.5}$ eV the spectrum is approximately power law shape: $f(E) \propto E^{-\gamma}$ with $\gamma \approx 1.5$. It is interesting to note that this is the same spectral index that is expected for direct acceleration without a guide field in a 2D current sheet (e.g. Heerikhuisen et al. 2002). However, for the case of Figure 4.21, the protons in this energy range have not entered the current sheet. Instead the energy gain occurs in the external region due to non-uniform drifts parallel to the electric field. The protons that do enter the current sheet gain the highest energies and can be seen as a flat tail at the hard end of the spectrum. We do not give a spectral index for this population as it has not reached steady state: as these protons are trapped in the sheet, the energy gain by direct acceleration depends upon the size of the simulation box. As a test we repeat the simulation but stop the protons at a spherical surface of radius $R = 10$ from the null point, instead of $R = 5$ that has been used consistently throughout these simulations. A comparison of the steady state distributions between this and the previous simulation is shown in Figure 4.22. Now the 'flat tail' at $10^{7.5-8}$ eV in Figure 4.21 becomes a 'bump on

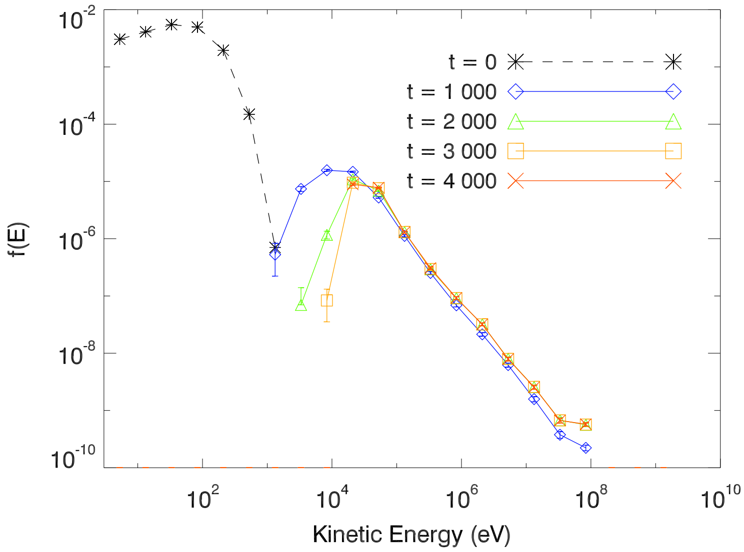

Figure 4.21: Energy spectrum for the many particle fan simulation for protons with parameters $\lambda = 0.75$, $B_s = \alpha = 10$, $\eta = 10^{-6}$. For particles leaving the $R = 5$ sphere, the energy at the time of crossing is used.

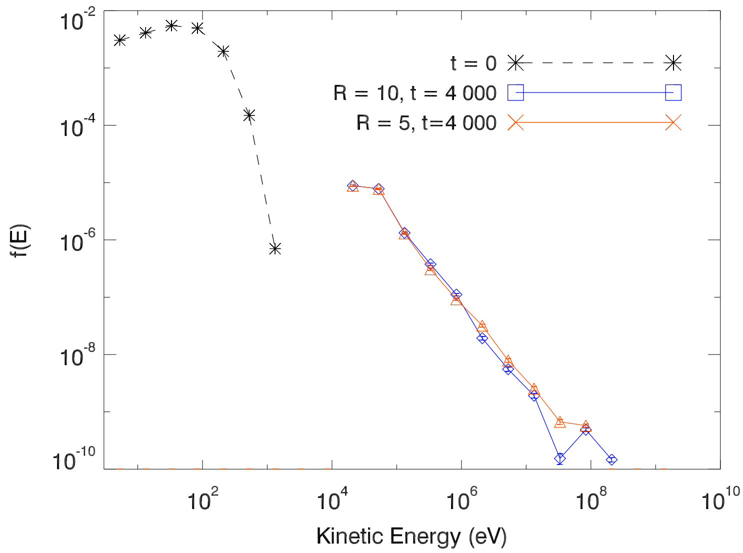

Figure 4.22: Comparison of steady state energy spectra for a simulation where the protons are stopped on the $R = 5$ sphere, and where they are stopped on the $R = 10$ sphere. For protons crossing these boundaries, the energy at the time of crossing is used. Also shown is the initial distribution that is used for both simulations. These simulations have parameters $\lambda = 0.75$, $B_s = \alpha = 10$, $\eta = 10^{-6}$.

tail' centred at 10^8 eV disconnected from the main distribution. The population of protons that is trapped in the sheet as it crosses $R = 5$ due to the strong 'guide field' remains trapped at $R = 10$ where $B_y(y)$ has doubled in strength. We do note that for the rest of the protons, which have not entered the current sheet, the energies remain approximately the same when stopped at $R = 10$. This can be understood as follows: the protons that do not enter the current sheet typically leave the simulation box parallel to the negative x-axis, so they do not cross contours of the electric potential, $V = V(y, z)$ in equation (4.25), after they have drifted around the null point and are in outflow.

4.3.3 Fan current sheet trajectories

The simulations considered thus far concern proton trajectories starting from the external region, at a distance $R = 1$ from the null point. In the following, protons are initially distributed within the fan current sheet close to the null, to investigate the reason why proton '2' (discussed above) was not ejected from the current sheet. The more general case, when the protons are within the current sheet but not close to the null point, is discussed afterwards.

Firstly, we place particles within the sheet so that they are initially unmagnetised by the $B_y(y)$ component of the background field. They are magnetised only by the strong $B_x(x, z)$. The protons are uniformly distributed in the area $|x| < 1$; $y = 0$; $|z| < z_\eta$ with initial thermal energy $T = 86$ eV. Figure 4.23 shows the position of 2 000 protons at $t = 2\,500\,T_{\omega,p}$ (a), and $t = 17\,500\,T_{\omega,p}$ (b), during this simulation for the parameters $\lambda = 0.75$, $B_s = \alpha = 5$, $\eta = 10^{-8}$. We increase the dimensional box length to $L_0 = 10^6$ m as velocities in the current sheet are typically fast, giving reasonable integration times. This makes our results more comparable to the approximate analytic solutions of Litvinenko (2006). Note that the dimensionless resistivity, η, decreases due to the increase in L_0, assuming other parameters are kept the same. We again artificially stop the particles as they cross the $R = 5$ spherical surface.

At $t = 2\,500\,T_{\omega p}$ most of the protons are strongly magnetised by the $B_x(x, z)$ magnetic field. Inside the current sheet, $|z| < z_\eta$, we can use equation (4.13) to get approximate expressions for the electric and magnetic fields,

$$\boldsymbol{E} \approx E_y \hat{\boldsymbol{y}} \approx \eta\, B_s/\bar{\eta}^{1/2} \hat{\boldsymbol{y}} \quad [v_0 B_0], \tag{4.30}$$

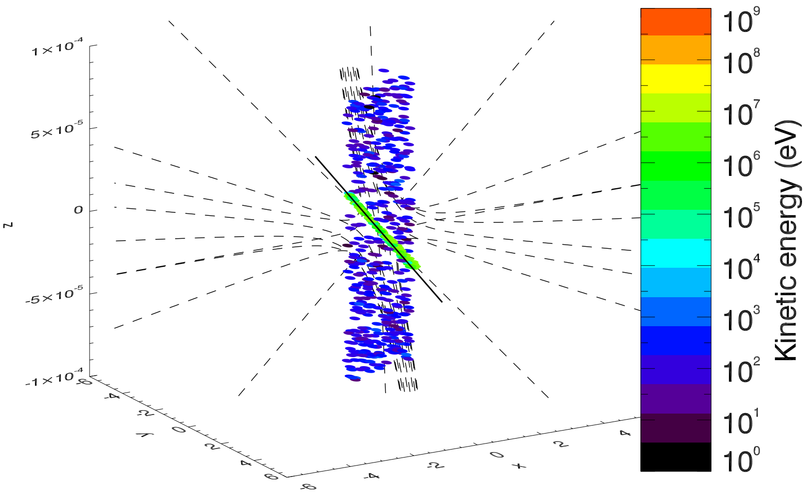

(a) $t = 2\,500$

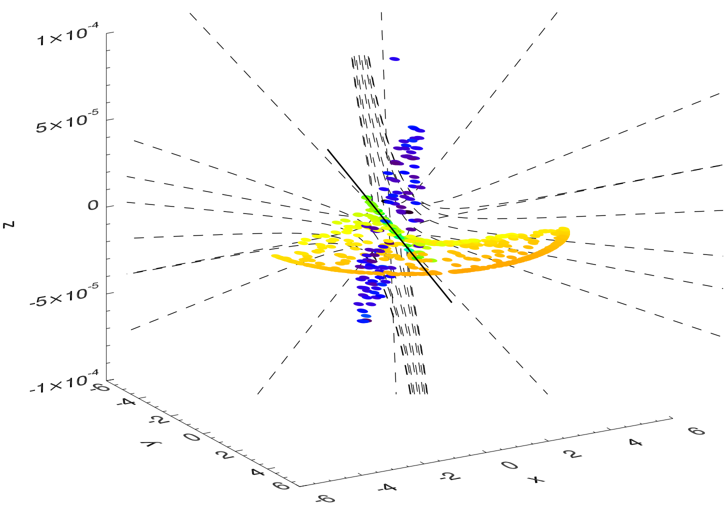

(b) $t = 17\,500$

Figure 4.23: Proton positions after initial distribution within the fan current sheet, such that $|x_0| < 1$, $|y_0| = 0$, $|z_0| < z_\eta = \sqrt{2\overline{\eta}}$. Parameters used are $\lambda = 0.75$, $B_s = \alpha = 5$, $\eta = 10^{-8}$, $L_0 = 10^6$ m. The dashed lines are representative magnetic field-lines inside the current sheet (note the difference in scale of the z-axis). The solid black line is the line $(x_1, 0, z_1)$ such that $B_x(x_1, 0, z_1) = 0$. The particles are stopped at $R = 5$ from the null point.

$$\boldsymbol{B} \approx \left(\frac{\lambda \alpha x}{2} + \frac{B_s z}{\bar{\eta}^{1/2}}, \frac{\lambda \alpha y}{2}, -\lambda \alpha z \right) \quad [B_0], \tag{4.31}$$

E_z is small except at global distance in y (see below).

For a proton starting at $x = 0$, $y = 0$, $z = z_\eta$, on the edge of the current sheet, the background components of the magnetic field are negligible. The proton drifts towards the vertical centre of the sheet $v_{Ez} \approx -(\eta/z)\,\hat{\boldsymbol{z}} \quad [v_0]$. It becomes unmagnetised at the fan plane, $z \approx 0$, very close to the null point and is directly accelerated in the y-direction. We compare this trajectory to the approximate analytical study of Litvinenko (2006), who considered the orbit stability and energy gain of particles in the fan current-sheet using the Taylor-expanded fields given in equations (4.30-4.31).

Litvinenko (2006) first noted that setting $\lambda = 0$ in equations (4.30-4.31) gives equivalent fields to the Speiser (1965) current-sheet with zero background field; equations (3.5-3.6) with $\epsilon_B = 0$. The result is the stable oscillations shown in Figure 3.1. For the case of $\lambda \neq 0$, Litvinenko (2006) gives an exact solution to the equations of motion (1.1-1.2), which is simply the direct electric field acceleration from the exact position of the null: $x = z = 0$ and $y = eEt^2/2m$. This is then perturbed in the x and z directions using the WKB method, which was first suggested by Bulanov & Cap (1988) as applicable to particle orbits close to null-points. An equation for the growth-rates of the small perturbation is obtained and, in the case of a real growth-rate, Litvinenko (2006) calculates the ejection time due to destabilisation by the background field.

The ejection time for a non-relativistic particle that is unmagnetised close the null point in the fan current sheet, $x \approx 0$, $z \approx 0$, for our parameters is

$$t_{ejec} \approx \left(\frac{m^2 B_s L_0}{q^2\, \bar{\eta}^{1/2}\, B_0 \lambda^2 \alpha^2 E_y} \right)^{1/3}, \tag{4.32}$$

(equation (21) in Litvinenko (2006)) provided that the particle remains within the non-adiabatic region and the displacement magnetic field gradient is much stronger than the gradient from the background component, $B_s/\bar{\eta}^{1/2} \gg \lambda\alpha$. The second assumption is valid for our simulation; however, we do not observe proton energy gain limited by ejection in these simulations. To understand this, we consider the distance travelled in the y-direction during this time,

$$y_{ejec} = y(t_{ejec}) \approx \frac{q E_y t_{ejec}^2}{2m}, \tag{4.33}$$

which we compare with size of the non-adiabatic region from the null in this direction. The particle begins to be re-magnetised by the background field at a global distance y^* such that

$$v(y^*)/y^* \approx \omega_{B_y(y^*)} \tag{4.34}$$

where $v(y)$ is a typical proton velocity and $\omega_{B_y(y)}$ is the gyro-frequency of a particle gyrating around $B_y(y)$. We use $v(y) = (2qE_y y/m)^{1/2}$ from direct acceleration (if we use $v(y) = E_y/B_y$ the value for y^* differs by $2^{1/3}$), assuming that there was no initial y-velocity and the particle entered the sheet at $y \approx 0$. We recover the result of Litvinenko (2006), that in dimensional form

$$y^* \approx \left(\frac{8mE_y}{q(B_0\lambda\alpha)^2 L_0}\right)^{1/3} L_0. \tag{4.35}$$

The ratio of these two distances is

$$y^*/y_{ejec} \approx \left(\frac{\lambda^2\alpha^2}{B_s^2/\bar{\eta}}\right)^{1/3}, \tag{4.36}$$

where we have ignored factors of order unity. The ratio of the two timescales is the square root of this. There is little gyro-turning for protons starting close to the null point as this ratio is necessarily small for the fan current sheet. The proton is magnetised by the $B_y(y)$ "guide field", that increases in magnitude as the particle travels in the y-direction, and is trapped in the sheet; the energy gain is only bounded by the length of the current sheet.

The approximate solutions of Litvinenko (2006) only hold for small perturbations around the exact solution $x = z = 0$, $y = y(t)$. Here, we extend this work by considering protons initially distributed within the fan-current sheet in the more general region of $y = 0$, $|z| < z_\eta$ and at a global distance in x. These protons are also shown in Figure 4.23. The protons drift vertically until they reach the diagonal line where $B_x(x, z) = 0$, that is $z = -\bar{\eta}^{1/2}\lambda\alpha x/(2B_s)$, at which they become unmagnetised and accelerated. We do appear to see some gyro-turning for protons starting at $|x| \approx 1$. This is probably due to the strong component of the Lorentz force, $v_y B_z$, that acts to turn the trajectory to the x-direction. For particles starting close to the null; $x \approx z \approx 0$, and so the background B_z component is approximately zero. However, for protons that are a global distance in x (e.g. $x \approx 1$) when they are unmagnetised at the $B_x(x,z) = 0$ line, they are below the fan plane (z is negative) and so B_z stays positive while the particles are accelerated in the y-direction. The proton is turned in the positive x-direction but is quickly magnetised by the guide field when it reaches a distance of about y^* (see equation 4.35). On the other hand, if the proton is close to $x = -1$ when it is unmagnetised, then it will be above the fan plane where B_z is negative, and be turned in the negative x-direction. In Figure 4.23 it can be seen that particles are accelerated radially outwards from the null. They continue to gain energy as they become magnetised about the background field $\boldsymbol{P}$, on a field-line with a parallel component of the electric field $E_\parallel = \boldsymbol{E} \cdot \boldsymbol{P}/|\boldsymbol{P}|$.

We artificially stop the protons at $R = 5\,L_0$ from the null point. At $t = 50\,000\,T_{\omega,p}$ all of the protons in the simulation have reached this distance without being ejected and we fit the energies of the particles by the expression

$$\begin{aligned} \epsilon_k(\phi) &\approx qE_\parallel(\phi)\,5L_0 \\ &\approx 5\,q\,\eta^{1/2}\,B_s^{3/2}\,(1-\lambda^2)^{1/2}\sin\phi \quad [v_0 B_0 L_0], \end{aligned} \tag{4.37}$$

using equation (4.30) and assuming the optimised solution $\alpha = B_s$, where ϕ is the azimuthal angle ($\phi = 90°$ is parallel to the current). Figure 4.24 shows the energies of 5 000 protons in three simulations with identical setup to Figure 4.23 but with different values of η and B_s. This expression (thin line) fits the energies of simulated particles (circles) as they cross $R = 5\,L_0$ very well.

In Figure 4.25 we place 1 000 protons in the fan current sheet with initial position in $|z| < z_\eta$, $-1 < x, y < 1$ so that a large number of protons are initially magnetised by the "guide field" $B_y(y)$. This is the more general case, as protons reaching the current sheet from the external region will not typically do so at $y \approx 0$, see Figure 4.20. The protons that do not start close to $y = 0$ are directly accelerated without the initial drift phase as they experience a parallel electric field. By $t = 19\,000\,T_{\omega,p}$ all of the protons have left the simulation box as shown in Figure 4.26; either through the $R = 5$ boundary, or through the edge of the current sheet $|z| = z_\eta$. The particles that cross $|z| = z_\eta$ in $y > 0$ start close to the edge and leave due to initial thermal velocity. However, those starting with $y < 0$ are ejected from well within the current sheet. These protons (19.7% of total number) are circled in Figure 4.25. Typically they remain magnetised, with $r_L/L_{\nabla B}$ in the range $10^{-4} - 10^{-2}$. They are not ejected due to gyro-turning in

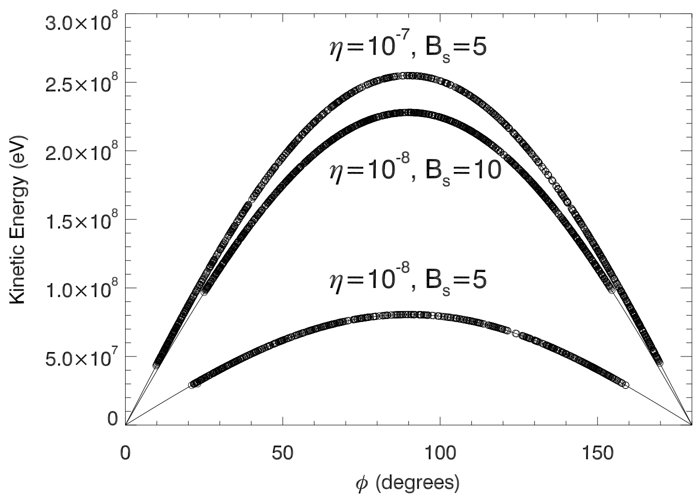

Figure 4.24: Energy distribution of particles as they cross the $R = 5$ boundary, where initial position is within $|x_0| < 1$, $|y_0| = 0$, $|z_0| < z_\eta = \sqrt{2\bar{\eta}}$. Here, $L_0 = 10^6$ m and the results for different values of η and B_s are plotted. The solid points are protons from the three simulations and the thin lines show the $\sin\phi$ relationship in equation (4.37).

the sense of Speiser (1965) as this requires non-adiabatic motion. As the protons are accelerated in the positive y-direction they follow the field-lines out of the current sheet in the $\pm z$ directions.

Note that although they seem to follow the field-lines closely in the y-z plane, there is an electric drift in the x-z plane due to the strong E_z component of the electric field. Within the current sheet, $|z| < z_\eta$ the truncated power series in equation (4.13) gives the z-component of the electric field from equation (4.23) as

$$E_z \approx \frac{B_s \alpha}{2\bar{\eta}^{1/2}}(1 - \lambda^2) y z, \tag{4.38}$$

which is stronger than the current electric field (4.30) for global y and $z \neq 0$. However, it only contributes to strong electric drift in negative x-direction for protons in the upper half of the sheet $0 < z < z_\eta$, and in the positive x-direction for $-z_\eta < z < 0$ (see the bottom panel in Figure 4.26).

The protons that are not ejected from the current sheet at $\pm z_\eta$, i.e. the ones that are stopped at $R = 5$, have an approximate sinusoidal dependence in kinetic energy gain, given by equation (4.37). However, there is a thicker spread of points about the predicted lines (not shown) than in Figure 4.24 due to differences in

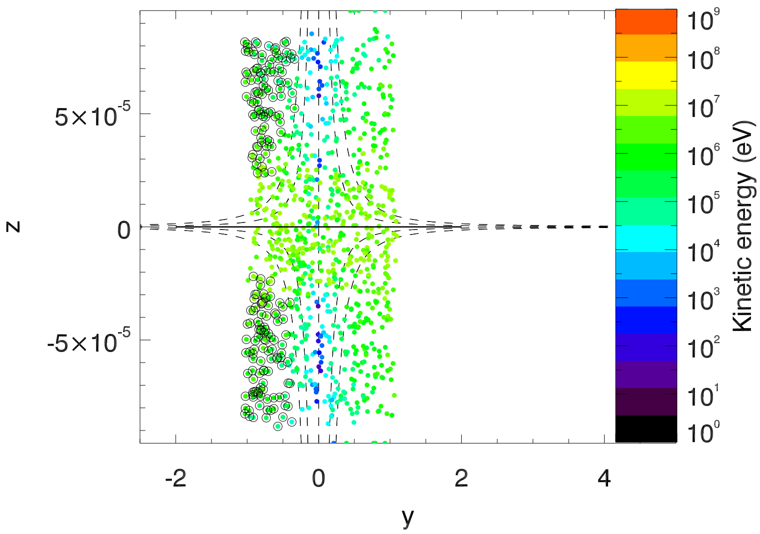

(a) $t = 1000$

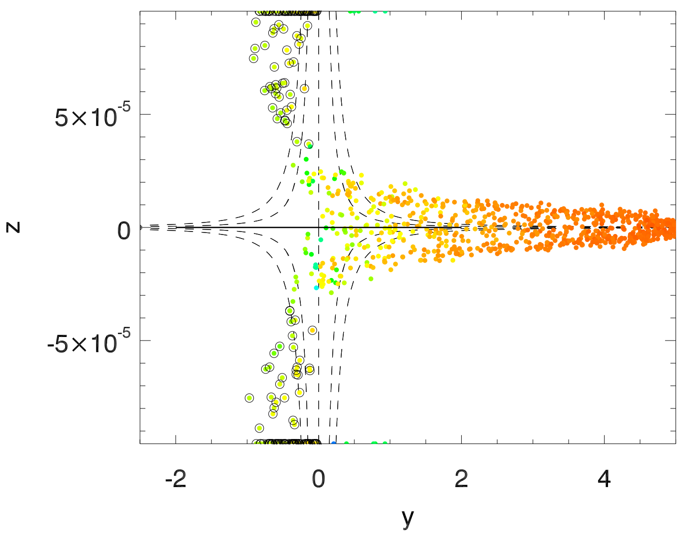

(b) $t = 8000$

Figure 4.25: Proton positions after initial distribution within the fan current sheet such that $|x_0|, |y_0| < 1$ and $|z_0| < z_\eta = \sqrt{2\bar{\eta}}$. Parameters used are $\lambda = 0.75$, $B_s = \alpha = 5$, $\eta = 10^{-8}$, $L_0 = 10^6$ m. Particles circled in black are those that start in $y < 0$ and cross $z = z_\eta \approx 9.6 \times 10^{-5}$ before $t = 19\,000\, T_{\omega,p}$.

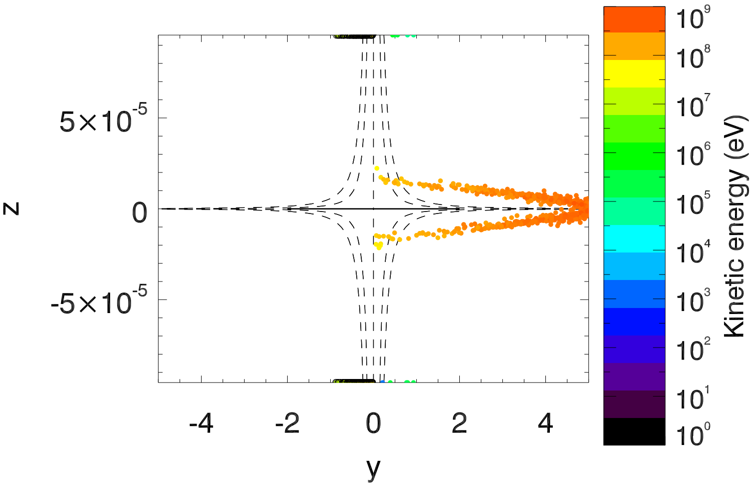

(a)

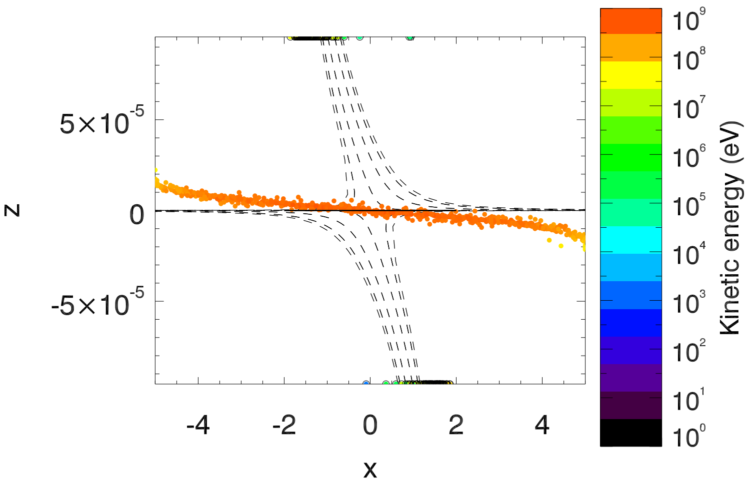

(b)

Figure 4.26: Proton positions at $t = 19\,000\,T_{\omega,p}$ for the simulation with initial distribution within the fan current sheet ($|x_0|, |y_0| < 1$ and $|z_0| < z_\eta = \sqrt{2\bar{\eta}}$). Parameters used are $\lambda = 0.75$, $B_s = \alpha = 5$, $\eta = 10^{-8}$, $L_0 = 10^6$ m. Particles circled in black at $\pm z_\eta \approx 9.6 \times 10^{-5}$ are those that start in $y < 0$ and cross z_η before this time, where they are stopped. a) In the y-z plane. b) In the x-z plane.

initial potential energy within the initial distribution (the potential energy within the current sheet is strongly dependent upon y-position).

4.3.4 Scalings

The global many-particle simulation in the fan model fields, shown in Figure 4.16, used the optimised ($\alpha = B_s$) parameters $\eta = 10^{-6}$, $B_s = 10$, $\alpha = 10$ and $\lambda = 0.75$. With consideration to the large variation in both scale and magnetic geometry, namely magnetic shear, in a given distribution of flares, it is important to see how these results scale when the simulation parameters are varied. This is particularly important for the normalised resistivity, η, because the effective (anomalous) value within the reconnection region is not well known. A value based on the classical Spitzer resistivity is in the region $10^{-12} - 10^{-14}$, but this may be enhanced by many orders of magnitude due to some turbulent process scattering electrons and increasing the effective electron collision rate.

It was found in the previous section that the parallel electric field within the fan current sheet was the most effective test-proton accelerator. Thus, it is interesting to study how varying the model parameters effects the fraction of protons entering the fan current sheet from the external region, and the average time taken to drift there from an initial position on the $R = 1$ sphere. These scalings are shown in Figure 4.27. They are from simulations of 5 000 protons at $T = 86\,\text{eV}$ starting at the upper inflow region at $R = 1$ (the initial conditions are the same as those for Figure 4.16, except for the values of B_s, η and λ). We define the current sheet as $z = z_\eta = \sqrt{2\overline{\eta}}$ for the fan model, although we note that not all of the protons reaching this height become non-adiabatic.

The average time taken for the particles to reach the current sheet gives a measure of the external electric drift speed. The approximate drift scaling of equation (4.28), $v_E \sim B_s^{3/4}\eta^{1/4}$, is in reasonable agreement with these drift times (time $\sim 1/v_E$).

The fraction of particles reaching the sheet typically increases with increasing η and decreasing B_s. Note that the size of the current sheet which we use to produce the scalings has the dependence $z_\eta \sim \eta^{1/2}B_s^{-1/2}(1-\lambda^2)^{-1/2}$, although this does not fully explain, for example, the apparent decrease at $B_s \approx 0.04$. Figure 4.28 shows how the energy spectra vary with these parameters. As might be expected the spectra shift to the right for an increase in both B_s and η. Both the convective electric field (and so external electric drift) and the direct electric

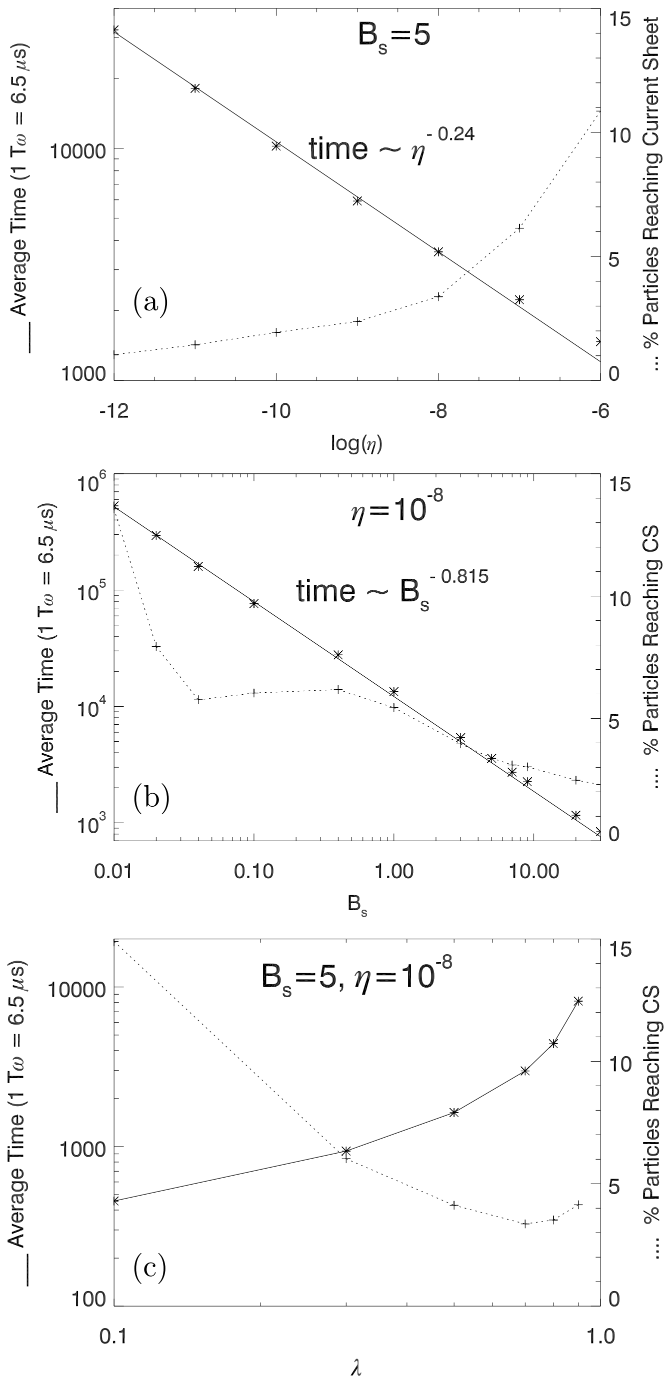

Figure 4.27: Percentage of total particles (+) reaching current sheet at $z = z_\eta$ from the external region ($R = 1$ in the inflow quadrant), and the mean time taken (*), for different values of η, B_s and λ. Each data point is from a many particle simulation with initial Maxwellian distribution ($T = 86$ eV) of 5 000 protons. The set-up is the same as that in Figure 4.16. a) Varying η with fixed $B_s = \alpha = 5$, $\lambda = 0.75$. The solid line is a Least Squares Fit (LSF) to the points. b) Varying B_s (with $B_s = \alpha$) with fixed $\eta = 10^{-8}$, $\lambda = 0.75$. The solid line is a LSF. c) Varying λ with fixed $B_s = \alpha = 5$, $\eta = 10^{-8}$ (no curve was fit).

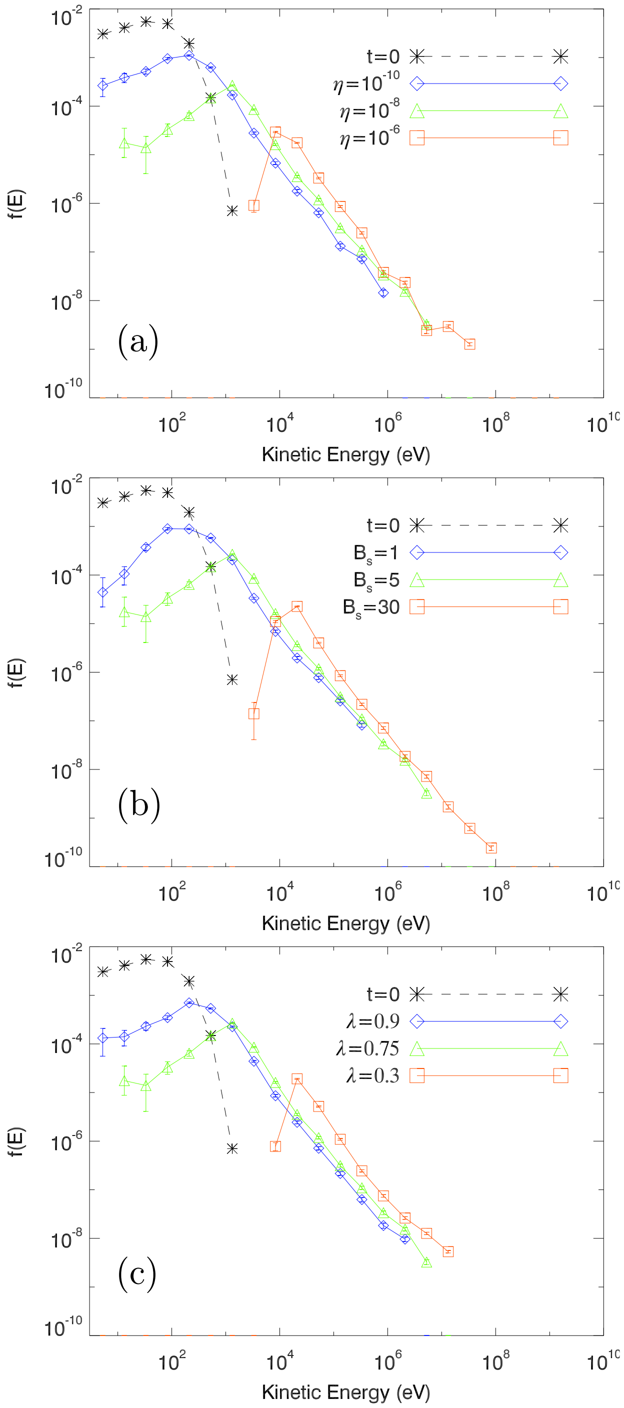

Figure 4.28: Steady-state energy spectra for global fan simulations. a) Varying η with fixed $B_s = \alpha = 5$, $\lambda = 0.75$. Steady-state was reached at $t = 8 \times 10^4$, $t = 2 \times 10^4$ and $t = 6.4 \times 10^3\, T_{\omega,p}$ for $\eta = 10^{-10}$, $\eta = 10^{-8}$ and $\eta = 10^{-6}$ respectively. b) Varying $B_s = \alpha$ with fixed $\eta = 10^{-8}$, $\lambda = 0.75$. Steady-state at $t = 2 \times 10^5$, $t = 2 \times 10^4$ and $t = 5 \times 10^3\, T_{\omega,p}$ for $B_s = 1$, $B_s = 5$ and $B_s = 30$ respectively. c) Varying λ with fixed $B_s = \alpha = 5$, $\eta = 10^{-8}$. Steady at $t = 10^5$, $t = 2 \times 10^4$ and $t = 8 \times 10^3\, T_{\omega,p}$ for $\lambda = 0.9$, $\lambda = 0.75$ and $\lambda = 0.3$ respectively.

field within the sheet increase with larger values of these parameters.

Up until now we have used $\lambda = 0.75$ as a constant in all of the simulations. This parameter has been typically left as constant in the calculation of MHD energy dissipation scalings (Craig et al. 1997; Craig & Watson 2000) for the fan model as it can only be varied within an order one range. However, it has a large effect on the efficiency of the fan model for particle acceleration (see Figure 4.27(c) and Figure 4.28(c)). Varying λ within $0 \leq \lambda < 1$ has a comparable effect on the fraction of particles reaching the current sheet as varying η by six orders of magnitude. Also, as shown in Figure 4.28, decreasing λ shifts the energy spectrum to higher energy and decreases the time taken to reach steady-state. These effects can be explained somewhat by an increase in external drift speed, although varying λ also has an effect on other quantities such as the current sheet height.

4.4 Electron acceleration

4.4.1 Global trajectories

Here we show the first results of this chapter using the guiding-centre switching code that was described in Chapter 3. The first many-particle simulation described is of 5000 electrons in the fan model fields (see Section 4.3.1) with $\eta = 10^{-6}$, $B_s = \alpha = 10$ and $\lambda = 0.75$. The particles are given initial energy from a Maxwellian distribution with temperature $T = 86$ eV, and uniformly distributed random pitch-angles and gyro-phase as before. However, unlike the proton simulations, the electrons are given the initial electric drift velocity corresponding to their initial position (this is done automatically with the guiding-centre formulation). We found that this extra initial drift velocity could lead to marginally different particle trajectories, as the particles drift onto a neighbouring guiding-centre; but for the many-particle simulations there was no observable difference in the final energy spectra. The times quoted in this section are in units of the electron gyro-time $T_{\omega,e} = 2\pi m_e / eB_0 = 3.572 \times 10^{-9}$ s.

Figures 4.29 (a) and (b) show the initial, $t = 0$, and final, $t = 3.68 \times 10^6\, T_{\omega,e}$ (when the energy spectrum is approximately steady), longitude and latitude from the null-point for these electrons. As before, they are coloured by final energy. It is immediately apparent that electrons starting in $\phi > 0$ ($y > 0$) gain much higher energies, in the range $\epsilon_k \sim 10^{4.5} - 10^7$, than those starting in $\phi < 0$ ($y < 0$). At the final time, 42.5% of electrons are found at low latitude ($\theta < 1°$) with high energy $\epsilon_k > 10^{4.5}$ eV and at longitudes $0° < \phi < 180°$. Unexpectedly, there are only three energetic electrons at the final time in the fan plane with longitude $\phi < 0°$ (these have energy $\epsilon_k > 10^7$ eV). It was expected that there would be more electrons in this population, as the electrons entering the current sheet would be accelerated in the negative y direction by the direct electric field (the opposite direction to the proton acceleration).

To see this more clearly, two-dimensional slices of the domain are shown in Figures 4.29 (c) and (d) at two times during the simulation. For $y < 0$ the electrons appear to be trapped in a region close to the spine, and they do not reach low latitudes, whereas for $y > 0$ they are accelerated at low latitudes until they exit the simulation box.

Figure 4.30 shows the time variation of various relevant quantities for a single electron trajectory in the population that starts in $\phi < 0°$ (the "trapped" population). To remove any possibility that this behaviour is due to the guiding-centre code, this calculation was performed with the full-orbit code for the whole trajectory. The electron follows a field-line towards the fan-plane (β is decreasing, and $v_{\|} > 0$ where the positive field is away from the null point along the fan plane; $\alpha > 0$ in equation (4.7)). However, the parallel velocity drops through zero, similar to what occurs in a mirror bounce. To explain this further, we plotted traces of the acceleration due to the mirror force, $-\mu_m \hat{\boldsymbol{b}} \cdot \boldsymbol{\nabla} B$ (green line, sixth panel), and the acceleration due to the parallel electric field, $q_e E_{\|}/m_e$ (green line, bottom panel). Surprisingly, as the electron is not within the current sheet, the parallel electric field acceleration is an order-of-magnitude larger than the mirror acceleration. The direct electric field gives the most significant contribution to the parallel acceleration of the electron, where the latter is also plotted in the bottom panel (black line) for comparison. The electric field is in the positive y-direction and is associated with the reversed current layers in the fan model, see Figure 4.15, combined with the large and spatially-uniform plasma resistivity. This parallel electric field prevents particles from reaching low latitudes for negative y, and accelerates them out of the domain for positive y; note that for the protons, this acceleration is a factor of m_p/m_e smaller and thus does not affect the parallel dynamics. For the remainder of this chapter, we will restrict the resistivity η to small values in the global simulations, such that this acceleration

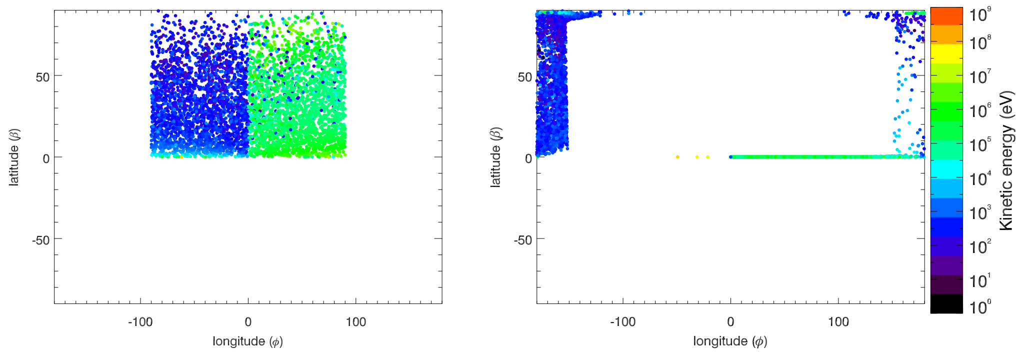

(a) $t = 0$ (b) $t = 3.68e6\,T_{\omega e}$

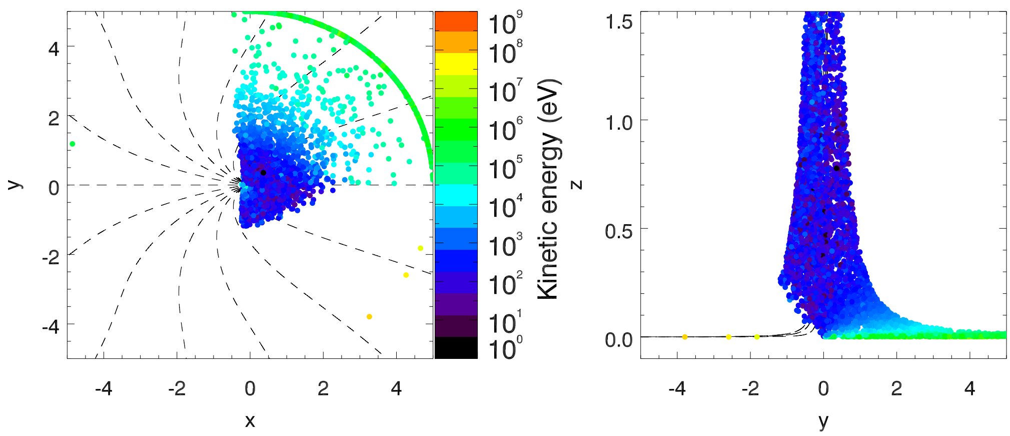

(c) $t = 4.6e5\,T_{\omega e}$

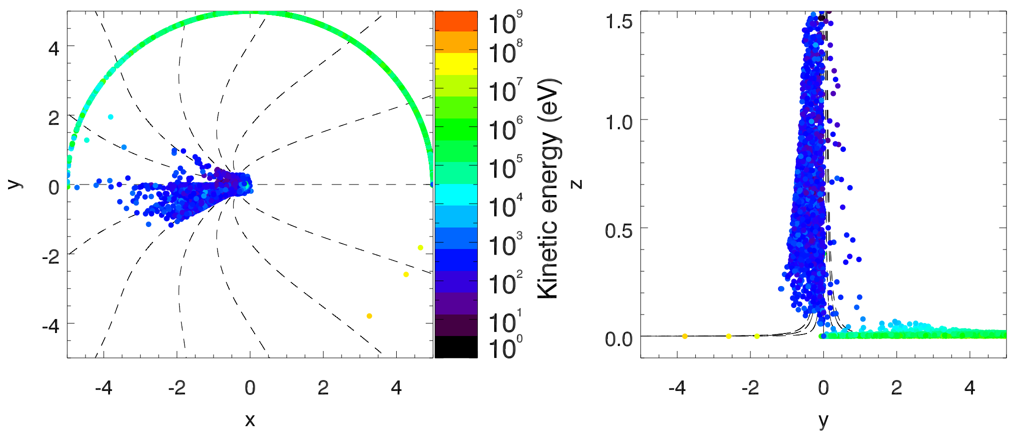

(d) $t = 3.68e6\,T_{\omega e}$

Figure 4.29: Electrons in the global many-particle fan simulation with $\lambda = 0.75$, $B_s = \alpha = 10$, $\eta = 10^{-6}$, $L_0 = 10^4$ m. a) and b) Longitude and latitude of electrons at the initial and final (approximately steady energy spectrum) snapshots. Electrons are coloured by the final energy gained (the energy at $t = 3.68e6\,T_{\omega e}$). c) and d) 2D slices in x-y and y-z planes for the same simulation. Electrons are coloured by their current energy at $t = 4.6e5\,T_{\omega e}$ and $t = 3.68e6\,T_{\omega e}$ respectively.

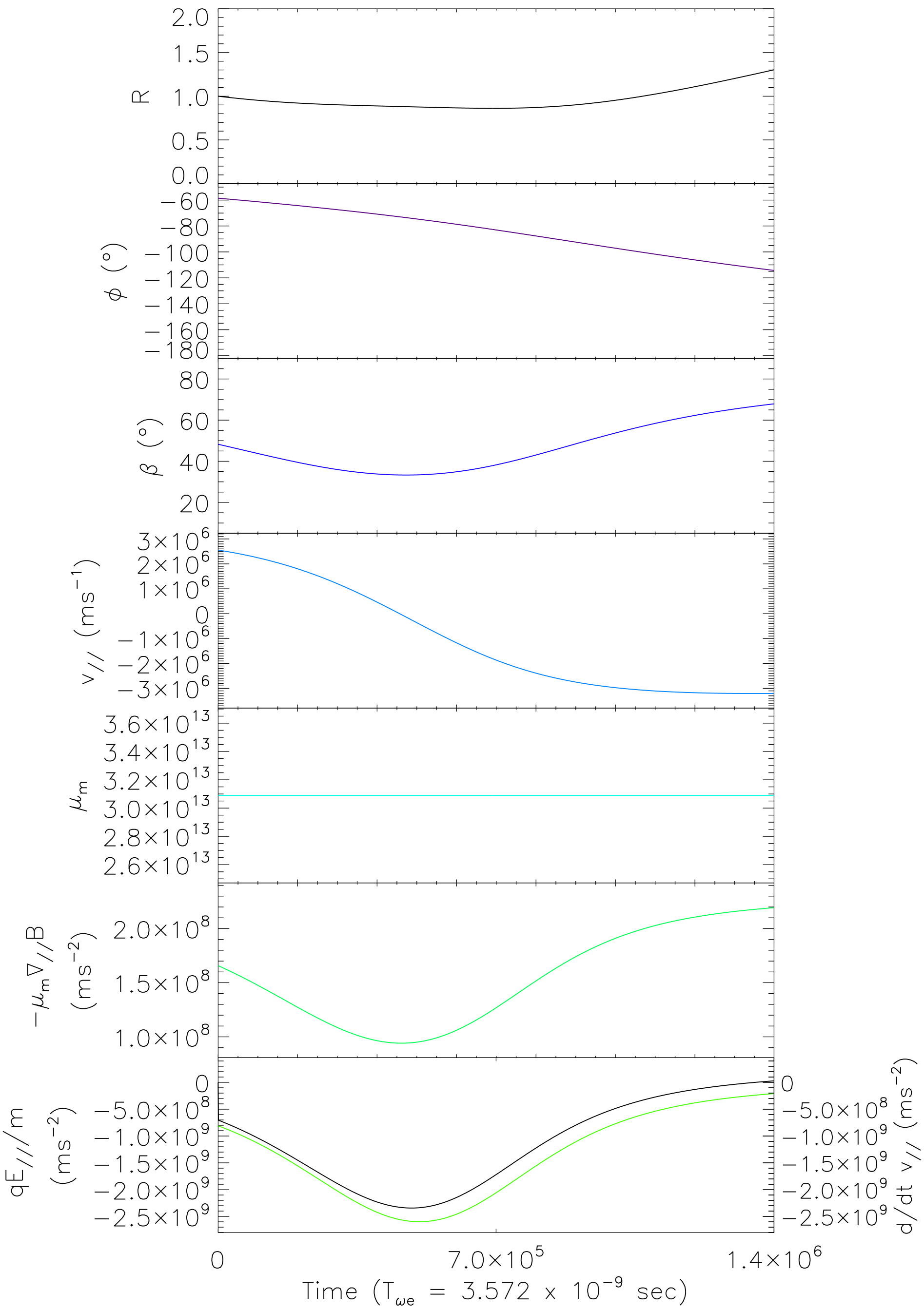

Figure 4.30: Parameter traces for an electron trajectory with initial longitude $\phi = -58.5°$ taken from the many particle simulation ($\lambda = 0.75$, $B_s = \alpha = 10$, $\eta = 10^{-6}$, $L_0 = 10^4$ m). The top three plots show the particle position (R, ϕ, β), the fourth shows the parallel velocity, $v_\parallel$, the fifth is the magnetic moment, μ_m in arbitrary units, the sixth is the acceleration due to the mirror force, and the seventh panel shows the acceleration due to parallel electric field (green) and the total parallel acceleration (the time derivative of panel 4) in black.

does not dominate the dynamics.

Figure 4.31 shows a many-particle electron simulation for parameters $\eta = 10^{-10}$, $\alpha = B_s = 5$, $\lambda = 0.75$ (thus the resistivity has been reduced by four orders-of-magnitude compared with the results above, this normalised resistivity is comparable to the Spitzer (1962) resistivity for the solar corona using our L_0, v_0 and T_0). There is now no obvious asymmetry in the final energy gain, between $\phi < 0°$ and $\phi > 0°$ in the initial conditions. The only structure in the final energy dependence of initial position, is that there are several high energy electrons at $\phi \approx 0°$ across all latitudes β (there are 32 electrons with $\epsilon_k > 5$ keV and $|\phi| < 10°$). At the final time, $t = 4 \times 10^8\, T_{\omega,e}$, the distribution is also quite symmetrical about $\phi = 0°$, compared with the proton many-particle distributions in Figure 4.16. However, we find that the angular distribution of protons with the same field parameters as this electron simulation is also much more symmetric than in Figure 4.16 (not shown), suggesting that the symmetry is a result of fewer particles reaching the current sheet. In Figure 4.31 there are 16 electrons that have left the simulation box at $z = 5$ with over 1 keV of energy (at longitude $\phi \approx 170°$). This is in contrast to the proton many-particle simulation where no protons left the simulation box along the spine axis. We checked several of these particles, finding that they enter the current sheet upstream of the null point (this is $y > 0$ for electrons, compared with $y < 0$ for protons, see Figure 4.25 and Section 4.4.2). They follow the field-lines out of the current sheet and out of the simulation box; they do not bounce at high latitude as they typically have small pitch angles.

In Figure 4.32, the trajectory of the electron with the highest energy from the many-particle simulation is plotted. Compared with the protons in Figure 4.17, the electron bounces many times before reaching the fan-plane. This is because the ratio between the electric drift and thermal velocity is much smaller, or in the terminology of Dalla & Browning (2005) they are in the weak-drift regime. As the electron reaches the fan current sheet, it starts to be accelerated in the positive y-direction by the electric field associated with the reversed currents; however, it quickly drifts into the current sheet (where $r_L/L_{\nabla B} > 1$ and the constancy of μ is violated) and is accelerated in the negative y-direction reaching an energy of 0.23 MeV without being ejected from the current sheet.

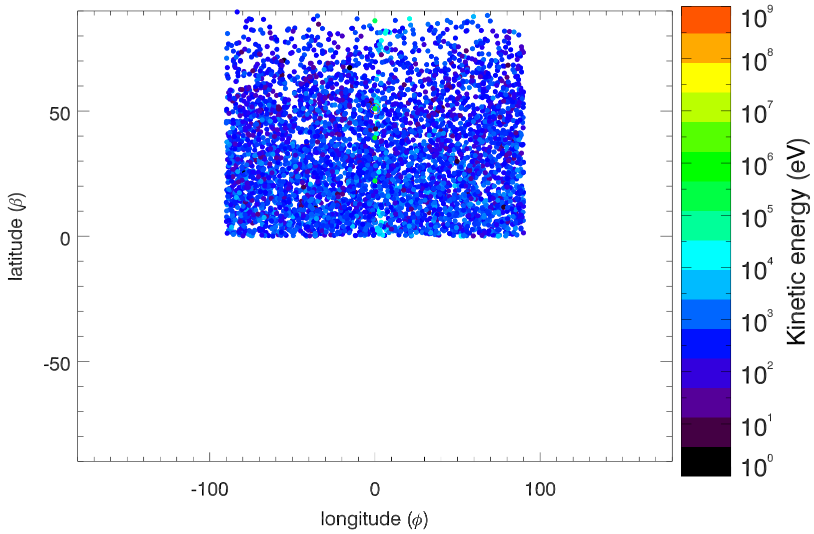

(a)

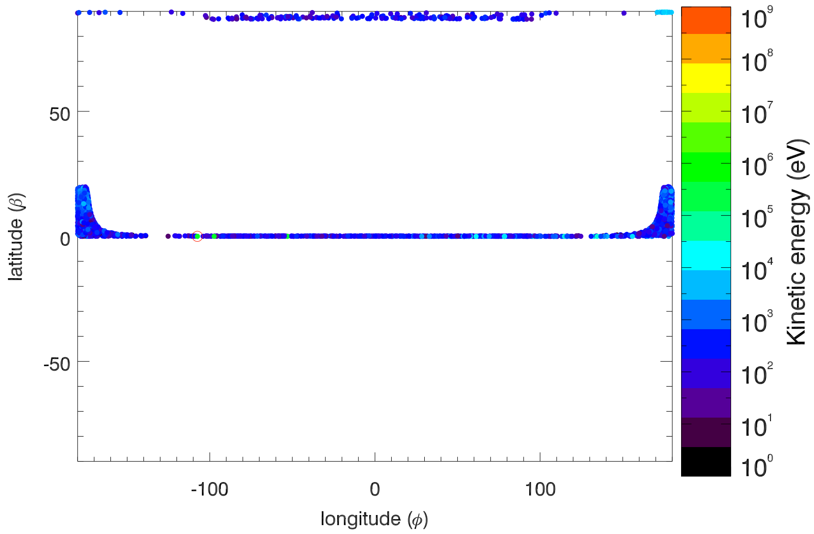

(b)

Figure 4.31: Many-electron simulation with $\eta = 10^{-10}$, $\alpha = B_s = 5$, $\lambda = 0.75$. The particle circled in red has the highest energy $\epsilon_k = 0.23$ MeV, and is shown in Figure 4.32.

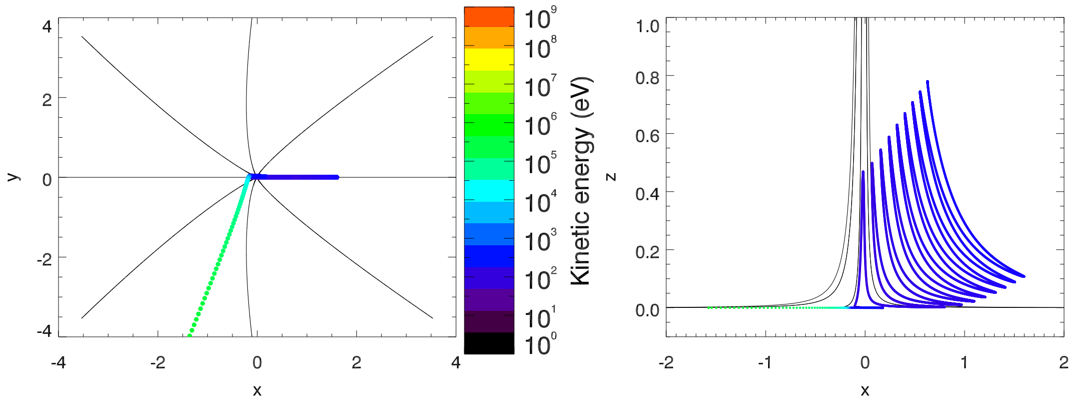

(a) (b)

Figure 4.32: Trajectory of the highest energy electron, that is circled in Figure 4.31.

4.4.2 Electrons within the current sheet

In Section 4.3.3 it was found that protons experience an increasing strength of the background magnetic field, $\boldsymbol{P}$, as they are accelerated away from the null-point, which acts to stabilise the orbits against gyro-ejection. We used the approximate analytical results of Litvinenko (2006) to argue that the distance the proton would travel on the ejection timescale, $y_{\rm eject} = y(t_{\rm eject})$ in equation (4.33), is much larger than the distance at which the proton becomes magnetised by the background field, y^* in equation (4.35). Crucially, the ratio between y^*/y_{eject}, given in equation (4.36), has no dependence upon the particle mass, so that we also expect electrons to be trapped within the current sheet.

Figure 4.33 shows the final snapshot of a simulation in which all the electrons are initially distributed in the region $|x| < 1$, $y = 0$, $|z| < z_\eta$, so that there is no component of the background field parallel to the electric field initially. This is an identical case to that shown in Figure 4.23 (a), but for electrons. It was performed with the full-orbit code, since $E_\|$ can be $\mathcal{O}(1)$ within the current sheet, violating the assumptions for the guiding-centre model (the simulation took approximately 1 month on 16 processors!). Similarly to the protons, the electrons drift down to the $B_x(x,z) = 0$ line, but they are accelerated in the opposite direction to the protons (the negative y direction). As expected, none of the electrons that are unmagnetised at the null point are ejected.

Figure 4.33 (b) shows that the analytical expression for the energy, given in

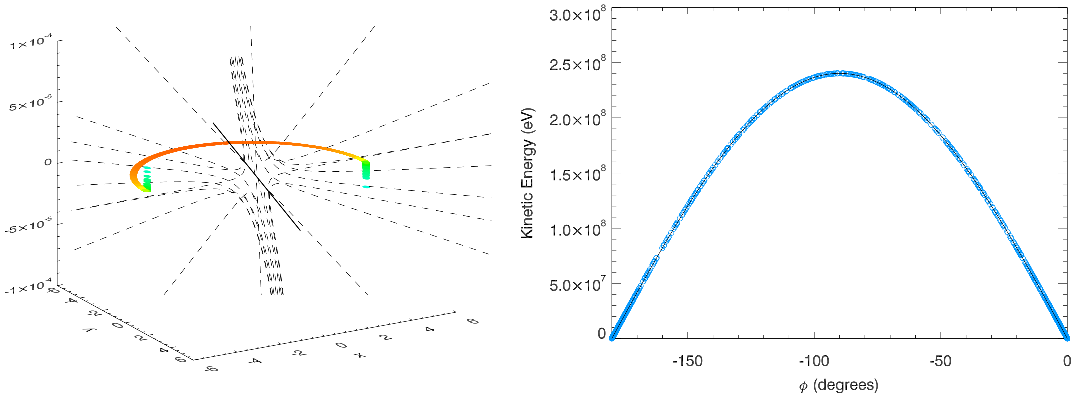

a) b)

Figure 4.33: a) Electron positions at $t = 6 \times 10^7\, T_{\omega,e}$ after initial distribution within the fan current sheet, with identical set-up and field parameters to equivalent proton simulation in Figure 4.23. b) Energy distribution of electrons (blue open circles) as they cross the $R = 5$ boundary for this simulation. The solid line shows the predicted energy from equation (4.37).

equation (4.37), also holds well for electrons. The only difference for electrons compared with protons (apart from being accelerated in the opposite direction) is that there are some electrons found very close to $\phi = -180°$ and $\phi = 0°$ compared with Figure 4.24. This is likely to be because electrons that start close to $x = \pm 1$ are more strongly magnetised by the B_x component of the field than protons.

The more general proton simulation, where the initial distribution is within $|x| < 1$, $|y| < 1$, $|z| < z_\eta$ was also run for electrons (not shown), with similar results to those shown in Figure 4.25. The main difference is that a higher percentage of electrons upstream of the null point, $y > 0$, are ejected (47% of electrons, compared with 19.7% of protons) as they follow the “diverging” fieldlines. This is also likely to be due to the stronger magnetisation of electrons; as $y^* \propto m^{1/3}$, there is a greater proportion of electrons that are magnetised initially.

4.5 Observational predictions

Both the test-particle approach and the analytic model-fields used have a number of limitations, and it is not clear whether the results presented so far will carry over to the solar corona, or even to self-consistent Particle-In-Cell (PIC) simulations. However, it is still useful to make some observational predictions from these models, that can be used for comparison with both future PIC simulations and observational Hard X-Ray (HXR) emission source data. This latter validation is increasingly important with advances in magnetic reconstruction techniques (see e.g. Wiegelmann & Sakurai 2012, for a review), which allow the spatial locations of HXR sources to be placed in context with the magnetic geometry of an Active Region (see Chapter 2 for some examples of this). Here we will briefly compare the spatial positions of high energy protons and electrons as they leave the simulation box at $R = 5$ (which we take as a proxy for leaving the acceleration site). It is interesting to see if there are differences between species, as recent RHESSI data suggests different acceleration mechanisms for protons and electrons (see Hurford et al. 2003, and Chapter 2).

We ran three simulations with normalised resistivity $\eta = 10^{-10}$ (this is the actual normalised Spitzer (1962) value for a coronal plasma of temperature $T_e \sim 10^6$ K, length-scale $L = 10^4$ m, and Alfvén velocity $v_A = 6.5 \times 10^6$ m s^{-1}), $B_s = \alpha = 5$, and varying the shear parameter λ such that $\lambda = 0.75$, 0.5 and 0.25. Until now, we have only considered particles starting in the inflow quadrant $-90° < \phi < 90°$, $\beta > 0°$. However, in these simulations we also include the inflow quadrant below the fan plane, so that there is no preferred direction imposed by choosing only one inflow region. We put 5000 protons and 5000 electrons within $-90° < \phi < 90°$ for $\beta > 0°$, and also $90° < \phi < 270°$ for $\beta < 0°$, at $R = 1$ from the null in the fan model fields. All particles are from a Maxwellian energy distribution of temperature $T_p = T_e = 86$ eV and uniform random pitch-angles and gyro-phase. They are initially given the local electric drift velocity.

Figure 4.34 shows the spatial positions of high-energy protons (> 1 MeV, orange) and electrons (> 10 keV, blue) with respect to the spine axis and fan surface for the simulations with $\lambda = 0.5$ and $\lambda = 0.25$ (for the simulation with $\lambda = 0.75$ there were only 0.2% of total electrons and 0.08% of total protons in these energy ranges, and so this case is not analysed further). For electrons, this energy cut-off corresponds to the minimum energy typically shown in HXR spectra, such as in Figure 2.4, and the value for protons is close to the 2.2 MeV neutron capture line, which was used for the γ-ray image of a solar flare in Hurford et al. (2003). The energy spectrum for each simulation is approximately steady-state at the time shown. The first thing to notice is that almost all of the high-energy particles exit the simulation box in the fan plane (although 3 high-energy electrons exit up the spine axis for the case of $\lambda = 0.5$; these enter the current

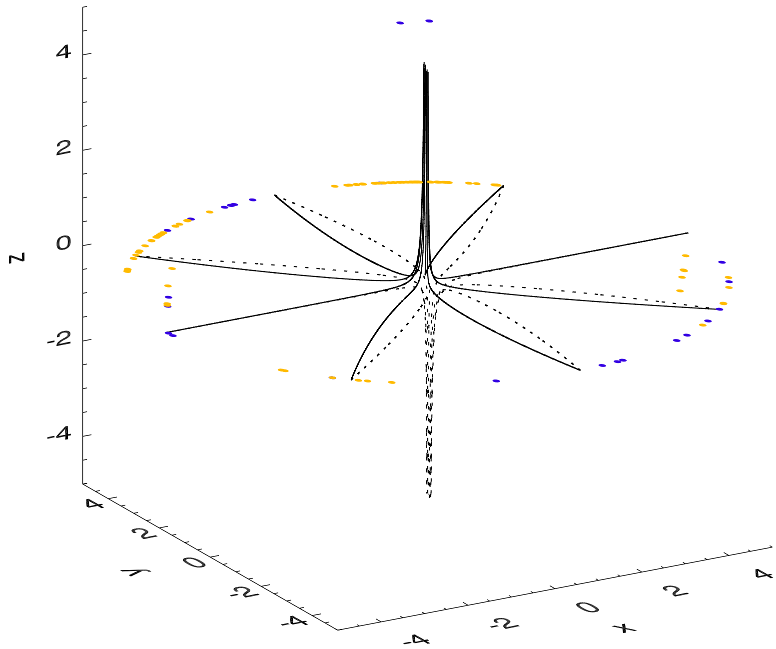

(a)

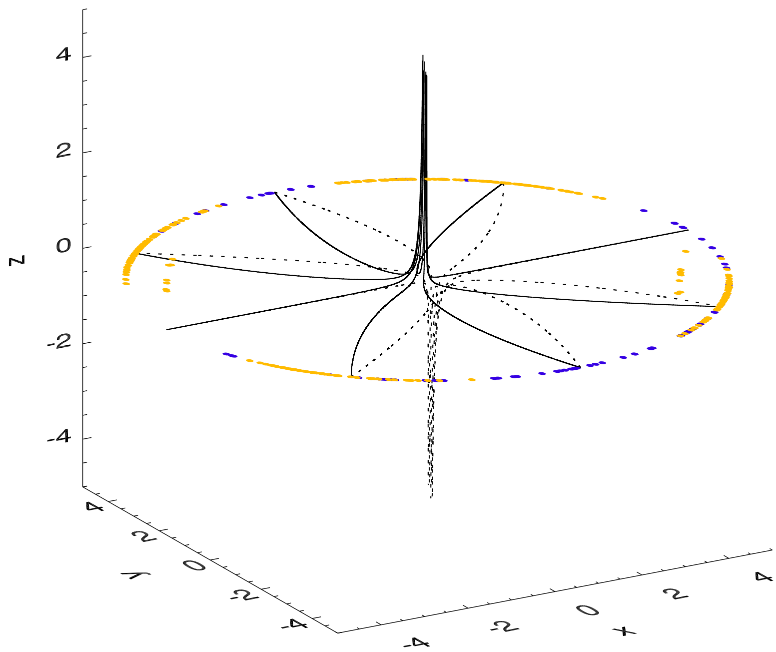

(b)

Figure 4.34: Spatial positions of high energy protons (> 1 MeV, orange) and electrons (> 10 keV, blue) for test-particle simulations in the fan model fields, with $B_s = \alpha = 5$, $\eta = 10^{-10}$. a) For $\lambda = 0.5$, the snapshot is at $t = 0.4$ sec (upper panel). b) For $\lambda = 0.25$, the snapshot is at $t = 0.2$ sec (lower panel). The field-lines are seeded from the fan-plane at $R = 5$ for both simulations.

sheet upstream of the null and are ejected on the “diverging” field-lines).

The effect of changing the value of λ on the magnetic field can be seen in the field lines plotted; for $\lambda = 0.25$ the spine-axis is sheared further in the x-direction, causing the field-lines within the fan plane to bend more. For the weaker shear ($\lambda = 0.5$), 1.6% of protons have final energy above 1 MeV, of which 90% of are found in the direction of the fan current (positive y-direction). However, only 2.5% of these are within the current sheet $z < z_\eta$. For stronger shear ($\lambda = 0.25$), there are 5.5% of protons with high energy, but only 60% of these high-energy protons are in $y > 0$, and 2% are within the current sheet. We followed the trajectories of these protons, finding that they were similar to proton ‘1’ shown in Figure 4.17 (although the protons exiting in $x > 0$ started from the inflow quadrant beneath the fan plane).

Only a small percentage of electrons achieve energies above 10 keV (0.7% for $\lambda = 0.5$; 1.9% for $\lambda = 0.25$), but more of these are in the current sheet (30% for $\lambda = 0.5$; 56% for $\lambda = 0.25$). The electrons in $y < 0$ (in the direction of the direct electric field at $z = 0$) typically have higher energy than those in $y > 0$ (in the direction of the parallel electric field caused by the reversed currents, see above).

Finally, Figure 4.35 shows the energy spectra for these two simulations. In both simulations ($\lambda = 0.5$ and $\lambda = 0.25$), the proton energy spectra reach a steady-state faster than the electron (note that at the later time shown, the electron energy spectrum is approximately steady). A power-law is fit to part of the final proton spectra for both $\lambda = 0.5$ and $\lambda = 0.25$. This has comparable spectral index $\gamma \approx 1.4$, where $f(E) = E^{-\gamma}$, for both simulations. However, there are fewer protons with energies $< 10^3$ eV for the case with greater shear.

4.6 Summary

In this chapter, we investigated test-particle motion in electromagnetic fields that are exact solutions (Craig & Fabling 1996; Craig et al. 1997) to the steady and incompressible MHD equations at a reconnecting 3D magnetic null point. We considered two reconnection solutions; in the first the fan-plane is sheared, which induces current and leads to reconnection in the spine-axis (called *spine-reconnection*), and in the second the spine-axis is sheared leading to current and reconnection in the fan-plane (*fan-reconnection*). These test-particle simulations were an extension of previous work by Dalla & Browning (2005, 2006, 2008)

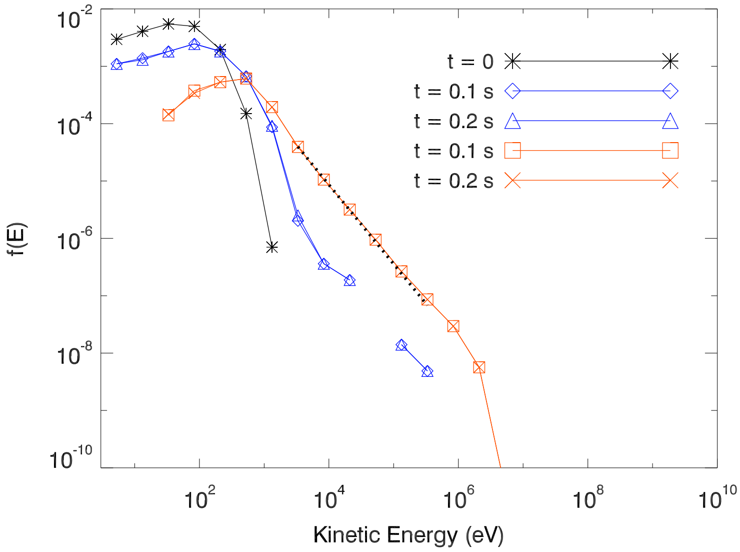

(a) $\lambda = 0.5$, $B_s = \alpha = 5$, $\eta = 10^{-10}$.

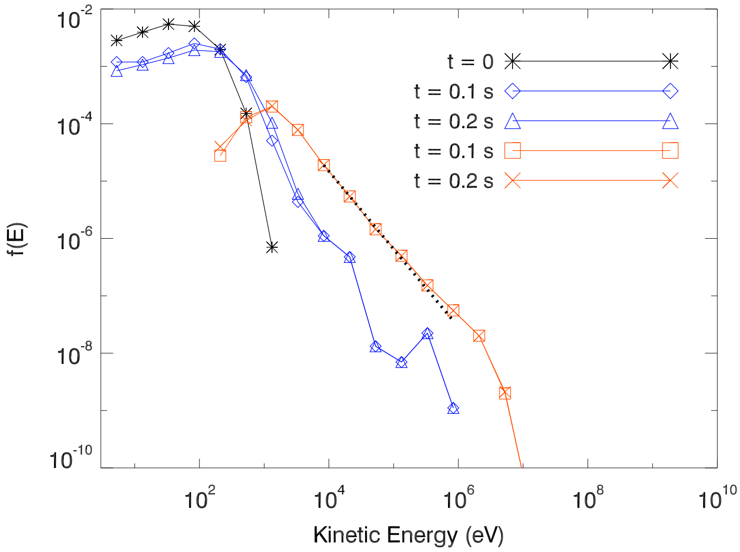

(b) $\lambda = 0.25$,$B_s = \alpha = 5$, $\eta = 10^{-10}$.

Figure 4.35: Comparison of energy spectra for protons (orange) and electrons (blue) in the fan model fields. The dotted lines show a power-law fit $f(E) \propto E^{-\gamma}$ used to calculate the spectral index. These are $\gamma = 1.38$ and $\gamma = 1.36$ for the simulations with $\lambda = 0.5$ and $\lambda = 0.25$, respectively.

and Browning et al. (2010), who considered test-particles in ideal model fields, without the resistive current sheets.

In all simulations, particles were initiated with thermal energy from a Maxwellian distribution with temperature $T = 86$ eV, and with uniformly distributed random pitch-angles and gyro-phase. Trajectories were then integrated with the full-orbit code for protons, and the guiding-centre switching code was used for a number of electron simulations.

For protons within the spine-model fields, starting at a global distance from the null-point, two energetic populations were identified: a population that becomes unmagnetised and is accelerated within the spine current layer, and a population that leaves the simulation box along the spine-axis. An energy spectrum was computed, see Figure 4.12, and the high-energy tail was shown to be associated with the first population. However, this energy gain was limited to the potential energy difference across the spine-axis current-layer, which is small due to the localisation of the resistive region. The external electric drift was also weak ($v_E(r \gg r_\eta) \sim \eta$) for the spine-model, so that protons have very long drift times before reaching the spine-axis (they are in the weak-drift regime, in the terminology of Dalla & Browning (2005)).

For the fan model, it was found that the external electric drift was faster ($v_E(z \gg z_\eta) \sim \eta^{1/4}$) than the comparable spine-model. Protons can gain high energy either by drifting directly into the fan resistive region, where they are accelerated by the electric field associated with the fan current sheet, or by strong and non-uniform electric drifts close to the fan plane (while remaining outside the resistive region). The energy spectrum for the proton simulation with parameters $\eta = 10^{-6}$, $B_s = \alpha = 10$ and $\lambda = 0.75$ has a power-law component at intermediate energies (with index ≈ -1.5 between 10^5 eV and $10^{7.5}$ eV), associated with the strong and non-uniform drift acceleration mechanism, and has a flat-tail, or bump-on-tail (depending on whether the protons are artificially stopped at $R = 5$ or $R = 10\, L_0$), distribution at high energies, associated with the population within the current sheet. We further studied this latter population, with simulations of protons distributed inside the fan resistive region.

In Section 4.3.3, we presented the results of two proton simulations that focused on the fan current sheet; one where the protons were initially distributed on $y \approx 0$, so that they have no component of the magnetic field parallel to the electric field initially, and one simulation where the protons are distributed globally in y (the more general case) so that they experience a direct electric field at $t = 0$. In the first, we found that protons unmagnetised very close to the null point undergo Speiser-like (Speiser 1965) oscillations before becoming magnetised by the background field, which acts to stabilise the proton orbits within the sheet. We extended the analytical results of Litvinenko (2006) to argue that protons will typically be magnetised before they can be ejected. Thus, the energy gain of these particles is only limited by the length of the current sheet. For the more general simulation ($y \neq 0$), we find an interesting result: that protons downstream of the null are trapped, but those upstream are ejected (while remaining magnetised). It would be interesting to study whether this also occurs in self-consistent Particle-In-Cell simulations.

Using the new guiding-centre switching code, we found that electrons were very sensitive to small parallel electric fields inside the external drift region for large values of the resistivity, η. These electric fields were associated with reverse current layers caused by the flux pile-up of the magnetic field in the fan model, and may be a generic effect in other flux pile-up reconnection models (see Section 5.3.1 for another example). However, in reality it seems unlikely that such a large scale parallel electric field could be maintained to global distances in the external region, so we did not analyse this simulation further. When the resistivity was reduced, the electrons are within the weak-drift regime, and only a small number enter the current sheet where they gain high energy. It was found that results for protons in the fan current-sheet carry across, in general, to the electrons: they are trapped downstream of the null, and ejected when they approach the null from the upstream region.

Finally, we compared the spatial positions and energy spectra of protons and electrons in global simulations with the fan-model fields. We compared the spatial distribution of energetic electrons ($\epsilon_k > 10$ keV) and protons ($\epsilon_k > 1$ MeV) for coronal parameters $\eta = 10^{-10}$ (calculated from the smaller equilibrium length $L_0 = 10^4$ m), a flux pile-up field of $\alpha = B_s = 5B_0 \equiv 0.05$ T, and various values of λ (which determines the shear between the velocity and magnetic fields). It was found that the high-energy protons are typically accelerated due to the fast non-uniform drifts, with few reaching the current sheet, and they exit the simulation box in four azimuthal locations within the fan-plane. In comparison, high-energy electrons were found to be directly accelerated by parallel electric fields associated with either the reversed current layers (due to the flux pile-up), or in the main current sheet (at $z \approx 0$). In Chapter 6.1 we discuss these results in context with the observational signatures from solar flares.

Chapter 5

Simulations of Merging Start-up

In this chapter we present the results from two-dimensional fluid simulations of the merging-compression start-up process in the Mega-Ampere Spherical Tokamak (MAST), see Chapter 2 for an introduction and a summary of the experimental data. This chapter has been adapted from Stanier et al. (2013a) and Stanier et al. (2013b). Before giving the results of the simulations, we will describe the fluid models used, and how the initial conditions are set-up.

5.1 Fluid model

To estimate the relative importance of different physical processes, we calculate dimensionless plasma parameters using typical pre-merging values for the temperature $T_0 = T_{e0} = T_{i0} = 1.2 \times 10^5$ K ($= 10$ eV), density $n_0 = 5 \times 10^{18}$ m^{-3}, magnetic field based on a typical toroidal field $B_0 = B_{T0} = 0.5$ T, and poloidal field of $B_{p0} = 0.1$ T. We take the typical length scale $L_0 = 1$ m, the order of the major and minor radii. With these values the toroidal Alfvén speed is $v_0 = 3.5 \times 10^6$ m s^{-1} and the time taken for an Alfvénic perturbation to cross L_0 is the characteristic Alfvén time $\tau_0 = L_0/v_0 = 0.29$ μs. Table 5.1 shows characteristic plasma parameters at merging-compression start-up. All of these parameters are written in normalised form, and their relation to dimensional parameters is given in the right-hand column.

The validity of fluid descriptions, such as those described in Chapter 1, usually requires that the distribution of particles is close to Maxwellian. This can be true if the time between collisions is small compared with typical fluid timescales within the system, as a distribution function will tend to Maxwellian after many

Quantity	Value	Definition
η	10^{-5}	$\eta_{Sp,\parallel}/(\mu_0 v_0 L_0)$
β_{T0}	8×10^{-5}	$2\mu_0 n_0 k_B T_0/B_{T0}^2$
β_{p0}	2×10^{-3}	$2\mu_0 n_0 k_B T_0/B_{p0}^2$
d_i	0.145	$c(n_0 e^2/\epsilon_0 m_i)^{-1/2} L_0^{-1}$
d_e	2.4×10^{-3}	$c(n_0 e^2/\epsilon_0 m_e)^{-1/2} L_0^{-1}$
ρ_i, $\rho_{is,0}$	9.3×10^{-4}	$\sqrt{m_i k_B T_0}/(eB_0 L_0)$
ρ_e	1.5×10^{-5}	$\sqrt{m_e k_B T_0}/(eB_0 L_0)$
μ	10^{-3}	$\mu_i^{\parallel}/(m_i n_0 v_0 L_0) = 1/Re$
$\kappa_\parallel$	10^{-1}	$\kappa_e^{\parallel}/(L_0 v_0 n_0)$
$\kappa_\perp$	10^{-7}	$\kappa_i^{\perp}/(L_0 v_0 n_0)$

Table 5.1: Characteristic plasma parameters calculated from n_0, T_0, L_0, B_{T0}, B_{p0}. These are the normalised resistivity η, the plasma beta calculated with the toroidal and poloidal fields β_{T0} and β_{p0}, the ion and electron skin-depths d_i and d_e, the ion and electron Larmor radii ρ_i and ρ_e, the ion-sound radius ρ_{is}, the normalised ion viscosity μ, and the normalised parallel and perpendicular heat conductivities $\kappa_\parallel$ and $\kappa_\perp$.

collisions. The τ_0 that is defined above is such a fluid timescale. However, this time is the time taken for compressional Alfvén waves to cross the minor radius, and it is faster than timescales of interest for merging-compression. For merging-compression we are interested in the longer timescale of flux-rope attraction due to parallel currents. This is related to the poloidal Alfvén time, $\tau_{A,p0} = (B_0/B_{p0})\tau_0 \approx 1.5 \times 10^{-6}$ s. This time can be compared with electron and ion collision times calculated from n_0 and T_0, which are $\tau_{e,0} \approx 10^{-7}$ s (see equation (1.21)) and $\tau_{i,0} = (m_i/m_e)^{1/2}(T_i/T_e)^{3/2}\,\tau_{e,0} \approx 7 \times 10^{-6}$ s respectively. The electrons are collisional at this temperature and strongly magnetised ($\Omega_{ce,0}\tau_{e,0} \sim 10^4 \gg 1$ where $\Omega_{ce,0}$ is the initial electron gyro-frequency), so we model them with fluid equations. The ions are also strongly magnetised ($\Omega_{ci,0}\tau_{i,0} \sim 10^2$) but only semi-collisional. In this thesis we will treat the ions as fully collisional, and leave the study of non-fluid effects and departures from classical transport for future work. It is worth noting that single-fluid (MHD) formulations are often used to model tokamaks at flat-top temperatures and densities ($T \sim 1$ keV and $n \sim 10^{19}\,\mathrm{m}^{-3}$ in a MAST flat-top), where the collision times can be orders of magnitude larger ($\tau_{i,e} \sim T_{i,e}^{3/2}/n$).

As discussed in Chapter 1, terms that introduce two-fluid effects (and finite-Larmor radius (FLR) effects from the pressure tensors) may become important when the current sheet width drops below the characteristic spatial scale for that term. Table 5.1 gives these spatial scales in normalised form. The current sheet width is not measured directly in experiment, because there are no magnetic probes inside the MAST plasma. However, a naive *a priori* estimate of this width can be made by assuming a Sweet-Parker scaling $\delta \approx S^{-1/2}\Delta$, see equation (1.45), where S is the Lundquist number (1.46) defined in terms of the current-sheet length Δ. Further assuming a current sheet length that is the same as the flux-rope widths in the fast-camera images (see Chapter 2) $\Delta \approx 0.5$ m, and assuming an outflow speed equal to the typical poloidal Alfvén speed, $v_{OUT} = v_{A,IN} = B_{p0}v_0/B_{T0}$, gives Lundquist number $S = v_{A,IN}\Delta\,(\eta L_0 v_0)^{-1} \approx 10^4$ and a current sheet width of $\delta \approx 5 \times 10^{-3}$ m. This is much smaller than the ion-skin depth, $d_i L_0 = 14.5$ cm, suggesting that decoupling of ion and electron flows due to ion inertia may become significant. The ion Larmor radius, ρ_i, and electron skin depth, d_e, are smaller than this estimate for δ, although they may become important if there are increases in temperature and decreases in density respectively. We leave the investigation of ion-FLR effects and electron inertia for a future study. However, we do include the effects due to finite ion-sound radius, $\rho_{is} = \sqrt{T_e/m_i}/\Omega_{ci} = \rho_{is,0}\sqrt{T_e/T_0}B_0/B$. As discussed in Chapter 1, some previous studies have shown this scale to be important in strong guide-field reconnection (Kleva et al. 1995; Simakov et al. 2010; Schmidt et al. 2009). These studies often use a reduced model, based partly on the assumptions of large-aspect ratio and uniform electron temperature. However, the MAST vessel is tight-aspect ratio and a large change in electron temperature is measured with the Thomson scattering diagnostic during the merging. We will use a fully compressible Hall-MHD fluid model in this thesis, that includes the scalar electron pressure term within Ohm's law.

For completeness, we give the governing equations here for the simulations which use a one-pressure formulation (the two-pressure formulation is discussed at the end of this chapter). These equations are the normalised Hall-MHD equations given by

$$\partial_t n + \boldsymbol{\nabla} \cdot (n\boldsymbol{v}_i) = 0, \tag{5.1}$$

$$\partial_t (n\boldsymbol{v}_i) + \boldsymbol{\nabla} \cdot (n\boldsymbol{v}_i\boldsymbol{v}_i + p\mathbb{I} + \boldsymbol{\pi}_i) = \boldsymbol{j} \times \boldsymbol{B}, \tag{5.2}$$

$$\boldsymbol{E} = -\boldsymbol{v}_e \times \boldsymbol{B} - \frac{d_i}{n}\boldsymbol{\nabla} p_e + \eta \boldsymbol{j} - \eta_H \nabla^2 \boldsymbol{j}, \tag{5.3}$$

$$\partial_t \boldsymbol{B} = -\boldsymbol{\nabla} \times \boldsymbol{E}, \tag{5.4}$$

$$\begin{aligned}(\gamma - 1)^{-1}[\partial_t p + \boldsymbol{v}_i \cdot \boldsymbol{\nabla} p + \gamma p \boldsymbol{\nabla} \cdot \boldsymbol{v}_i] \quad &= \eta j^2 + \eta_H (\boldsymbol{\nabla} \boldsymbol{j})^2 \\ &-\boldsymbol{\pi}_i : \boldsymbol{\nabla} \boldsymbol{v}_i - \boldsymbol{\nabla} \cdot \boldsymbol{q}.\end{aligned} \tag{5.5}$$

Here, n is the plasma density, $\boldsymbol{v}_i$ the ion (centre of mass) velocity, $\boldsymbol{v}_e = \boldsymbol{v}_i - d_i\boldsymbol{j}/n$ is the electron velocity where d_i is the normalised ion skin-depth (Table 5.1), $\boldsymbol{B}$ the magnetic field, $p = p_i + p_e$ the total (sum of ion and electron) thermal pressures where we assume $p_i = p_e = p/2$, $\mathbb{I}$ is the unit tensor, $\boldsymbol{j} = \boldsymbol{\nabla} \times \boldsymbol{B}$ is the current density, and $\boldsymbol{E}$ the electric field. We use an unmagnetised form of the ion stress tensor for simplicity, $\boldsymbol{\pi}_i = -\mu(\boldsymbol{\nabla} \boldsymbol{v}_i + \boldsymbol{\nabla} \boldsymbol{v}_i^T)$. The hyper-resistive term takes the place of an electron viscous term. However, when this term becomes important in regions of strong current density, and provided electrons carry most of this current, this has similar form to a collisional electron viscous term (for $|\boldsymbol{v}_e| \gg |\boldsymbol{v}_i|$ the term $-\eta_H \nabla^2 \boldsymbol{j} \approx \eta_H \nabla^2 n \boldsymbol{v}_e / d_i$). We use a heat-flux vector, $\boldsymbol{q}$, that is simplified with respect to the Braginskii (1965) form, but does emulate the anisotropic properties parallel and perpendicular to the field. It is given by $\boldsymbol{q} = -\kappa_\parallel \boldsymbol{\nabla}_\parallel T - \kappa_\perp \boldsymbol{\nabla} T$ where $\boldsymbol{\nabla}_\parallel = \hat{\boldsymbol{b}}(\hat{\boldsymbol{b}} \cdot \boldsymbol{\nabla})$. We solve these equations in two-dimensional Cartesian and toroidal axisymmetric geometries (see below).

The coefficients in equations (5.1-5.5) are the normalised resistivity η, the hyper-resistivity η_H, the ratio of specific heats $\gamma = 5/3$, the normalised ion viscosity μ, and the normalised parallel and perpendicular heat conductivities $\kappa_\parallel$ and $\kappa_\perp$. These transport parameters are defined in terms of the dimensional coefficients of Braginskii (1965) and Spitzer (1962), although they are taken to be constant and uniform with the values in Table 5.1 for all results unless explicitly stated otherwise. The parallel and perpendicular heat conductivities are calculated using the parallel electron $\kappa_e^\parallel$ and perpendicular ion $\kappa_i^\perp$ conductivities of Braginskii (1965) at n_0, T_0. We neglect the parallel ion and perpendicular electron heat conductivities, $\kappa_i^\parallel$ and $\kappa_e^\perp$ respectively, as they are smaller. The ion viscosity μ is based on the initial parallel value $\mu_i^\parallel$, rather than the perpendicular value, for numerical stability. The resistivity, η, viscosity μ and hyper-resistivity η_H are treated as free parameters in the model, and are varied in the simulations described below.

It is important to mention the physical processes we do not include in this model, due to the assumptions and simplifications we have made. As stated, we do not include any effects due to electron inertia, or electron and ion-FLR effects. We also do not include wave-particle interactions, such as Landau damping, that can be an important electron heating mechanism in collisionless plasmas (see e.g. Loureiro et al. 2013). We do not include the full form of the electron and ion-pressure tensors, which, as discussed in Chapter 1, may be important for breaking the frozen-in condition in collisionless plasmas (Hesse et al. 2002; Ricci et al. 2004). Finally, as the simulations are 2D, we do not include 3D effects such as kink instabilities (Wesson 2011). Although, as far as we are aware, there is no evidence for such instabilities during merging-compression in the experimental data.

5.2 Initial conditions

5.2.1 Initial set-up

The initial conditions are taken to be two flux-ropes with parallel toroidal current and strong toroidal (guide) field inside the MAST vacuum vessel $R \in [0.2, 2.0]\,\mathrm{m}, Z \in [-2.2, 2.2]\,\mathrm{m}$, where the inner radial value is the radius of the centre post, and the other values specify the outer walls of the vessel. We do not model the in-vessel poloidal field coils, and thus the complex breakdown and flux-rope formation phase, which is outside the scope of our model. These initial conditions thus correspond to the time after the flux-ropes have detached from the P3 coils, but before they have moved towards the mid-plane (see Figure 2.10 and discussion in Section 2.2.4).

It is common in modelling tokamak plasmas to calculate an equilibrium solution to the Grad-Shafranov equation (Grad & Rubin 1958; Shafranov 1966) with a code such as EFIT (Lao et al. 1990). However, these codes usually assume a set of nested flux-surfaces with a single magnetic axis. In merging-compression there are two separate sets of flux-surfaces each with a magnetic axis. For this reason, there has been no reconstruction of the magnetic structure of the flux-ropes prior to merging at present. However, the total current in the domain is known, I_{plasma}, and the width of the flux-ropes is estimated from the fast camera images. We construct the flux-ropes in the Cartesian simulations (R, T, Z) using an idealised

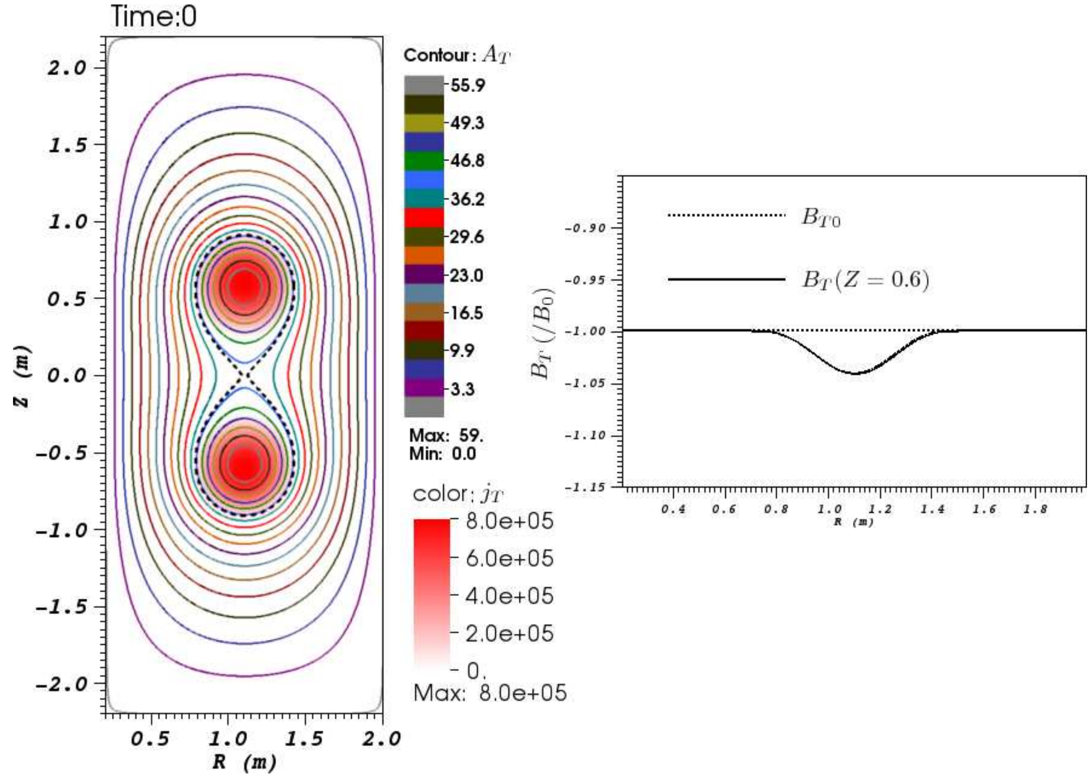

Figure 5.1: Left: The initial out-of-plane current density, j_T measured in $\mathrm{A\,m^{-2}}$, with coloured contours of the out-of-plane magnetic potential, A_T measured in $\mathrm{mWb\,m^{-1}}$, for the merging start-up simulations in Cartesian geometry. The dashed contour has the value $A_T = A_{T,Xpt} = 38.9\,\mathrm{mWb\,m^{-1}}$, and coincides with the magnetic separator at $t = 0$. Right: The normalised out-of-plane magnetic field, B_T in units of $B_0 = 0.5\,\mathrm{T}$ (solid line), in a radial profile across the centre of the flux-rope (at $Z = 0.6$). Also shown is $B_{T0} = -1B_0 = -0.5\,\mathrm{T}$ (dotted line) for comparison. Here the initial half-separation is $a = 0.6$ m, the flux-rope radius is 0.4 m, and the peak current density is $j_{T,\max} = 800\mathrm{kA\,m^{-2}}$.

1D smooth current profile

$$j_T(r) = \begin{cases} j_m \left(1 - (r/w)^2\right)^2 & \text{if } r \leq w, \\ 0 & \text{if } r > w, \end{cases}$$

where j_T is the out-of-plane current density, $r = \sqrt{(R - R_i)^2 + (Z \mp Z_i)^2}$ is the radial distance from the centre of each flux rope ($R = R_i$, $Z = \pm Z_i$), w is the flux-rope radius, and j_m is the maximum current density. In all of the simulations presented we use $w = 0.4$ m and $j_m = 2\,[B_0/(\mu_0 L_0)] = 0.8\,\mathrm{MA\,m^{-2}}$ to give total current $I_{\text{plasma}} = 2 \times (\pi j_m w^2/3) = 268\,\mathrm{kA}$, the same as MAST shot 25740 which is discussed in Chapter 2.

Due to the low poloidal beta $\beta_{p0} = 2 \times 10^{-3}$, see Table 5.1, we balance the internal pinch-force of each flux-rope with a paramagnetic increase in B_T. This kind of magnetic profile has been measured in ideally relaxing flux-ropes under a strong toroidal field in the TS-3 merging device (Ono et al. 2012). Firstly, the poloidal magnetic field due to the 1D current profile was found, matching the outer potential solution to the solution inside the flux-rope at $r = w$. This was then used in the 1-D force-free equilibrium equation

$$\partial_r (B_\theta^2/2 + B_T^2/2) + B_\theta^2/r = 0,$$

where B_θ is the poloidal magnetic field for the flux-rope, to find the required B_T for radial force balance. We find this to be

$$B_T = \begin{cases} -j_m (B_{T0}^2/j_0^2 + 47w^2/360 - r^2/2 + 3r^4/4w^2 & \\ -5r^6/9w^4 + 5r^8/24w^6 - r^{10}/30w^8)^{1/2} & \text{if } r \leq w, \\ -B_{T0} & \text{if } r > w, \end{cases}$$

where the sign is determined by the respective orientations of the toroidal field and plasma current in MAST (the toroidal field is clock-wise as viewed from above). The out-of-plane magnetic potential is found by solving the Poisson equation $-\nabla^2 A_T = j_T$, subject to the boundary condition $A_T = 0$, with the HiFi framework, see Chapter 3 for a discussion of how this can be done. With this method each flux rope is balanced against the internal pinch force, but there is finite Lorentz force between the flux-ropes that causes them to mutually attract. A large initial separation, $2a = 1.2$ m, is chosen so that this force is small at

$t = 0$.

The initial conditions for the Cartesian simulations are shown in Figure 5.1. The left-hand panel shows the initial current density, j_T, and contours of the out-of-plane magnetic potential, A_T, in the full simulation domain. A two-dimensional separatrix, with an X-point, separates the "public flux" contours that enclose both flux-ropes without breaking, and the "private flux" of each flux-rope which is available for reconnection. The right-hand panel shows the structure of the out-of-plane toroidal field in a radial cut through the centre of one of the flux-ropes.

The initial conditions for the 2D toroidal axisymmetric simulations (R, ϕ, Z) are set up in the same manner, but the toroidal magnetic potential A_ϕ is solved subject to the boundary conditions $A_\phi = B_v R/2$. This gives a uniform vertical field of magnitude B_v that reduces the radially outwards hoop force on the flux-ropes. We use $B_v = -0.06B_0 = -0.03$ T unless specified otherwise. In toroidal geometry, the vacuum toroidal field is $B_{\phi 0} = -B_{T0}R_0/R$ where $R_0 = 0.85$ m is the major radius. Figure 5.2 shows, in the left-hand panel, the initial current density, j_ϕ, and contours of the flux, defined here as $\psi = RA_\phi$, in the full simulation domain. The right-hand panel shows the toroidal field in a cut through the centre of one of the flux-ropes. Note there is a small paramagnetic increase in the magnitude of this field over the vacuum field as it passes through the centre of the flux-ropes.

After the initial conditions are set up by solving the Poisson equation, the simulation is restarted with the set of equations (5.1-5.5). These are given in flux-source form in Appendix A.4. In Cartesian geometry these equations are advanced with conducting wall boundary conditions $\partial_t A_T = 0$, zero tangential current $\hat{\boldsymbol{n}} \cdot \boldsymbol{\nabla} B_T = 0$, $j_T = 0$, perfect slip solid wall $\hat{\boldsymbol{n}} \cdot \boldsymbol{\nabla}(\hat{\boldsymbol{n}} \times \boldsymbol{v}_i) = \boldsymbol{0}$ and $\hat{\boldsymbol{n}} \cdot \boldsymbol{v}_i = 0$, and no temperature gradient $\hat{\boldsymbol{n}} \cdot \boldsymbol{\nabla} T = 0$. In toroidal geometry, where there is a normal component of the field intersecting the vertical boundaries, the stricter condition $\boldsymbol{v}_i = 0$ is used to ensure there is no tangential convective electric field and associated normal Poynting flux through the boundary.

5.2.2 Numerical grid and time-step

As described in Chapter 3, the HiFi grid is split into $N_R \times N_Z$ finite elements, each with order N_p polynomial basis functions. For all of the simulations described

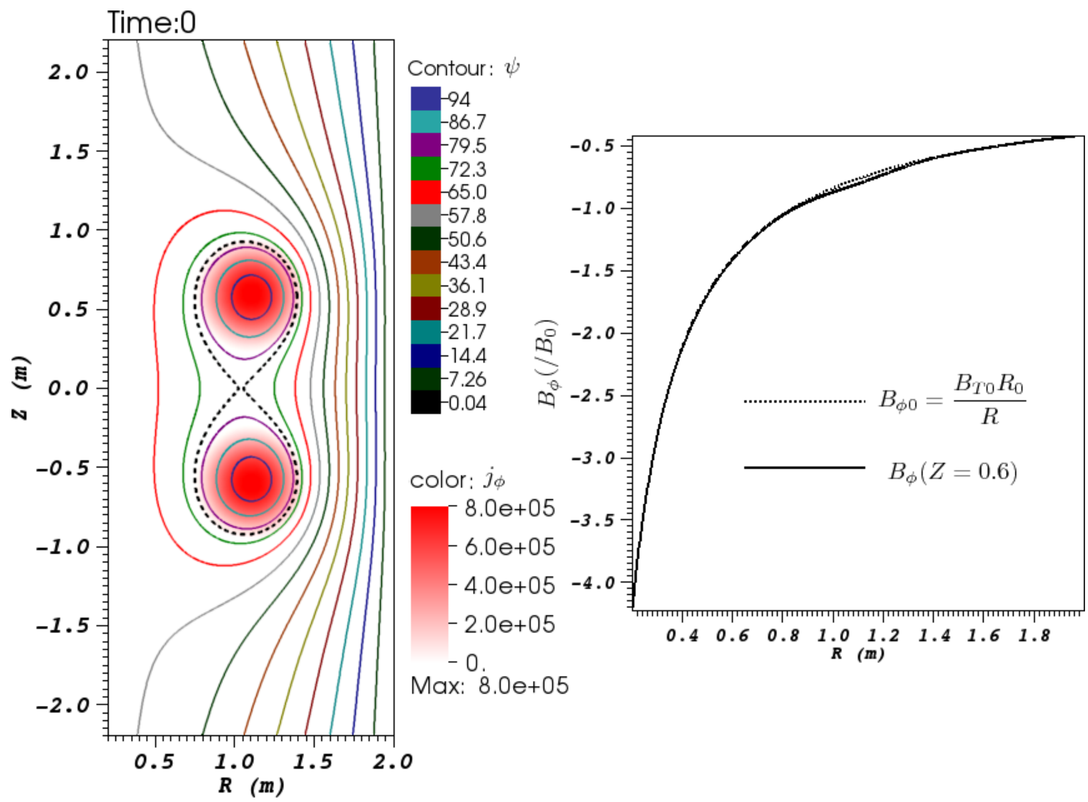

Figure 5.2: Left: The initial toroidal current density, j_ϕ (in $\mathrm{A\,m^{-2}}$), with coloured contours of the toroidal flux, $\psi = RA_\phi$ (in mWb), for the merging simulations in toroidal-axisymmetric geometry. The dashed contour has the value $\psi = \psi_{\mathrm{Xpt}} = 76.5\,\mathrm{mWb}$, and coincides with the magnetic separator at $t = 0$. Right: The normalised toroidal magnetic field, B_ϕ in units of $B_0 = 0.5\,\mathrm{T}$ (solid line), in a radial profile across the centre of the flux-rope (at $Z = 0.6$). Also shown is $B_{\phi 0} = B_{T0}R_0/R$ (dotted line), where $B_{T0} = -1B_0$ is the vacuum toroidal field at the major radius, $R_0 = 0.85$ m. Here the initial half-separation is $a = 0.6$ m, the flux-rope radius is 0.4 m, the vertical field is $B_v = -0.06B_0 \equiv -0.03$ T, and the peak current density is $j_{\phi,\mathrm{max}} = 800\mathrm{kA\,m^{-2}}$.

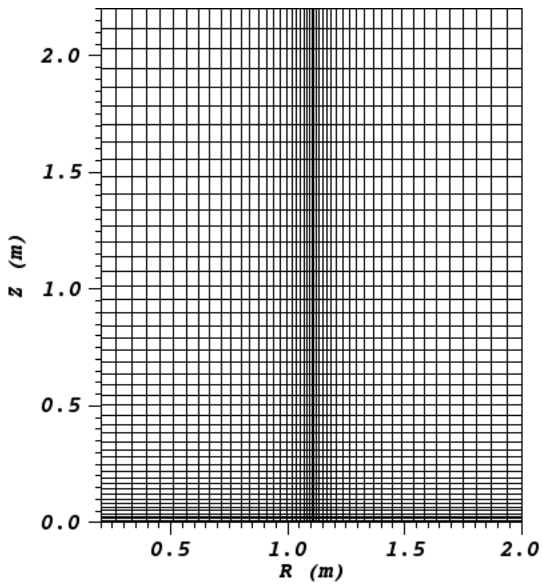

Figure 5.3: Low resolution example of the numerical grid in the top-half ($z > 0$) of the domain. Here, $N_R = 10$, $N_R = 20$, $N_p = 4$ giving an effective resolution of 40×80. The grid stretching parameters are $r_c = 0.2$, $z_c = 0.08$, $L_R = 1.8$ m, $L_Z = 2.2$ m and $r_p = 0.2$ m.

below we use $N_p = 4$, and the N_R, N_Z is given for each simulation. The computational grid is stretched through a grid-packing function that maps the logical domain $\xi, \zeta \in [0.0, 1.0]$, where HiFi computes the solution, to the simulation box $R \in [0.2, 2.0], Z \in [-2.2, 2.2]$. These functions are

$$R = \operatorname{sgn}(2\xi - 1)\frac{L_R\left[(2\xi-1)^2 + r_c|2\xi-1|\right]}{2(1+r_c)} + L_R/2 + r_p, \tag{5.6}$$

$$Z = \operatorname{sgn}(2\zeta - 1)\frac{L_Z\left[(2\zeta-1)^2 + z_c|2\zeta-1|\right]}{2(1+z_c)}, \tag{5.7}$$

where r_c, z_c are parameters that change the grid stretching from quadratic ($r_c, z_c \to 0$) to linear ($r_c, z_c \to \infty$). Here $\operatorname{sgn}(x)$ is the sign function (that returns the sign of the argument), $|x|$ gives the absolute value, $L_R = 1.8$ m, $L_z = 2.2$ m, and $r_p = 0.2$ m for all simulations presented in this thesis. As the grid stretching is done through a smoothly-varying function, and that function varies less than quadratically, the change in cell size is gradual which should minimise artificial wave reflection at cell boundaries. A low resolution example of the grid stretching is shown for the top half of the domain in Figure 5.3.

As mentioned in Chapter 3, all of the simulations described in this thesis use the implicit Crank-Nicolson method for time advance, which is $\mathcal{O}((\Delta t)^2)$ accurate in time and is not restricted to the CFL-limited time-step (3.36). However, we do impose an upper limit on the timestep to ensure accuracy. For resistive MHD simulations ($d_i = 0$) the maximum timestep is limited to $\Delta t = 5 \times 10^{-2}\tau_0$, and the maximum timestep used for Hall-MHD simulations is $\Delta t = 10^{-2}\tau_0$. Note that the actual timestep is adaptively determined by the code, depending on how quickly the Newton iterations converge, and is often much shorter than this.

5.3 Resistive MHD: Cartesian geometry

The first set of simulations described here are resistive MHD simulations (the equations (5.1-5.5) were solved with $d_i = \eta_H = 0$) in Cartesian (R, T, Z) geometry, where T is the invariant out-of-plane direction. The simulations use a grid of $N_R = 180$ times $N_Z = 360$ finite elements, each with $N_p = 4$ Jacobi polynomial basis functions, thus giving an effective resolution of 720×1440. We use the grid-stretching parameters $r_c = 0.2$, $z_c = 0.08$, which give the minimum grid spacings $\Delta R = 4.2 \times 10^{-4}$, $\Delta Z = 2.3 \times 10^{-4}$ at the X-point $(R = 1.1, Z = 0)$.

5.3.1 Control run

The initial conditions are shown in Figure 5.1; there is $A_{T,\mathrm{pr}} = A_{T,max} - A_{T,Xpt} = 59 - 38.9 = 20.1\,\mathrm{mWb\,m^{-1}}$ of private flux within each flux-rope at the start of the simulation. In these initial conditions, the thermal pressure is uniform, but there is a finite Lorentz force between the flux-ropes due to their parallel toroidal currents. This causes them to be mutually attracted, and they move towards the mid-plane, $Z = 0$. As they move together, the out-of-plane field, B_T, increases in the plasma between the flux-ropes, and the associated magnetic pressure build-up reduces the initial acceleration (this dominates the force due to thermal pressure gradients because of the low β).

Figure 5.4 shows the out-of-plane current density, j_T, the in-plane plasma velocity, $\boldsymbol{v}_{ip} = (v_{iR}, v_{iZ})$, and the flux, A_T, at three snapshots during the merging. At $t = 7.54\tau_0$ the X-point between the two flux-ropes has collapsed, forming a thin sheet of negative toroidal current (blue). Before any significant heating occurs, the inward Lorentz force, $-j_T B_R$, is mostly balanced by the increase in out-of-plane field $j_R B_T$ (not shown), similar to a force-free current sheet. The plasma between the flux-ropes is accelerated in the radial direction in two jets towards the

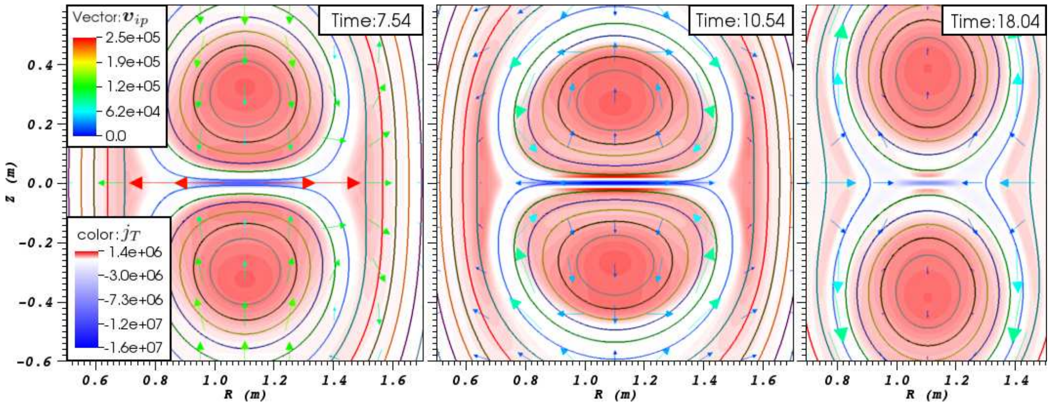

Figure 5.4: Snapshots of the flux-ropes at $t = 7.54\tau_0$, $t = 10.54\tau_0$, and $t = 18.04\tau_0$ (where $\tau_0 = 0.29$ μs) for the Cartesian resistive MHD simulation ($d_i = \eta_H = 0$) with $\eta = 10^{-5}$ and $\mu = 10^{-3}$. The current density (in A m^{-2}) is shown in colour, the coloured lines are contours of A_T, and the coloured vectors show the in-plane velocity $\boldsymbol{v}_{ip}$ (in m s^{-1}).

inboard and outboard sides, reaching a maximum velocity of $v_{R,max} \approx 2.5 \times 10^5$ m s^{-1} at $t = 7.54\tau_0$.

At $t = 10.54\tau_0$ (middle panel), the outflow speed drops to $v_R = 5 \times 10^4$ m s^{-1} (small blue outflow arrows), and the vortical plasma flows that bring in flux to the current sheet have reversed direction. The front edges of the flux-ropes are flattened, and there are two layers of positive current (red) on the vertical edges of the current sheet. The repulsive Lorentz force between the negative current sheet and these oppositely directed current layers can prevent plasma from entering the sheet.

At $t = 18.04$ the O-points at the centre of the two flux-ropes have clearly moved apart, similar to the sloshing motion found in simulations of the coalescence instability (see Biskamp & Welter 1980, and Chapter 1). The value of the resistivity, η, used in this simulation is below the threshold value $\eta \approx 2 \times 10^{-5}$, found by Knoll & Chacón (2006a), for which the O-point motion can reverse direction. However, it should be noted that Knoll & Chacón (2006a) set $\mu = \eta$ to find this threshold value, whereas we have $\mu > \eta$ in this simulation.

Figure 5.5 shows the reconnecting field, B_R, in the upstream region (at $R = 1.1$ m, and plotted against Z) at four times during this collision of the flux-ropes. At $t = 7.54\tau_0$ the maximum upstream field is $B_{R,\max} = 0.245B_0 = 0.12$ T at $Z = -3$ cm, increasing to $B_{R,\max} = 0.29B_0 = 0.145$ T at $t = 9.54\tau_0$. This later time is when the current sheet ($j_T \approx \partial_Z B_R$) is thinnest, $\delta \approx 2 \times 1$ cm, and corresponds

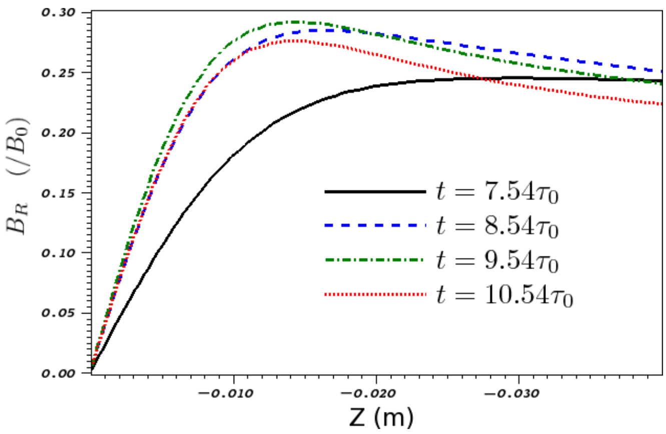

Figure 5.5: Time evolution of the normalised ($B_0 = 0.5$ T) reconnecting magnetic field component, B_R, plotted against vertical position, Z, for the Cartesian resistive MHD simulation ($d_i = \eta_H = 0$) with $\eta = 10^{-5}$ and $\mu = 10^{-3}$.

to a local maximum in the reconnection rate (see also Figure 5.6 and discussion below). Upstream of the current sheet, $-4\,\mathrm{cm} < Z < -1.5\,\mathrm{cm}$, the gradient in B_R is reversed, indicating weak flux pile-up on the sheet edge (it is weak compared to the flux pile-up shown in Figure 4.13, that was responsible for the reversed current layers for the fan model in Figure 4.15). This pile-up is responsible for the layers of positive current seen in the middle panel of Figure 5.4.

At the local maximum rate ($t = 9.54\tau_0$) the diffusion region is quasi-steady and we can perform a Sweet-Parker analysis (we find E_T is close to uniform within the diffusion region at this time, see Section 1.3.2). The upstream Alfvén speed is estimated using $B_{\mathrm{IN}} = B_{R,\mathrm{max}} = 0.29B_0$, and density $n_{\mathrm{IN}} \approx n_0$ to give $v_{A,\mathrm{IN}} \approx (B_{\mathrm{IN}}/B_0)\sqrt{n_0/n_{\mathrm{IN}}}v_0 = 1.02 \times 10^6$ m s^{-1}. The maximum outflow jet velocity at this time is $v_R = 9.7 \times 10^4$ m s^{-1}, which is in good agreement with the Sweet-Parker outflow velocity modified for the effects of finite viscosity (Park et al. 1984) in equation (1.48): for $\mu = 10^{-3}$ and $\eta = 10^{-5}$, $v_R \approx v_{A,\mathrm{IN}}\sqrt{\eta/\mu} \approx 10^5\,\mathrm{m\,s^{-1}}$. The large viscosity is slowing the outflow jet here by a factor of 10 compared with the expected outflow speed for $\mu = \eta$.

5.3.2 Reconnection rate and scalings

Varying the resistivity and ion-viscosity

The reconnection rate in two-dimensional reconnection is $\partial_t A_T = -E_T$ (see equation (1.40)) at the location of the X-point; $R = 1.1$ m, $Z = 0$. We plot in

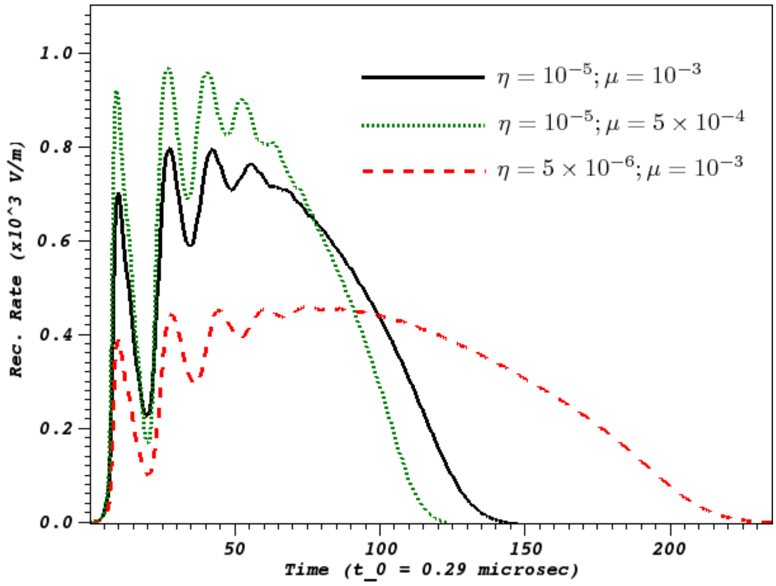

Figure 5.6: Reconnection rate ($\partial_t A_T = -E_T$ measured at the X-point) in $\mathrm{V\,m^{-1}}$, plotted against normalised time ($t_0 = 0.29\mu s$), for the Cartesian resistive-MHD simulations with $\eta = 10^{-5}$, $\mu = 10^{-3}$ black-solid line; $\eta = 10^{-5}$, $\mu = 5 \times 10^{-4}$ green-dotted line; $\eta = 5 \times 10^{-6}$, $\mu = 10^{-3}$ the red-dashed line.

Figure 5.6 the reconnection rate against time for the simulation under discussion (black-solid line). The repeated sloshing of the flux-ropes modulates the reconnection rate through large amplitude oscillations with a period of a few poloidal Alfvén times, $\approx 4\tau_p$ (where $\tau_p \approx 5\tau_0$). This is followed by a gradual decaying phase as the flux-ropes shrink, until all of the available flux is reconnected. The global maximum reconnection rate is $800\mathrm{V\,m^{-1}}$ at $t = 27.54\tau_0$ (second peak), when the Full-Width Half-Minimum (FWHM) length of the current sheet is $\Delta_{\mathrm{FWHM}} \approx 0.32$ m, and the width is $\delta_{\mathrm{FWHM}} \approx 1.1 \times 10^{-2}$ m. This gives an aspect ratio of 30 that is consistent with the visco-resistive scaling for the Sweet-Parker sheet (Park et al. 1984), $\delta_{\mu\eta} \sim \eta_{\mathrm{eff}}^{1/4}\,\mu_{\mathrm{eff}}^{1/4}\Delta \approx \Delta/29.6$, where $\eta_{\mathrm{eff}} \equiv S^{-1} = \eta\, v_0\, L_0/(v_{A,\mathrm{IN}}\,\Delta)$ and $\mu_{\mathrm{eff}} = \mu\, v_0\, L_0/(v_{A,\mathrm{IN}}\,\Delta)$ are the effective inverse Lundquist number and inverse Reynolds number respectively, defined in terms of the current sheet length $\Delta = \Delta_{\mathrm{FWHM}}$, and the Alfvén velocity due to the reconnecting component of the field at the sheet edge $v_{A,\mathrm{IN}} = (B_{R,\mathrm{IN}}/B_0)\sqrt{n_0/n_{\mathrm{IN}}}\, v_0 = 0.2742 v_0$. That the agreement is excellent, despite the coupling to the macroscopic driver, shows that this kind of Sweet-Parker analysis can be effective at the time of a local peak in the reconnection rate.

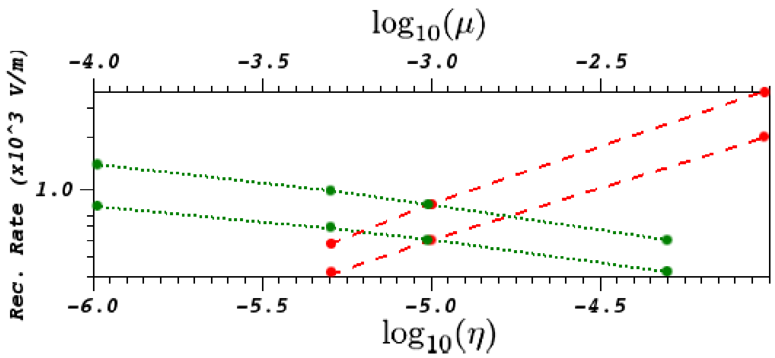

Figure 5.7: The peak reconnection rates $(\partial_t A_T)_{\max}$ (top lines), and average reconnection rates $\langle \partial_t A_T \rangle$ (bottom lines), plotted in $\mathrm{V\,m^{-1}}$ for fixed $\eta = 10^{-5}$ and varying μ (green-dotted lines, top axis), and for fixed $\mu = 10^{-3}$ and varying η (red-dashed lines, bottom axis). The coloured dots indicate a simulation was run using the value of μ (green, top axis) or η (red, bottom axis).

Figure 5.6 also shows the reconnection rate against time for two other simulations. When the viscosity is reduced by a factor of two ($\eta = 10^{-5}$, $\mu = 5 \times 10^{-4}$ green-dotted) the peak reconnection rate increases and the total merge time decreases from $T_{\text{merge}} = 142.7\tau_0$ to $122\tau_0$. A factor of two reduction in resistivity ($\eta = 5 \times 10^{-6}$, $\mu = 10^{-3}$ red-dashed line) increases the merge time to $231\tau_0$. For the latter, the peak reconnection rate actually occurs at the start of the gradual phase ($t = 73.5\tau_0$), rather than at the second bounce as for the other two simulations. As the total flux reconnected is the same in each simulation, $A_{T,\text{pr}} = 20.1\text{mWb m}^{-1}$, we can calculate the average reconnection rate as $\langle \partial_t A_T \rangle = A_{T,\text{pr}}/T_{\text{merge}}$. For the case of the standard simulation $\eta = 10^{-5}$, $\mu = 10^{-3}$ with $B_{T0} = 1B_0 = 0.5T$ the averaged reconnection rate is $\langle \partial_t A_T \rangle = 486\,\mathrm{V\,m^{-1}}$.

Figure 5.7 shows scalings for the peak, $(\partial_t A_T)_{max}$, and average, $\langle \partial_t A_T \rangle$, reconnection rates in $\mathrm{V\,m^{-1}}$ against resistivity (red-dash line, bottom axis) and against viscosity (green-dotted line, top axis). The peak reconnection rates scale as $(\partial_t A_T)_{\max} \sim \eta^{0.69}\mu^{-0.26}$, and the average reconnection rates as $\langle \partial_t A_T \rangle \sim \eta^{0.62}\mu^{-0.23}$. These are in good agreement with both the visco-resistive scalings (Park et al. 1984) for a Sweet-Parker current sheet in equation (1.49), as they are roughly between $\sim \eta^{1/2}$ (weak viscosity) and $\sim \eta^{3/4}\mu^{-1/4}$ (strong viscosity). These scalings are also in agreement with a previous study by Breslau & Jardin (2003) of coalescing flux-ropes with large magnetic Prandtl number $Pr_m = \mu/\eta$, who find $\eta^{0.6}\mu^{-0.3}$. Note that the latter study does not mention the

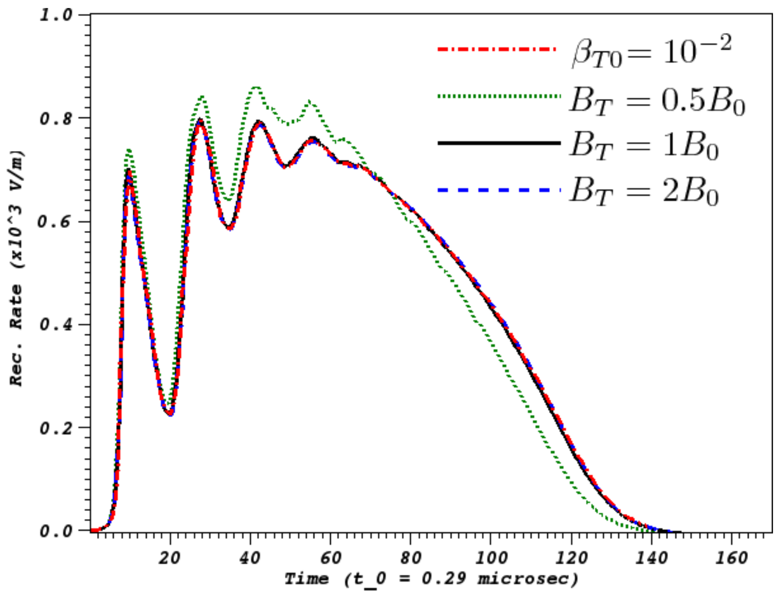

Figure 5.8: Reconnection rate ($\partial_t A_T = -E_T$ measured at the x-point) in V m^{-1}, plotted against normalised time ($t_0 = 0.29\mu$s), for four Cartesian resistive-MHD simulations with fixed dissipation $\eta = 10^{-5}$, $\mu = 10^{-3}$, but varying guide field B_T and plasma-β. The simulations with $\beta_{T0} = 8 \times 10^{-5}$ are shown for $B_T = 1B_0$ black-solid line (the control run); $B_T = 0.5B_0$ green-dotted line; $B_T = 2B_0$ blue-dashed line. Also shown is a simulation with $\beta_{T,0} = 10^{-2}$ and $B_T = 1B_0$ red dash-dashed line.

sloshing effect, and gives scalings only for the average reconnection rate. They also do not have a strong-guide field, the effects of which will now be examined.

Varying the out-of-plane field and plasma-beta

The out-of-plane field, B_T, does not directly enter the equation for the reconnection rate, as

$$\partial_t A_T = -E_T = v_Z B_R - v_R B_Z - \eta(\partial_Z B_R - \partial_R B_Z),$$

where only the resistive terms contribute at the x-point. However, it may indirectly affect this rate by modifying the plasma compressibility, and thus modifying flows that carry the frozen-in flux (ultimately changing the pile-up value of B_R). To investigate this, we ran two simulations with the same parameters as the standard simulation (in Figure 5.4), but for $B_{T0} = 0.5B_0 = 0.25$ T and $B_{T0} = 2.0B_0 = 1$ T. These values are within the range of toroidal field values in MAST (where the toroidal field $B_\phi \propto 1/R$). The reconnection rates are plotted against time in Figure 5.8. The peak reconnection rate at $t = 27.54\tau_0$ increases to $(\partial_t A_T)_{\max} = 838\mathrm{V\,m^{-1}}$ for $B_{T0} = 0.5B_0$, a change of 5%, and decreases to $(\partial_t A_T)_{\max} = 789.5\mathrm{V\,m^{-1}}$ for $B_{T0} = 2B_0$, a change of 0.7%. The average reconnection rate changes to $\langle \partial_t A_T \rangle = 502\mathrm{V\,m^{-1}}$ for $B_{T0} = 0.5B_0$ and $484\mathrm{V\,m^{-1}}$ for $B_{T0} = 2B_0$. The reconnection rate thus appears to be insensitive to $\mathcal{O}(1)$ changes in B_{T0}. Compressibility is also dependent on the thermal pressure; we also overplot a simulation with a much larger $\beta_{T0} = 10^{-2}$ ($\beta_{p0} = 25$) and $B_T = 1B_0$, finding that this also has a weak effect on the reconnection rate in resistive MHD. However, it should be noted that in all three simulations order one density variations do occur at later times within the current sheet, as the plasma is heated the current sheet density drops to around 0.5 times the initial value (not shown). The larger change in reconnection rate when B_{T0} decreases to $0.5B_0$, than when it is increased to $2B_0$, is likely due to the fact that the in-plane motions are approaching the Alfvén speed, which can cause strong compression of the plasma as it enters the sheet and increase the reconnection rate (see e.g. Priest & Forbes 2000).

5.3.3 Hyper-resistive MHD

The Hall-MHD simulations in the next section differ from the resistive MHD simulations in that they have $d_i, \eta_H \neq 0$. Before the Hall-MHD results are presented, we briefly show how setting $\eta_H \neq 0$ (with $d_i = 0$) affects the reconnection rate for the values of η_H used below. We will refer to this as the hyper-resistive MHD regime.

Figure 5.9 shows the reconnection rate for four non-zero values of the hyper-resistivity, $\eta_H = 10^{-7}, 10^{-8}, 10^{-9}$, and 10^{-10}. Despite four orders of magnitude change in the hyper-resistive coefficient there is only a single order of magnitude change in the peak reconnection rate. The reconnection rate for the lowest value of the hyper-resistivity, $\eta_H = 10^{-10}$, is similar to the reconnection rate for the standard resistive-MHD simulation (with $\eta_H = 0$), suggesting that the resistivity is larger than the hyper-resistivity in supporting the reconnection electric field at the X-point for this simulation.

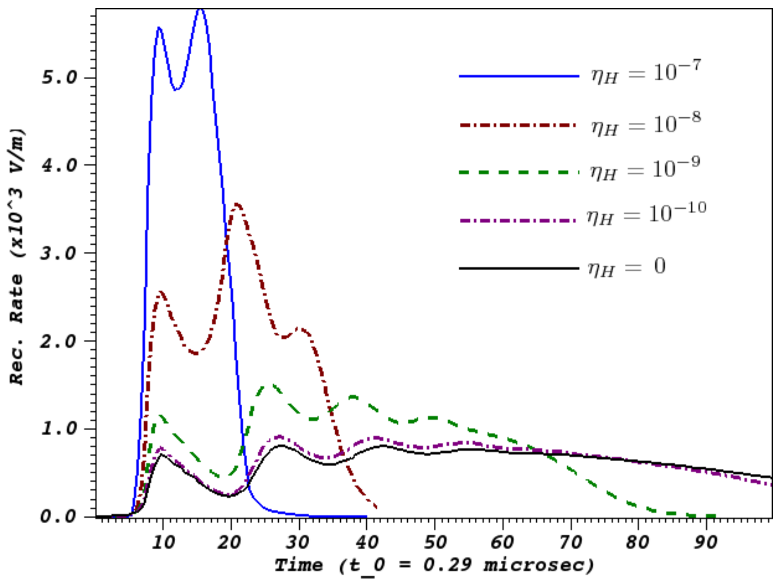

Figure 5.9: Reconnection rate ($\partial_t A_T = -E_T$ measured at the X-point) in V m^{-1}, plotted against normalised time ($t_0 = 0.29\mu$s), for four hyper-resistive MHD simulations with $\eta_H = 10^{-7}$ (blue-solid), $\eta_H = 10^{-8}$ (dark red dash-dot), $\eta_H = 10^{-9}$ (green dashed) and $\eta_H = 10^{-10}$ (purple dash-dot). Also plotted for comparison, as a black-solid line, is the reconnection rate for $\eta_H = 0$ (which is the control resistive MHD simulation).

5.4 Hall-MHD: Cartesian geometry

5.4.1 Control run

The combined effects of the Hall and hyper-resistive terms on the merging are given in this section. The standard Hall-MHD simulation has the same parameters as the standard resistive MHD simulation ($\eta = 10^{-5}$, $\mu = 10^{-3}$, and other parameters from Table 5.1) but with $d_i L_0 = 0.145$ m and $\eta_H = 10^{-8}$.

A snapshot of the out-of-plane current density, j_T, and in-plane ion velocity, $\boldsymbol{v}_{ip}$, at $t = 7.54\tau_0$ is shown in Figure 5.10. There are several differences evident when comparing this figure with the standard resistive-MHD simulation of Figure 5.4. Quantitatively, the time average reconnection rate up to this snapshot is 361 V m^{-1}, compared to 50 V m^{-1} for the resistive simulation (the amount of flux reconnected at this time in the Hall-MHD simulation is roughly the same as that in the third panel of Figure 5.4). However, as discussed above, the non-zero hyper-resistivity alone provides a large contribution to this reconnection rate. The effect on the reconnection rate specifically due to the Hall term is discussed

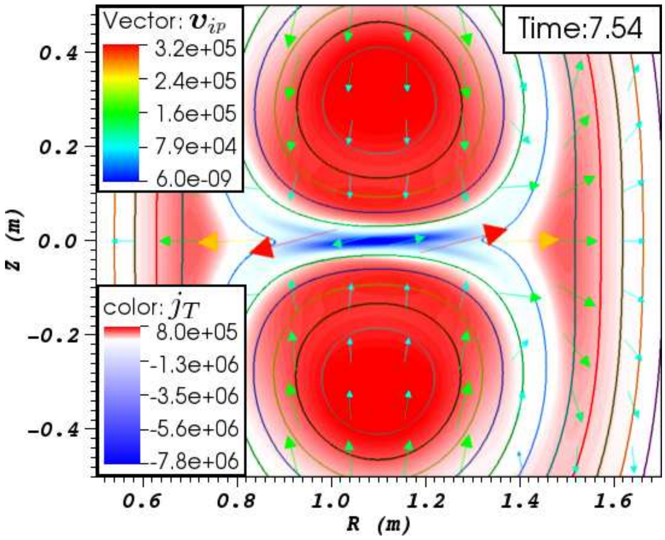

Figure 5.10: Snapshot of the standard Hall-MHD simulation (same as the standard resistive MHD simulation, but with $\eta_H = 10^{-8}$, $d_i = 0.145$). The out-of-plane current density, j_T (in A m^{-2}), is shown in colour, and the out-of-plane potential, A_T, is shown as coloured contours. Coloured arrows show the in-plane ion velocity, $\boldsymbol{v}_{ip}$ (in m s^{-1}), where the middle of the arrow is the point at which the velocity field is sampled.

in more detail below; here we discuss the qualitative effects.

Firstly, there is a clear tilt of the ion outflow jets when the Hall term is switched on (this tilt is not present for $d_i = 0$ with $\eta_H \neq 0$). The outflow jets have a positive (negative) vertical component on the outer (inner) radial side. There also appears to be a tilt of the main current sheet, as the current density is stronger across the bottom separator on the inner radial side, and the top separator on the outer side. The radial length of the current sheet measured at $Z = 0$ at this time is $L \approx 20$ cm, which is of the same order as the initial flux-rope radius ($w = 0.4$ m).

Figure 5.11 shows the plasma density, n, for the same simulation and at the same time as in Figure 5.10. There are $\mathcal{O}(1)$ density variations in a quadrupole-like shape (like a quadrupole after the background density is subtracted) within the diffusion region between the flux-ropes. Over-plotted are streamlines of bulk electron velocity, which is calculated as $\boldsymbol{v}_e = \boldsymbol{v}_i - d_i\boldsymbol{j}/n$. Within the flux-ropes the motion of the electrons is dominated by perpendicular drifts towards the current sheet. However, within the diffusion region, the streamlines become parallel to the in-plane field. The electrons are accelerated in bulk within the density cavities and slow down as they enter the high-density regions.

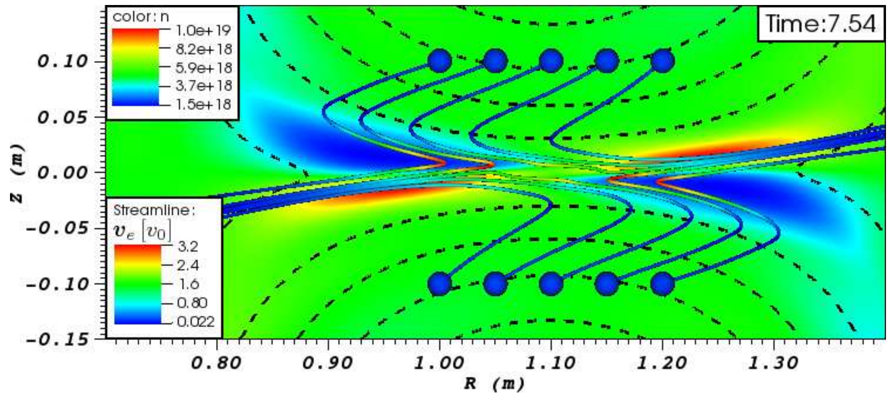

Figure 5.11: The plasma density, n (in m^{-3}), is shown for the standard Hall-MHD simulation in colour scale. Also plotted are bulk electron velocity streamlines, $\boldsymbol{v}_e$ in units of $v_0 = 3.5 \times 10^6\,\mathrm{m\,s}^{-1}$, shown as coloured tubes which start at the locations of the blue circles. The black-dashed lines show contours of the out-of-plane magnetic potential A_T.

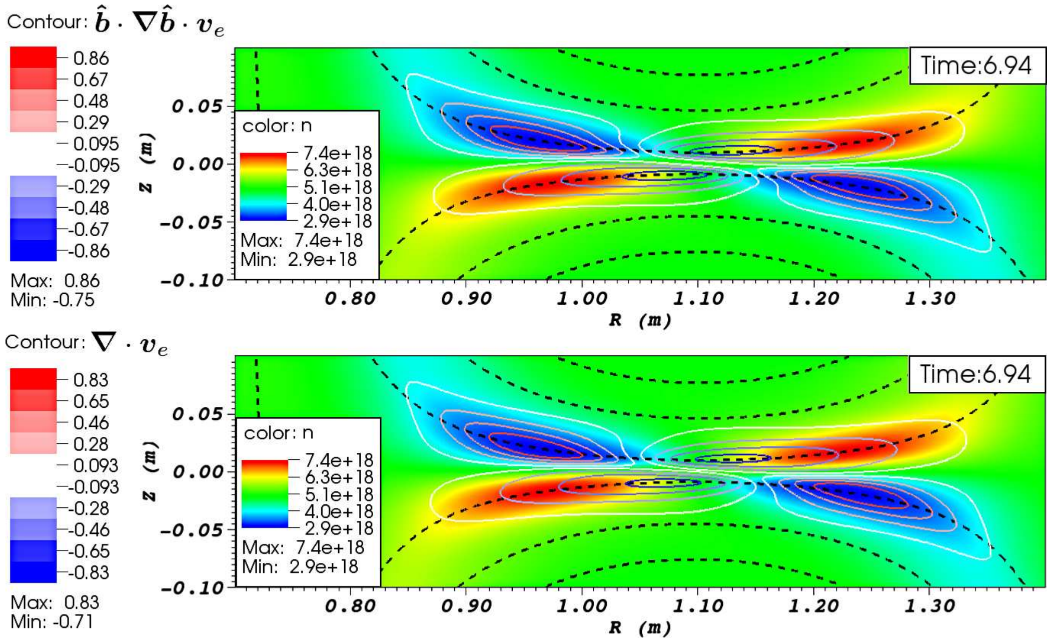

Figure 5.12: Top: The plasma density, n (in m^{-3}), and contours of parallel electron velocity gradient, $\nabla_{\|}\boldsymbol{v}_{e\|} = (\hat{\boldsymbol{b}}\cdot\boldsymbol{\nabla})(\hat{\boldsymbol{b}}\cdot\boldsymbol{v}_e)$ in normalised units, at $t = 6.94\,\tau_0$ for the Hall-MHD control simulation. Bottom: The same as the top image, but with contours of the divergence of the electron velocity $\boldsymbol{\nabla}\cdot\boldsymbol{v}_e$ (there is a difference in contour scale). Also shown as black dashed lines are contours of the flux.

A previous study by Kleva et al. (1995), using a reduced two-fluid formulation, has suggested that this kind of density structure can be caused by parallel electron compressibility in strong guide-field reconnection. These density gradients form in response to parallel electric field on newly reconnected field-lines. We verified this by over-plotting contours of $(\hat{\boldsymbol{b}} \cdot \boldsymbol{\nabla})(\hat{\boldsymbol{b}} \cdot \boldsymbol{v}_e)$, finding that large positive (negative) values overlie the density cavities (peaks), see Figure 5.12 for a snapshot at $t = 6.94\,\tau_0$ when the density asymmetry is being formed. Also, the magnitude and spatial position of this term is in good agreement with the magnitude and position of $\boldsymbol{\nabla} \cdot \boldsymbol{v}_e$ at this time. Thus it does appear that the parallel electron velocity gradient is responsible for this density pattern. The same study suggests that these features are localised within an ion-sound Larmor radius $\rho_{is} = \sqrt{k_B T_e/m_i}/\Omega_{ci} = \sqrt{\beta_e/2}d_i$. In these simulations the value of ρ_{is} varies in space and time, strongly depending on the balance between the heating and thermal conduction terms in the energy equation. At $t = 7.54\tau_0$, the value of $\rho_{is} \approx 0.01$ m within the current sheet, comparable with the size of density features shown in Figure 5.11.

5.4.2 Reconnection rate and scalings

Varying hyper-resistivity

To examine how the strength of dissipation affects the merging, we vary the hyper-resistivity η_H (we show below that hyper-resistivity is dominant over normal resistivity in breaking the frozen-in condition for these Hall-MHD simulations, even for values as low as $\eta_H = 10^{-10}$). Figure 5.13 shows the out-of-plane current density j_T, and contours of the out-of-plane magnetic potential A_T, for five simulations with identical parameters apart from the hyper-resistive coefficient. The snapshots shown are at a time when the same amount of flux has been reconnected (dark green contour) in all simulations.

The simulation in the middle panel ($\eta_H = 10^{-8}$) is the standard Hall-MHD simulation described above, and shown in Figures 5.10 and 5.11, but at a later time. The current sheet, that was forming in Figure 5.10, has become unstable to a tearing type instability resulting in an island at the centre of the sheet. This occurs before any local peak in the reconnection rate, so it is not possible to obtain scalings of the current sheet width across the range of η_H shown in this figure. A 180° rotational symmetry that is present in the initial conditions

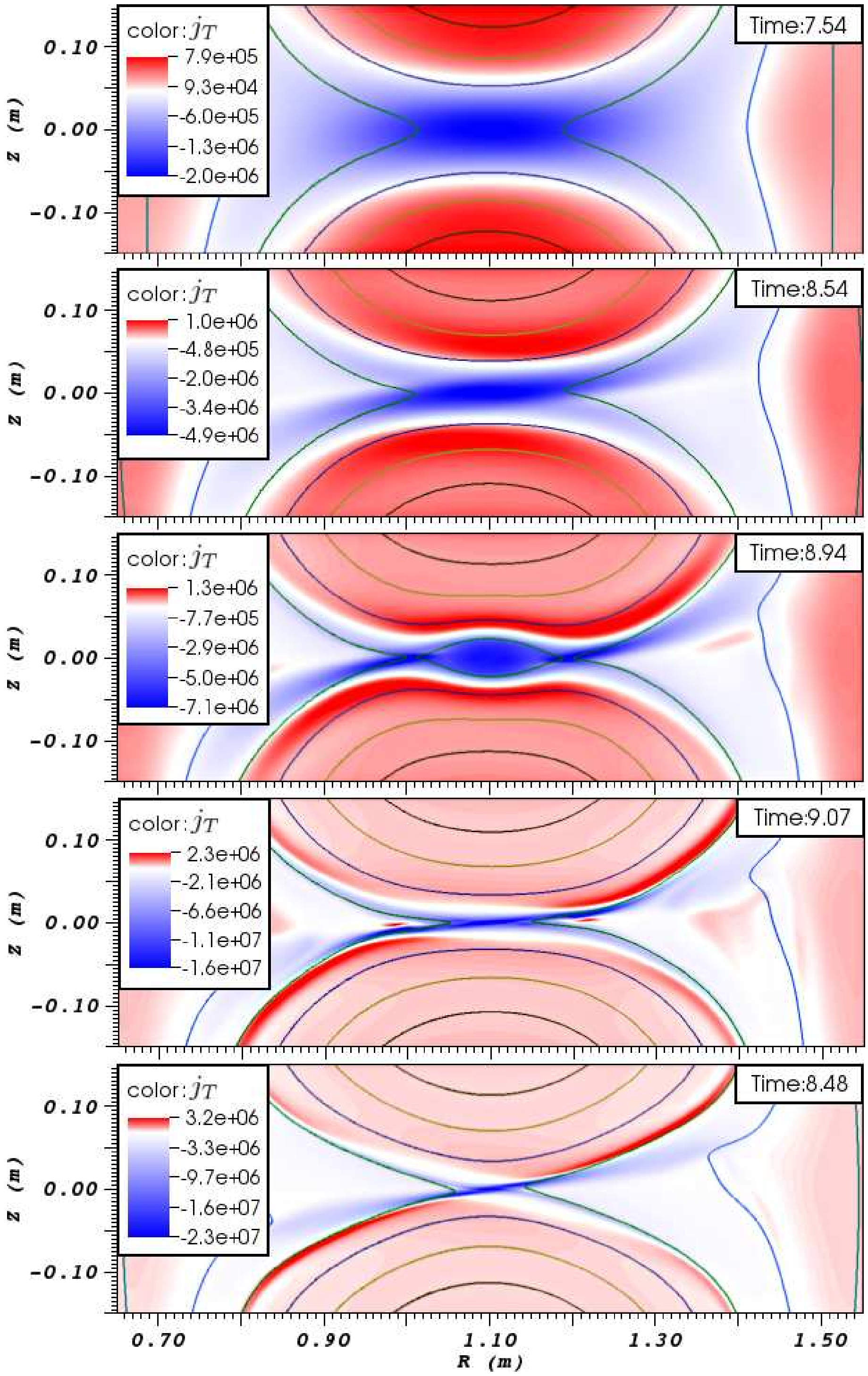

Figure 5.13: The current density, j_T in $\mathrm{A\,m^{-2}}$ shown in colour, and contours of the potential, A_T, for five Cartesian Hall-MHD simulations with different hyper-resistivity η_H. The values taken are $\eta_H = 10^{-6}$ (top), $\eta_H = 10^{-7}$ (second), $\eta_H = 10^{-8}$ (middle), $\eta_H = 10^{-9}$ (fourth) and $\eta_H = 10^{-10}$ (bottom). All other parameters are kept constant ($\eta = 10^{-5}$, $\mu = 10^{-3}$ and $d_i = 0.145$). Approximately the same amount of flux has been reconnected in each (dark green contour).

is preserved by the governing equations (5.1-5.5) and so there is no preferred direction for this island to be ejected. Instead reconnection proceeds at two X-points on either side of the island, causing it to grow until the magnetic pressure within the island balances the attractive force (the drive due to parallel currents) between the flux-ropes. This leads to the reconnection stalling and an oscillating motion of the whole system as it relaxes.

For the case of $\eta_H = 10^{-6}$ the width and length of the current sheet are $\delta_{FWHM} = 7.3\,\mathrm{cm}$ and $\Delta_{FWHM} = 33\,\mathrm{cm}$ respectively, and so the current sheet is low-aspect-ratio (note that this is slightly before the peak in the reconnection rate, see Figure 5.15, but the sheet does not become much thinner at the peak). There is no clear tilt of the current sheet, suggesting that the two-fluid effects responsible for this tilting are weak. We measure the ion-sound Larmor radius in the current sheet to be $\rho_{is} \approx 1\,\mathrm{cm}$ at this time, much less than δ_{FWHM}, which is consistent with this picture of a collisional current sheet. The sheet is stable against fragmentation for the duration of the merging.

For $\eta_H = 10^{-7}$ (second panel) the current sheet begins to tilt, but it is stable for the duration of the merging. At this time, $t = 8.54\tau_0$, the current sheet width is $\delta_{FWHM} = 3.6\,\mathrm{cm}$, compared to the ion-sound Larmor radius $\rho_{is} = 1.44\,\mathrm{cm}$ measured at the X-point.

The simulation with $\eta_H = 10^{-9}$ (fourth panel) has no central island, but the current layer is beginning to fragment at this timestep. The current sheet width is $\delta_{FWHM} = 9.1$ mm compared to an ion-sound radius of $\rho_{is} = 2.1$ cm. In comparison with the simulations with stronger dissipation, the current sheet is localised in the radial direction, but this is more obvious for the final panel (see discussion below).

Figure 5.14 shows the late-time behaviour of the simulation with $\eta_H = 10^{-9}$. The long current sheet that spreads along the inner-lower outer-upper separatrix arm is unstable. In the top panel, an additional flux-contour with value $A_T = 43.5\,\mathrm{mWb\,m^{-1}}$ has been plotted (orange) to show that the islands are regions of closed flux, and there are additional x-points between the islands and the public vertical field. In the third panel the connectivity of this flux-contour has changed again, indicating that reconnection has occurred at these x-points. The regions of strong positive current density in the middle and bottom panels may be additional current sheets caused by this secondary reconnection. It must be noted that the stretched grid is concentrated at the main x-point, and therefore such small-scale

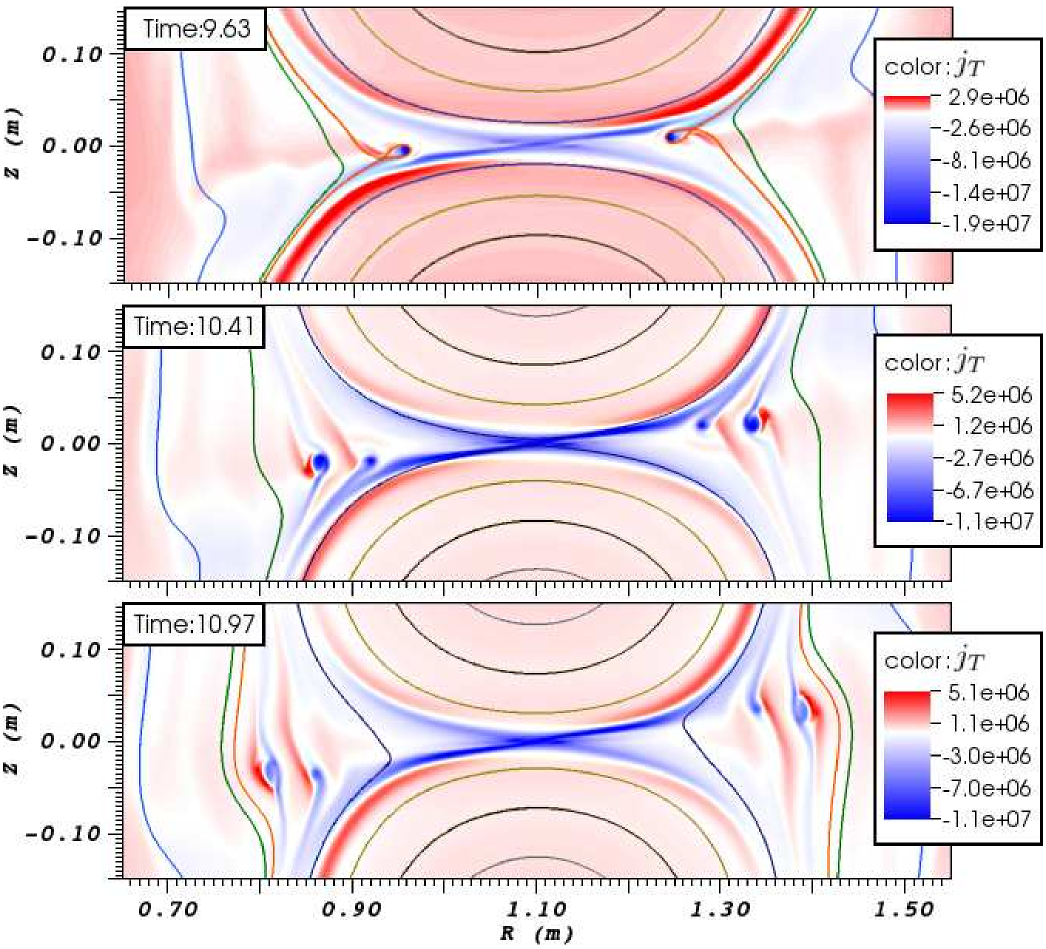

Figure 5.14: Instability of the current sheet for the Cartesian Hall-MHD simulation with $\eta_H = 10^{-9}$. The current density, j_T in $\mathrm{A\,m^{-2}}$, is shown in colour-scale, and the coloured contours are of the magnetic potential, A_T. The additional orange contour shown in the first and third panel has value $A_T = 43.5\,\mathrm{mWb\ m^{-1}}$.

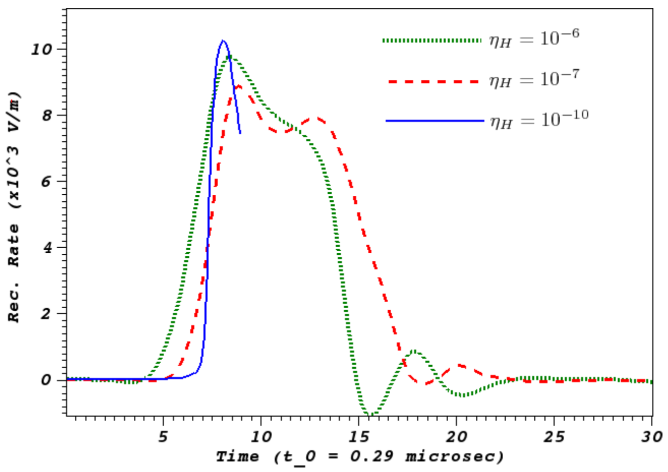

Figure 5.15: The reconnection rate $\partial_t A_T$ plotted against normalised time for the Cartesian Hall-MHD simulations with hyper-resistivity $\eta_H = 10^{-6}$ (green dotted), $\eta_H = 10^{-7}$ (red dashed), and $\eta_H = 10^{-10}$ (blue solid) up until the time of fragmentation. All other parameters are kept constant ($\eta = 10^{-5}$, $\mu = 10^{-3}$ and $d_i = 0.145$).

secondary current sheets may not be well resolved. However, this should only mean that the islands dissipate faster, and it should not change the qualitative picture.

Finally, the simulation with $\eta_H = 10^{-10}$ (bottom panel in Figure 5.13) has an extended tilted current sheet, but also has a localised region of strong out-of-plane current, j_T, at the X-point. The FWHM length of the current sheet across $Z = 0$ is measured to be $\Delta_{FWHM} = 4.4$ cm and the width is $\delta_{FWHM} = 6.5$mm, compared to $\rho_{is} = 3.1$cm measured at the X-point at this time. Note that the strong gradients in current density give rise to localised hyper-resistive heating, which further increases ρ_{is} despite reductions in η_H. The separatrices of the x-point have opened up in the outflow region, and there are sharp gradients in the current density across the separatrix arms consistent with classical pictures of fast reconnection (see, for example, Section 1.3.3). However, at later times, $t \approx 9.5\,\tau_0$, the x-point collapses again and islands are formed (not shown).

The time of the snapshot in the bottom panel of Figure 5.13 ($\eta_H = 10^{-10}$) is greater than that for the top-panel ($\eta_H = 10^{-6}$), suggesting a slower average reconnection rate despite the large localised current density at the x-point. To investigate this we plot the reconnection rate against time for three values of the hyper-resistivity, $\eta_H = 10^{-6}$, 10^{-7} and 10^{-10}, in Figure 5.15. Note that for $\eta_H = 10^{-8}$, 10^{-9} the sheet becomes unstable before any peak in the reconnection rate. For $\eta_H = 10^{-6}$ the peak rate is $(\partial_t A_T)_{\max} = 9.76\,\mathrm{kV\,m^{-1}}$ at $t = 8.34\tau_0$, and the average rate is $\langle \partial_t A_T \rangle = 4.68\,\mathrm{kV\,m^{-1}}$. For $\eta_H = 10^{-7}$ the peak is $(\partial_t A_T)_{\max} = 8.83\,\mathrm{kV\,m^{-1}}$ at $t = 8.79\tau_0$ and the average is $\langle \partial_t A_T \rangle = 3.87\,\mathrm{kV\ m^{-1}}$. Both the peak and the average reconnection rates decrease as η_H is reduced from 10^{-6} to 10^{-7}. The simulation with $\eta_H = 10^{-10}$ has much slower reconnection rate initially, but begins to enter an explosive phase at $t \approx 6.5\tau_0$. This is very close to the time when the current sheet width, δ_{FWHM}, drops below ρ_{is} (which occurs at $t = 7\tau_0$). The separatrices open up in the outflow direction only after the width drops below this threshold. The trend of decreasing reconnection rate with decreasing dissipation is broken, as the peak reconnection rate here is $(\partial_t A_T)_{\max} = 10.2\,\mathrm{kV\,m^{-1}}$, higher than both the $\eta_H = 10^{-6}$ and $\eta_H = 10^{-7}$ cases. Note that we do not calculate the average reconnection rate for $\eta_H = 10^{-10}$ because the current sheet in this simulation does fragment at $t \approx 9.5\tau_0$.

The out-of-plane electric field is uniform for steady-state reconnection in two dimensions (see Chapter 1). Although these simulations are not steady-state, the diffusion region can become quasi-steady at around the time of a peak in the reconnection rate. Figure 5.16 shows 1D profiles of the out-of-plane electric field, E_T, plotted against R and Z for the simulation with $\eta_H = 10^{-7}$. The time $t = 8.79\tau_0$ corresponds to the peak reconnection rate (see Figure 5.15). This electric field is calculated by the time difference of A_T (a primary variable that is output in these simulations) between snapshots. In Cartesian geometry (R, T, Z) this electric field $E_T = -\partial_t A_T$ can be written in component form as

$$E_T = -(v_Z B_R - v_R B_Z) + \frac{d_i}{n}(j_Z B_R - j_R B_Z) + \eta j_T - \eta_H \nabla^2 j_T. \tag{5.8}$$

In Figure 5.16 we also plot the profiles of each term of equation 5.8 to show how it contributes to the total out-of-plane electric field. At the x-point ($R = 1.1$ m, $Z = 0$) the poloidal field goes to zero, $B_R = B_Z = 0$, and so both the Hall electric field $E_{T,\mathrm{Hall}} = (d_i/n)(\boldsymbol{j} \times \boldsymbol{B})_T = 0$ and the convective electric field $E_{T,\mathrm{conv}} = -(\boldsymbol{v} \times \boldsymbol{B})_T = 0$ there. Away from the x-point these two terms have the same order-of-magnitude contribution to E_T, and in fact the Hall term is larger closer to the x-point, suggesting that two-fluid effects are non-negligible for the simulation with $\eta_H = 10^{-7}$. At the X-point the only non-zero terms that can support the reconnection electric field are the resistive, $E_{T,\mathrm{res}} = \eta j_T$, and hyper-resistive $E_{T,\mathrm{hyp}} = -\eta_H \nabla^2 j_T$ electric fields. It is clear in Figure 5.16 that the hyper-resistive term supports E_T, dominating the resistive term in magnitude, for the region around the x-point. We have also plotted in Figure 5.16 the sum of all the terms on the right hand side of equation (5.8), $E_{T,\mathrm{tot}} = \sum E_{T,\mathrm{terms}}$. This does not exactly match the $-\partial_t A_T$ curve, as the snapshots were output infrequently for this simulation. Note that both measures of the total electric field $E_T = -\partial_t A_T$ and $E_{T,\mathrm{tot}} = \sum E_{T,\mathrm{terms}}$ are not uniform against R or Z, and so the reconnection is only quasi-steady rather than a true steady-state.

Figure 5.17 also shows the contributions to E_T from terms in equation (5.8), but for the simulation with hyper-resistivity $\eta_H = 10^{-10}$. This is also at the peak reconnection rate, $t = 7.9\tau_0$. Here the Hall electric field is clearly larger than the convective electric field in the region around the current sheet, $Z \in [-1, 1]$ cm at $R = 0$, and across R for several cm when $Z = 0$. The hyper-resistive electric field is still dominant over the resistive electric field, despite three orders-of-magnitude reduction in the hyper-resistive coefficient. Thus it is the balance between $E_{T,\mathrm{hall}}$ and $E_{T,\mathrm{hyp}}$ that sets the current sheet width in these Hall-MHD simulations.

Varying the out-of-plane field

In the resistive-MHD simulations it was found that the reconnection rate was insensitive to $\mathcal{O}(1)$ changes in the out-of-plane field, see Figure 5.8. Here, we see if this is also true for the Hall-MHD simulations.

Figure 5.18 shows the reconnection rate for three Hall-MHD simulations ($d_i = 0.145$ m, $\eta = 10^{-7}$) with out-of-plane field of $B_T = -1B_0$, $-2B_0$ and $-5B_0$ respectively. Also plotted for comparison is a hyper-resistive MHD simulation with $d_i = 0$, $\eta_H = 10^{-7}$ and $B_{T0} = -1B_0$. Note that the curves for the Hall-MHD simulation and hyper-resistive MHD simulation with $B_{T0} = -1B_0$ are the same as those plotted in Figures 5.15 and 5.9 respectively. It is clear that increasing the out-of-plane field reduces the reconnection rate towards the collisional limit (the simulation with $d_i = 0$). The reconnection rate is much more sensitive to the effects of plasma compressibility in the two-fluid regime, than in the resistive MHD regime in Figure 5.8.

Figure 5.19 shows the density asymmetry (only the half in $R > 1.1$, the other half is identical after reflection in $R = 1.1$ and $z = 0$) for the same Hall-MHD simulations as in Figure 5.18, for varying B_{T0}. Increasing the out-of-plane field decreases (increases) the maximum (minimum) value of the density towards the background value. The values of the ion-sound Larmor radius at the X-point for

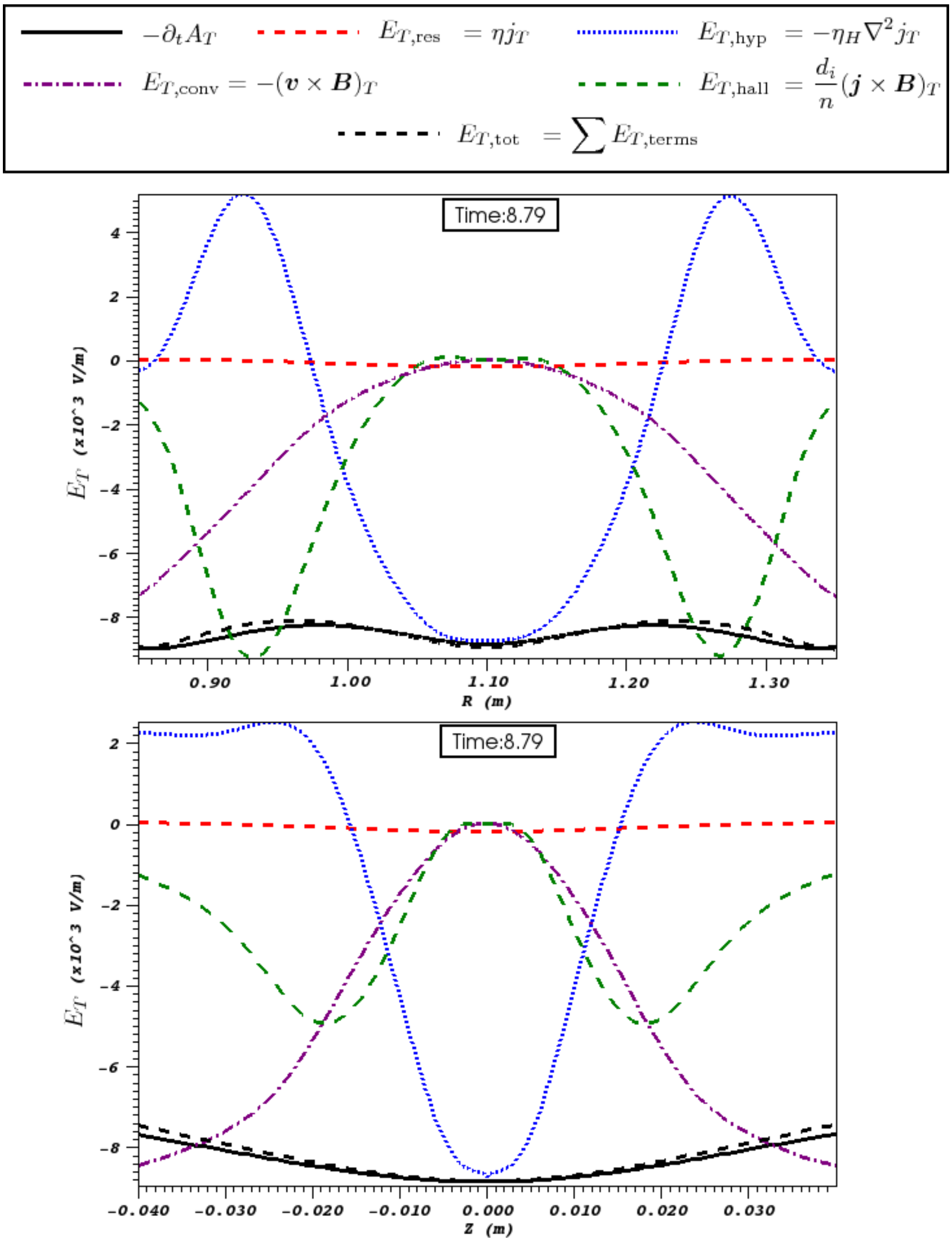

Figure 5.16: Contributions from terms in Ohm's law to the out-of-plane electric field, E_T measured in $\mathrm{V\,m^{-1}}$, for the Hall-MHD simulation with hyper-resistivity $\eta_H = 10^{-7}$. Also plotted is $-\partial_t A_T$, calculated by the time difference of the out-of-plane potential A_T between snapshots. Top: Plotted against radius R at $Z = 0$. Bottom: Plotted against height Z for $R = 0$.

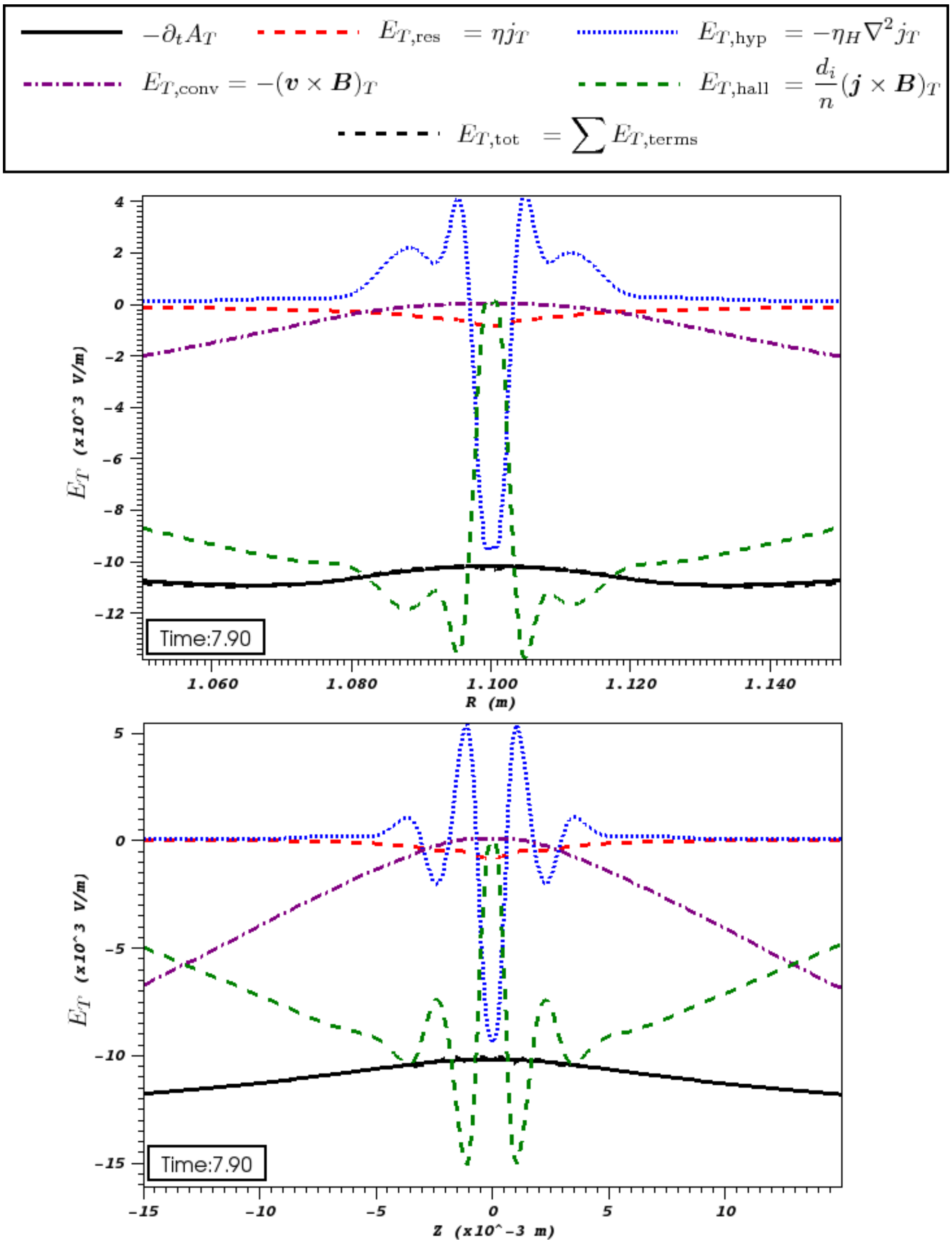

Figure 5.17: Contributions from terms in Ohm's law to the out-of-plane electric field, E_T measured in $\mathrm{V\,m^{-1}}$, for the Hall-MHD simulation with hyper-resistivity $\eta_H = 10^{-10}$. Also plotted is $-\partial_t A_T$, calculated by the time difference of the out-of-plane potential A_T between snapshots. Top: Plotted against radius R at $Z = 0$. Bottom: Plotted against height Z for $R = 0$. Note the values for the horizontal axis differ from Figure 5.16.

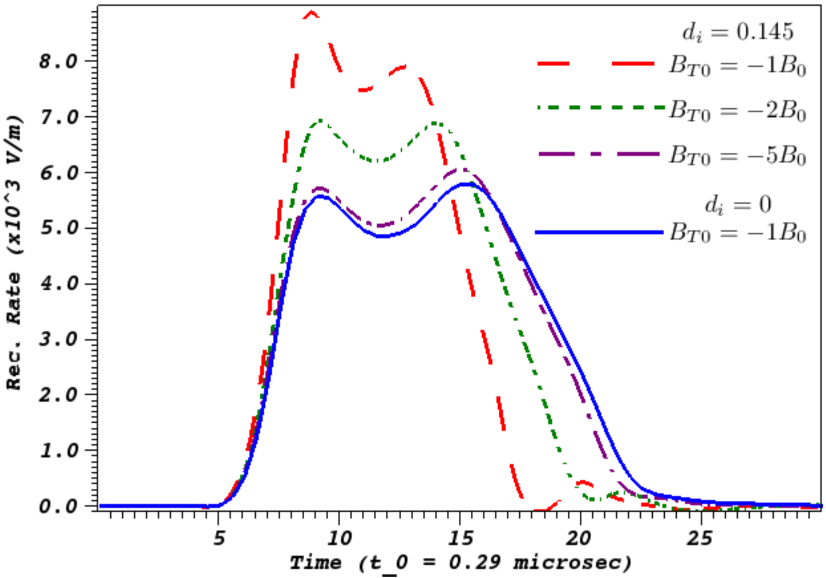

Figure 5.18: The reconnection rate, $\partial_t A_T$, measured in $\mathrm{V\,m^{-1}}$, for Hall-MHD simulations ($d_i = 0.145$ m, $\eta_H = 10^{-7}$) with $B_{T0} = -1, -2$, and $-5B_0$ for the red-dashed, green-dotted and purple dot-dashed lines respectively. Also plotted for comparison is the reconnection rate for the hyper-resistive MHD simulation ($d_i = 0$) with $\eta_H = 10^{-7}$, $B_T = -1B_0$.

$B_T = -1B_0$, $-2B_0$ and $-5B_0$ are $\rho_{is} = 1.52$ cm, 0.7 cm and 0.25 cm, respectively. However, the current sheet width does not vary much: it is $\delta_{FWHM} = 3.64$ cm, 3.94 cm and 4.3 cm, respectively. As $\rho_{is} \propto B_T^{-1}$, it is more plausible that these two fluid effects become important at the scale-length ρ_{is} rather than d_i (as d_i does not depend on B_T).

5.4.3 Discussion

It is important to determine whether merging-compression start-up in MAST lies within the purely collisional, or open x-point regimes. It was shown above that the open x-point regime occurs when the current sheet width, δ, drops below the ion-sound radius, ρ_{is}.

The value of ρ_{is} can be estimated directly from the experimental data. In merging-compression experiments electron temperatures have been measured in the range $10\,\mathrm{eV} \lesssim T_e \lesssim 1000\,\mathrm{eV}$, see Chapter 2. This, along with a typical toroidal field strength of 0.5 T, gives $\rho_{is} \approx 1 - 10$ mm. Within the series of resistive and Hall-MHD simulations listed above, some runs with the lowest dissipation coefficients have current sheet widths within this range (e.g. the Hall-MHD simulations

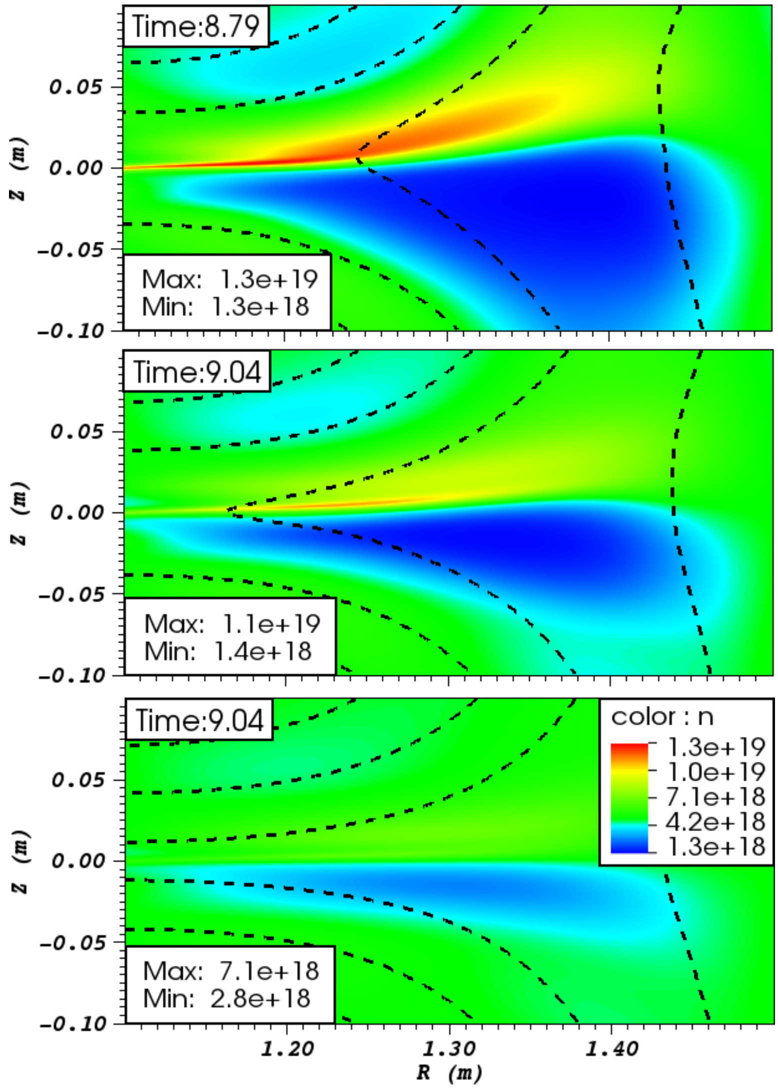

Figure 5.19: Plasma density, n in m^{-3}, and dashed-contours of the magnetic potential, A_T, for Hall-MHD simulations ($d_i = 0.145$ m, $\eta_H = 10^{-7}$) with $B_{T0} = -1B_0$ (top), $B_{T0} = -2B_0$ (middle) and $B_{T0} = -5B_0$ (bottom). The density colour scale is the same for all three plots and is given in the bottom plot. The maximum and minimum density values for each plot are indicated.

with $\eta_H = 10^{-9}$, $\eta_H = 10^{-10}$, or the resistive MHD simulation with $\eta = 10^{-5}$, $\mu = 10^{-4}$ that has a minimum width of $\delta = 7.59$ mm at the peak reconnection rate). Also, for numerical reasons, the values of the ion viscosity and hyper-resistivity (electron viscosity) have been enhanced with respect to the perpendicular values. For instance, a normalised perpendicular ion-viscosity (Braginskii 1965) calculated using the initial T_0 and n_0 would be $\mu = 10^{-7}$. It seems likely that the current sheet width can drop below the ion-sound radius for realistic merging-compression values of the ion and electron viscosities. This open x-point configuration, with a radially localised current sheet, may explain a narrow electron temperature peak of 2-3 cm width found in the experimental data (see Figure 2.11 with discussion in Chapter 2, and also Ono et al. 2012), provided that the electron heating is co-spatial with current (e.g. Ohmic heating).

5.4.4 Grid convergence study

It is important to check that the results presented thus far are converged, particularly for the simulations with the lowest dissipation coefficients. With the spectral element method, grid convergence can be examined by either refining/coarsening the size of the finite elements, via N_R and N_Z, or by changing the polynomial degree of the basis functions N_p. Here we do this by changing N_R and N_Z, while keeping N_p fixed.

Figure 5.20 shows a convergence test for the simulation with the lowest dissipation. The reconnection rate is a sensitive quantity to both global (driving) and local (e.g. numerical dissipation) effects, and so it is a suitable quantity to compare at different resolutions. The simulation with $N_R = 360$, $N_Z = 540$ is the same as that shown in Figures 5.13 and 5.15. The simulation with $N_R = 180$, $N_Z = 270$ has half the resolution in both directions, but the change in the peak reconnection rate is only 0.02% (from $(\partial_t A_T)_{\max} = 10.214\,\mathrm{kV\,m^{-1}}$ at $t = 7.94\,\tau_0$, for the higher resolution, to $10.231\,\mathrm{kV\,m^{-1}}$ at $t = 7.8\,\tau_0$ for the lower resolution run). Unfortunately, we are not able to reduce the resolution again by a factor of two due to numerical instabilities, and not able to double the resolution due to memory requirement (the highest resolution run uses 480 processors with a total of 864 GB of memory available). However, due to very good agreement in the peak reconnection rate we are confident that this simulation is converged in resolution up to this peak.

Figure 5.21 shows a convergence test for the simulation with $\eta_H = 10^{-8}$.

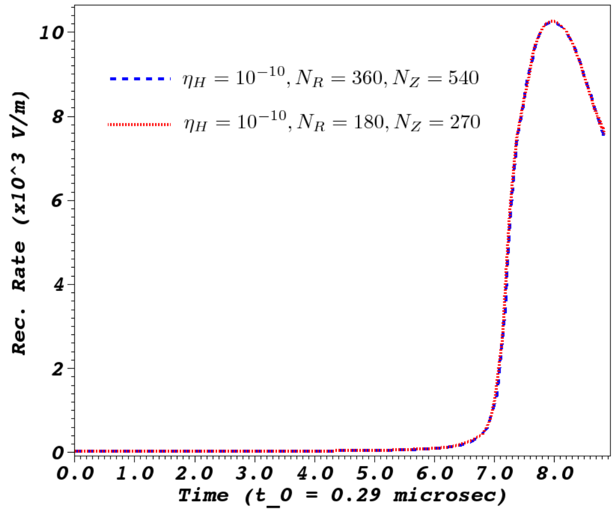

Figure 5.20: Convergence test of the reconnection rate, $\partial_t A_T$ at the x-point in $\mathrm{V\,m^{-1}}$, for the Hall-MHD simulation with $\eta_H = 10^{-10}$. The blue-dashed lines are from the simulation previously described, at $N_R = 360$, $N_Z = 540$, $N_p = 4$, and the red-dotted line is from a simulation with $N_R = 180$, $N_Z = 270$, $N_p = 4$.

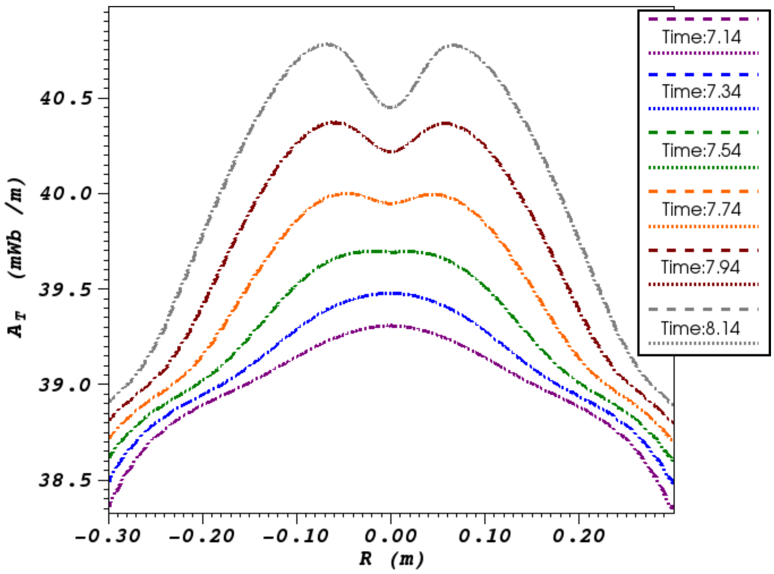

Figure 5.21: Plots of A_T against R, at $Z = 0$, for equally spaced times from the Hall-MHD control simulation performed at two different resolutions. The dashed lines are from a simulation with $N_R = 180$, $N_Z = 360$, and the dotted lines are from a simulation with $N_R = 90$, $N_Z = 180$.

The out-of-plane magnetic potential is plotted against R at $Z = 0$ at equally spaced times (every $0.2\,\tau_0$) during the time of the tearing-type instability. As $B_Z = \partial_R A_T$, and $B_R \approx 0$ on $Z = 0$ the points on the curves with zero gradient correspond to null points of the poloidal field, where a local maximum is an x-point and a local minimum is an o-point. Crucially, the solution bifurcates from one x-point to an x-o-x configuration at the same time $t = 7.54\,\tau_0$ (green line) for both simulations (in fact this is the time of the snapshot shown in Figures 5.10 and 5.11).

5.5 Toroidal-axisymmetric geometry

5.5.1 Effects on merging

The standard toroidal Hall-MHD simulation described here has the same plasma parameters as the standard Cartesian Hall-MHD simulations ($\eta = 10^{-5}, \mu = 10^{-3}, \eta_H = 10^{-8}$), but the initial conditions are as shown in Figure 5.2. The flux-ropes have radius $w = 0.4$ m, half-separation $a = 0.6$ m, radial position $R_i = 1.1$ m, and there is $B_v = -0.06B_0 = -0.03$ T of line-tied vertical flux.

When switching from Cartesian to toroidal axisymmetric geometry, the most obvious qualitative difference in the ideal (approach) phase of the merging is in the radial force balance of the flux-ropes. In Figure 5.22 the positions of the flux-rope o-points are plotted over time for three simulations. The toroidal simulations used are the standard toroidal axisymmetric simulation ($B_v = -0.06B_0$), and another identical simulation but with less vertical flux ($B_v = -0.04B_0$). Also plotted is the o-point position for the standard Hall-MHD simulation in Cartesian geometry for comparison. In the toroidal simulations, the flux-ropes oscillate radially due to the in-balance of the Lorentz forces from the vertical field, and the restoring hoop-force (there may also be forces due to image currents in the conducting walls). This radial motion of the flux-ropes could be minimised by a suitable choice of B_v. However, we do not do this here, as there is clear radial motion of the flux-ropes towards the central post in the experimental fast-camera images (see Figure 2.10). These radial oscillations have only small effect on the rate at which the o-points move to the mid-plane in the toroidal simulations. In the Cartesian simulation, the o-point does not get to the mid-plane due to the formation of the central island that stalls the reconnection. Islands are also formed in the toroidal

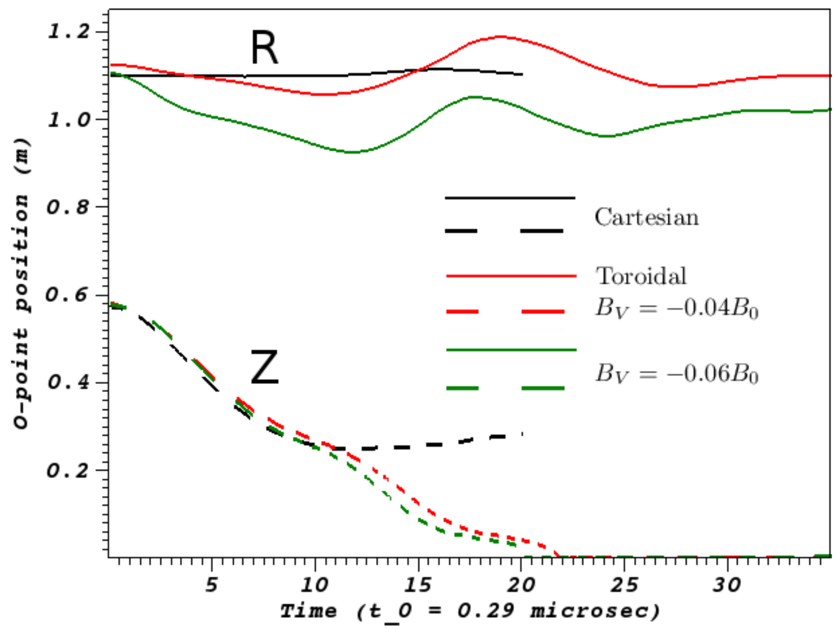

Figure 5.22: The o-point positions in R (top, solid lines) and Z (bottom, dashed lines) for the standard Cartesian Hall-MHD simulation (black), and the standard toroidal axisymmetric Hall-MHD simulation with vertical flux of $B_v = -0.04\, B_0 \equiv -0.02\,\mathrm{T}$ (red) and $B_v = -0.06\, B_0 \equiv -0.03\,\mathrm{T}$ (green).

simulations, see Figure 5.23 (the initial conditions for this simulation are shown in Figure 5.2). However, this island is quickly ejected as the symmetries present in the Cartesian simulations are broken in toroidal geometry. The total merge time is $T_{merge} \approx 25\tau_0$ for both toroidal simulations.

5.5.2 Final state

The two o-points in the standard toroidal simulation finish merging together at $t \approx 25\,\tau_0$, shortly after the last snapshot shown in Figure 5.23. The coalescence process triggers a lot of wave activity, which takes some time to dissipate. Figure 5.24 shows contours of the flux, $\psi = RA_\phi$, and toroidal current density, j_ϕ, at the final snapshot in this simulation ($t = 60\,\tau_0$), when the system is closer to a relaxed state.

This final state shows nested flux-surfaces in a tight-aspect ratio geometry, namely, a single spherical tokamak plasma. The current density is centrally peaked, but is also peaked in a ring structure just outside the dashed line (this flux contour has the same value of flux as the one overlying the separator at $t = 0$, see Figure 5.2). This ring structure overlies a region of high density, which

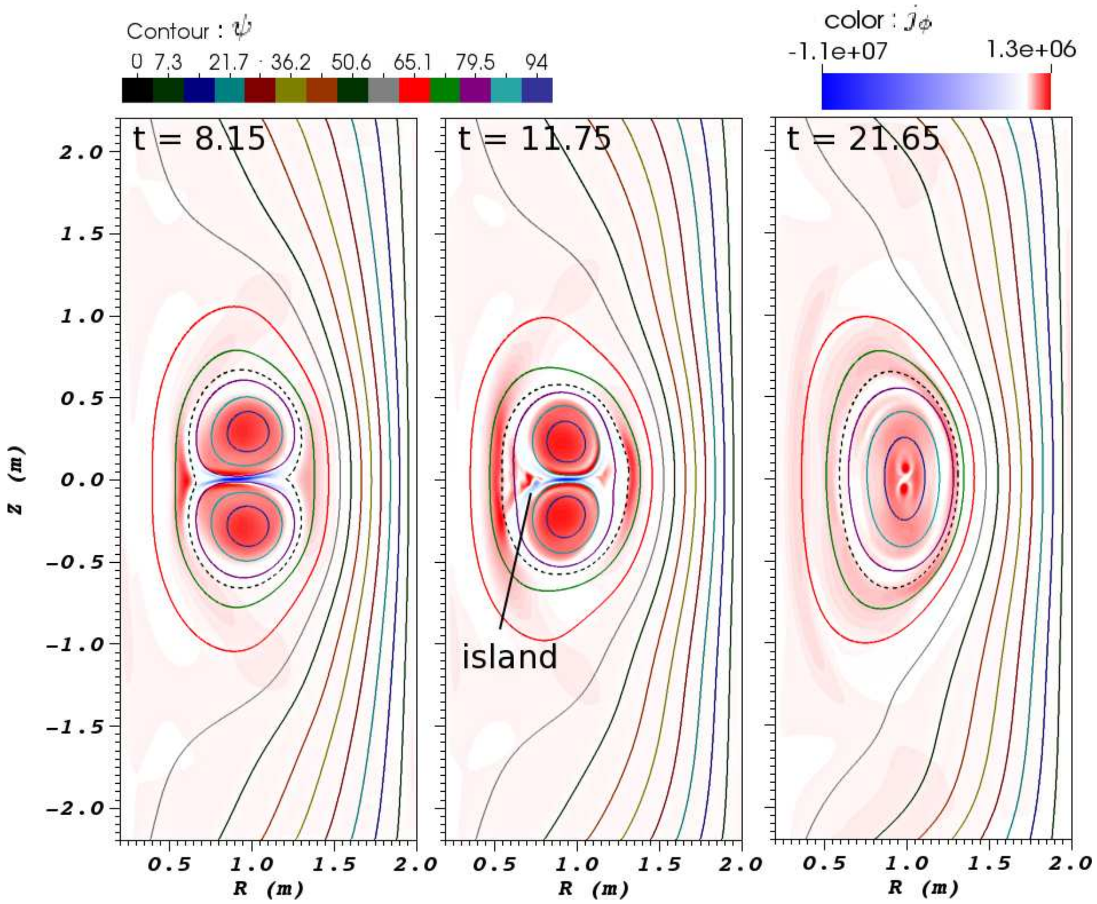

Figure 5.23: Snapshots of the merging for the toroidal Hall-MHD simulation with $\eta_H = 10^{-8}$, $\eta = 10^{-5}$, $\mu = 10^{-3}$ and $B_v = -0.06B_0 \equiv= -0.03$ T. Shown in each panel are contours of the flux, $\psi = RA_\phi$ (in mWb), and the current density in colour-scale, j_ϕ in $\mathrm{A\,m^{-2}}$. Also shown is the flux-contour with $\psi = \psi_{\mathrm{Xpt}} = 76.5\,\mathrm{mWb}$ that is the same contour as in Figure 5.2.

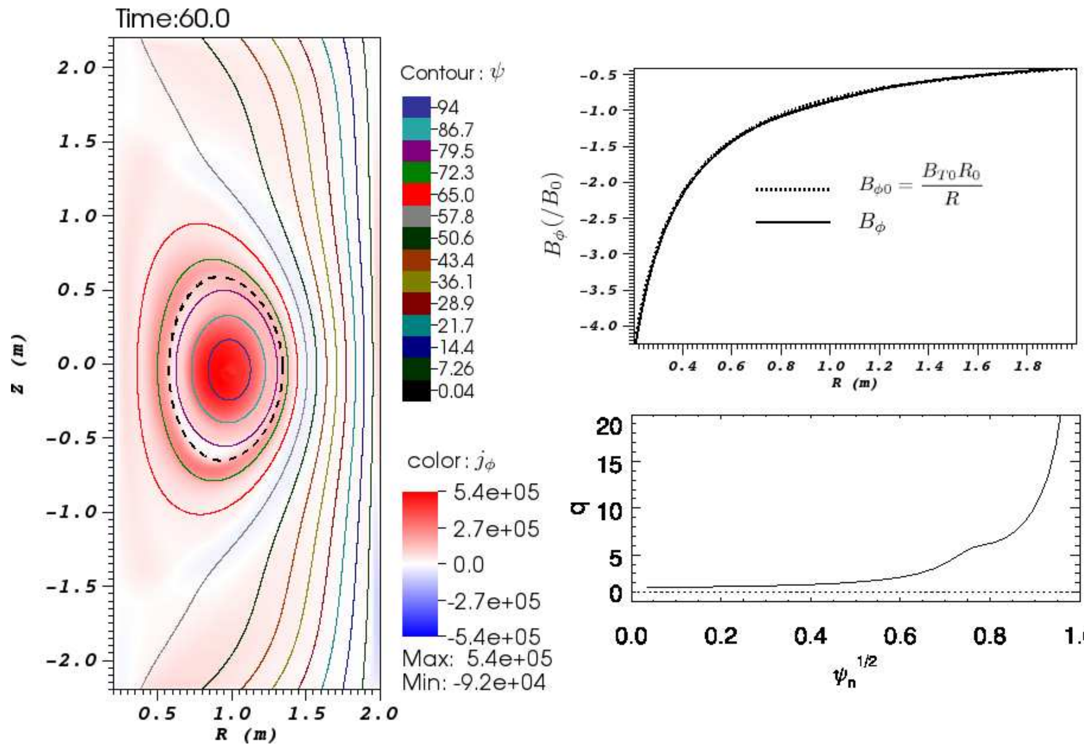

Figure 5.24: Left: Contours of the flux, $\psi = RA_\phi$ in mWb, and current density, j_ϕ in $\mathrm{A\,m^{-2}}$, in colour-scale, for the toroidal Hall-MHD simulation with $\eta_H = 10^{-8}$, $\eta = 10^{-5}$, $\mu = 10^{-3}$, $B_v = -0.06B_0 \equiv -0.03$ T), after the two flux-ropes are fully merged. Right-top: Toroidal magnetic field (solid-line), B_ϕ in units of $B_0 = 0.5$ T, against major radius in a cut through the magnetic-axis. Also shown for comparison is the vacuum field $B_{\phi 0}$ (dotted-line). Right-bottom: The safety factor, or q-profile, of the magnetic configuration at this time, plotted against the square-root of the normalised flux.

is discussed below. In the top-right panel of Figure 5.24 we plot a radial profile of the toroidal field through the centre of the nested flux surfaces, along with the vacuum toroidal field for comparison. The spherical tokamak is narrowly paramagnetic, as the reconnection heating is not sufficient to suppress the paramagnetic configuration of the initial flux-ropes, see Figure 5.2.

The bottom right panel of Figure 5.24 gives the q-profile, or safety factor, for the magnetic configuration at $t = 60\,\tau_0$. This q-profile is a measure of the number of times the field-lines loops around the vessel toroidally for each poloidal rotation, which is important for stability analysis of the tokamak plasma with respect to current driven instabilities (see e.g. Wesson 2011). This q-profile is calculated by performing the integral

$$q = \frac{1}{2\pi} \oint \frac{1}{R} \frac{B_\phi}{B_p} ds$$

around closed flux contours, where $B_p = \sqrt{B_R^2 + B_Z^2}$ and ds is along the contour. It is plotted against the root of the normalised flux, defined by $\psi_n^{1/2} = \sqrt{[\psi(R_{\mathrm{mag}}) - \psi(R)] \,/\, [\psi(R_{\mathrm{mag}}) - \psi(R = 0.2)]}$, where R_{mag} is the position of the magnetic axis, and $R = 0.2$ is the centre column which bounds the last closed flux surface.

A complete stability analysis of this final state is rather involved, and beyond the scope of this thesis. However, we do note that the safety factor is above the critical value of unity for all values of $\psi_n^{1/2}$. For $q < 1$, the magnetic configuration may become unstable to the $m = n = 1$ internal kink instability Wesson (2011), which would require 3D simulations to properly model.

In the current experimental campaign in MAST (Summer 2013), there are plans to experimentally measure the q-profiles directly after merging. This q-profile can be compared with the results, but some care must be taken when doing so. For instance, we do not include the P2 poloidal field coils within this model, or neoclassical effects such as the boot-strap current (see e.g. Wesson (2011)). The latter may be significant after merging when the plasma β has increased and there are significant thermal pressure gradients.

5.6 Comparison with experimental data

5.6.1 Synthetic CCMV signal

Here, we present the results of toroidal axisymmetric simulations with $R_i = 0.9$ m and $Z = \pm a = \pm 0.8$ m. This initial position, for the centre of the flux-rope current distributions, is chosen so that the ideal (approach) phase is more similar to that for MAST experimental shots 25636 and 25740, where the flux-ropes appear to move down the central post (see e.g. Figure 2.10). This is done in order to produce synthetic Thomson Scattering profiles (the TS lasers take data in the range $R \in [0.2, 1.2]$, see Figure 2.11) that can be compared with the experimental data for these shots. The effect of changing the initial position on the merging can be seen in the top panel of Figure 5.25. This panel shows the o-point positions for a resistive-MHD ($\eta = 10^{-5}$, $\mu = 10^{-3}$, $d_i = \eta_H = 0$) and a Hall-MHD ($d_i = 0.145$ m, $\eta_H = 10^{-8}$) simulation, both starting at this new initial position. The merge-time for the Hall-MHD simulation has increased from $T_{\mathrm{merge}} \approx 25\,t_0$ to $80\,t_0$, and the resistive-MHD simulation takes close to $300\,t_0$ to merge. Note that there is fast radial motion of the o-point in the Hall-MHD simulation at $t \approx 60\,t_0$, after the flux-ropes have shrank considerably due to reconnection. This motion occurs as the reconnection outflow is directed radially inwards (causing the merging o-points to be pushed radially outwards).

The bottom panel of Figure 5.25 shows synthetic CCMV20 (Central Column MirnoV 20, which measures $\partial_t B_Z$ at $R = 0.2$ m, $Z = 0$, see Figure 2.9) profiles from these two simulations. These synthetic profiles were produced by time-differencing the value of B_Z between snapshots at $R = 0.22$ m, $Z = 0$. The first peak for both signals coincides at $t = 16\,t_0$, and after this the subsequent oscillations have similar period, even after the flux-ropes in the Hall-MHD simulation are fully merged at $t \approx 80\,t_0$. To explain this, we took the time derivative of the radial position for the o-point in the resistive-MHD simulation (and also changed the sign for clearer comparison) which is plotted as the radial-velocity $-v_R$(o-point). The period of oscillation in $-v_R$(o-point) clearly lines up with the CCMV20 signal, except for the first peak. For the first peak, it is apparent that the motion of the flux-ropes towards the mid-plane (the vertical motion) has a greater effect on $\partial_t B_Z$ than the radial motion.

The synthetic CCMV20 signals can be compared to the experimental data shown in Figure 2.11. In the simulations the period of the oscillations is $\approx$

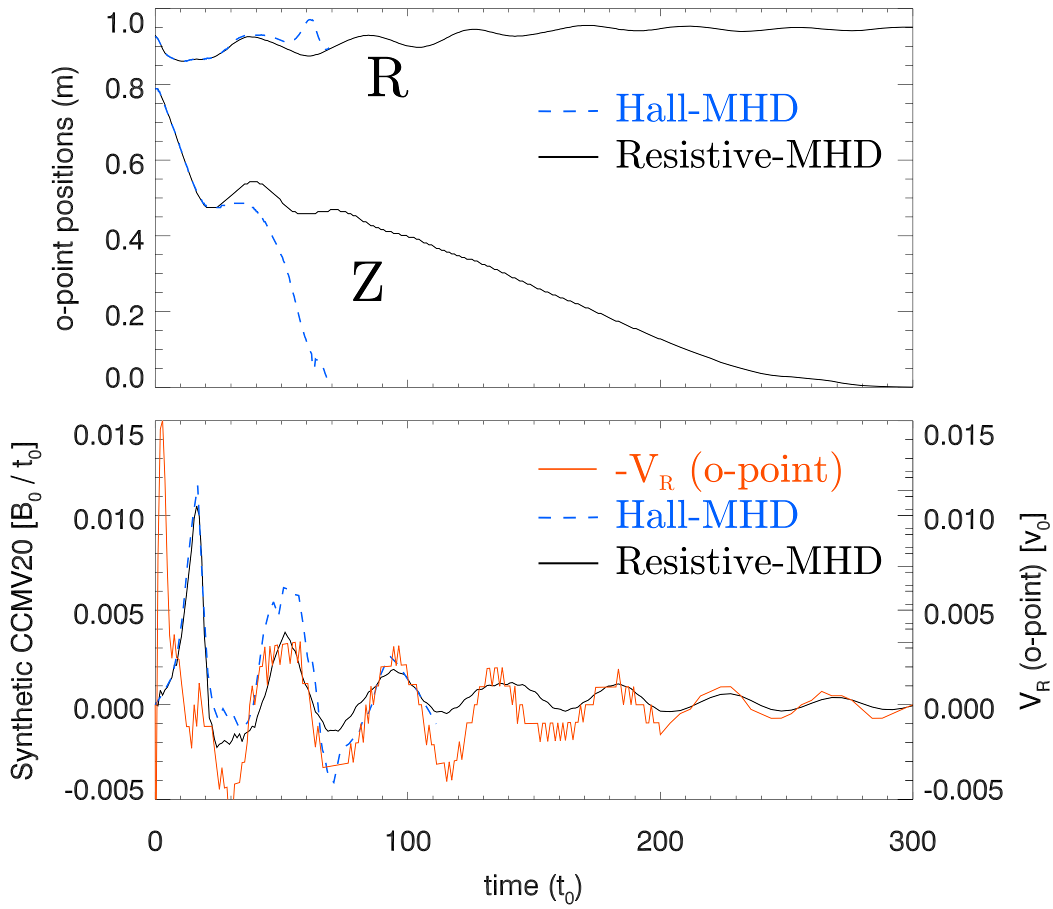

Figure 5.25: Top: The o-point positions in R (top lines) and Z (bottom lines) for a Hall-MHD simulation (blue-dashed), and a resistive-MHD simulation (black-solid), with initial radial position $R_i = 0.9$ m, half-separation $a = 0.8$ m and flux-rope radius $w = 0.4$ m. Bottom: Synthetic CCMV20 (central post pick-up coil measuring $\partial_t B_Z$ at $R = 0.2$ m, $Z = 0$; see Figure 2.9) for the same Hall-MHD and resistive-MHD simulations. The orange line is the (negative) time derivative of the resistive-MHD o-point radial position (the o-point radial velocity $-v_R$(o-point)). Note the high-frequency spikes on the orange line are an artifact of numerically differentiating the infrequent snapshots.

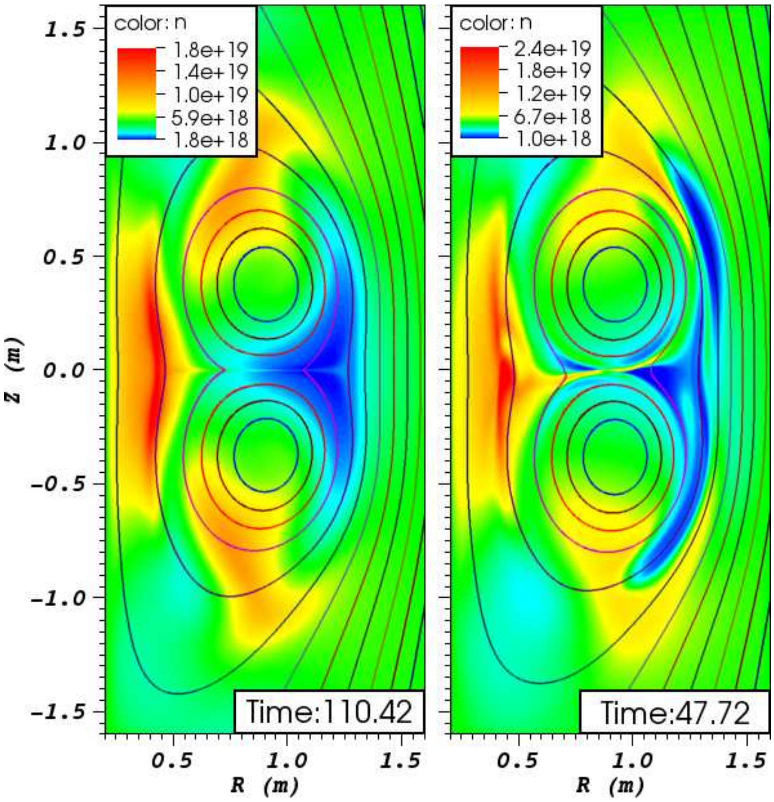

Figure 5.26: Contours of the flux, $\psi = RA_\phi$ in mWb, and density in colour scale, n in m^{-3}, for a resistive $d_i = \eta_H = 0$ (left), and Hall-MHD simulation $d_i = 0.145$, $\eta_H = 10^{-8}$ (right). The simulations start from the same initial conditions, with vertical flux $B_v = -0.06B_0$, initial radial position $R = 0.09$, and initial half-separation $a = 0.8$. The snapshot times are chosen for comparison when an equal amount of flux has been reconnected.

$45\, t_0 \approx 13\,\mu$s, compared with a period of $\approx 30\,\mu$ s in the experimental data. The difference may be due to an overestimate of the current in the flux-ropes in this simulation (we use $I_{\text{plasma}} = 268$ kA based on shot 25740, and we assume that all of this is within the flux-ropes. However, in reality, some of this current density may remain around the P3 coils).

5.6.2 Density profiles

Figure 5.26 shows the plasma density for these resistive and Hall-MHD toroidal-axisymmetric simulations (with $a = 0.8$ m, $R_i = 0.9$ m, $B_v = -0.06B_0$, $w = 0.4$ m). In the resistive MHD simulation there is an $\mathcal{O}(1)$ inboard-outboard asymmetry in the plasma density. To understand the origin of this asymmetry, we consider the mass continuity equation in component form

$$\partial_t n = -\partial_R(nv_R) - nv_R/R - \partial_Z(nv_Z),$$

where the second term on the right-hand-side is due to the geometrical effects of toroidal geometry; it is related to the smaller volume on the inboard side compared with the outboard side. If a large negative (positive) radial momentum flux, nv_R, is generated by the Lorentz forces in the plasma during the merging, the plasma flow is more convergent (divergent) than a similar flow pattern in Cartesian geometry.

In the resistive MHD simulation, the density begins to increase on the inboard side, and decrease on the outboard side, early in the approach phase, as there is a net inwards radial motion of the flux-ropes towards the centre post. This asymmetry becomes more pronounced as the reconnection outflow jets fill up the inboard side, and when the flux-ropes are very close to the central post. The low plasma β means that the density variations can be $\mathcal{O}(1)$, and equalise on timescales larger than the merge time. In fact, the inner density peak persists even after the flux-ropes are fully merged (and until the end of the simulation).

The density plot for the Hall-MHD simulation appears more complex. However, it can be understood as the super-position of the toroidal resistive-MHD density asymmetry just described, and the Cartesian Hall-MHD density "quadrupole" that was shown in Figure 5.11. A region of higher density lies along the inner-lower outer-upper separator, that, on combining with the resistive-toroidal density asymmetry, gives the highest density on the inner-lower quadrant. The lowest value of the density lies in the density cavity of the outer-lower quadrant. The quadrupole part of this density profile becomes weaker as flux-ropes fully merge, as it is supported by the parallel electric field on newly reconnected field lines (see also Kleva et al. 1995).

Figure 5.27 shows a series of synthetic Thomson Scattering density profiles from the Hall-MHD simulation of Figure 5.26, and the experimental Nd:YAG TS profiles of electron density, n_e, from MAST shot 25740 (see also Figure 2.11). The synthetic density profiles are taken at $R \in [0.2, 1.2]$ m and at $Z = 0.015$ cm, the same position as the Nd:YAG laser profiles (note the upper and lower P6 coil currents were approximately equal for this shot, so there should not be any vertical shift of the plasma). The synthetic profiles are equally spaced in time during the simulation, at every $20\tau_0$ until merging completes. At $t = 20\tau_0$,

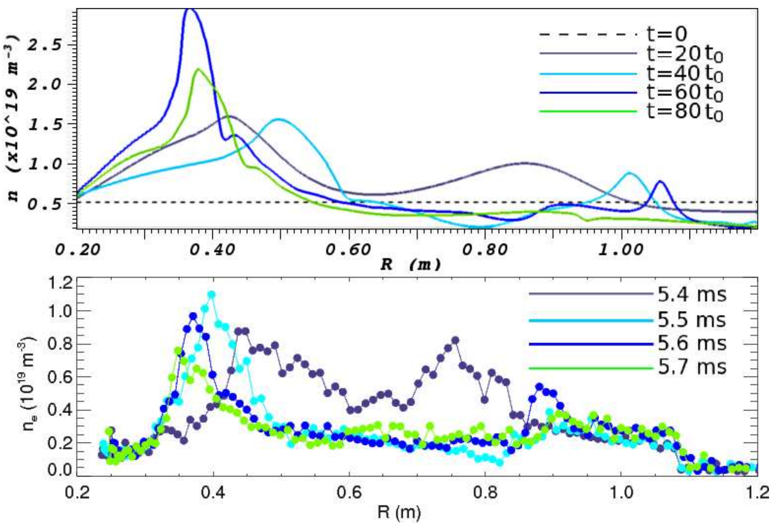

Figure 5.27: Top: Simulated Thomson scattering density traces in the Hall-MHD simulation of Figure 5.26 at $Z = 0.015$ m and $R \in [0.2, 1.2]$ at $t = 0, 20, 40, 60, 80\tau_0$. Bottom: Electron density profiles from experiment measured by the Nd:YAG TS laser across the same radial chord at $t = 5.5$ ms, 5.6 ms, 5.7 ms and 5.8 ms. This density plot is also shown in Ono et al. (2012), for a narrower range of R.

there is a clear double peak in the density profile as the cut intersects the high-density region on the inboard side and the high-density separator arm on the outboard side. As the merging progresses, the radial position of the inner peak changes, depending on the position of the inner edge of the radially oscillating flux-ropes. The second peak is pushed radially outwards, as the flux-ropes collide, and over time it decreases in magnitude. At $t = 80\tau_0$ (green line) the flux-ropes in the simulation are fully merged and the quadrupole-like density feature has disappeared; it is only present during reconnection. The time evolution of the density peaks is similar to the experimental data. As discussed above, both two-fluid effects and tight aspect-ratio toroidal geometry are needed to explain this double-peaked profile in the simulations.

5.6.3 Separate temperature simulations

As well as experimental density profiles, there are 1D TS profiles of electron temperature, T_e, taken with a time resolution of $0.1-1$ ms during the merging, and 2D T_e profiles taken several milliseconds after the merging (see Figures 2.11 and 2.12, and the discussion in Section 2.2.4). Also, there is a possibility of measuring 2D ion temperature profiles in the current experimental campaign in MAST, using a Doppler-tomography system. In this section, we present some initial results of simulations that separately evolve the ion and electron temperatures. We do not attempt to reproduce the exact experimental temperature profiles, as this would require additional physics outside of this model. For ions, this would require anisotropic ion viscosity with corrections for weak collisionality. Adding these effects into the model will be a subject of future work. For electrons, a precise model of the electron diffusion region in a semi-collisional regime is needed. Simulations have explored the collisionless strong guide-field regime (e.g. Hesse et al. 2002; Ricci et al. 2004), but no work has been done from first principles (PIC simulations with collisions) for semi-collisional strong-guide field reconnection. This model of the diffusion region may need to include electron inertia and kinetic effects such as Landau damping, which can be an important electron heating mechanism in the collisionless regime (Loureiro et al. 2013). The present results, however, will be useful as a basis to compare different transport models in the future.

For these simulations, we use separate ion and electron pressure equations, where the ion (electron) flows advect the ion (electron) thermal pressures, and the resistive and hyper-resistive heating is applied to electrons, while the ion viscous heating is applied to ions only. Here we also use an electron temperature dependent resistivity (see equation (1.20), and Spitzer 1962). For numerical reasons, the ion viscosity and hyper-resistivity have no temperature dependence. We do not include the ion-electron equilibration term (see equation (1.22), and Braginskii 1965), as the collisional equilibration time is $\tau_{eq} \gtrsim 0.2$ ms (see equation (2.6)), which is much longer than the merge time. The modified energy equations below take the place of equation (5.5):

$$(\gamma - 1)^{-1} \left[\partial_t p_e + \boldsymbol{v}_e \cdot \boldsymbol{\nabla} p_e + \gamma p_e \boldsymbol{\nabla} \cdot \boldsymbol{v}_e\right] = \eta j^2 + \eta_H (\boldsymbol{\nabla} \boldsymbol{j})^2 - \boldsymbol{\nabla} \cdot \boldsymbol{q}_e, \tag{5.9}$$

$$(\gamma - 1)^{-1} \left[\partial_t p_i + \boldsymbol{v}_i \cdot \boldsymbol{\nabla} p_i + \gamma p_i \boldsymbol{\nabla} \cdot \boldsymbol{v}_i\right] = -\boldsymbol{\pi}_i : \boldsymbol{\nabla} \boldsymbol{v}_i - \boldsymbol{\nabla} \cdot \boldsymbol{q}_i, \tag{5.10}$$

where the heat fluxes are given by $\boldsymbol{q}_{i,e} = -\kappa_{i,e}^{\parallel} \boldsymbol{\nabla}_{\parallel} T_{i,e} - \kappa_{i,e}^{\perp} \boldsymbol{\nabla}_{\perp} T_{i,e}$. The parallel and perpendicular thermal conductivities $\kappa_{i,e}^{\parallel}$ and $\kappa_{i,e}^{\perp}$ are the Braginskii (1965) parallel and perpendicular coefficients evaluated at the initial T_0. These equations are given in flux-source form in Appendix A.6 for Cartesian geometry. However, here we present results only for toroidal axisymmetric geometry.

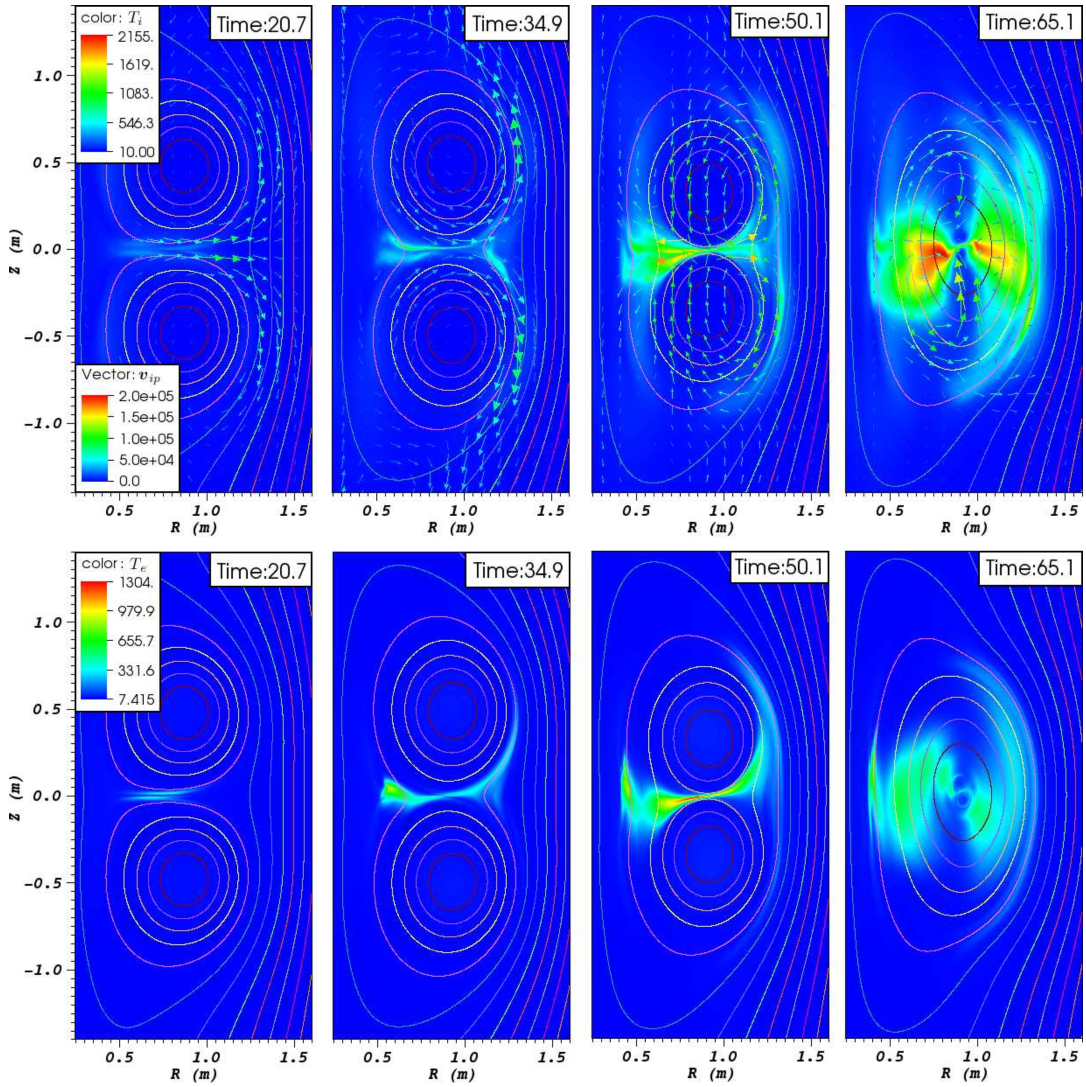

Figure 5.28: Ion (top) and electron (bottom) temperatures, T_i and T_e (in eV), at four times for the two-temperature toroidal-axisymmetric Hall-MHD simulation with $d_i = 0.145$, $\eta_H = 10^{-8}$. Also plotted in the top row are the ion in-plane velocity vectors, $\boldsymbol{v}_{ip}$ (in $\mathrm{m\,s^{-1}}$).

Figure 5.28 shows the ion (top-row) and electron (bottom-row) temperatures, as well as the ion in-plane bulk velocity vectors (arrows) at four snapshots during the merging ($t = 20.7, 34.9, 50.1, 65.1\tau_0$). The ions appear to be heated as they outflow from the diffusion region, rather than where the jets hit the public flux. We checked the magnitude of the different components of the viscous heating term, $-\boldsymbol{\pi}_i : \boldsymbol{\nabla}\boldsymbol{v}_i$, in equation (5.10). The dominant viscous heating terms for the snapshots at $t = 20.7, 34.9$ and $50.1\,\tau_0$ are $\mu(\partial_Z v_{iR})^2$ and $\mu(\partial_Z v_{iZ})^2$ (at the last snapshot the outflow jets have stopped and the heating rate is reduced). We find that the second of these terms is much smaller in resistive-MHD simulations, and is large here due to the tilt of the outflow jets (see also Figure 5.10).

At $t = 65.1\,\tau_0$, the ion temperature profile has a hollow structure, and spreads around the flux-surfaces due to a combination of parallel heat conduction and flows generated by the oscillating flux-rope as it relaxes. The ion temperature profile is also tilted in the same direction as the tilted ion outflow jets. This tilting may be an observable signature of two-fluid reconnection with a strong toroidal field, and can be compared with possible future ion temperature data.

For electrons, we find that the strongest dissipative heating term within equation (5.9) is $\eta_H(\partial_Z j_\phi)^2$ for the snapshots at $t = 20.7$, 34.9, and $50.1\tau_0$. The resistive heating terms are typically orders-of-magnitude smaller (due to both the temperature dependence, and because the hyper-resistive term is setting the dissipation scale; see Figures 5.16 and 5.17) at these times. Thus the electron heating here is not co-spatial with the current (it heats on the gradients of $j_\phi \propto v_{e\phi}$, similar to an electron viscous heating). There is no clear central peak in the electron temperature here, in contrast to the experimental data (see Figure 2.11).

The maximum electron temperature in this simulation is similar to the maximum T_e achieved during merging-compression experiments ($\approx 1.2\,\mathrm{keV}$ in shot 9177, see Ono et al. 2012). However, the total current within the vessel for that shot was $400\,\mathrm{kA}$, which is somewhat larger than the value of $I_{\mathrm{plasma}} = 267\,\mathrm{kA}$ used in these simulations. The discrepancy in both magnitude and spatial distribution of the high temperature electrons will be a subject of future investigation (see Section 6.2).

5.7 Summary and conclusions

In this chapter we have presented results from 2D fluid simulations of merging-compression plasma start up within the Mega-Ampere Spherical Tokamak (MAST). In resistive MHD ($d_i = \eta_H = 0$), the flux-ropes enter the sloshing-regime due to magnetic pressure pile-up on the sheet edge for low resistivities ($\eta \lesssim 10^{-5}$). In the Hall-MHD simulations ($d_i = 0.145$ m, $\eta_H \neq 0$), the qualitative behaviour of the merging depends upon the ratio of the collisional current sheet width, δ, to the ion-sound radius, $\rho_{is} = \sqrt{T_e/m_i}/\Omega_{ci} = \sqrt{\beta_e/2}\, d_i$. We varied δ by changing η_H, as the hyper-resistivity balances the reconnection electric field at the X-point. In the limit of $\delta \gg \rho_{is}$, the reconnection rate tends to the collisional limit. For $\delta \ll \rho_{is}$, the outflow separatrices open up and the peak reconnection rate increases, in agreement with previous studies (Kleva et al. 1995; Simakov et al. 2010; Schmidt et al. 2009). However, in the intermediate regime, $\delta \gtrapprox \rho_{is}$, we find that the current sheet is highly unstable to a fast tearing-type instability, see e.g. Figure 5.14. This instability is not observed for the purely collisional case ($\rho_{is} = d_i = 0$) for the same dissipation coefficients (e.g. the hyper-resistive simulation with $\eta = 10^{-6}$, $\eta_H = 10^{-9}$, $\mu = 10^{-3}$). For $\eta_H = 10^{-8}$, a central island forms and stalls the reconnection, and for lower dissipation $\eta_H = 10^{-9}, 10^{-10}$ we typically see multiple islands that are formed off-centre and ejected.

In toroidal axisymmetric geometry, the flux-ropes oscillate radially between the hoop-force and additional vertical flux. This breaks symmetries present in the Cartesian case, and the central island for the simulation with $\eta_H = 10^{-8}$ can be radially ejected. The final state after merging and relaxation is a single spherical tokamak plasma with nested flux-surfaces and a monotonically increasing q-profile (with $q > 1$ everywhere). The density profiles in these toroidal Hall-MHD simulations are affected both by the tight-aspect ratio toroidal geometry and two-fluid effects. Simulated line profiles of the plasma density against major radius, in a slice along the current sheet, show double-peaked profiles that have very similar time evolution to those seen in experimental Thomson Scattering profiles.

Finally, we presented results using a two-temperature formulation with separate ion and electron heat conduction and advection. Hollow temperature profiles were found resembling those seen in experimental 2D electron temperature profiles, see Chapter 2. However, the electron heating was found to be dominated by hyper-resistive heating, which is not co-spatial with current.

Chapter 6

Conclusions and Future Investigations

6.1 Conclusions

In this thesis, magnetic reconnection was studied in two semi-collisional (where the collision frequencies are non-zero, but small enough so that the plasma is not completely described by visco-resistive MHD) and low-β (magnetically-dominated) plasma environments; within flares of the solar corona, and within the start-up phase of the Mega-Ampere Spherical Tokamak (MAST). More detailed conclusions for these two investigations are presented in Sections 4.6 and 5.7, here we summarise the main conclusions.

For the investigation into a possible solar flare particle acceleration region, presented in Chapter 4, we studied collisionless test-particle trajectories within the electromagnetic fields of reconnecting 3D magnetic null-points. It is the first test-particle study at 3D null-points to include both the outer external drift region and the resistive current sheet. We compared the efficiency of proton acceleration in both the spine and fan-reconnection models of Craig & Fabling (1996); Craig et al. (1997). We found that the spine model, which gave promising results for proton acceleration in the ideal case (see Chapter 1, and Dalla & Browning 2005), is less efficient than the fan model used in this study. The maximum energy gain in the spine model is limited by the localisation of the resistive region, and in the external region the electric drift was found to be weak. The apparent contrast with the ideal results of Dalla & Browning (2005, 2008) is related to the restrictions on the field parameters that could be used, to avoid unrealistic pressures in the resistive models. In the ideal models, the electric field strength can be set independently of the magnetic field strength, and is set in Dalla & Browning (2005, 2008) to an equal value at a global distance from the null-point for the spine and fan models. However, if the same were done for the resistive models used in this thesis, there would be unphysical magnetic pressures on the current sheet edge due to the flux pile-up effect. This problem is more serious for the spine model than the fan model, see Sections 4.2.1 and 4.3.1. To avoid these unphysical magnetic pressures, the same saturation value is chosen in both models for the magnetic field at the current sheet edge. However, this means that the electric field is much weaker in the external region for the spine model.

For the fan reconnection model, it was found that protons could be efficiently accelerated by fast and non-uniform electric drifts. This mechanism is promising, as protons do not have to enter the current sheet to gain energy and so large numbers of protons can potentially be accelerated. These protons have a power-law energy spectrum, similar to a non-uniform drift acceleration mechanism found for 2D x-points by Vekstein & Browning (1997). However, the electrons are not accelerated so effectively by this mechanism, as the ratio of the electric drift to the thermal velocity is lower. A new mechanism, that was not present in the ideal models, is that of direct acceleration by the resistive electric field. This is responsible for the highest energy particles of both species, provided that the particles enter the current sheet, as the background field can stabilise the particles against ejection and the energy gain is only limited by the current sheet length.

In Section 2.1.3, we discussed the stringent requirements, set by the Hard X-Ray and γ-ray data, of a solar-flare particle acceleration mechanism. The main requirement is on the number of electrons that need to be accelerated. For example, Krucker et al. (2010) calculate that all of the electrons within the acceleration site need to reach energies over 16 keV. The simulations presented in Section 4.5 attempt to address this question, by using realistic coronal parameters (assuming a Spitzer (1962) resistivity). We find that the number of electrons with energy > 10 keV ranges from $0.7\% - 1.9\%$ for the two shear parameters used. Thus, it appears that the efficiency of the fan-model fields is well below the requirements set by the observations for large flares. However, it is still possible that null-points can be a site of particle acceleration within smaller flares, particularly as there may be many null-points in the corona (see e.g. Longcope & Parnell 2009). We do note that the same simulations predict different acceleration mechanisms for high-energy protons (fast non-uniform drift acceleration) and electrons (direct acceleration) as discussed above. To compare this with γ-ray imaging of solar flares (e.g. Hurford et al. 2003), more work would be needed to map the connectivity of the 3D null acceleration site to the chromospheric footpoints where emission is observed, and the different transport processes on these accelerated populations would also have to be considered.

For the second plasma environment, in Chapter 5 we presented results from simulations of the merging start-up method on MAST, with the aim of understanding the relevant physics involved in the merging, and to better interpret the experimental data. As these simulations are not from first principles (compared with PIC simulations, for example), the simulation results clearly have strong dependence on the choice of fluid equations used. In this project, we have initiated studies including two-fluid effects, namely the Hall term and the electron pressure scalar term, and also incorporating the effects of the tight aspect-ratio toroidal geometry of the MAST device. It was found that the latter gave radial oscillations of the flux-ropes, that look similar to the experimental data from the central post pick-up coil signal (the CCMV20). In addition, including both two-fluid effects and the toroidal geometry gives a double-peaked profile in density, that has similar time evolution to the electron density profiles measured during merging-compression. Another effect that was found when the Hall terms were included, was the fast tearing-type instability that is not present for the same dissipation parameters in the resistive model. The exact cause of this instability is not clear at present, and will be a subject for future work. It is also unclear whether such instabilities can be measured experimentally in the MAST device, due to the absence of magnetic probes inside the plasma.

Finally, we have begun to model the separate temperature evolution of the ions and electrons during merging-compression. In these simulations, hollow ion temperature profiles were found, which may explain the late-time heating of electrons via collisional relaxation in spatial profiles such as that shown in the bottom panel of Figure 2.12. However, a more realistic model for ion dissipation needs to be explored before any firm conclusions can be drawn.

6.2 Future investigations

As mentioned in Section 1.4.3, there is still a considerable amount of work to be done to better understand self-consistent particle acceleration at 3D magnetic null points. Particle-In-Cell simulations, which include both the external drift region and the current layers, are the most attractive option. However, there are still significant difficulties in using this approach within the solar corona, due to the large separation of scales. The smallest scale that needs to be resolved for an explicit PIC simulation is the Debye length, which in the corona is of order 10^{-3} m (Priest & Forbes 2000). Thus, for an acceleration region of length-scale $L_0 = 10^4$ m, as we have used here there is 10^7 orders of magnitude difference in every dimension (for realistic mass ratio and electron temperature). An intermediate step would be to use a combined test-particle and fluid approach, where the electromagnetic fields are taken from fluid simulations of reconnecting 3D null points. Such an approach has been used before for 3D magnetic null-points by Guo et al. (2010) for global field configurations, although without the inclusion of resistive effects. We have already begun to simulate reconnecting 3D magnetic null points using the Lare3D resistive MHD code (Arber et al. 2001), and the 3D version of the HiFi code (Glasser & Tang 2004; Lukin 2007). With the latter, we plan to examine the effect of the Hall term on reconnecting 3D null-points, to extend simulations of Pontin et al. (2007a,b) who used a resistive MHD formulation. The guiding-centre switching code will be further modified to include the time-dependent terms, and the effects of time-dependent Hall-MHD fields on test-particle acceleration will be studied. We will also consider the application of these simulations to 3D magnetic null points of the magnetotail, and compare the results with the recent *in-situ* measurements from the cluster satellites (Xiao et al. 2006; He et al. 2008).

For the merging-compression simulations, we plan to explore the effects of additional physics on the merging, and to continue developing the two-temperature formulation to better compare with both the experimental data on electron temperatures, and possible future ion temperature data. We are motivated to explore additional physics as the thickness of the current sheets with the smallest strength of dissipation, simulated in Chapter 5, can fall below the electron-skin depth and the ion-Larmor radius. The first thing we will include in the model will be electron inertia, to see if this has any effect on the electron dissipation scale, or if it changes the energetics of the merging (with finite electron mass the electrons can have non-zero bulk kinetic energy). We will also consider the off-diagonal terms in the ion and electron pressure tensors (i.e. *gyro-viscosity*, see Braginskii 1965). This may have an important role in setting the dissipation scale. For the two-temperature formulation, we have already begun working on a flux-limited temperature dependence for the ion and electron parallel heat conduction terms. In future work, we will also include the effects of an anisotropic viscous stress tensor, with temperature dependent coefficients (see also Braginskii 1965), and explore the possibility of using different fluid closures closures that are valid for low-collisionality. The effect of these modified fluid equations on the hollow ion-temperature profiles will be studied, and results compared with both possible future experiments in MAST, and with ion temperature results from a similar flux-rope merging experiment, the TS-3 merging device (see e.g. Ono et al. 2012).

Appendix A

Code Development

A.1 Computing the hypergeometric function

The function $M(a, b, x)$ is the hypergeometric, or Kummer, function. It is an analytic function with power series

$$M(a, b, x) = \sum_{p=0}^{\infty} \frac{(a)_p}{(b)_p} \frac{x^p}{p!}. \tag{A.1}$$

Here, $(a)_p$ is the Pochhammer symbol which is defined using the gamma function, $\Gamma(a)$, as

$$(a)_p = \frac{\Gamma(a+p)}{\Gamma(a)}; \quad (a)_0 = 1. \tag{A.2}$$

For all of the model fields used in Chapter 4 the value of x is negative. For example, in the fan model fields $x = -z^2/2\bar{\eta}$, see equation (4.22). To compute the Kummer function for this range of values we follow the technique of Zhang & Jin (1996). Firstly the Kummer function is computed for the positive value, $-x$, then the Kummer transformation is used to evaluate $M(a, b, x)$. This transformation is (Abramowitz & Stegun 1972)

$$M(a, b, x) = e^x M(b - a, b, -x). \tag{A.3}$$

For values of $-x \leq 30 + |b|$, $M(b - a, b, -x)$ is computed using the power series (A.1), which converges quickly. Otherwise, the following asymptotic formula

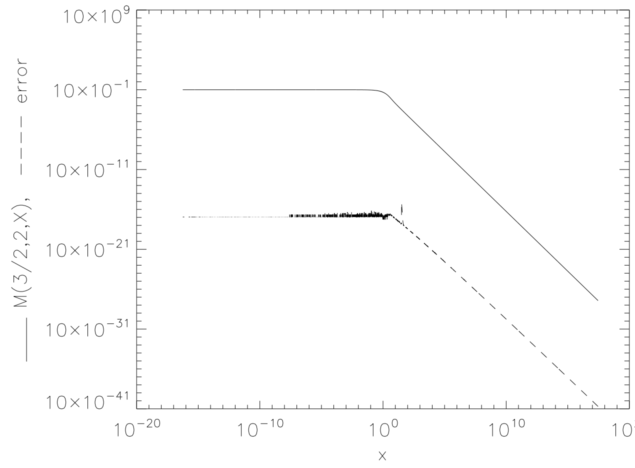

Figure A.1: Values of the Kummer function $M(3/2, 2, x)$ computed using equation (A.1) and equation (A.4). The error is the difference between the calculated value, and a value from a table of values produced by `Mathematica 8` (Wolfram Research, Inc. 2010)

is used (Zhang & Jin 1996; Abramowitz & Stegun 1972)

$$\begin{aligned} M(a,b,x) &= \frac{\Gamma(b)}{\Gamma(a)} e^x\, x^{a-b} \left[\sum_{k=0}^{S-1} \frac{(b-a)_k (1-a)_k\, x^{-k}}{k!} + O(|x|^{-S}) \right] \\ &+ \frac{\Gamma(b)}{\Gamma(b-a)} e^{i\pi a} x^{-a} \left[\sum_{k=0}^{R-1} \frac{(a)_k (1+a-b)_k (-x)^{-k}}{k!} + O(|x|^{-R}) \right]. \end{aligned} \tag{A.4}$$

However, a necessary condition for both the power series and asymptotic series to converge quickly is $a < 2$. In the model fields discussed in Chapter 4, there are values of $a \geq 2$. For these, we use the following recurrence routine

$$M(j{+}1, b, x) = \frac{1}{j} \left[(2h - b + x) M(j, b, x) + (b - j) M(j-1, b, x) \right] \quad \text{until } j = a{-}1. \tag{A.5}$$

This algorithm was tested extensively, by comparing it against tables of values generated by the proprietary software `Mathematica 8` (Wolfram Research, Inc. 2010). Figure A.1 shows the computed value of the Kummer function with arguments $a = 3/2$, $b = 2$ for a large range of x values. The values chosen cover all those that are required to be computed for the spine-model magnetic field, see equation (4.8). The calculated differences between the values are also plotted in Figure A.1 for reference; as the line labelled “error”. This is typically a factor of

10^{16} (and at most 10^{14}) less than the actual value of the function. This is close to the round-off error for double precision, and was deemed satisfactory. We also checked this for $a = 5/2$ with $b = 3$, $a = 3/4$ with $b = 3/2$, and $a = 7/4$ with $b = 5/2$, covering all the Kummer function arguments in the electric and magnetic fields for both models given in Chapter 4 (not shown but the errors look very similar to Figure A.1).

A.2 Tensor quantities for fan model fields

Here we give the analytic tensor quantities for the fan model fields, that are used in evaluating the complicated terms in the relativistic guiding centre equations. These are then used in the calculation of the electron trajectories in Chapter 4.

Using the fan magnetic field (4.5,4.7,4.21), the components of $\boldsymbol{\nabla}|B|$ can be calculated as

$$\frac{\partial|\boldsymbol{B}|}{\partial x} = \frac{\lambda^2 P_x P_x' + \lambda P_x' X(z)}{|\boldsymbol{B}|}, \tag{A.6}$$

$$\frac{\partial|\boldsymbol{B}|}{\partial y} = \frac{\lambda^2 P_y P_y'}{|\boldsymbol{B}|}, \tag{A.7}$$

$$\frac{\partial|\boldsymbol{B}|}{\partial z} = \frac{\lambda P_x X'(z) + X(z)X'(z) + \lambda^2 P_z P_z'}{|\boldsymbol{B}|}. \tag{A.8}$$

These expressions were used to calculate gradient drifts $\boldsymbol{v}_{\nabla B}$, in the parameter traces, and $L_{\nabla B}$ for use in the guiding-centre switching code.

The $\boldsymbol{\nabla}\hat{\boldsymbol{b}}$ tensor can be written as

$$\frac{\partial \hat{\boldsymbol{b}}}{\partial x_j} = \frac{\partial}{\partial x_j}\frac{\boldsymbol{B}}{|B|} = \frac{1}{B}\frac{\partial \boldsymbol{B}}{\partial x_j} - \frac{\boldsymbol{B}}{B^2}\frac{\partial |B|}{\partial x_j}, \tag{A.9}$$

in terms of the components of $\boldsymbol{\nabla}|B|$ given above. Using this form, the components of $\boldsymbol{\nabla}\hat{\boldsymbol{b}}$ can be calculated as

$$\frac{\partial \hat{b}_x}{\partial x} = \frac{\lambda P_x'}{B} - \frac{(\lambda P_x + X)}{B^2}\frac{\partial B}{\partial x}, \tag{A.10}$$

$$\frac{\partial \hat{b}_x}{\partial y} = -\frac{(\lambda P_x + X)}{B^2}\frac{\partial B}{\partial y}, \tag{A.11}$$

$$\frac{\partial \hat{b}_x}{\partial z} = \frac{X'}{B} - \frac{(\lambda P_x + X)}{B^2}\frac{\partial B}{\partial z}, \tag{A.12}$$

$$\frac{\partial \hat{b}_y}{\partial x} = -\frac{\lambda P_y}{B^2}\frac{\partial B}{\partial x}, \tag{A.13}$$

$$\frac{\partial \hat{b}_y}{\partial y} = \frac{\lambda P_y'}{B} - \frac{\lambda P_y}{B^2}\frac{\partial B}{\partial y}, \tag{A.14}$$

$$\frac{\partial \hat{b}_y}{\partial z} = -\frac{\lambda P_y}{B^2}\frac{\partial B}{\partial z}, \tag{A.15}$$

$$\frac{\partial \hat{b}_z}{\partial x} = -\frac{\lambda P_z}{B^2}\frac{\partial B}{\partial x}, \tag{A.16}$$

$$\frac{\partial \hat{b}_z}{\partial y} = -\frac{\lambda P_z}{B^2}\frac{\partial B}{\partial y}, \tag{A.17}$$

$$\frac{\partial \hat{b}_z}{\partial z} = \frac{\lambda P_z'}{B} - \frac{\lambda P_z}{B^2}\frac{\partial B}{\partial z}. \tag{A.18}$$

In component form, the electric drift can be written

$$v_{Ex} = \frac{\lambda P_z E_y - \lambda P_y E_z}{B^2}, \tag{A.19}$$

$$v_{Ey} = \frac{(\lambda P_x + X)E_z}{B^2}, \tag{A.20}$$

$$v_{Ez} = -\frac{(\lambda P_x + X)E_y}{B^2}. \tag{A.21}$$

Now $\boldsymbol{E} = E_y(z)\hat{\boldsymbol{y}} + E_z(y,z)\hat{\boldsymbol{z}}$, so that $\partial_x E_y = \partial_x E_z = \partial_y E_y = 0$. The non-zero derivatives are given by

$$\frac{\partial E_y}{\partial z} = \left[\eta X'' - (1-\lambda^2)P_z' X - (1-\lambda^2)P_z X'\right], \tag{A.22}$$

$$\frac{\partial E_z}{\partial y} = (1-\lambda^2)P_y' X, \tag{A.23}$$

$$\frac{\partial E_z}{\partial z} = (1-\lambda^2)P_y X'. \tag{A.24}$$

With these, the components of $\boldsymbol{\nabla} \boldsymbol{v}_E$ are given by the following expressions

$$\frac{\partial v_{Ex}}{\partial x} = -\frac{2(\lambda P_z E_y - \lambda P_y E_z)}{B^3}\frac{\partial B}{\partial x}, \tag{A.25}$$

$$\frac{\partial v_{Ex}}{\partial y} = -\frac{(\lambda P_y' E_z + \lambda P_y(\partial_y E_z))}{B^2} - \frac{2(\lambda P_z E_y - \lambda P_y E_z)}{B^3}\frac{\partial B}{\partial y}, \tag{A.26}$$

$$\frac{\partial v_{Ex}}{\partial z} = \frac{\lambda P_z' E_y + \lambda P_z(\partial_z E_y) - \lambda P_y(\partial_z E_z)}{B^2} - \frac{2(\lambda P_z E_y - \lambda P_y E_z)}{B^3}\frac{\partial B}{\partial z}, \quad \text{(A.27)}$$

$$\frac{\partial v_{Ey}}{\partial x} = \frac{\lambda P_x' E_z}{B^2} - \frac{2(\lambda P_x + X)E_z}{B^3}\frac{\partial B}{\partial x}, \quad \text{(A.28)}$$

$$\frac{\partial v_{Ey}}{\partial y} = \frac{(\lambda P_x + X)(\partial_y E_z)}{B^2} - \frac{2(\lambda P_x + X)E_z}{B^3}\frac{\partial B}{\partial y}, \quad \text{(A.29)}$$

$$\frac{\partial v_{Ey}}{\partial z} = \frac{X' E_z + (\lambda P_x + X)(\partial_z E_z)}{B^2} - \frac{2(\lambda P_x + X)E_z}{B^3}\frac{\partial B}{\partial z}, \quad \text{(A.30)}$$

$$\frac{\partial v_{Ez}}{\partial x} = -\frac{\lambda P_x' E_y}{B^2} + \frac{2(\lambda P_x + X)E_y}{B^3}\frac{\partial B}{\partial x}, \quad \text{(A.31)}$$

$$\frac{\partial v_{Ez}}{\partial y} = \frac{2(\lambda P_x + X)E_y}{B^3}\frac{\partial B}{\partial y}, \quad \text{(A.32)}$$

$$\frac{\partial v_{Ez}}{\partial z} = -\frac{X' E_y + (\lambda P_x + X)(\partial_z E_y)}{B^2} + \frac{2(\lambda P_x + X)E_y}{B^3}\frac{\partial B}{\partial z}. \quad \text{(A.33)}$$

All nine components were checked by numerically differentiating components of $\boldsymbol{v}_E$ across a range of values (not shown).

A.3 Existing Hall-MHD formulation

The two-dimensional Hall-MHD formulation that is included in the current release of the HiFi code evolves the primary dependent variables

$$\boldsymbol{U} = (n, -A_z, B_z, nv_x, nv_y, nv_z, j_z, p),$$

where n is the normalised density, A_z is the out-of-plane (z is the invariant direction) magnetic potential, B_z is the out-of-plane magnetic field, v_x and v_y are the in plane components of the ion velocity and v_z is the out-of-plane component, j_z is the out-of-plane current density and p is the total thermal pressure. These are evolved with the following equations (these are also given in Lukin 2007), in flux-source form,

$$\partial_t n + \boldsymbol{\nabla}\cdot[n\boldsymbol{v} - D_n\boldsymbol{\nabla} n] = 0, \quad \text{(A.34)}$$

$$\partial_t(-A_z) + \boldsymbol{\nabla}\cdot\left[-d_i\mu_e\frac{\boldsymbol{\nabla} v_{ez}}{n}\right] = -\hat{\boldsymbol{z}}\cdot\boldsymbol{v}_e\times\boldsymbol{B} - d_i\mu_e\frac{\boldsymbol{\nabla} v_{ez}\cdot\boldsymbol{\nabla} n}{n^2} + \eta j_z, \quad \text{(A.35)}$$

$$\partial_t B_z + \boldsymbol{\nabla}\cdot\left[\boldsymbol{v}B_z - v_{ez}\boldsymbol{B} + d_i\frac{\beta_e}{\beta_0}\hat{\boldsymbol{z}}\times\frac{\boldsymbol{\nabla} p}{n} - \eta\boldsymbol{\nabla} B_z\right] = d_i B_z\frac{\hat{\boldsymbol{z}}\cdot\boldsymbol{\nabla} B_z\times\boldsymbol{\nabla} n}{n^2}, \quad \text{(A.36)}$$

$$\partial_t(nv_x) + \boldsymbol{\nabla}\cdot[n\boldsymbol{v}v_x + p\hat{\boldsymbol{x}} - \mu(\boldsymbol{\nabla} v_x + \partial_x\boldsymbol{v})] = -\partial_x B_z^2/2 - j_z\partial_x(-A_z), \quad \text{(A.37)}$$

$$\partial_t(nv_y) + \boldsymbol{\nabla}\cdot\left[n\boldsymbol{v}v_y + p\hat{\boldsymbol{y}} - \mu\left(\boldsymbol{\nabla}v_y + \partial_y\boldsymbol{v}\right)\right] = -\partial_y B_z^2/2 - j_z\partial_y(-A_z), \quad \text{(A.38)}$$

$$\partial_t(nv_z) + \boldsymbol{\nabla}\cdot\left[n\boldsymbol{v}v_z - \mu\boldsymbol{\nabla}v_z\right] = -\boldsymbol{\nabla}A_z \times \boldsymbol{\nabla}B_z, \quad \text{(A.39)}$$

$$\boldsymbol{\nabla}\cdot\left[\boldsymbol{\nabla}(-A_z)\right] = j_z, \quad \text{(A.40)}$$

$$\begin{aligned}(\gamma-1)^{-1}\partial_t p + \boldsymbol{\nabla}\cdot\left[\gamma(\gamma-1)^{-1}p\boldsymbol{v} - \kappa_\parallel\boldsymbol{\nabla}_\parallel T - \kappa_\perp\boldsymbol{\nabla}_\perp T\right] \\ = \boldsymbol{v}\cdot\boldsymbol{\nabla}p + \eta j^2 + \mu\left(\boldsymbol{\nabla}\boldsymbol{v} + \boldsymbol{\nabla}\boldsymbol{v}^T\right) : \boldsymbol{\nabla}\boldsymbol{v},\end{aligned} \quad \text{(A.41)}$$

where $\boldsymbol{v}$ is the (normalised) ion velocity, $\boldsymbol{v}_e = \boldsymbol{v}_i - d_i\boldsymbol{j}/n$ is the electron velocity, $\boldsymbol{j}$ the current density and d_i the normalised ion-skin-depth, μ and μ_e are the normalised ion and electron viscosities, η is the normalised resistivity, $\kappa_\parallel$ and $\kappa_\perp$ the parallel and perpendicular heat conductivities, D_n is a density diffusion (note that we do not use density diffusion for any simulation in this thesis: we set $D_n = 0$ always), β_e is the electron-beta (see Section 1.2 for a remark on including p_e in one-temperature formulation) and β_0 is the total plasma-beta.

Equation (A.40) is static, this is needed because the pressure equation (A.41) includes the term $\eta j_z^2 = \eta(\nabla^2 A_z)^2$, where the right hand side cannot be put into flux-source form. Also note that these are written in Cartesian geometry, but they are also included in cylindrical geometry within HiFi.

A.4 Modified Hall-MHD formulation

The electron viscosity in equation (A.35) is a high-order dissipation term that can help to set a dissipation scale for the Whistler wave in a numerical code. However, the viscosity is only applied to the out-of-plane electron velocity. We found that this term provides sufficient dissipation for reconnection simulations with zero guide-field ($B_z = 0$ in the initial conditions). However, for the strong guide field case, this dissipation term was not enough to suppress numerical instabilities, such as that shown in Figure 3.9. We decided to try a high-order dissipation term that acts on the in-plane components of the electron velocity as well. To do this within the HiFi Hall-MHD formulation above required the creation of a new static equation, as the in-plane electron velocities (depending on the in-plane currents) involve derivatives of B_z. Specifically, an electron viscous term in equation (A.36) would require fourth-order derivatives of B_z. The simplest way to provide this dissipation is through hyper-resistivity, rather than electron viscosity, with the above formulation. Equation (A.42) defines a new static equation, that is then used in (A.43) to provide this fourth-order derivative term. Also, in equation (A.44) the out-of-plane electron viscosity, that was in equation (A.35), has been changed to hyper-resistivity

$$\boldsymbol{\nabla} \cdot [\boldsymbol{\nabla} B_z] = D_H, \tag{A.42}$$

$$\partial_t B_z + \boldsymbol{\nabla} \cdot \left[\boldsymbol{v} B_z - v_{ez} \boldsymbol{B} + d_i \frac{\beta_e}{\beta_0} \hat{\boldsymbol{z}} \times \frac{\boldsymbol{\nabla} p}{n} - \eta \boldsymbol{\nabla} B_z + \eta_H \boldsymbol{\nabla} D_H \right] = d_i B_z \frac{\hat{\boldsymbol{z}} \cdot \boldsymbol{\nabla} B_z \times \boldsymbol{\nabla} n}{n^2}, \tag{A.43}$$

$$\partial_t(-A_z) + \boldsymbol{\nabla} \cdot [\eta_H \boldsymbol{\nabla} j_z] = -\hat{\boldsymbol{z}} \cdot \boldsymbol{v}_e \times \boldsymbol{B} + \eta j_z. \tag{A.44}$$

In addition we add the hyper-resistive heating term, $\eta_H (\boldsymbol{\nabla j})^2 \equiv \boldsymbol{\nabla j} : \boldsymbol{\nabla j}$, into equation A.41, to give the new version in equation (A.45):

$$(\gamma - 1)^{-1} \partial_t p + \boldsymbol{\nabla} \cdot \left[\gamma (\gamma - 1)^{-1} p \boldsymbol{v} - \kappa_\parallel \boldsymbol{\nabla}_\parallel T - \kappa_\perp \boldsymbol{\nabla}_\perp T \right] = \boldsymbol{v} \cdot \boldsymbol{\nabla} p + \eta j^2 + \mu \left(\boldsymbol{\nabla v} + \boldsymbol{\nabla v}^T \right) : \boldsymbol{\nabla v} + \eta_H \boldsymbol{\nabla j} : \boldsymbol{\nabla j}. \tag{A.45}$$

In two-dimensional Cartesian geometry this term is

$$\eta_H \left[(\partial_x j_x)^2 + (\partial_y j_x)^2 + (\partial_x j_y)^2 + (\partial_y j_y)^2 + (\partial_x j_z)^2 + (\partial_y j_z)^2 . \right]$$

However, this has terms such as $(\partial_x j_x)^2 = (\partial_{xy} B_z)^2$ that cannot be put into flux-source form directly. We use $\boldsymbol{\nabla} \cdot \boldsymbol{j} = \boldsymbol{\nabla} \cdot \boldsymbol{B} = 0$, and $\hat{\boldsymbol{z}} \cdot \boldsymbol{\nabla} \times \boldsymbol{j} = -\nabla^2 B_z = -D_H$ to re-write the hyper-resistive heating term as

$$\eta_H \left[2(\partial_x j_x)^2 + (\partial_y j_x)^2 + (\partial_y j_x - D_H)^2 + (\partial_x j_z)^2 + (\partial_y j_z)^2 \right],$$

which requires the creation of one extra static equation,

$$j_x = \partial_y B_z. \tag{A.46}$$

These equations were also modified for cylindrical geometry, to be used in the toroidal-axisymmetric simulations of Chapter 5 (with extra terms that arise from vector calculus operations in cylindrical geometry). Finally, HiFi requires the Jacobian used in the Newton iterations 3.37 be entered into the code manually.

To make the changes detailed here and below it was necessary to calculate and supply the code with the spatial derivatives of all terms, with respect to all primary variables.

A.5 Energy conservation and the hyper-resistive heating term

Here we show that the hyper-resistive heating above in the internal energy equation balances the hyper-resistive dissipation of magnetic energy. For convenience we do not use flux-source, and we write the ion viscous terms in stress tensor form $\boldsymbol{\pi}_i$. The momentum equation is thus

$$n\left(\partial_t + \boldsymbol{v}_i \cdot \boldsymbol{\nabla}\right)\boldsymbol{v}_i = -\boldsymbol{\nabla} p - \boldsymbol{\nabla}\cdot\boldsymbol{\pi}_i + \boldsymbol{j}\times\boldsymbol{B},$$

This can be converted into an equation for kinetic energy, using the identity $\boldsymbol{v}\cdot\boldsymbol{\nabla}\boldsymbol{v} = \boldsymbol{\nabla}(1/2v^2) - \boldsymbol{v}\times\boldsymbol{\nabla}\times\boldsymbol{v}$, also taking the scalar product with $\boldsymbol{v}$, and substituting the mass conservation equation (1.25) multiplied by $v^2/2$, to give

$$\partial_t(nv^2/2) + \boldsymbol{\nabla}\cdot\left(nv^2/2\,\boldsymbol{v}\right) = -\boldsymbol{v}\cdot\boldsymbol{\nabla} p + \boldsymbol{v}\cdot\boldsymbol{j}\times\boldsymbol{B} - \boldsymbol{v}\cdot\boldsymbol{\nabla}\cdot\boldsymbol{\pi}_i.$$

Now the term $\boldsymbol{v}\cdot\boldsymbol{\nabla}\cdot\boldsymbol{\pi}_i$ is split into flux and dissipation form. Using index notation,

$$-v_j\frac{\partial}{\partial x_k}\pi_{jk} = -\left(\frac{\partial}{\partial x_k}v_j\pi_{jk} - \pi_{jk}\frac{\partial v_j}{\partial x_k}\right),$$

which in vector notation is $-\boldsymbol{v}\cdot(\boldsymbol{\nabla}\cdot\boldsymbol{\pi}) = -\boldsymbol{\nabla}\cdot(\boldsymbol{v}\cdot\boldsymbol{\pi}_i) + \boldsymbol{\pi}_i : \boldsymbol{\nabla}\boldsymbol{v}$. The resulting equation is the kinetic energy equation

$$\partial_t(1/2nv^2) + \boldsymbol{\nabla}\cdot\left(1/2nv^2\boldsymbol{v} + \boldsymbol{v}\cdot\boldsymbol{\pi}_i\right) = -\boldsymbol{v}\cdot\boldsymbol{\nabla} p + \boldsymbol{v}\cdot\boldsymbol{j}\times\boldsymbol{B} + \boldsymbol{\pi}_i : \boldsymbol{\nabla}\boldsymbol{v}. \quad \text{(A.47)}$$

Next consider Ohm's law (1.27) with the hyper-resistive term,

$$\boldsymbol{E} = -\boldsymbol{v}_i\times\boldsymbol{B} + \frac{d_i}{n}(\boldsymbol{j}\times\boldsymbol{B} - \boldsymbol{\nabla} p_e) + \eta\boldsymbol{j} - \eta_H\nabla^2\boldsymbol{j},$$

which can be written as an evolution equation for normalised magnetic energy, $B^2/2$, using the identity $\boldsymbol{\nabla}\cdot(\boldsymbol{E}\times\boldsymbol{B}) = \boldsymbol{B}\cdot\boldsymbol{\nabla}\times\boldsymbol{E} - \boldsymbol{E}\cdot\boldsymbol{\nabla}\times\boldsymbol{B}$, which with Faraday's equation (1.15) can be written as the Poynting flux, and the dissipation:

$\partial_t B^2/2 = -\boldsymbol{\nabla}\cdot(\boldsymbol{E}\times\boldsymbol{B}) - \boldsymbol{E}\cdot\boldsymbol{j}$. Expanding out the latter by substituting the Ohm's law above, and also re-writing the hyper-resistive term $j_i\partial_k^2 j_i = \partial_k(j_i\partial_k j_i) - (\partial_k j_i)(\partial_k j_i)$ gives in vector form

$$\partial_t B^2/2 = -\boldsymbol{\nabla}\cdot(\boldsymbol{E}\times\boldsymbol{B} - \boldsymbol{j}\cdot\boldsymbol{\nabla}\boldsymbol{j}^T) - \boldsymbol{j}\times\boldsymbol{B}\cdot\boldsymbol{v}_i + \frac{d_i}{n}\boldsymbol{\nabla}p_e\cdot\boldsymbol{j} - \eta j^2 - \eta_H\boldsymbol{\nabla}\boldsymbol{j} : \boldsymbol{\nabla}\boldsymbol{j} \tag{A.48}$$

Finally, the internal energy equation as

$$\partial_t[p/(\gamma-1)] + \boldsymbol{\nabla}\cdot\left[\frac{\gamma}{\gamma-1}p\boldsymbol{v} - \kappa_\perp\boldsymbol{\nabla}T - \kappa_\parallel\boldsymbol{\nabla}_\parallel T\right] = \boldsymbol{v}\cdot\boldsymbol{\nabla}p + H \tag{A.49}$$

where H are the "unknown" heating terms $H = H_\mu + H_\eta + H_{\eta H}$. Adding all of the above equations together, and integrating over the total volume gives

$$\begin{aligned} &\frac{\partial}{\partial t}\int_V \left[\frac{nv^2}{2} + \frac{p}{\gamma-1} + \frac{B^2}{2}\right] dV \qquad\qquad (A.50)\\ &+ \int_S \left[\frac{nv^2}{2}\boldsymbol{v} + \frac{\gamma p\boldsymbol{v}}{\gamma-1} - \kappa_\perp\boldsymbol{\nabla}T - \kappa_\parallel\boldsymbol{\nabla}_\parallel T + \boldsymbol{E}\times\boldsymbol{B} + \boldsymbol{v}\cdot\boldsymbol{\pi}_i - \boldsymbol{j}\cdot(\boldsymbol{\nabla}\boldsymbol{j})^T\right]\cdot\hat{\boldsymbol{n}}dS\\ &= \int_V \left[H + \boldsymbol{\pi} : \boldsymbol{\nabla}\boldsymbol{v} - \eta j^2 - \eta_H\boldsymbol{\nabla}\boldsymbol{j} : \boldsymbol{\nabla}\boldsymbol{j} + (d_i/n)\boldsymbol{j}\cdot\boldsymbol{\nabla}p_e\right] dV, \end{aligned}$$

after cancellation of terms. For conservation of energy, the flux through the boundary must be set equal to zero, and the right hand side must also be zero. The first point gives the necessary boundary conditions for energy conservation. These are; conducting wall boundaries $\hat{\boldsymbol{n}}\times\boldsymbol{E} = 0$, zero temperature gradient $\hat{\boldsymbol{n}}\cdot\boldsymbol{\nabla}T = 0$, non-penetrating walls $\hat{\boldsymbol{n}}\cdot\boldsymbol{v} = 0$, and with the condition that the hyper-resistive and viscous fluxes through the boundary must be set to zero.

From equation (A.50), the heating terms are $H_\eta = \eta j^2$, $H_{\eta H} = \eta_H\boldsymbol{\nabla}\boldsymbol{j} : \boldsymbol{\nabla}\boldsymbol{j}$ and $H_\mu = -\boldsymbol{\pi} : \boldsymbol{\nabla}\boldsymbol{v}$. However, there is still a non-zero term $(d_i/n)\boldsymbol{j}\cdot\boldsymbol{\nabla}p_e = (\boldsymbol{v}_i - \boldsymbol{v}_e)\cdot\boldsymbol{\nabla}p_e$ that arises from the assumption that the centre of mass (ion) velocity advects the electron pressure (this is actually a flux-term $\boldsymbol{\nabla}\cdot[\boldsymbol{j}p_e]$). This term can be small, see Section 1.2. However, to set it to zero requires a separate temperature formulation for ions and electrons, this is given in flux-source form below.

A.6 Separate temperature formulation

For the separate temperature runs in Chapter 5 we modify the HiFi Hall-MHD module to add an extra equation for electron pressure. We do this for both Cartesian and cylindrical (toroidal-axisymmetric) geometry, the equations in Cartesian geometry are

$$\partial_t n + \boldsymbol{\nabla} \cdot [n\boldsymbol{v}] = 0, \tag{A.51}$$

$$\partial_t(-A_z) + \boldsymbol{\nabla} \cdot [\eta_H \boldsymbol{\nabla} j_z] = -\hat{\boldsymbol{z}} \cdot \boldsymbol{v}_e \times \boldsymbol{B} + \eta j_z, \tag{A.52}$$

$$\partial_t B_z + \boldsymbol{\nabla} \cdot \left[\boldsymbol{v} B_z - v_{ez}\boldsymbol{B} + d_i \hat{\boldsymbol{z}} \times \frac{\boldsymbol{\nabla} p_e}{n} - \eta \boldsymbol{\nabla} B_z + \eta_H \boldsymbol{\nabla} D_H\right] = d_i B_z \frac{\hat{\boldsymbol{z}} \cdot \boldsymbol{\nabla} B_z \times \boldsymbol{\nabla} n}{n^2}, \tag{A.53}$$

$$\partial_t(nv_x) + \boldsymbol{\nabla} \cdot [n\boldsymbol{v}v_x + (p_i + p_e)\hat{\boldsymbol{x}} - \mu\left(\boldsymbol{\nabla} v_x + \partial_x \boldsymbol{v}\right)] = -\partial_x B_z^2/2 - j_z \partial_x(-A_z), \tag{A.54}$$

$$\partial_t(nv_y) + \boldsymbol{\nabla} \cdot [n\boldsymbol{v}v_y + (p_i + p_e)\hat{\boldsymbol{y}} - \mu\left(\boldsymbol{\nabla} v_y + \partial_y \boldsymbol{v}\right)] = -\partial_y B_z^2/2 - j_z \partial_y(-A_z), \tag{A.55}$$

$$\partial_t(nv_z) + \boldsymbol{\nabla} \cdot [n\boldsymbol{v}v_z - \mu \boldsymbol{\nabla} v_z] = -\boldsymbol{\nabla} A_z \times \boldsymbol{\nabla} B_z, \tag{A.56}$$

$$\boldsymbol{\nabla} \cdot [\boldsymbol{\nabla}(-A_z)] = j_z, \tag{A.57}$$

$$\begin{aligned}(\gamma-1)^{-1}\partial_t(p_i + p_e) + \boldsymbol{\nabla} \cdot \big[\gamma(\gamma-1)^{-1}(p_i\boldsymbol{v} + p_e\boldsymbol{v}_e) - \kappa_\parallel^i \boldsymbol{\nabla}_\parallel T_i - \kappa_\parallel^e \boldsymbol{\nabla}_\parallel T_e \\ - \kappa_\perp^i \boldsymbol{\nabla}_\perp T_i - \kappa_\perp^e \boldsymbol{\nabla}_\perp T_e\big] = \boldsymbol{v} \cdot \boldsymbol{\nabla} p_i + \boldsymbol{v}_e \cdot \boldsymbol{\nabla} p_e \\ + \eta j^2 + \mu\left(\boldsymbol{\nabla}\boldsymbol{v} + \boldsymbol{\nabla}\boldsymbol{v}^T\right) : \boldsymbol{\nabla}\boldsymbol{v} + \eta_H \boldsymbol{\nabla}\boldsymbol{j} : \boldsymbol{\nabla}\boldsymbol{j},\end{aligned} \tag{A.58}$$

$$\begin{aligned}(\gamma-1)^{-1}\partial_t p_e + \boldsymbol{\nabla} \cdot \big[\gamma(\gamma-1)^{-1} p_e \boldsymbol{v}_e - \kappa_\parallel^e \boldsymbol{\nabla}_\parallel T_e - \kappa_\perp^e \boldsymbol{\nabla}_\perp T_e\big] \\ = \boldsymbol{v}_e \cdot \boldsymbol{\nabla} p_e + \eta j^2 + \eta_H \boldsymbol{\nabla}\boldsymbol{j} : \boldsymbol{\nabla}\boldsymbol{j},\end{aligned} \tag{A.59}$$

$$\boldsymbol{\nabla} \cdot [\boldsymbol{\nabla} B_z] = D_H, \tag{A.60}$$

$$j_x = \partial_y B_z. \tag{A.61}$$

Appendix B

Model Field Derivations

In this appendix we give some derivations relating to the spine model fields in Chapter 4For the spine-model we show the form of displacement field is a solution to the governing equations, following Craig & Fabling (1996) but giving more intermediate steps in the calculations for reference. We also give the derivation of the thermal pressure profile for the spine model from Craig et al. (1997). We do not give the derivations for the fan model here, as the method to get the solutions is the same as for the spine solutions.

B.1 Spine displacement field solution

Substituting the expressions for $\boldsymbol{B}$ and $\boldsymbol{v}$, from equations (4.5) and (4.6), into the momentum equation (4.1) gives

$$\boldsymbol{\nabla} \times \left[(\lambda^2 - 1) \left(\boldsymbol{\nabla} \times \boldsymbol{Q} \right) \times \boldsymbol{Q} \right] = \boldsymbol{0}, \tag{B.1}$$

which is identically satisfied for $\boldsymbol{Q} = \boldsymbol{Q}_s = Z(r, \phi)\hat{\boldsymbol{z}}$, as $\boldsymbol{\nabla} \times \boldsymbol{Q}_s = \boldsymbol{\nabla} Z \times \hat{\boldsymbol{z}}$.

Next, substituting $\boldsymbol{v}$ and $\boldsymbol{B}$ into the induction equation (4.2) gives

$$\boldsymbol{\nabla} \times \left[(1 - \lambda^2) \boldsymbol{P} \times \boldsymbol{Q} - \eta \boldsymbol{\nabla} \times \boldsymbol{Q} \right], \tag{B.2}$$

which, given the definitions of $\boldsymbol{P}$ from equation (4.7) and $\boldsymbol{Q} = \boldsymbol{Q}_s$ from above, gives

$$\partial_r \left[-r(1 - \lambda^2) P_r Z + \eta r \partial_r Z \right] + \partial_\phi \left[\eta \frac{\partial_\phi Z}{r} \right] = 0 \tag{B.3}$$

Further assuming $Z(r, \theta)$ has the form $Z(r, \theta) = f(r)e^{im\theta}$, gives the radial spine equation of Craig & Fabling (1996)

$$f + \frac{1}{2} r \dot{f} = \frac{\eta}{\alpha(1-\lambda^2)} \left(\ddot{f} + \frac{\dot{f}}{r} - \frac{m^2}{r^2} f \right), \tag{B.4}$$

where $\dot{f} = df/dr$.

Transforming this radial spine equation (B.4) to the variable $x(r)$, where

$$x(r) = \left[\frac{\eta}{\alpha\,(\lambda^2 - 1)} \right]^{-1/2} r, \tag{B.5}$$

and, assuming $\alpha < 0$ and $\lambda < 1$, gives

$$x^2 f'' + \left(x + \frac{1}{2} x^3 \right) f' + \left(x^2 - m^2 \right) f = 0, \tag{B.6}$$

which is given in the appendix of Craig & Fabling (1996).

Assuming that the solution to this equation is in the form

$$f(r) = A \left(\frac{r^2}{4\bar{\eta}} \right)^{m/2} M(r), \tag{B.7}$$

where $M(r)$ is a yet unknown function, and

$$\bar{\eta} = \frac{\eta}{\alpha(1-\lambda^2)}, \tag{B.8}$$

gives that $x^2 = r^2/|\bar{\eta}|$ and

$$f(x) = A \left(\frac{x^2}{4} \right)^{m/2} M(x). \tag{B.9}$$

Substituting $f(x)$, along with $f'(x)$ and $f''(x)$ into equation (B.6) gives, after some working

$$x^2 M''(x) + \left[(2m+1)x + \frac{x^3}{2} \right] M'(x) + \left(\frac{m}{2} + 1 \right) x^2 M(x) = 0. \tag{B.10}$$

It is unclear which form $M(x)$ should take to satisfy this equation but, by using the transformation $M(x) \to M(z)$ with $z = -x^2/4$, this reduces to the confluent hypergeometric equation.

$$zM''(z) + (c - z)M'(z) - aM = 0, \tag{B.11}$$

where $a = 1+m/2$, $c = m+1$ and $z = -x^2/4$. The solution to this equation is the confluent hypergeometric function, or Kummer function, which has the form (see e.g. Chapter 13 of Abramowitz & Stegun 1972)

$$M(a, c, z) = \sum_{r=0}^{\infty} \frac{(a)_r}{(c)_r} \frac{z^r}{r!}, \tag{B.12}$$

where $(a)_r$ is the Pochhammer symbol given in terms of the gamma function, $\Gamma(x)$, by

$$(a)_r = \frac{\Gamma(a + r)}{\Gamma(a)}; \quad (a)_0 = 1. \tag{B.13}$$

It is worth noting that another solution can be found for the case of $\alpha > 0$, which was not mentioned by Craig & Fabling (1996). For this the transformation used is

$$x = \left[\frac{\eta}{\alpha\,(1 - \lambda^2)}\right]^{-1/2} r, \tag{B.14}$$

which gives the form of the radial spine equation (in terms of the variable x) to be

$$x^2 f'' + \left(x - \frac{1}{2}x^3\right) f' - \left(x^2 + m^2\right) f = 0. \tag{B.15}$$

and after some working, gives the differential equation

$$zM''(z) + (c + z)M'(z) + aM = 0, \tag{B.16}$$

with a solution of the form

$$M(z) = Ae^{-z}U(c - a, c, z) \tag{B.17}$$

where U(z) is the confluent hypergeometric function of the second kind Abramowitz & Stegun (1972). We do not use this model in this thesis, but it may be investigated in future work.

B.2 Thermal pressure for spine model

The incompressible steady-state momentum equation is the uncurled form of equation (4.1), it is

$$(\boldsymbol{v} \cdot \boldsymbol{\nabla})\, \boldsymbol{v} = \boldsymbol{J} \times \boldsymbol{B} - \boldsymbol{\nabla} p = -\boldsymbol{\nabla}(p + B^2/2) + \boldsymbol{B} \cdot \boldsymbol{\nabla} \boldsymbol{B}. \tag{B.18}$$

Now the definition of $\boldsymbol{B}$ and $\boldsymbol{v}$ from equations (4.5) and (4.6) are used in equation (B.18), with the definition of $\boldsymbol{P}$ from equation (4.7), and using $\boldsymbol{Q} = Z(x, y)\hat{\boldsymbol{z}}$. After the cancellation of many terms, and discarding the terms identical to zero, equation (B.18) becomes

$$(\boldsymbol{P} \cdot \boldsymbol{\nabla})\boldsymbol{P} = \alpha z(\partial_x Z\hat{\boldsymbol{x}} + \partial_y Z\hat{\boldsymbol{y}}) + \alpha \boldsymbol{Z} - \frac{1}{2}(2Z\partial_x Z\hat{\boldsymbol{x}} + 2Z\partial_y Z\hat{\boldsymbol{y}}) - \boldsymbol{\nabla} p. \tag{B.19}$$

This can be integrated to give

$$p = p_0 - \frac{Z^2}{2} - \frac{\alpha^2}{8}(x^2 + y^2 + 4z^2) + \lambda\alpha z Z, \tag{B.20}$$

which, from the definition of Z and P is

$$p = p_0 - \frac{1}{2}(Z^2 + P^2) + \lambda\alpha z Z, \tag{B.21}$$

the form given in Craig et al. (1997).

Bibliography

Abramowitz M., Stegun I.A., 1972, Handbook of Mathematical Functions. Dover Publications

Angelopoulos V., et al., 2008, Science, 321, 931

Arber T.D., Longbottom A.W., Gerrard C.L., Milne A.M., 2001, Journal of Computational Physics, 171, 151

Aulanier G., DeLuca E.E., Antiochos S.K., McMullen R.A., Golub L., 2000, ApJ, 540, 1126

Baker D.A., 1984, In Hones Jr. E.W., ed., Magnetic Reconnection in Space and Laboratory Plasmas, p. 332

Balay S., et al., 2013, Petsc users manual. Tech. Rep. ANL-95/11 - Revision 3.4, Argonne National Laboratory

Ballegooijen A., 1994, Space Science Reviews, 68, 299

Battaglia D., Bongard M., Fonck R., Redd A., 2011, Nucl. Fusion, 51, 073029

Baumann G., Haugbølle T., Nordlund Å., 2013, ApJ, 771, 93

Birn J., Priest E.R., 2007, Reconnection of magnetic fields : magnetohydrodynamics and collisionless theory and observations. Cambridge University Press

Birn J., Thomsen M.F., Hesse M., 2004, Physics of Plasmas, 11, 1825

Birn J., Hesse M., Nakamura R., Zaharia S., 2013, Journal of Geophysical Research (Space Physics), 118, 1960

Birn J., et al., 2001, J. Geophys. Res., 106, 3715

Biskamp D., 1986, Physics of Fluids, 29, 1520

Biskamp D., 2000, Magnetic Reconnection in Plasmas. Cambridge University Press

Biskamp D., Welter H., 1980, Phys. Rev. Lett., 44, 1069

Braginskii S.I., 1965, Reviews of Plasma Physics, 1, 205

Breslau J.A., Jardin S.C., 2003, Physics of Plasmas, 10, 1291

Brown J.C., 1971, Sol. Phys., 18, 489

Brown M.R., 1999, Phys. Plasmas, 6, 1717

Browning P.K., Vekstein G.E., 2001, Journal of Geophysical Research: Space Physics, 106, 18677

Browning P.K., Dalla S., Peters D., Smith J., 2010, A&A, 520, A105+

Bulanov S.V., Cap F., 1988, Soviet Ast., 32, 436

Carmichael H., 1964, NASA Special Publication, 50, 451

Carrington R.C., 1859, MNRAS, 20, 13

Cerutti B., Werner G.R., Uzdensky D.A., Begelman M.C., 2013, ApJ, 770, 147

Craig I.J.D., Fabling R.B., 1996, ApJ, 462, 969

Craig I.J.D., Henton S.M., 1995, ApJ, 450, 280

Craig I.J.D., Litvinenko Y.E., 2002, ApJ, 570, 387

Craig I.J.D., Watson P.G., 2000, Sol. Phys., 191, 359

Craig I.J.D., Fabling R.B., Henton S.M., Rickard G.J., 1995, ApJL, 455, L197+

Craig I.J.D., Fabling R.B., Watson P.G., 1997, ApJ, 485, 383

Craig I.J.D., Fabling R.B., Heerikhuisen J., Watson P.G., 1999, ApJ, 523, 838

Dalla S., Browning P.K., 2005, A&A, 436

Dalla S., Browning P.K., 2006, ApJL, 640

Dalla S., Browning P.K., 2008, A&A, 491, 289

Daughton W., Scudder J., Karimabadi H., 2006, Physics of Plasmas, 13, 072101

de Blank H.J., 2008, In Fusion Science and Technology, vol. 53, pp. 59–67

De Pontieu B., McIntosh S.W., Hansteen V.H., Schrijver C.J., 2009, ApJL, 701, L1

Dennis B.R., Hudson H.S., Krucker S., 2007, In Klein K.L., MacKinnon A.L., eds., Lecture Notes in Physics, Berlin Springer Verlag, vol. 725 of Lecture Notes in Physics, Berlin Springer Verlag, p. 33

Des Jardins A., Canfield R., Longcope D., Fordyce C., Waitukaitis S., 2009, ApJ, 693, 1628

Dungey J.W., 1961, Physical Review Letters, 6, 47

Egedal J., Fasoli A., Nazemi J., 2003, Phys. Rev. Lett., 90

Emslie A.G., et al., 2004, Journal of Geophysical Research (Space Physics), 109, 10104

Finn J.M., Kaw P.K., 1977, Physics of Fluids, 20, 72

Fletcher L., Metcalf T.R., Alexander D., Brown D.S., Ryder L.A., 2001, ApJ, 554, 451

Forbes T.G., Priest E.R., Seaton D.B., Litvinenko Y.E., 2013, Physics of Plasmas, 20, 052902

Freund R., Golub G.H., Nachtigal N.M., 1992, Acta Numerica, 1, 57

Furno I., et al., 2003, Rev. Sci. Inst., 74, 2324

Furth H.P., Killeen J., Rosenbluth M.N., 1963, Physics of Fluids, 6, 459

Garabedian P.R., 2006, Proceedings of the National Academy of Sciences, 103, 19232

Garbet X., Idomura Y., Villard L., Watanabe T.H., 2010, Nuclear Fusion, 50, 043002

Gates D.A., Delgado-Aparicio L., 2012, Phys. Rev. Lett., 108, 165004

Gerhardt S.P., et al., 2011, Nuclear Fusion, 51, 073031

Glasser A.H., Tang X.Z., 2004, Computer Physics Communications, 164, 237

Goedbloed J.P., Keppens R., Poedts S., 2010, Advanced Magnetohydrodynamics. Cambridge University Press

Goedbloed J.P.H., Poedts S., 2004, Principles of Magnetohydrodynamics. Cambridge University Press

Golub L., Pasachoff J.M., 1997, The Solar Corona. Cambridge University Press

Gordovskyy M., Browning P.K., Vekstein G.E., 2010a, A&A, 519, A21+

Gordovskyy M., Browning P.K., Vekstein G.E., 2010b, ApJ, 720, 1603

Grad H., Rubin H., 1958, Hydromagnetic equilibria and force-free fields. Tech. rep., New York Univ., New York. Inst. of Mathematical Sciences

Gray T., Lukin V.S., Brown M.R., Cothran C.D., 2010, Phys. Plasmas, 17, 102106

Greenwald M., Terry J., Wolfe S., Ejima S., Bell M., Kaye S., Neilson G., 1988, Nuclear Fusion, 28, 2199

Gryaznevich M., Shevchenko V., Sykes A., 2006, Nucl. Fusion, 46, S573

Gryaznevich M., et al., 1992, In Plasma Physics and Controlled Nuclear Fusion Research, vol. 2

Gryaznevich M., et al., 1998, Physical Review Letters, 80, 3972

Guo J., Büchner J., Otto A., Santos J., Marsch E., Gan W., 2010, A&A, 513, A73+

Hamilton B., Fletcher L., McClements K.G., Thyagaraja A., 2005, ApJ, 625, 496

Hannah I.G., Fletcher L., 2006, Sol. Phys., 236, 59

He J.S., et al., 2008, Geophys. Res. Lett., 35, 14104

Heerikhuisen J., Litvinenko Y.E., Craig I.J.D., 2002, ApJ, 566, 512

Hesse M., Schindler K., Birn J., Kuznetsova M., 1999, Physics of Plasmas, 6

Hesse M., Kuznetsova M., Hoshino M., 2002, Geophys. Res. Lett., 29, 1563

Heyvaerts J., Priest E.R., 1983, A&A, 117, 220

Hirayama T., 1974, Sol. Phys., 34, 323

Horiuchi R., Sato T., 1994, Physics of Plasmas, 1, 3587

Huang Y.M., Bhattacharjee A., 2013, Physics of Plasmas, 20, 055702

Hurford G.J., Schwartz R.A., Krucker S., Lin R.P., Smith D.M., Vilmer N., 2003, ApJL, 595, L77

Imazawa R., 2009. Ph.D. thesis, University of Tokyo

Ishikawa S., Krucker S., Takahashi T., Lin R.P., 2011, ApJ, 737, 48

ITER/EDA, 2001, Summary of the iter final design report. Tech. rep., IAEA

Jardin S.C., Ferraro N., Luo X., Chen J., Breslau J., Jansen K.E., Shephard M.S., 2008, Journal of Physics Conference Series, 125, 012044

Johnson L., Riess R., 1982, Numerical analysis. Mathematics Series, Addison-Wesley Pub. Co.

Jones C.A., Thompson M.J., Tobias S.M., 2010, Space Sci. Rev., 152, 591

Karniadakis G., Sherwin S., 1999, Spectral/hp Element Methods for CFD. Numerical mathematics and scientific computation, Oxford University Press

Keilhacker M., et al., 1999, Nuclear Fusion, 39, 209

Kiplinger A.L., Garcia H.A., 2004, In Bulletin of the American Astronomical Society, vol. 36 of Bulletin of the American Astronomical Society, pp. 739–+

Kleva R.G., Drake J.F., Waelbroeck F.L., 1995, Phys. Plasmas, 2, 23

Knoll D.A., Chacón L., 2006a, Phys. Plasmas, 13, 032307

Knoll D.A., Chacón L., 2006b, Physical Review Letters, 96, 135001

Kopp R.A., Pneuman G.W., 1976, Sol. Phys., 50, 85

Krucker S., Hudson H.S., Glesener L., White S.M., Masuda S., Wuelser J.P., Lin R.P., 2010, ApJ, 714, 1108

Kulsrud R.M., 2011, Physics of Plasmas, 18, 111201

Lao L., Ferron J., Groebner R., Howl W., John H.S., Strait E., Taylor T., 1990, Nucl. Fusion, 30, 1035

Lau Y., Finn J.M., 1990, ApJ, 350, 672

Lawson J.D., 1957, Proceedings of the Physical Society B, 70, 6

Le A., Egedal J., Ohia O., Daughton W., Karimabadi H., Lukin V.S., 2013, Physical Review Letters, 110, 135004

Lemen J.R., et al., 2012, Sol. Phys., 275, 17

Lin R.P., 2006, Space Sci. Rev., 124, 233

Lin R.P., et al., 1995, Space Sci. Rev., 71, 125

Lin R.P., et al., 2002, Sol. Phys., 210, 3

Litvinenko Y.E., 1996, ApJ, 462, 997

Litvinenko Y.E., 2006, A&A, 452, 1069

Litvinenko Y.E., Craig I.J.D., 1999, Sol. Phys., 189, 315

Litvinenko Y.E., Somov B.V., 1993, Sol. Phys., 146, 127

Litvinenko Y.E., Forbes T.G., Priest E.R., 1996, Sol. Phys., 167, 445

Longcope D.W., Parnell C.E., 2009, Sol. Phys., 254, 51

Loureiro N.F., Schekochihin A.A., Cowley S.C., 2007, Physics of Plasmas, 14, 100703

Loureiro N.F., Schekochihin A.A., Zocco A., 2013, Physical Review Letters, 111, 025002

Lowrie W.B., 2011. Ph.D. thesis, University of Washington

Lukin V.S., 2007. Ph.D. thesis, Princeton University

Lukin V.S., Linton M.G., 2011, Nonlinear Processes in Geophysics, 18, 871

Ma Z.W., Bhattacharjee A., 2001, J. Geophys. Res., 106, 3773

Malyshkin L.M., Linde T., Kulsrud R.M., 2005, A&A, 436, 1103

Mandrini C.H., Demoulin P., Schmieder B., Deluca E.E., Pariat E., Uddin W., 2006, Sol. Phys., 238, 293

Mandt M.E., Denton R.E., Drake J.F., 1994, Geophys. Res. Lett., 21, 73

Masson S., Pariat E., Aulanier G., Schrijver C.J., 2009, ApJ, 700, 559

Masuda S., Kosugi T., Hara H., Tsuneta S., Ogawara Y., 1994, Nature (London), 371, 495

Max-Planck-Institut fur Plasmaphysik, 2009, Tokamak

Meier E.T., 2011. Ph.D. thesis, University of Washington

Miller J.A., et al., 1997, J. Geophys. Res., 102, 14631

Murphy R.J., Kozlovsky B., Share G.H., Hua X.M., Lingenfelter R.E., 2007, ApJS, 168, 167

Northrop T.G., 1963, The Adiabatic Motion of Charged Particles. Wiley

Olshevsky V., Lapenta G., Markidis S., 2013, Physical Review Letters, 111, 045002

Ono Y., Morita A., Katsurai M., Yamada M., 1993, Phys. Fluids B: Plasma Phys., 5, 3691

Ono Y., et al., 2012, Plasma Phys. & Controlled Fusion, 54, 124039

Park W., Monticello D.A., White R.B., 1984, Physics of Fluids, 27, 137

Parker E.N., 1957, J. Geophys. Res., 62, 509

Parker E.N., 1988, ApJ, 330, 474

Parnell C.E., De Moortel I., 2012, Philosophical Transactions of the Royal Society A: Mathematical, Physical and Engineering Sciences, 370, 3217

Parnell C.E., Smith J.M., Neukirch T., Priest E.R., 1996, Physics of Plasmas, 3, 759

Peng Y.K.M., et al., 2005, Plasma Phys. and Control. Fusion, 47, B263

Petschek H.E., 1964, NASA Special Publication, 50, 425

Pontin D.I., Bhattacharjee A., Galsgaard K., 2007a, Physics of Plasmas, 14, 052106

Pontin D.I., Bhattacharjee A., Galsgaard K., 2007b, Physics of Plasmas, 14, 052109

Pontin D.I., Al-Hachami A.K., Galsgaard K., 2011, A&A, 533

Priest E., Forbes T., 2000, Magnetic Reconnection: MHD Theory and Applications. Cambridge University Press

Priest E.R., 2000, In R. Ramaty & N. Mandzhavidze, ed., High Energy Solar Physics Workshop - Anticipating HESSI, vol. 206 of Astronomical Society of the Pacific Conference Series, pp. 13–+

Priest E.R., Pontin D.I., 2009, Physics of Plasmas, 16, 122101

Priest E.R., Titov V.S., 1996, Royal Society of London Philosophical Transactions Series A, 354, 2951

Raman R., et al., 2010, Phys. Rev. Lett., 104, 095003

Reale F., 2010, Living Reviews in Solar Physics, 7

Ren Y., Yamada M., Gerhardt S., Ji H., Kulsrud R., Kuritsyn A., 2005, Physical Review Letters, 95, 055003

Ricci P., Lapenta G., Brackbill J.U., 2002, Geophys. Res. Lett., 29, 2088

Ricci P., Brackbill J.U., Daughton W., Lapenta G., 2004, Physics of Plasmas, 11, 4102

Rutherford P.H., 1973, Physics of Fluids, 16, 1903

Scannell R., et al., 2010, Rev. Sci. Inst., 81, 100000

Schindler K., Hesse M., Birn J., 1988, J. Geophys. Res., 93, 5547

Schmidt S., Günter S., Lackner K., 2009, Phys. Plasmas, 16, 072302

Schou J., et al., 2012, Sol. Phys., 275, 229

Shafranov V., 1966, Reviews of Plasma Physics, 2, 103

Shibata K., Tanuma S., 2001, Earth, Planets, and Space, 53, 473

Shibata K., Masuda S., Shimojo M., Hara H., Yokoyama T., Tsuneta S., Kosugi T., Ogawara Y., 1995, ApJL, 451, L83+

Shiraiwa S., et al., 2004, Phys. Rev. Lett., 92, 035001

Simakov A.N., Chacón L., Zocco A., 2010, Phys. Plasmas, 17, 060701

Somov B.V., Kosugi T., 1997, ApJ, 485, 859

Sovinec C.R., et al., 2004, Journal of Computational Physics, 195, 355

Speiser T.W., 1965, J. Geophys. Res., 70, 4219

Spitkovsky A., 2008, In Bassa C., Wang Z., Cumming A., Kaspi V.M., eds., 40 Years of Pulsars: Millisecond Pulsars, Magnetars and More, vol. 983 of American Institute of Physics Conference Series, pp. 20–28

Spitzer L., 1962, Physics of Fully Ionized Gases. Interscience Publishers

Stanier A., Browning P., Dalla S., 2012, A&A, 542, A47

Stanier A., Browning P., Gordovskyy M., McClements K.G., Gryaznevich M.P., Lukin V.S., 2013a, ArXiv e-prints, http://arxiv.org/abs/1308.2855

Stanier A., Browning P., Gordovskyy M., McClements K.G., Gryaznevich M.P., Lukin V.S., 2013b, In 40th EPS Conference on Plasma Physics, http://ocs.ciemat.es/EPS2013PAP/pdf/O2.401.pdf

Strait E.J., 1994, Physics of Plasmas, 1, 1415

Sturrock P.A., 1966, Nature (London), 211, 695

Su Y., Veronig A.M., Holman G.D., Dennis B.R., Wang T., Temmer M., Gan W., 2013, Nature Physics, 9, 489

Sui L., Holman G.D., 2003, ApJL, 596, L251

Sun X., Hoeksema J.T., Liu Y., Chen Q., Hayashi K., 2012a, ApJ, 757, 149

Sun X., Hoeksema J.T., Liu Y., Wiegelmann T., Hayashi K., Chen Q., Thalmann J., 2012b, ApJ, 748, 77

Sweet P.A., 1958, In Lehnert B., ed., Electromagnetic Phenomena in Cosmical Physics, vol. 6 of IAU Symposium, p. 123

Swisdak M., Drake J.F., Opher M., 2013, The Astrophysical Journal Letters, 774, L8

Sykes A., et al., 2001, Nucl. Fusion, 41, 1423

Taylor J.B., 1974, Physical Review Letters, 33, 1139

Taylor J.B., 1986, Reviews of Modern Physics, 58, 741

The Numerical Algorithms Group (NAG), 2013, The NAG Fortran Library. Oxford. United Kingdom. www.nag.com

Tsuneta S., Hara H., Shimizu T., Acton L.W., Strong K.T., Hudson H.S., Ogawara Y., 1992, PASJ, 44, L63

Ugai M., Tsuda T., 1977, Journal of Plasma Physics, 17, 337

Uzdensky D.A., 2011, Space Sci. Rev., 160, 45

Uzdensky D.A., Knigl A., Litwin C., 2002, The Astrophysical Journal, 565, 1205

Vandervoort P.O., 1960, Annals of Physics, 10, 401

Vekstein G.E., Browning P.K., 1997, Physics of Plasmas, 4, 2261

Vilmer N., MacKinnon A.L., Hurford G.J., 2011, Space Sci. Rev., 159, 167

Voss G., Bond A., Hicks J., Wilson H., 2002, Fusion Eng. & Design, 63-64, 65

Wesson J., 2011, Tokamaks. International Series of Monographs on Physics, OUP Oxford

Wiegelmann T., Sakurai T., 2012, Living Reviews in Solar Physics, 9

Wolfram Research, Inc., 2010, Mathematica Edition: Version 8.0. Champaign, Illinois

Wood P., Neukirch T., 2005, Sol. Phys., 226, 73

Xiao C.J., et al., 2006, Nature Physics, 2, 478

Yamada M., Levinton F.M., Pomphrey N., Budny R., Manickam J., Nagayama Y., 1994, Physics of Plasmas, 1, 3269

Yamada M., et al., 1997, Phys. Plasmas, 4, 1936

Yamada T., et al., 2010, Plasma and Fusion Research, 5, S2100

Yamada T., et al., 2012, In 39th EPS Conference on Plasma Physics, http://ocs.ciemat.es/epsicpp2012pap/pdf/P1.013.pdf

Yamada T., et al., 2013, Phys. Rev. Lett., in preparation

Yeates A.R., Hornig G., Wilmot-Smith A.L., 2010, Physical Review Letters, 105, 085002

Yokoyama T., Akita K., Morimoto T., Inoue K., Newmark J., 2001, ApJL, 546, L69

Zhang S., Jin J., 1996, Computation of special functions. John Wiley & Sons, New York

Zharkova V.V., Gordovskyy M., 2004, ApJ, 604, 884

Zharkova V.V., Gordovskyy M., 2005, MNRAS, 356, 1107

Zhu Z., Parks G., 1993, J. Geophys. Res., 98, 7603